

THE INFLUENCE OF THE EARTH'S ROTATION ON THE WIND-DRIVEN FLOW
IN HECATE STRAIT, BRITISH COLUMBIA

By

Charles Gordon Hannah

B. A. Sc. (Engineering Physics) University of British Columbia, 1985

A THESIS SUBMITTED IN PARTIAL FULFILLMENT OF
THE REQUIREMENTS FOR THE DEGREE OF
DOCTOR OF PHILOSOPHY

in

THE FACULTY OF GRADUATE STUDIES
PHYSICS

We accept this thesis as conforming
to the required standard

THE UNIVERSITY OF BRITISH COLUMBIA

September 1992

© Charles Gordon Hannah, 1992

In presenting this thesis in partial fulfilment of the requirements for an advanced degree at the University of British Columbia, I agree that the Library shall make it freely available for reference and study. I further agree that permission for extensive copying of this thesis for scholarly purposes may be granted by the head of my department or by his or her representatives. It is understood that copying or publication of this thesis for financial gain shall not be allowed without my written permission.

Physics

The University of British Columbia

2075 Wesbrook Place

Vancouver, Canada

V6T 1W5

Date:

Sept 23/92

Abstract

A regional model of the depth-averaged currents in Hecate Strait, British Columbia has been developed: the Hecate Strait Model. When driven by local winds the model simulates the winter transport fluctuations and captures the character of the observed circulation patterns. The modelled currents are consistent with the historical view of the winter circulation and contain the counter-current observed in southern Hecate Strait. The counter-current is due to topographic steering: the tendency, in a rotating fluid, for the flow to follow the local depth contours. The model results suggest a new interpretation of the observed currents in southern Hecate Strait, which has implications for particle transport.

The influence of the earth's rotation on the water transport through Hecate Strait is investigated using the concept of rotation-limited-flux. The effect of rotation is to reduce the flux through the strait compared with a non-rotating strait. Numerical experiments with the Hecate Strait Model show that the earth's rotation reduces the steady state transport by a factor of three. The relationship between the steady-state transport and the Coriolis parameter is consistent with rotation-limited-flux.

Table of Contents

Abstract	ii
List of Tables	ix
List of Figures	xii
Acknowledgement	xxiv
1 Introduction	1
1.1 Motivation for this Work	3
1.1.1 Fisheries	3
1.1.2 Oil Spills	3
1.2 Objectives	4
1.3 Plan of the Thesis	5
2 Physical Oceanography of the Queen Charlotte Islands Region	8
2.1 Geography and Bathymetry	8
2.2 Tides	11
2.2.1 Residual Tidal Currents	11
2.3 Temperature, Salinity, Density, and Fresh Water	16
2.4 Winds	18
2.5 Circulation	19
2.5.1 Hecate Strait 1983-1984	20
2.5.2 Queen Charlotte Sound 1982	21

2.5.3	Dixon Entrance	24
2.5.4	Outer Shelf and the Deep Ocean	27
2.6	Summary	29
3	Hecate Strait: Data for Model Comparison	30
3.1	Calculation of Wind Stress	30
3.2	Wind and Current Fluctuations	32
3.2.1	Spatial Patterns	35
3.2.2	Water Transport Through the Strait	38
3.2.3	Transport and the Mode 1 Currents	43
3.3	Drifters	45
3.4	Summary	54
4	Low Frequency Flow in Sea Straits	56
4.1	Cross-strait Geostrophic Balance	56
4.2	Frictional Adjustment	58
4.3	Rotation-limited-flux	59
4.3.1	Derivation	62
4.3.2	Wind and Pressure Driven Sea Level Responses	66
4.3.3	Comparison with Observations in Hecate Strait	68
5	The Hecate Strait Model	73
5.1	The Depth-Averaged, Non-Linear Shallow Water Equations	74
5.1.1	Topographic Steering	77
5.1.2	Geostrophic Balance	77
5.2	Numerical Formulation	79
5.2.1	Discrete Equations: Arakawa-Lamb, 1981	79

5.2.2	Time Stepping: Leap-frog Scheme	80
5.3	Bathymetry, Grid Size and Time Step	81
5.4	Energy Dissipation Mechanisms	83
5.5	Lateral Boundary Conditions	85
5.5.1	Side Walls	85
5.5.2	Open Boundary Conditions	85
5.5.3	Implementation of the Open Boundary Conditions	86
5.6	Atmospheric Forcing Fields	89
5.6.1	Wind Stress	89
5.6.2	Pressure Gradients	90
5.7	Computer Program	90
6	Evolution from Rest to Steady State in the Hecate Strait Model	91
6.1	Frictional Adjustment	92
6.2	The Basic Experiment: Spin-up	94
6.3	Selecting Friction Parameters	96
6.4	Adjustment Time-Scales in Hecate Strait	98
6.4.1	Basin Resonance	103
6.5	Circulation Patterns: A Preview	103
6.6	Force Balance	106
7	Rotational Limitations on the Water Transport Through Hecate Strait	108
7.1	Winter 1984	108
7.2	Friction, Coriolis Parameter, and Transport	112
7.3	Frequency Response	120
7.4	Summary	122

8	Wind-Driven Flow Patterns in Hecate Strait	125
8.1	Basic Patterns	126
8.1.1	Vorticity Balance	130
8.1.2	Effect of Rotation	134
8.1.3	Chatham Sound Diversion	137
8.2	Comparison with Observations in Hecate Strait	138
8.2.1	Currents: Winter 1984	139
8.2.2	Drifters	144
8.3	Regional Circulation Patterns	150
8.3.1	Southern Hecate Strait	155
8.4	Summary	157
9	Conclusion	159
9.1	Future Work	161
	Bibliography	164
A	List of symbols	170
B	Empirical Orthogonal Function Analysis	172
C	Butterworth Filter: End Effects	176
D	Hecate Strait Model: Details	177
D.1	Numerical formulation	177
D.1.1	Arakawa and Lamb, 1981	178
D.1.2	Discussion	182
D.1.3	Leap-frog Scheme	183

D.1.4	The Robert Filter	184
D.2	Model Bathymetry	185
D.2.1	Creating the Bathymetry	187
D.3	Drifter Algorithm	189
D.3.1	Trajectory Computations	190
D.4	Lateral Boundary Conditions	191
D.4.1	Side Walls and Boundary Layers	191
D.4.2	Open Boundary Conditions	193
D.4.3	Cross-shelf Boundary	196
D.4.4	Off-shore Boundary	196
E	Tests in Rectangular Domains	198
E.1	Flat Bottom	198
E.1.1	Uniform Along-Shore Wind	200
E.1.2	Bell-Shaped Wind	203
E.2	Sloping Shelf	203
E.3	Frictional Adjustment on a Sloping Shelf	210
E.4	Stories	213
F	Hecate Strait Model: Tests and Experiments	214
F.1	Open Boundary Condition Tests	214
F.2	Adjustment Time-Scales in Hecate Strait	217
F.3	Steady State Velocity Fields	225
F.3.1	Bottom Friction	225
F.3.2	Bathymetry	225
F.3.3	Spatially Varying Wind	229

G Friction, Coriolis Parameter and Transport	231
G.1 Steady State Transport	231
G.2 Adjustment Time	234
G.3 Discussion	235

List of Tables

3.1	Statistics for the current EOF analysis for the winter of 1984. The Λ_i are the first three eigenvalues. Scaled refers to whether each time series was scaled by its standard deviation before EOF analysis.	36
3.2	Characteristics of time series in winter, 20 Jan to 4 Apr, 1984. The last two columns give maximum correlations and phase leads in hours of a given time series with transport through W-line. EOF 1 is the lowest (first) mode of wind from the the empirical orthogonal function analysis. Table 1c in Crawford et al.(1988).	39
3.3	Correlation of transport with various wind time series for the period 25 Jan - 30 Mar 1984. The maximum correlation r_{max} was obtained for the lead given (lead of the wind with respect to the transport). Wind time series are the along-shore component of wind speed (W), wind stress using a constant drag coefficient (τ_1), and wind stress using Smith (1988) (τ_2).	42
4.4	Estimates of parameters for Hecate Strait	66
4.5	Sub-surface pressure EOF modes in Hecate Strait. Each mode has two columns: the dimensionless eigenvector, and the eigenvector with units of cm of water. The eigenvalues are dimensionless. Fall 1983: 28 September to 20 December 1984. Winter 1984: 20 January to 4 April 1984. (Courtesy W.R. Crawford.)	70
6.6	Standard regional model parameters.	96

6.7	Linear friction. Steady state transport (Sv) for a range of k and μ . Along-shore wind stress $\tau = 0.1$ Pa.	96
6.8	Quadratic friction. Steady state transport (Sv) for a range of C_d and u_0 . Along-shore wind stress $\tau = 0.1$ Pa. Rayleigh friction $\mu = 3.0 \cdot 10^{-7} \text{ s}^{-1}$	97
7.9	Model verification experiments.	109
7.10	Model verification. Comparison of the simulated and observed transport through Hecate Strait for the period 25 Jan - 30 March 1984. The correlations are the maximum linear correlation coefficients of the transport time series with the along-shore wind stress and with the observed transport.	111
8.11	The first two eigenvalues from the EOF analysis of the simulated and observed velocities for the period 25 January - 30 March 1984. Each eigenvalue, Λ_i , is represented by two values; its magnitude and the fraction of total energy that this represents (in brackets).	139
A.12	List of symbols used.	171
D.13	Amplitude response of the time domain filter for sinusoidal input. For periods of an hour or more the amplification factor is very close to 1 and is written in the form $1 - \epsilon$, where ϵ is a small number. $\Delta t = 10$ s and $\gamma = 0.01$	185
E.14	Parameters for open boundary condition tests with a flat bottomed ocean	199
E.15	Parameters for open boundary condition tests with a sloping shelf	207

E.16 Frictional adjustment. Comparison of theoretical frictional adjustment times and the steady state velocity with the model results. The model results were fit to $v = v_{\infty}(1 - e^{-t/t_0})$. Fits were computed using time series of length 167 hours. Wind stress $\tau = 0.1$ Pa. Density $\rho = 1025$ kg m^{-3}	212
F.17 Steady state transport in domains of different size with an along-shore wind ($\tau = 0.1$ Pa) and the standard friction parameters. Domain sizes are given in grid points. The open boundary conditions (OBC) are the flow relaxation scheme (FRS) and closed boundaries. The results for standard, big, and long were the same for FRS zone widths of 20 and 40 grid cells.	215
G.18 Steady-state transport (Sv) through Hecate Strait as a function of Coriolis parameter. The wind stress $\tau = 0.1$ Pa, $f_0 = 1.1 \times 10^{-4}$ s^{-1} , and $\mu = 3 \times 10^{-3}$ s^{-1}	231
G.19 Localized wind experiment. Estimating the parameter W/L from the steady-state transport. The wind stress $\tau = 0.1$ Pa, $f_0 = 1.1 \times 10^{-4}$ s^{-1} , and $\mu = 3 \times 10^{-3}$ s^{-1}	232
G.20 Uniform wind experiment. Estimating the parameter W/L from the steady-state transport. The wind stress $\tau = 0.1$ Pa, $f_0 = 1.1 \times 10^{-4}$ s^{-1} , and $h^* = 70$ m.	232
G.21 Localized wind experiment. Estimating the parameter W/L from the spin-up time constant data. The wind stress $\tau = 0.1$ Pa, $f_0 = 1.1 \times 10^{-4}$ s^{-1} , and $\mu = 3 \times 10^{-3}$ s^{-1}	235

List of Figures

1.1	The Queen Charlotte Islands region.	2
2.2	Chart of the Queen Charlotte Islands region. Depth contours are in metres. Courtesy of M.G.G. Foreman.	10
2.3	Co-range and co-phase values for the semi-diurnal tide. Tidal range (broken line) in metres; tidal phase (solid line) in degrees. Difference of 29° corresponds to time difference of 1 h. (Fig. 14.5 in Thomson, 1981). . .	12
2.4	Observed semi-diurnal tidal streams in the upper 50 m depth. Solid lines and arrows give orientation of major flow and ebb directions: dashed lines give minor flow directions. Scale measures speed relative to the midpoint of each axis. (Fig. 22 in Thomson, 1989)	13
2.5	Barotropic residual tidal velocities. (Courtesy of M.G.G. Foreman, 1992.)	15
2.6	The seasonal cycle of density at a station in central Hecate Strait, 1960-62. (Fig. 84 in Dodimead, 1980)	17
2.7	The seasonal cycle of density at a station on the northern flank of Middle Bank in Queen Charlotte Sound, 1954-55. (Fig. 82 in Dodimead, 1980) .	17
2.8	Average currents and winds in Hecate Strait. Solid arrows represent currents within 50 m of the surface, dashed lines, currents at intermediate depths and dotted lines, currents within 15 m of the bottom. Wide shaded arrows represent winds. (a) summer, 16 May to 9 September 1983, (b) fall, 28 September to 20 December 1983, (c) winter, 20 January to 4 April 1984. (Fig. 2 in Crawford et al., 1988).	22

2.9	Currents and winds in Queen Charlotte Sound for the period 4 June - 15 September 1982. Vectors of average currents, and winds at Cape St. James and McInnes Island are the solid lines and the principal axes of variance are the dotted lines. a) near-surface currents and winds, b) near-bottom currents. (Fig. 7 in Crawford et al., 1985)	23
2.10	Smoothed drifter tracks from Dixon Entrance summer 1984. Tidal currents are averaged out. The solid circles mark the position of the drifters at the onset of a storm on 21 June 1984, with winds of 15 m s^{-1} from the southeast. (Fig. 3 in Crawford and Greisman, 1987.)	25
2.11	Average currents and winds in Dixon Entrance for the period 22 April-19 August 1984. Solid arrows represent currents within 50 m of the surface, dashed lines, currents at intermediate depths and dotted lines, currents within 15 m of the bottom. The wide arrows at D7S and Langara Island represent winds. (Fig. 5 in Crawford and Greisman, 1987.)	26
2.12	Prevailing surface currents in the North Pacific Ocean. Double arrows are intense boundary currents, speeds typically 1-2 m/s: over most of the rest of the region speeds are less than 0.25-0.50 m/s. Arrows correspond to prevailing winter time flow off the west coast of North America. (Fig. 13.17 in Thomson, 1981)	28
3.13	Dependence of drag coefficient C_d on wind speed for winds measured at 10 m and neutral atmospheric stability (Smith, 1988).	31
3.14	Locations of current meters, pressure gauges and anemometers in Hecate Strait from Jan - April 1984. Fig. 1 from Crawford et al. (1985, with permission).	33

3.15	Vectors of the empirical orthogonal functions for the period 20 January-4 April, 1984. Fig. 8 from Crawford et al., 1990.	37
3.16	The observed transport and along-shore wind stress fluctuations in Hecate Strait from 25 Jan – 30 Mar 1984. Both time series have been normalized by subtracting the mean and dividing by the standard deviation.	42
3.17	Comparison of the transport and mode 1 currents for the period 25 Jan - 31 Mar 1984. Both time series have been normalized by subtracting the mean and dividing by the standard deviation.	44
3.18	Path of satellite tracked drifter for 9 Sept – 29 Nov 1983. The winds at Cape St. James are shown in the lower left corner (1 day low-pass filtered). The free end of the wind vectors point in the direction the wind is blowing to. (Adapted from Fig.13 Hannah et al., 1991.)	46
3.19	Drifter tracks near Cape St. James for the period 12–20 March 1986. (Adapted from Fig. 12a in Thomson and Wilson, 1987.)	48
3.20	Drifter tracks in southern Hecate Strait from 8–29 July 1990. The winds were from the NW or N. (Adapted from Fig. 14 in Hannah et al., 1991.)	49
3.21	Paths of two satellite tracked drifters from 19 January to 20 March 1991. The starting locations are marked by the two black dots east of Cape St. James. The winds were generally from the SE.	51
3.22	Drifters in northern Hecate Strait from July 1991. The abrupt change in direction displayed by drifters a35, c22, and b40 corresponds to the change in wind direction from NE to SE on July 10. Drifter b32 was launched after the wind changed direction. The arrows on the drifter paths mark 2 days elapsed time.	52

3.23	Two drifters in northern Hecate Strait from 11 to 13 July 1991. The drogue on drifter b32 was centred at 10 m, the drogue on b34 at 3.5 m. The two drifters were launched at the same time and b34 (shallow) travelled twice as far as b32 (deep). The arrows mark 1 day elapsed time.	53
4.24	Schematic diagram of Hecate Strait.	57
4.25	Plan view of the strait. η_1 and η_2 are the far-field sea level elevations. The other η_i are the sea levels at the respective corners. The corner labelling scheme is for the northern hemisphere.	57
4.26	Frictional adjustment with sinusoidal forcing. The solid line is the velocity and the dotted line is the wind stress. The frictional scale $\lambda = \omega/6$	60
4.27	The sea level structure for the wind-driven mode, N_w	67
4.28	The sea level structure for the pressure-driven mode, N_p	67
4.29	Spatial patterns of the observed sub-surface pressure fluctuations in Hecate Strait. Plotted are the first two modes of the empirical orthogonal function analysis for the fall of 1983 and the winter of 1984. The modal amplitudes are in cm of water. The arrow in Hecate Strait is the direction of the geostrophic current implied by the cross-strait pressure difference. The data are listed in Table 4.5.	69
5.30	Sketch of the ocean defining the axis system.	75
5.31	A sea strait	78
5.32	The model domain	82
6.33	Frictional adjustment in a simple channel. Spin-up time as function of the water depth for $k = 0.5 \cdot 10^{-3} \text{ s}^{-1}$ and (a) $\mu = 0$; (b) $\mu = 3 \cdot 10^{-8} \text{ s}^{-1}$; (c) $\mu = 3 \cdot 10^{-7} \text{ s}^{-1}$; (d) $\mu = 3 \cdot 10^{-6} \text{ s}^{-1}$	93

6.34	Frictional adjustment in a simple channel. Steady state velocity as a function of the water depth for $k = 0.5 \cdot 10^{-3} \text{ s}^{-1}$ and (a) $\mu = 0$; (b) $\mu = 3 \cdot 10^{-8} \text{ s}^{-1}$; (c) $\mu = 3 \cdot 10^{-7} \text{ s}^{-1}$; (d) $\mu = 3 \cdot 10^{-6} \text{ s}^{-1}$	93
6.35	The standard model domain. The cross-shore flow relaxation zones are not shown; they extend 100 km off the top and bottom of the figure. The line on the left-hand side is the off-shore open boundary.	95
6.36	Spin-up test. Time series of transport through Hecate Strait for an impulsively started wind. (a) R-line, (b) W-line, (c) M-line. The dotted line in (b) is the transport when the wind was started smoothly (see text). . .	99
6.37	Spin-up test. Time series of sea levels in Hecate Strait. a) Atli and b) Beauchemin.	100
6.38	Spin-up test. Time series of sea levels on the outer coast. a) Cape Muzon, b) W. QCI, and c) Cape Scott.	100
6.39	Spin-up test. Cross strait pressure difference Beauchemin minus Atli. . .	100
6.40	Spin-up test. Along-shore pressure difference Cape Scott minus Cape Muzon.	101
6.41	Spin-up test. Comparison of transport through R-line with a two component adjustment.	101
6.42	The high frequency oscillation at W-line.	104
6.43	The power spectrum of the oscillation at W-line.	104
6.44	Steady-state transports with a uniform SE wind. The wind direction is indicated with an arrow on Graham Island. The 200 m contour is the heavy dark line. Only 1/4 of the vectors are plotted. The vectors were suppressed for depths greater than 500 m.	105
6.45	The along-strait force balance at R-line after two days of steady along-shore SE wind.	107

7.46	The wind stress time series used to drive the verification experiments. The vectors are oriented to conform to the orientation of the model domain; up represents a SE wind. The winds were measured at W4S.	109
7.47	Transport through W-line from 25 Jan - 30 Mar 1984. Comparison of simulation E501a (solid) and the observations (dotted).	110
7.48	Time series of along-shore wind stress (dotted) and simulated transport (solid) in Hecate Strait from 25 Jan - 30 Mar 1984. Both time series have been normalized.	110
7.49	Cross-strait sea level difference Beauchemin minus Atli for the period 25 Jan - 30 Mar 1984. Comparison of E501a (solid) with the observations (dotted).	113
7.50	Steady state transport as a function of Coriolis parameter for a wind localized over Hecate Strait. The Coriolis parameter has been normalized with $f_0 = 1.1 \times 10^{-4} \text{ s}^{-1}$	115
7.51	Steady-state transport as a function of Coriolis parameter for a uniform along-shore wind stress (triangle) and for a wind stress localized over Hecate Strait. In both cases $k = 0.5 \cdot 10^{-3} \text{ s}^{-1}$. The Coriolis parameter has been normalized with $f_0 = 1.1 \times 10^{-4} \text{ s}^{-1}$	115
7.52	Transport spin-up for an along-shore wind localized over Hecate Strait for $k = 0.5 \cdot 10^{-3} \text{ s}^{-1}$. (a) $f = 0$ and (b) $f = 1.1 \cdot 10^{-4} \text{ s}^{-1}$	118
7.53	Relaxation time as a function of Coriolis parameter for a wind localized over Hecate Strait. a) $k = 0.5 \cdot 10^{-3} \text{ s}^{-1}$, b) $k = 2.0 \cdot 10^{-3} \text{ s}^{-1}$	118
7.54	Amplitude spectrum computed from the response of the transport through Hecate Strait to oscillating winds (data points). The solid line is an approximate spectrum (see text).	121

7.55	Phase spectrum computed from the response of the transport through Hecate Strait to oscillating winds.	121
7.56	Transport time series for an oscillating along-shore wind with period 6 days. The solid line is the transport, the dotted is the wind forcing. Both time series have been normalized by the amplitude of the respective sine waves (0.15 Sv, 0.1 Pa).	123
7.57	The transport spin-up in Hecate Strait for a non-rotating (solid) and rotating (dashed) version of the model. For the non-rotating case $k = 1.3 \cdot 10^{-3} \text{ m s}^{-1}$ and for the rotating case $k = 0.5 \cdot 10^{-3} \text{ m s}^{-1}$. The bottom friction for the non-rotating case was chosen so that the steady-state transports were similar.	123
8.58	Evolution of the velocity field with a steady SE wind. The wind direction is indicated with an arrow on Graham Island. The 200 m contour is the heavy dark line. Only 1/4 of the vectors are plotted.	127
8.59	The velocity field and transport vector field at Day 8, with a steady SE wind - typical winter storm winds. On the shelf the velocities have reached a steady state. In the deep ocean the velocities are still adjusting, but this does not affect the velocity field on the shelf. The 200 m contour is shown.	128
8.60	Steady-state velocity fields for two different wind directions.	131
8.61	Steady-state velocity field for a SE wind and a non-rotating earth ($f = 0$).	135
8.62	Steady-state velocity field when: (a) northern Hecate Strait is blocked off; (b) the constriction at the northern end of Hecate Strait is removed (see text). This was for a SE wind and a rotating earth, $f = 1.1 \times 10^{-4} \text{ s}^{-1}$.	136
8.63	Close up of the northeast corner of Hecate Strait.	137

8.64	Model verification. Comparison of the simulated (E501a) and observed currents in Hecate Strait from 25 January to 30 March 1984. The depth-averaged observations are shown with open arrow heads; the simulated currents with solid arrow heads. The model was driven with winds measured near W04.	140
8.65	Time series of modal amplitudes of the EOF-mode-1 velocities. Comparison of simulation E501a (solid) with the observations (dotted) in Hecate Strait from 25 January to 30 March 1984.	143
8.66	Comparison of an observed drifter trajectory and simulated drifters in Moresby Trough from 12 to 18 July 1990. The observed drifter (solid) started at the cross. Simulated drifters (dashed) were started at daily intervals (circles) along the observed drifter trajectory. The simulated drifter trajectories are 4 days long. In cases where the simulated drifter did not move very far an extra drifter was started 1 grid point away. The winds were measured at a weather buoy located 80 km below the bottom of the figure (see text). The wind stress time series is shown in the lower left corner. The free end of the wind vectors indicates the direction the wind is blowing to. The 200 m contour is shown for reference.	145
8.67	Comparison of an observed drifter trajectory and simulated drifters near Cape St. James from 21 to 26 July 1990. See Fig. 8.66 for details. . . .	146
8.68	Observed and simulated drifter trajectories in northern Hecate Strait from 11 to 19 July 1991. Drifter b32 was launched shortly after the winds changed direction on July 10. The wind stress time series shown in the lower left corner was measured at the * in the center of the strait. The free end of the wind vectors indicates the direction the wind is blowing to.	148

8.69	Observed and simulated drifter trajectories in northern Hecate Strait from 8 to 10 July 1991. All the trajectories are 2 days long. During this time the wind was steady and from the NW. The end of the trajectories corresponds to the change in wind direction near July 10. The wind stress time series shown in the lower left corner was measured at the * in the center of the strait.	149
8.70	Simulated drifters in the northern half of the model domain for 25 Jan to 30 Mar 1984. The starting location of each drifter is marked by a cross. The drifter trajectories are marked with arrows at 20 d intervals.	151
8.71	Simulated drifters in Queen Charlotte Sound for 25 Jan to 30 Mar 1984. The starting location of each drifter is marked by a cross. The drifter trajectories are marked with arrows at 20 d intervals.	152
8.72	Simulated drifters near Cape St. James. The starting location of each drifters is marked by a cross. The drifter trajectories are marked with arrows at 20 d intervals.	153
8.73	Sketch of the circulation in Hecate Strait and Queen Charlotte Sound under a SE wind.	156
C.74	The end effect of the Butterworth filter used to filter the time series data. The filter was an 8-th order filter with 1/2 power at 40 h. The time step was 15 m. The solid line is the filter output and the dashed line is the input.	176
D.75	The C-grid.	179
D.76	Boundaries in the C-grid.	192

E.77 Model domain for the open boundary condition tests. The flow relaxation zones are marked by shading.	199
E.78 Uniform along-shore wind experiment. Time series of along-shore velocity at the coast (site B). The time series at sites A,C are identical.	201
E.79 Uniform along-shore wind experiment. The steady state a) sea level contours (cm), and b) velocity vectors.	202
E.80 Bell-shaped wind experiment. Sea level after 48 hours. The contour interval is 0.5 cm.	204
E.81 Bell-shaped wind experiment. Time series of along-shore velocity at sites A, B, C. Data from the test domain is plotted as solid lines and data from the extended domain is plotted as dotted lines.	205
E.82 Bell-shaped wind experiment. Time series of excess mass. Data from the test domain is plotted as solid lines and data from the extended domain is plotted as dotted lines.	206
E.83 Cross-section of the sloping shelf. Topography taken from regional model.	207
E.84 Sloping shelf experiment. Time series of along-shore velocity at three different depths. The depth $h = 77$ m corresponds to location $(i,j) = (25,36)$. The depths $h = 155$ m and $h = 1786$ m correspond to $(i,j) = (20,36)$ and $(10,36)$ respectively.	208
E.85 Sloping shelf experiment. a) sea level field (cm), and b) velocity field, after 6.5 days.	209

E.86 Sloping shelf experiment. Along-shore velocity as a function of along-shore position. The velocity field was sampled at 3 distances off-shore, corresponding to depths of 77 m, 155 m, 1786 m. The model was forced with a uniform along-shore wind $\tau = 0.1$ Pa and the Rayleigh friction $\mu = 0$. The velocity field was sampled after 6.5 days of integration. The flow relaxation zones occupy along-shore locations 1 to 11 and 61 to 71. There are no kinks in the velocity field but there is a slight downward slope in the in the down-wind direction (from left to right).	211
F.87 Comparison of the transport through W-line for two different open boundary conditions: (a) flow relaxation method (E321,solid); and (b) closed (E320, dashed). The domain is the long domain.	215
F.88 The velocity field after 6 days near the northern cross-shore boundary. The top of the figure is the open boundary. All of the vectors are shown.	216
F.89 The steady state velocity field forced by an along-shore wind localized over Hecate Strait. The maximum wind stress is 0.1 Pa.	219
F.90 The steady state velocity field forced by an along-shore wind localized over central Queen Charlotte Sound. The maximum wind stress is 0.1 Pa. . .	220
F.91 Comparison of the transport spin-up for three along-shore wind scenarios: (a) spatially uniform, (b) localized over Hecate Strait and (c) localized over Queen Charlotte Sound. The maximum wind stress is 0.1 Pa. . . .	221
F.92 Curve fit to the transport time series for a wind localized over Hecate Strait.	222
F.93 Curve fit to the time series of sea level at Cape Scott minus sea level at Cape Muzon. The wind forcing was the standard spatially uniform wind.	222

F.94	The sea level field for a spatially uniform along-shore wind ($\tau = 0.1$ Pa). The contours are labelled in cm.	223
F.95	Quadratic friction experiment. The steady state velocity field for a spatially uniform along-shore wind. The drag coefficient $C_d = 2.5 \times 10^{-3}$ and the background velocity $u_0 = 0/0$. The wind stress $\tau = 0.1$ Pa.	226
F.96	Spatially varying linear friction experiment. The rms tidal velocity field (cm/s) and the resulting steady state velocity field from the Hecate Strait Model. The wind stress was spatially uniform with $\tau = 0.1$ Pa.	227
F.97	Velocity field with altered bathymetry. The wind stress was spatially uniform with $\tau = 0.1$ Pa. Standard linear friction was used.	228
G.98	Uniform wind experiment. Steady-state transport as a function of Coriolis parameter for three values of k and $\mu = 2.7 \times 10^{-6} \text{ s}^{-1}$. The wind stress $\tau = 0.1$ Pa.	233

Acknowledgement

A graduate student's most important decision is the first one, the choice of supervisor. I thank Paul LeBlond for making my choice seem inspired. His insight, guidance, and support were crucial to the success of this work. I owe a special debt of gratitude to William Crawford at the Institute of Ocean Sciences (IOS), Sidney, B.C., who provided the observational data discussed in this thesis, and was responsible for much of my education as an oceanographer. Thanks Bill. The members of my committee have each made an important contribution to my education, I thank Boye Ahlborn, Luis Sobrino and Paul Budgell.

None of this would have been possible without the support of my family. Thanks to Susan for her support, encouragement, and faith throughout; to Elizabeth and Theodore for the daily reminders of the important things in life.

I have been blessed with good friends, they have contributed to my education and kept me sane. I thank Warren Lee, Mike St. John, the Sunday morning quantum group, the members of FOMI, and the oceanography softball team. A special thanks to the Tuesday morning hockey players.

During my extended visit to the Institute of Ocean Sciences, it was my pleasure to work with many dedicated people. Thanks to the Tides and Currents Section, especially Allan, Anne W., Anne B., Keith, and Tony for letting me abuse their computer system; and to Mike Woodward for the experience of Queen Charlotte Sound in January. My thanks to Greg Holloway and Mike Foreman for the time spent.

I gratefully acknowledge the financial support of the Panel for Energy Research and Development (PERD) Grant 67146, NSERC Grant A7490 and a UBC graduate fellowship. Computer time, the life blood of numerical models, was generously provided by William Hsieh at UBC, by the Institute of Ocean Sciences, and by the Ontario Centre for Large Scale Computing.

Chapter 1

Introduction

The subject of this thesis is the wind-driven ocean currents on the continental shelf around the Queen Charlotte Islands. This work is one of a group of projects whose ultimate goal is the prediction of the movement of particles in the waters of British Columbia's north coast. Particles of interest include fish larvae, nutrients, sediments and pollutants. The work reported here concentrates on the contribution of the wind-driven currents to the circulation: the low frequency component of the flow, with time-scales of days to weeks. The daily oscillations of the tides are ignored.

The focus of this thesis is the winter circulation in Hecate Strait (Fig. 1.1). The historical view was that of a broad current flowing north from Queen Charlotte Sound into Dixon Entrance. Only recently has this description been modified to include a counter-current in south-central Hecate Strait (Crawford et al., 1988; Crawford et al., 1990). The central theme of this work is the influence of the earth's rotation on the wind-driven flow. Two aspects are singled out: 1) the role of rotation in the existence of the counter-current, and 2) the role of rotation in limiting the flux of water through the strait.

The primary tool is a numerical model of the vertically integrated, or depth-averaged, currents in the Queen Charlotte Islands region. The observations indicate that a depth-averaged, wind-driven model is most applicable to Hecate Strait in the winter. This model is called the Hecate Strait Model throughout this thesis. The Hecate Strait Model is used to probe the dynamics and to suggest interpretations of the observations. A

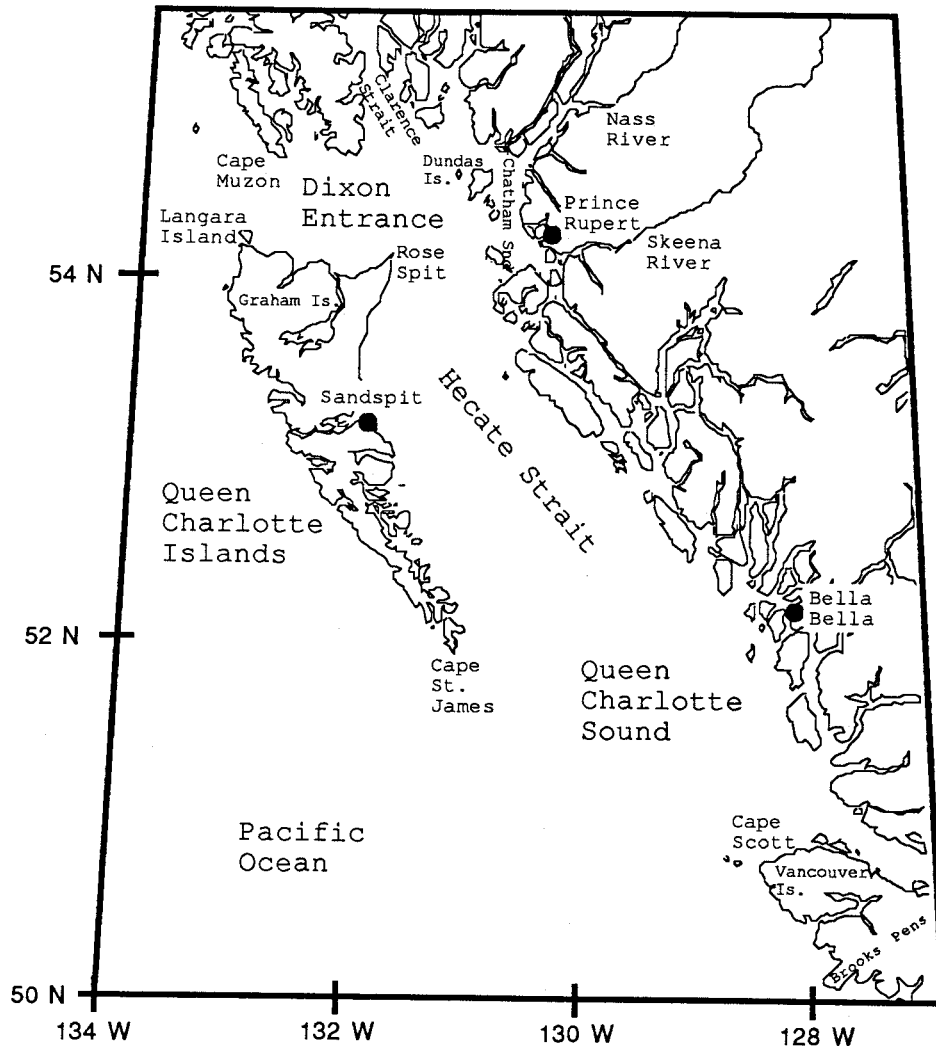


Figure 1.1: The Queen Charlotte Islands region.

practical question addressed is: Does the Hecate Strait model provide a useful guide to the circulation patterns in the region?

1.1 Motivation for this Work

1.1.1 Fisheries

Demonstrating a causal relationship between fluctuations in ocean currents or temperature and fluctuations in the number of fish caught in Hecate Strait is very difficult. This is due in part to the inherent difficulty of estimating the size of the fish stock and in part to our limited knowledge of the ocean. In Hecate Strait there is evidence that fluctuations in the year-class-strengths of English sole (*Parophrys vetulus*) and Pacific cod (*Gadus macrocephalus*) are linked to inter-annual fluctuations in water transport through Hecate Strait in the first quarter of the year (Ketchen, 1956; Tyler and Westrheim, 1986; Tyler and Crawford, 1991).

The regional model results presented in this thesis are being used in a project aimed at illuminating the relationship between the physical oceanography and the recruitment rates of the fish. The project involves hind-casting the transport and current patterns in Hecate Strait for the past 40 years and combining this information with a biological model to investigate the transport of English sole larvae from the spawning grounds in southern Hecate Strait to the nursery areas in northwestern Hecate Strait (Walters et al., 1992).

1.1.2 Oil Spills

The Hecate Strait Model began as one component of a larger project intended to address the physical oceanographic aspect of the recommendations of the West Coast Offshore Exploration Environment Assessment Panel (April 1986, p.96):

The Panel recommends that the Department of Fisheries and Oceans, in cooperation with other agencies, develop a comprehensive research program designed to reduce data gaps necessary to develop a credible model of the impact of an oil blowout on important fish species at their various life stages.

The overall objective of the project is to improve the prediction of oil spill trajectories in northern British Columbia waters. Oil spills are fundamentally a surface phenomenon and the Hecate Strait Model looks at the currents averaged over the water column. Therefore this model will not form the basis for operational prediction of oil-spill trajectories. The goal is to gain insight into the gross features of the circulation patterns and to provide a framework for interpreting near-surface drifter observations. Future modelling will build on this work. In an indirect fashion, the application of the regional model to study the early stages of the life of English sole in Hecate Strait also helps fulfill the mandate.

1.2 Objectives

The principal objective of this thesis is to describe the influence of the earth's rotation on the wind-driven flow in Hecate Strait. The primary tool used is the Hecate Strait model, a numerical model of the depth-averaged currents in the Queen Charlotte Islands region. The creation of the model required:

- The development of a numerical model of the depth-averaged currents on the continental shelf surrounding the Queen Charlotte Islands.
- Verification of the model by comparison with current meter measurements in Hecate Strait from 25 January to 30 March 1984.
- Comparison of simulated and observed drifter trajectories for drifter deployments in Hecate Strait during July 1990 and July 1991.

- Comparison of the overall circulation pattern in the Hecate Strait Model with the observed flow patterns to determine whether the model provides a useful tool for understanding the circulation.

Understanding the role of rotation in limiting the flux through Hecate Strait requires more than the Hecate Strait Model. A simple analytic model of flow through sea straits is needed to illustrate the important physical concepts. A secondary goal of this thesis is the extension of an existing conceptual model of flow in straits of finite length to include local wind forcing. The extended version is called the rotation-limited-flux model.

Considerable time is spent on details in order to create confidence in the numerical results. Testing a numerical model requires more than comparing model output with observations and then tuning parameters. For valid physical insight the model results must depend on the physics, not on the details of the numerics. This concern for detail is one of the reasons that numerical modelling becomes an end in itself. Writing this thesis has required balancing the opinion that God is in the details, with the sentiment of Richard Hamming: ‘The purpose of computing is insight, not numbers.’

1.3 Plan of the Thesis

The thesis is organized as follows.

Chapter 2 contains a review of the physical oceanography of the Queen Charlotte Islands region. The observations indicate that a depth-averaged numerical model is most applicable to Hecate Strait in the winter. Thus the name of the regional numerical model: the Hecate Strait Model.

Chapter 3 is a detailed discussion of the observations used to test the Hecate Strait Model. Analysis of the winds, currents, and water transport through Hecate Strait for the period January to April 1984 is reviewed and a previously unnoticed relationship

between the transport fluctuations and the spatial pattern of the velocity fluctuations is discovered. Drifter trajectories from all seasons are reviewed. The observations indicate that the local wind is an important forcing mechanism in Hecate Strait.

Chapter 4 introduces some simple ideas about low frequency flow in sea straits. The rotation-limited-flux model provides a description of how the interaction between the earth's rotation (Coriolis force) and the finite length of the strait limits the flux through the strait. The original work here is the extension of the rotation-limited-flux model to include wind forcing and the application to Hecate Strait. The concept of rotation-limited-flux is used to interpret the relationship between the flux through Hecate Strait, the bottom friction, and the Coriolis force as seen in the Hecate Strait Model results (Chapter 7).

Chapter 5 provides an over-view of the Hecate Strait Model. The equations of motion, the shallow water equations, are discussed and the concept of topographic steering is introduced. Topographic steering, the tendency for the low frequency flow to follow the depth contours, is used extensively in the discussion of the flow patterns in Chapter 8. The numerical scheme for integrating the shallow water equations is discussed, as are the open boundary conditions and the bottom friction representation. What is important is not the details, but a sense of how the model works.

Chapter 6 builds basic understanding of the behaviour of the Hecate Strait Model using the model's evolution from rest to a steady state as a test case. Important topics are the adjustments time-scales and the sensitivity of the steady-state water transport (flux) through Hecate Strait to the friction parameters. This discussion lays the foundation for understanding the simulations of the winter of 1984.

Chapter 7 investigates the rotational limitations on the water transport through Hecate Strait. The Hecate Strait Model is shown to provide good simulation of the observed transport for the period 20 January to 30 March 1984. The model is then

used to examine the relationship between the transport, bottom friction and the Coriolis force. Rotation-limited-flux provides an explanation for two features of the Hecate Strait Model: 1) the steady state transport increases by a factor of 3 when the rotation of the earth is ignored, and 2) the transport is not sensitive to the friction parameters.

The flow pattern, or circulation, in Hecate Strait is investigated in Chapter 8. The Hecate Strait Model captures the character of the observed flow pattern. The modelled flow is dominated by the interaction between the Coriolis force and topography: topographic steering. A new interpretation of the the observed current patterns in southern Hecate Strait is suggested.

The technical details and the results of preliminary tests of the Hecate Strait Model, including the open boundary conditions, are contained in the appendices.

Chapter 2

Physical Oceanography of the Queen Charlotte Islands Region

This chapter contains a review of the physical oceanography of the Queen Charlotte Islands region. The review looks to the application of a wind-driven, depth-averaged model of the circulation. Such a model assumes that the density and velocity do not vary significantly with depth and that the wind is the primary forcing mechanism. Circulation due to the density structure of the ocean is ignored as are the tides and the effects of fresh water input. The review of the observations in this chapter and the next, indicates that such a model is most applicable to Hecate Strait in the winter. In particular, the analysis of the moored current meter records in Hecate Strait for the winter of 1983/84 indicates that the barotropic response is important. The mean currents are discussed in Section 2.5.1 and an empirical orthogonal function analysis of the fluctuations is presented in Chapter 3.

Thomson (1981, 1989) has written reviews of the physical oceanography of the Queen Charlotte Islands region for a general audience. Much of the material presented in this chapter can be found there.

2.1 Geography and Bathymetry

The continental shelf around Queen Charlotte Islands is generally divided into four regions: Queen Charlotte Sound, Hecate Strait, Dixon Entrance, and the narrow shelf along the west coast (Figures 1.1 and 2.2). These divisions are useful because each region has its own distinct bathymetry and experiences different atmospheric and oceanographic

forcing. On the other hand the bathymetric features which separate the regions are the source of many of the interesting current patterns. The region must be considered as a whole so that important features are not lost in the boundaries.

The bathymetric features of interest here (Figures 1.1 and 2.2) are:

- Moresby Trough (or Gully) which cuts across the shelf from Cape St. James to the mainland and then turns north to form the axis of Hecate Strait.
- Dogfish Bank, the extensive shallow region in north-western Hecate Strait. This is the nursery area for Pacific cod and English sole. The larval advection problem mentioned in the Introduction involves the transport of the larvae from the spawning grounds in southern Hecate Strait to Dogfish Bank.
- the steep escarpment that runs northeast from Rose Spit and provides the dividing line between Dixon Entrance and Hecate Strait.
- Learmonth Bank, the shallow ridge which dominates the mouth of Dixon Entrance.
- the shallow banks and deep troughs that comprise Queen Charlotte Sound.
- the narrow continental shelf on the west coast of the Queen Charlotte Islands. At the southern end the shelf is less than 5 km wide (depth < 200 m) and depths of 2500 m are reached within 30 km of shore.

For the purpose of this thesis, Hecate Strait extends from Moresby Trough to the escarpment at the north end.

There is a wealth of detail along the coastline with numerous islands, rocks, fjords, and channels. The fine detail is not included in the numerical model. The re-connection of Clarence Strait with the Pacific Ocean after its narrow, winding journey through the Alaska Panhandle is not part of the model.

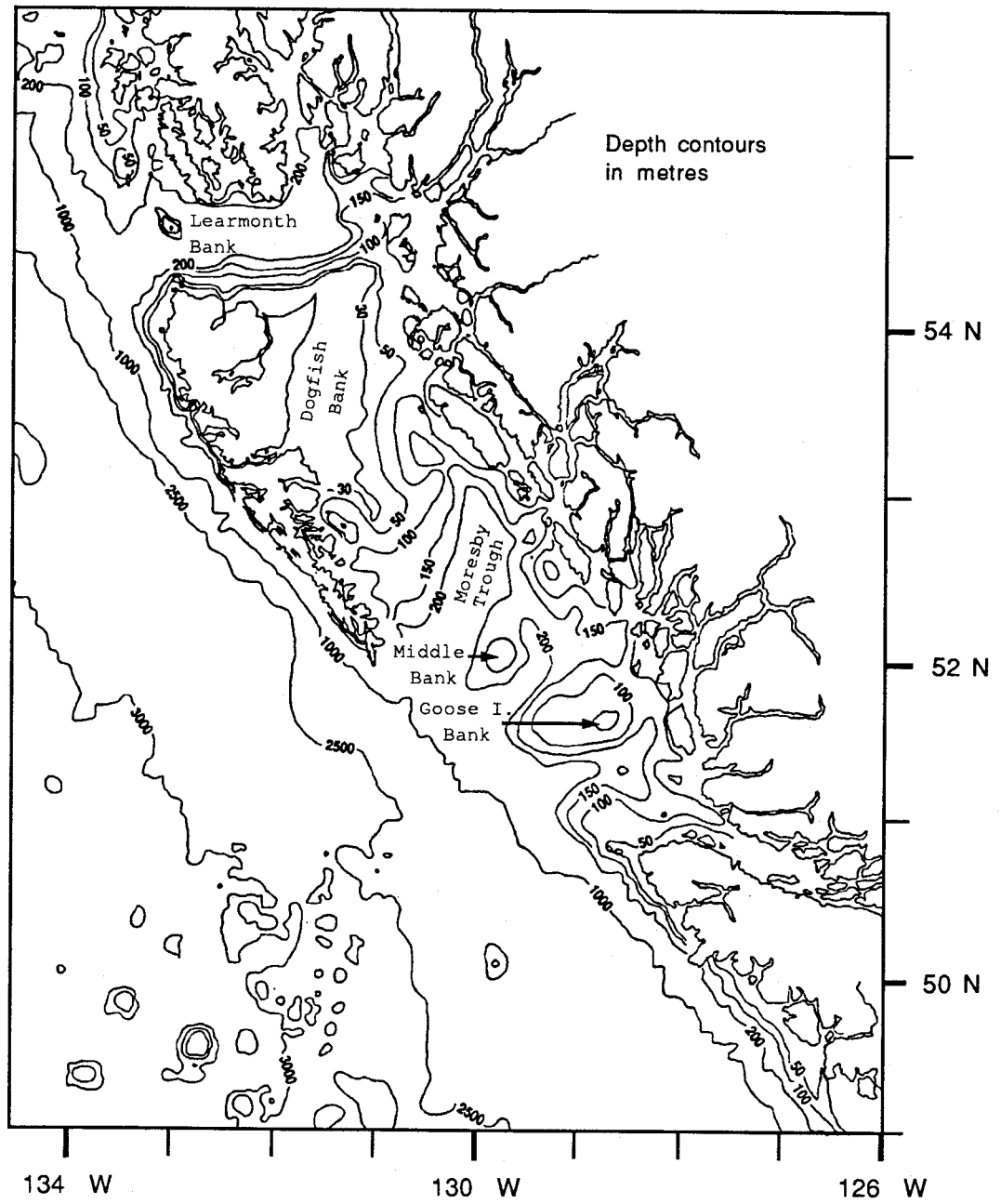


Figure 2.2: Chart of the Queen Charlotte Islands region. Depth contours are in metres. Courtesy of M.G.G. Foreman.

2.2 Tides

This thesis concentrates on the wind-driven circulation and does not consider the tides. Nevertheless the tides are the most energetic phenomenon in the region and they deserve to be discussed if only to appreciate what is being ignored.

Figure 2.3 is the co-tidal chart for the semi-diurnal (M_2) tide. Notice that the phase of the tide is almost constant along the outer coast of the Queen Charlotte Islands and that the tides from the two ocean entrances meet in northern Hecate Strait. It takes about 30 minutes for the tide to reach northeastern Hecate Strait from the open ocean, and another 15 minutes for the combined tide to swing across the strait and reach Graham Island (Thomson, 1981). The maximum tidal elevations are in northern Hecate Strait.

The tidal currents are rotary in the open waters of Queen Charlotte Sound and become rectilinear in Hecate Strait (Figure 2.4). The maximum surface tidal currents are of the order of 50 cm/s (1 knot) during spring tide and about half this during neap tide.

The tidal currents can affect the long term transport of particles in two ways: 1) through the generation of residual tidal currents, and 2) by moving particles from one current regime to another over part of a tidal cycle. In regions where the wind-driven currents exhibit large horizontal shear the second effect makes particle trajectories sensitive to the phase of the tide.

2.2.1 Residual Tidal Currents

A residual tidal current is the net current found when the current is averaged over a tidal cycle. These residuals can be thought of in two separate ways: Eulerian residuals, the non-zero mean current measured at a moored current meter, and Lagrangian residuals, the net displacement of a fluid parcel. The Lagrangian residual is what is measured by a drifter and is the important parameter for tracking particles in the water. Residual tidal

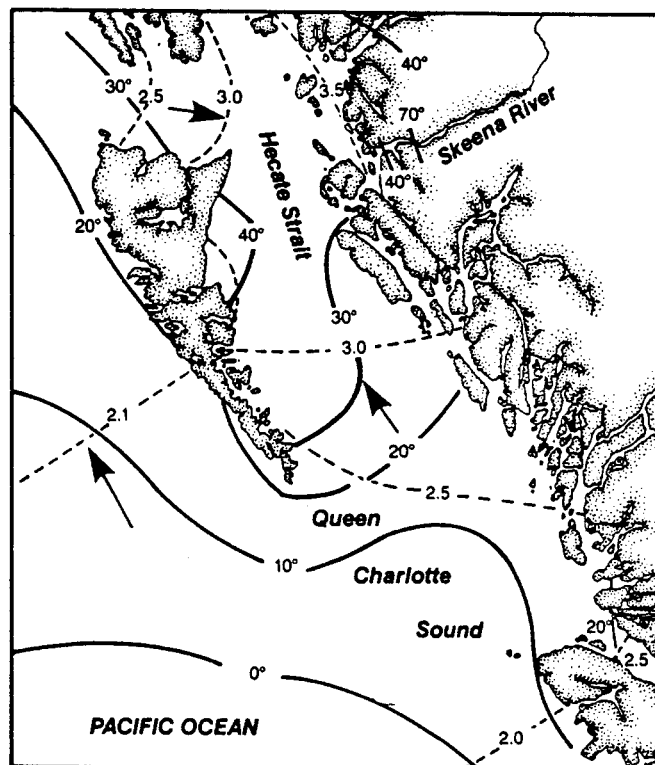


Figure 2.3: Co-range and co-phase values for the semi-diurnal tide. Tidal range (broken line) in metres; tidal phase (solid line) in degrees. Difference of 29° corresponds to time difference of 1 h. (Fig. 14.5 in Thomson, 1981).

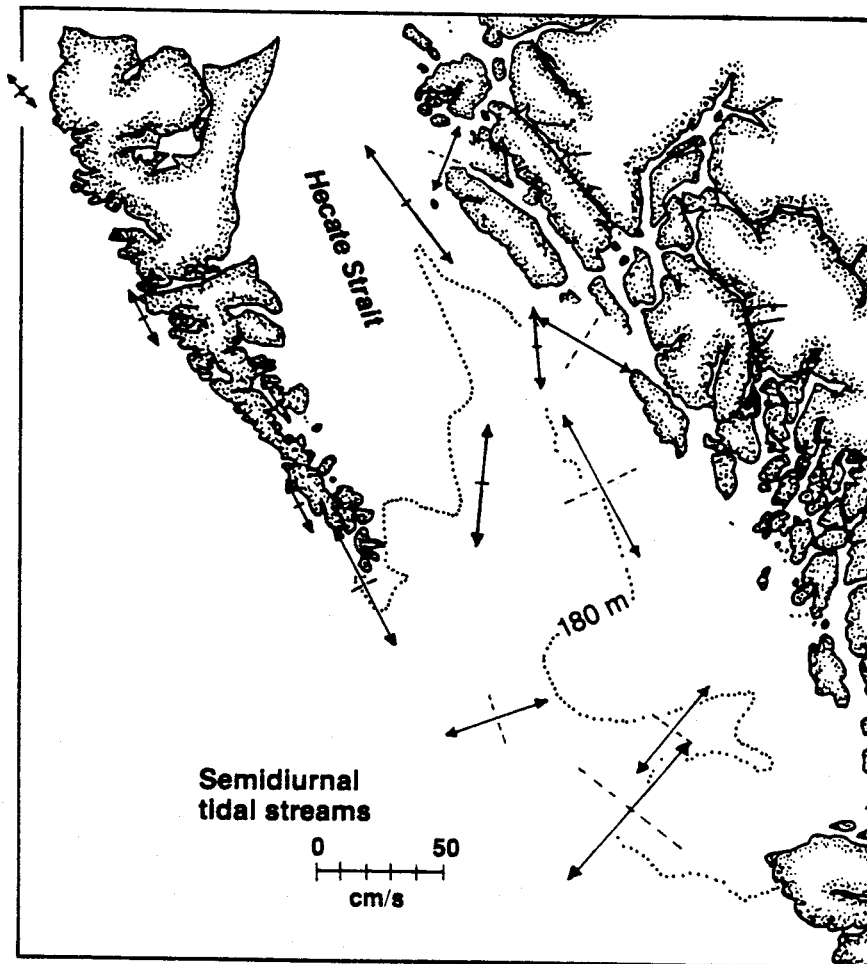


Figure 2.4: Observed semi-diurnal tidal streams in the upper 50 m depth. Solid lines and arrows give orientation of major flow and ebb directions; dashed lines give minor flow directions. Scale measures speed relative to the midpoint of each axis. (Fig. 22 in Thomson, 1989)

currents have many causes including the non-linear interaction of tidal constituents, the interaction of the tidal currents with topography (tidal rectification), bottom friction, and the spatial variability of the tidal current field. The last one will not contribute to the Eulerian residual.

One region where residual tidal currents have been thought to be important is Dixon Entrance. The existence of the Rose Spit Eddy (or Dixon Entrance Eddy) was one of the predictions of the large hydraulic model *Project Hecate* (Bell and Boston, 1963; Bell, 1963). This prediction prompted a field program to observe the feature (Crean 1967). Recent work by Bowman et al. (1992) suggests that the presence of the eddy in the model was an artifact due to the way the model was forced at the open boundaries. The Rose Spit Eddy is not seen in the tidal residuals of the non-linear tidal model of Foreman et al. (1992). The eddy does exist and is discussed in section 2.5.3 as part of the circulation in Dixon Entrance. This is a warning to interpret all model results with extreme care.

The results of Foreman et al. (1992; Fig. 2.5) show significant residual tidal currents at Cape St. James, over Learmonth Bank, over the escarpment that separates Hecate Strait from Dixon Entrance, and in the shallow water of northern and western Hecate Strait. The results near Cape St. James are in general agreement with the observations and analytical results of Thomson and Wilson (1987). Extreme caution is called for when interpreting the wind-driven model results in the vicinity of Cape St. James.

The southward currents on the western side of Hecate Strait will have an impact on the advection of larvae onto Dogfish Bank. The contribution of these residual currents to the net transport through Hecate Strait is $0.03 \times 10^6 \text{ m}^3 \text{ s}^{-1}$ to the south (Ian Jardine, pers. comm., 1991). This represents 50% of the observed mean transport during the summer of 1983 but only 10% of the observed mean transport in the fall of 1983 and the winter of 1984 (Crawford et al., 1988).

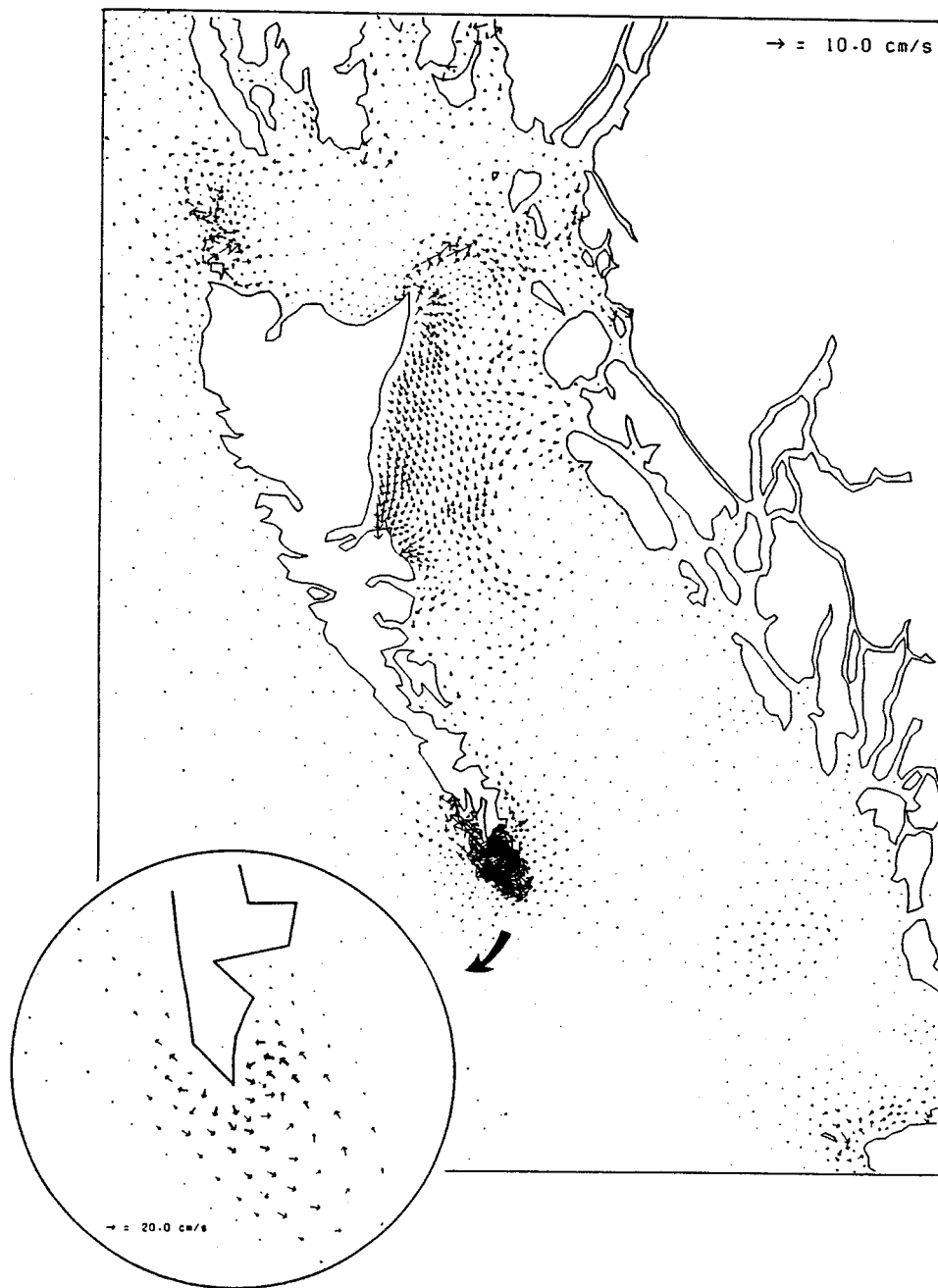


Figure 2.5: Barotropic residual tidal velocities. (Courtesy of M.G.G. Foreman, 1992.)

2.3 Temperature, Salinity, Density, and Fresh Water

Dodimead (1980) described the temperature, salinity, and density structure in Queen Charlotte Sound and Hecate Strait in terms of two states and the transitions between them. Summer conditions are characterized as consisting of a thin surface-mixed layer overlying a marked thermocline (a large vertical temperature gradient) and pycnocline (a large vertical density gradient). Below this the water has a lower temperature, higher salinity and higher density. Summer conditions usually prevail in July and August. Winter conditions are characterized by a thick mixed layer which reaches its maximum depth in December. Isothermal conditions can extend to depths of 150-200 m (Dodimead 1980). The deepening of the mixed layer is due to surface cooling, increased wind mixing, and downwelling. Due to runoff from the coastal mountains, the water is generally fresher (less saline) on the eastern side of the strait at all times of the year (Dodimead, 1980; Thomson, 1981).

The seasonal change in the density structure in Hecate Strait is dramatic (Fig. 2.6). The strongly stratified surface layer completely disappears in the winter. The seasonal cycles in Queen Charlotte Sound (Fig. 2.7) and Dixon Entrance (Crean, 1967; Thomson, 1989) are less dramatic. The stratification is significantly reduced in winter but never disappears.

The north coast receives an enormous amount of rainfall, but runoff from winter rainfall is thought to have only a marginal influence on the surface currents in Hecate Strait and Queen Charlotte Sound (Thomson, 1981). The major sources of fresh water are the spring/summer freshets of the Nass and Skeena rivers which discharge into Chatham Sound at the eastern end of Dixon Entrance.

The influence of freshwater discharge is most strongly felt in Dixon Entrance in late spring and summer when runoff from the Nass and Skeena rivers tends

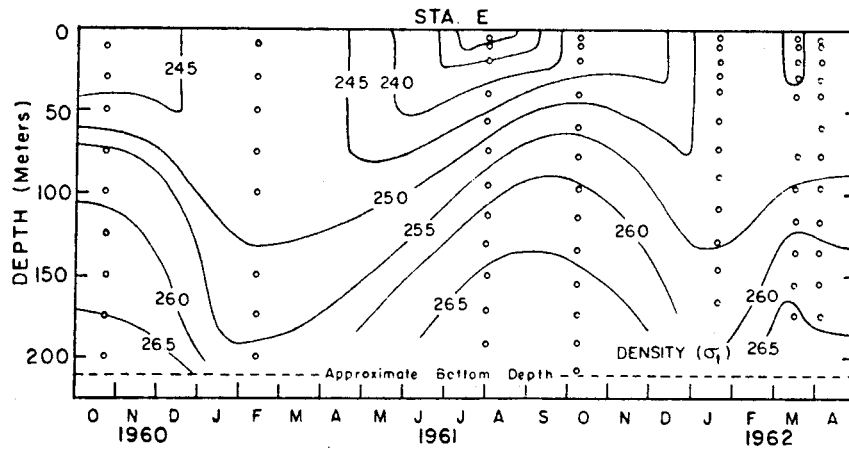


Figure 2.6: The seasonal cycle of density at a station in central Hecate Strait, 1960-62. (Fig. 84 in Dodimead, 1980)

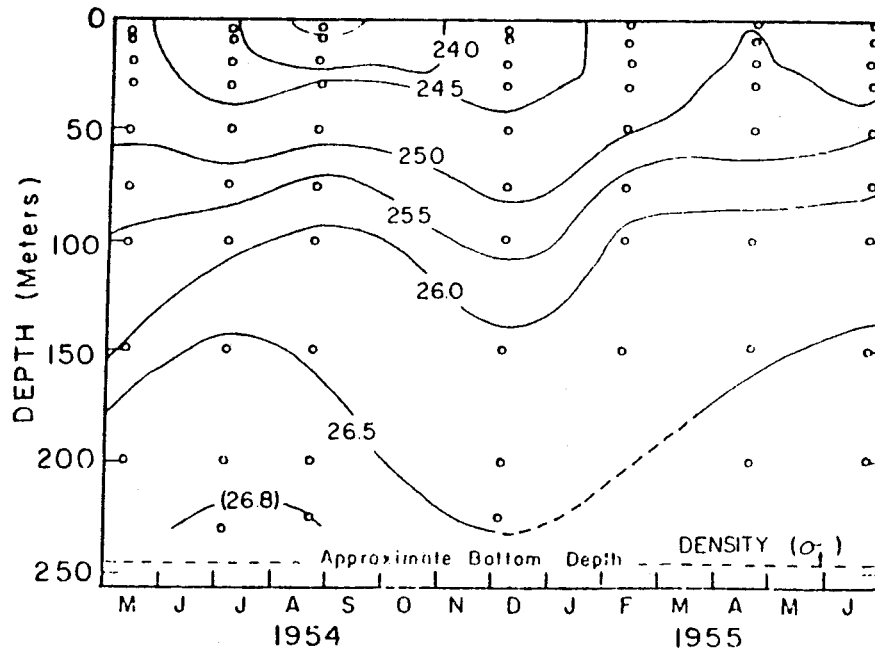


Figure 2.7: The seasonal cycle of density at a station on the northern flank of Middle Bank in Queen Charlotte Sound, 1954-55. (Fig. 82 in Dodimead, 1980)

to flow seaward within a comparatively warm brackish layer 10-20 m thick that hugs the northern side of the channel. In contrast, cooler, saltier oceanic water generally prevails over the southern half of the channel at this time. (Thomson, 1981)

An example of the impact of the fresh water input on the circulation was observed in July 1991. During strong SE winds three drifters were carried through Brown Passage, south of Dundas Island, into Chatham Sound. Two of the drifters had drogues centred at 3 m and one at 10 m. The two shallow drifters stopped when they hit the front created by the Skeena River discharge. The deeper drifter carried on into Chatham Sound and off to the north (W.R. Crawford, pers. comm., 1991).

2.4 Winds

The general features of the winds in the Queen Charlotte Islands region are quite simple. Winter storms are generally more severe and more frequent than summer storms and the winds are generally from the southeast. Summer storms can be either from the southeast or the northwest. The large scale weather patterns from the Pacific Ocean are heavily modified by the coastal mountains. In Hecate Strait the coastal mountain ranges channel the wind to southwest/northeast directions. In Dixon Entrance the winds are more nearly east/west. At Cape St. James the wind is less constrained but most of the wind energy is directed parallel to the coastal mountains.

Information on the spatial distribution of wind speed is sketchy. Thomson (1981) notes that

... the frequency and intensity of southeasterlies is greater over the northern sector of the seaway than over the southern sector, whereas the frequency and intensities of northeasterlies is greater in the south than in the north.

This is not sufficient to construct forcing fields for a numerical model. Compilation of reliable wind fields from the atmospheric pressure observations and the lighthouse winds is a major undertaking and to my knowledge has never been done for the Queen Charlotte Islands region. Lighthouse winds are considered unreliable estimators of the wind speed over the ocean. They are generally biased by blockage from trees and hills and are considered to be overly influenced by the coastal boundary layer. Only in the last year or so has the Atmospheric Environment Service (AES) had enough weather buoys in operation to even consider defining a spatially variable wind field from over-the-ocean measurements.

The winds are discussed with the current observations in the next section and in Chapter 3.

2.5 Circulation

The first program of current meter observations devoted to obtaining a clear picture of the circulation in Queen Charlotte Sound, Hecate Strait and Dixon Entrance was carried out from 1982 to 1985. Current meter observations were made in Queen Charlotte Sound during the summer of 1982 (Crawford et al., 1985) in Hecate Strait from May 1983 to April 1984 (Crawford et al., 1988), and in Dixon Entrance from May 1984 to May 1985 (Crawford and Greisman, 1987; Bowman et al, 1992).

Before that time the bulk of the current meter studies concentrated on measuring tidal currents for navigation purposes. These studies were usually limited to the summer months because it is extremely difficult to work in these areas in the fall and winter. The circulation was studied using hydrographic measurements (temperature, salinity, oxygen) with current patterns inferred from the density fields. The enormous amount of hydrographic data collected during the 1950's and 1960's is reviewed by Dodimead

(1980). The circulation as understood before the 1982/85 observations is discussed by Crean (1967), Dodimead (1980), and Thomson (1981, 1989). The accepted view of the wind-driven circulation before 1981 is summarized concisely by Bell and Boston (1962):

Observations have shown that during the winter period of strong southeast winds, light surface waters accumulate along the coast, displacing the deepest waters to an offshore position. During the summer period of weak northwest winds, the accumulated surface waters move offshore allowing the return of the deep waters. The winter accumulation is accompanied by a northward flowing coastal current which appears to be continuous from California to the Gulf of Alaska. During the summer, this current is small or absent.

The winter downwelling and displacement of the deep water has the added effect of decreasing the stratification of the water column - making it more homogeneous. In the summer the replacement of the deep water increases the stratification of the water column.

2.5.1 Hecate Strait 1983-1984

The 1983/84 observations in Hecate Strait do not contradict the historical picture so much as add a new twist. An unwary reader might think that the description given implies that the water flows between Hecate Strait and Queen Charlotte Sound in the direction of the wind. The observed mean winds and mean currents in Hecate Strait (Fig. 2.8) show that in southern Hecate Strait (M-line) the water does not simply flow down-wind. In the fall and winter, the observations clearly show flow along the axis of Moresby Trough against the prevailing wind. The mass transport through the northern part of Hecate Strait (W-line or R-line) is the small difference between the large northern and southern transports through the M-line (Crawford et al., 1988). In the words of Crawford, Tyler

and Thomson (1990, hereafter CTT90)

The historical view of the winter circulation, which described a simple current flowing through Hecate Strait into Dixon Entrance, is clearly not correct.

For scientists concerned with tracking fish larvae this twist changes everything. CTT90 remark that without some sort of recirculation pattern, particles deposited in the southern end of Hecate Strait in the winter should be swept into Dixon Entrance in about 25 days (typical current of 10 cm/s, length of strait 250 km). The larval stage of Pacific cod and English sole, which spawn in the winter, ranges from 6-10 weeks depending on the temperature (CTT90, Walters et al., (1992), Ketchen, 1956) so they would be carried through the strait before they settle onto the bottom. CTT90 note that there is no reason to believe that Hecate Strait is restocked from other regions since 'the species dominant in Hecate Strait give way to other species in Dixon Entrance and the Alaska Panhandle.'

The conditions in Hecate Strait in the winter are well approximated by a depth-averaged wind-driven model: the density stratification disappears in the winter; at most meter locations the currents are reasonably approximated by a single depth-averaged current, and are generally confined to a single quadrant; the currents are predominately wind driven (CTT90). The relationship between the winds and the currents is investigated further in Chapter 3.

2.5.2 Queen Charlotte Sound 1982

The current meter observations in Queen Charlotte Sound for the summer of 1982 are summarized in Fig 2.9. At most locations the magnitude of the fluctuations (represented by the principal axes of variance) are comparable to the means. A sensible pattern does not leap off the page. The counter-clockwise flow around the Goose Island Bank (meters G01-G07) may be due to tidal rectification (Freeland et al., 1984).

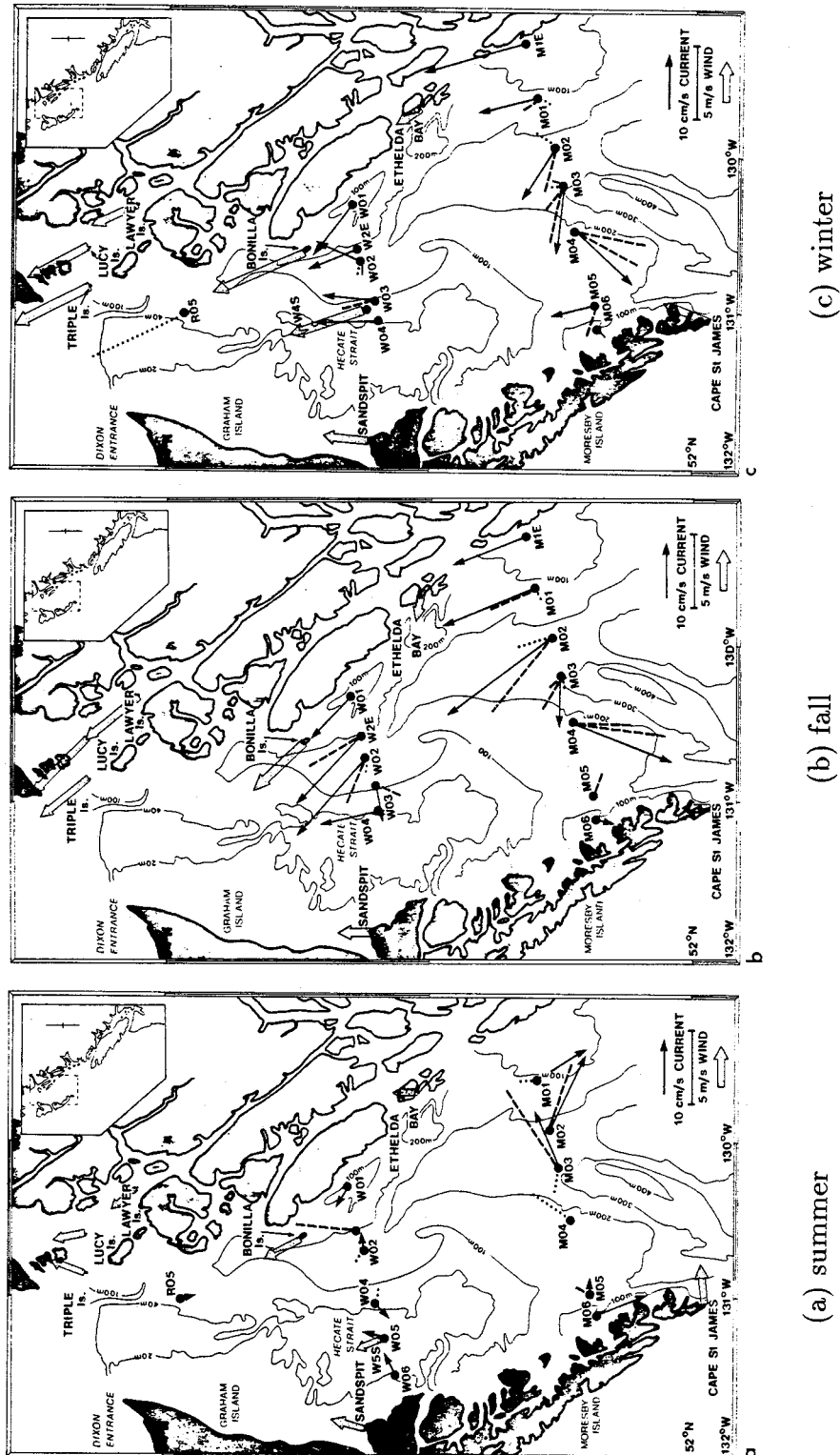
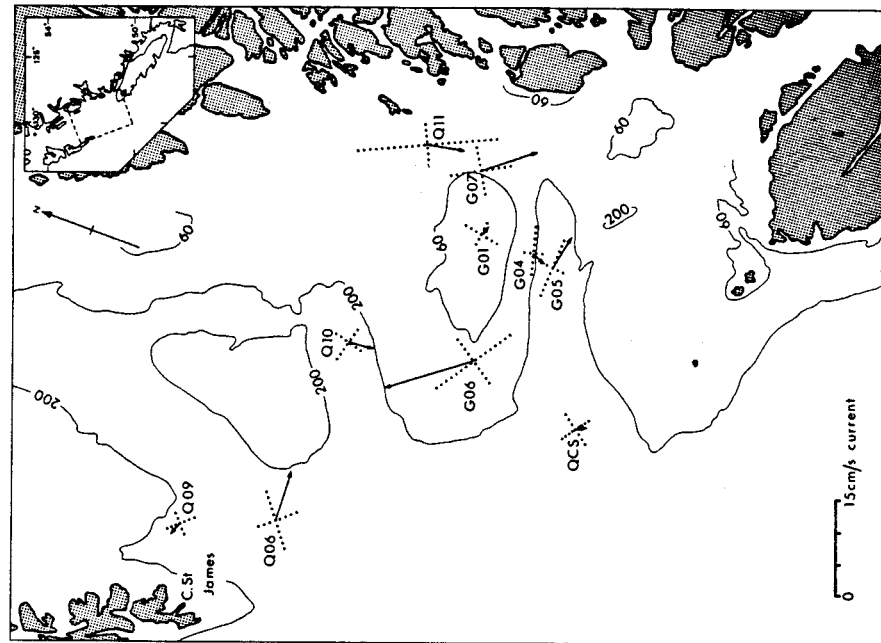
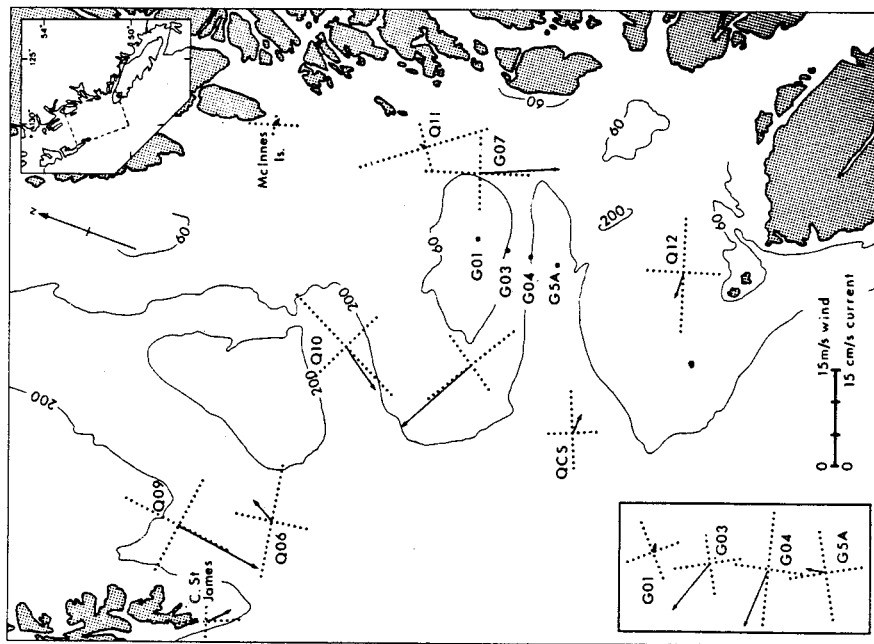


Figure 2.8: Average currents and winds in Hecate Strait. Solid arrows represent currents within 50 m of the surface, dashed lines, currents at intermediate depths and dotted lines, currents within 15 m of the bottom. Wide shaded arrows represent winds. (a) summer, 16 May to 9 September 1983, (b) fall, 28 September to 20 December 1983, (c) winter, 20 January to 4 April 1984. (Fig. 2 in Crawford et al., 1988).



(b) near-bottom currents



(a) near-surface currents

Figure 2.9: Currents and winds in Queen Charlotte Sound for the period 4 June - 15 September 1982. Vectors of average currents, and winds at Cape St. James and McInnes Island are the solid lines and the principal axes of variance are the dotted lines. a) near-surface currents and winds, b) near-bottom currents. (Fig. 7 in Crawford et al., 1985)

Crawford et al. (1985) found that while the wind observations were well represented by the mean and first EOF mode, the currents did not partition neatly into a few modes. This suggests that a simple wind-driven model will not reproduce the currents in Queen Charlotte Sound. Empirical Orthogonal Function (EOF) analysis is discussed in Appendix B.

2.5.3 Dixon Entrance

Observations from the summer of 1984 (Fig. 2.10 and Fig 2.11) suggest two eddies, one in the eastern end near Rose Spit and a second near the mouth of Dixon Entrance (perhaps centred over Learmonth Bank). In the summer of 1991 a drifter actually completed two circuits of the Rose Spit Eddy, thus confirming the existence of a closed loop (W.R. Crawford pers. comm.).

Unlike the situation in Hecate Strait, the current pattern in Dixon Entrance does not change with the seasons. The mean currents from October 1984 to May 1985 (Bowman et al., 1992) look like the summer currents in Fig. 2.11. The change in the wind regime was reflected only in the currents at R05, in Hecate Strait, which were southward in the summer and northward in the winter. The circulation in Dixon Entrance is discussed at length in Crean (1967), Thomson (1981), Crawford and Greisman (1987), and Bowman et al. (1992). The consensus is that the Rose Spit Eddy is driven by tidal rectification and thermohaline circulation. The wind forcing is of secondary importance.

A movie of the low-pass filtered current observations shows that when a strong south-east wind starts up in autumn the eddy is temporarily obliterated by a pulse of water from Hecate Strait. The eddy quickly re-establishes itself when the winds subside (W.R. Crawford pers. comm., 1990).

A depth-averaged wind-driven model is not a good approximation to the dynamics in Dixon Entrance. The water is always stratified and the wind is not the primary forcing

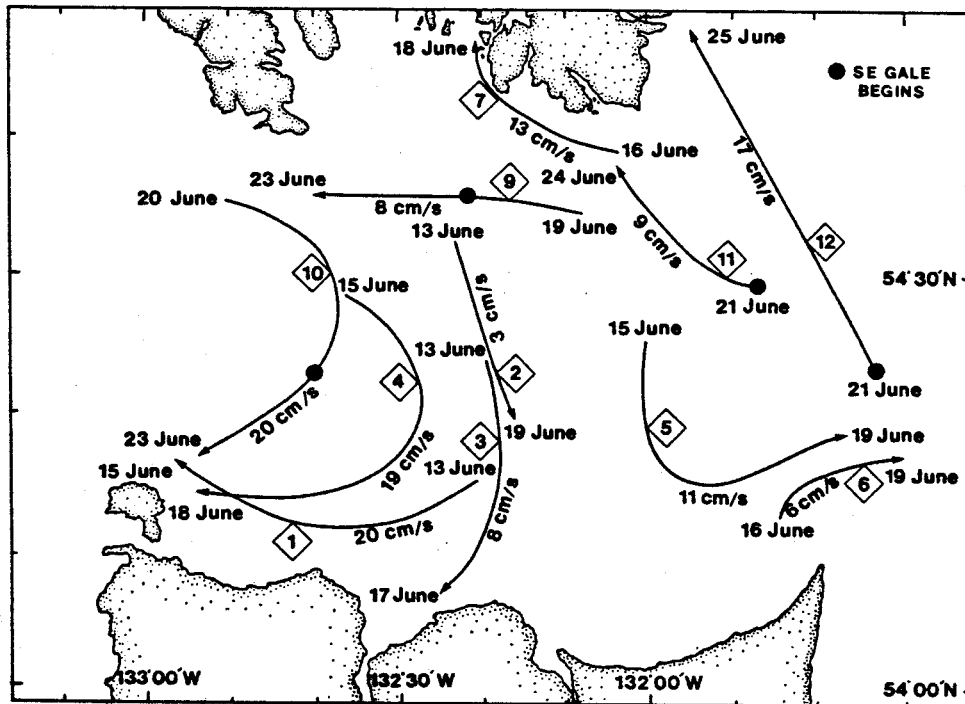


Figure 2.10: Smoothed drifter tracks from Dixon Entrance summer 1984. Tidal currents are averaged out. The solid circles mark the position of the drifters at the onset of a storm on 21 June 1984, with winds of 15 m s^{-1} from the southeast. (Fig. 3 in Crawford and Greisman, 1987.)

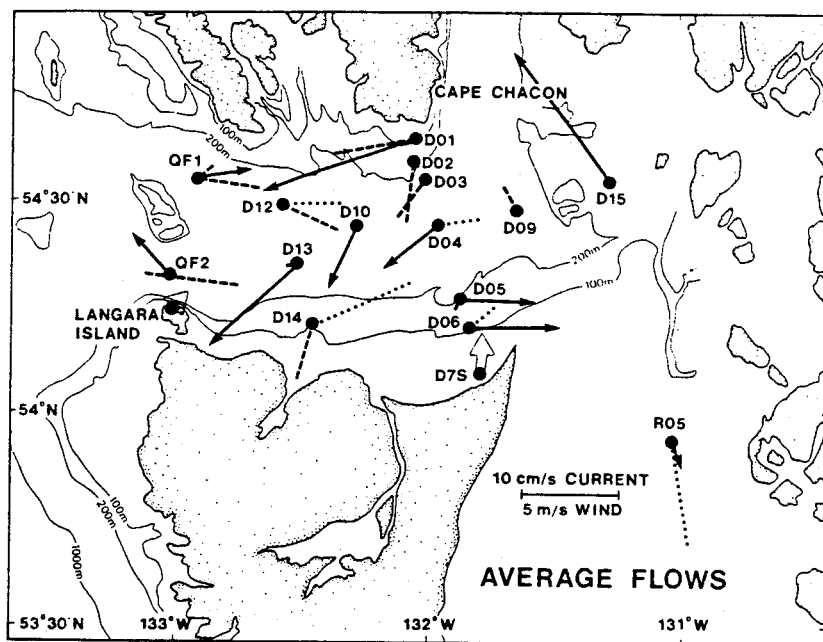


Figure 2.11: Average currents and winds in Dixon Entrance for the period 22 April-19 August 1984. Solid arrows represent currents within 50 m of the surface, dashed lines, currents at intermediate depths and dotted lines, currents within 15 m of the bottom. The wide arrows at D7S and Langara Island represent winds. (Fig. 5 in Crawford and Greisman, 1987.)

mechanism.

2.5.4 Outer Shelf and the Deep Ocean

The currents along the shelf break appear to be wind-driven. From southern Vancouver Island to Cape St. James the monthly average currents are generally in the direction of the prevailing wind: to the northwest in the winter and to the southeast in the summer (Freeland et al., 1984). Along the west coast of the Queen Charlotte Islands, a warm northward flowing surface current, probably wind-driven, has been observed in the winter (Thomson and Emery, 1986). However the water is strongly stratified and poorly approximated by a depth-averaged model. Nevertheless, it is important to include the west coast of the Queen Charlottes and the open ocean in order to provide the outside connection between the Queen Charlotte Sound and Dixon Entrance.

The circulation and water properties in the open ocean are believed to have only a minor impact on the circulation on the shelf. The Queen Charlotte Islands sit in a bifurcation zone of the offshore currents (Fig. 2.12). As a result, the mean ocean currents off the British Columbia coast are generally weak and confused (Thomson, LeBlond and Emery, 1990). There is no feature such as the Gulf Stream to provide a source of energetic eddies or persistent along-shore pressure gradients. Very little is known about the impact of the intrusion of open ocean water masses on the shelf circulation. Besides the weak forcing, the steep shelf break has an insulating effect, partially decoupling the shelf circulation from the deep ocean (Wang, 1982).

Shelf waves

Shelf waves, or coastal trapped waves, are sub-inertial waves which travel parallel to the coastline and are trapped against the coast by topographic gradients (Allen 1980, Mysak 1980). In the northern hemisphere they travel with the coast to the right. They

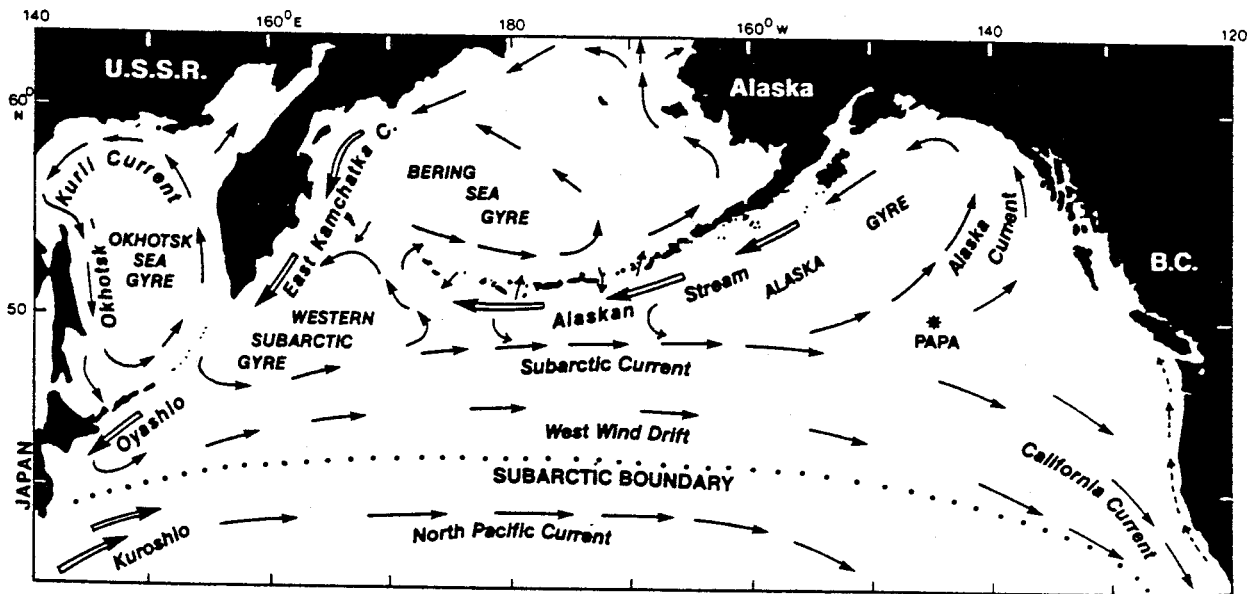


Figure 2.12: Prevailing surface currents in the North Pacific Ocean. Double arrows are intense boundary currents, speeds typically 1-2 m/s; over most of the rest of the region speeds are less than 0.25-0.50 m/s. Arrows correspond to prevailing winter time flow off the west coast of North America. (Fig. 13.17 in Thomson, 1981)

provide a mechanism by which events to the south can influence the circulation in the Queen Charlotte Islands region. At this time it is not known whether shelf waves have an impact on the circulation around the Queen Charlotte Islands. Shelf waves have been observed off the coast of Washington and Oregon (Allen, 1980) and along the west coast of Vancouver Island (Crawford and Thomson, 1984). Halliwell and Allen (1984, 1987) found evidence for forced wave propagation in their studies of the response of sea level to wind forcing along the west coast of North America (Baja California to Prince Rupert). To date there is no firm evidence for shelf wave propagation in the current meter records north of Brooks Peninsula on the west coast of Vancouver Island (Crawford and Thomson, 1984; Yao et al., 1984).

2.6 Summary

Winter conditions in Hecate Strait are reasonably approximated by a depth-averaged, wind-driven model. In the other regions significant density stratification is present in all seasons and in Dixon Entrance wind forcing appears to be of secondary importance. The observations in Hecate Strait are discussed in detail in Chapter 3.

At this time there is no compelling evidence that the shelf circulation is dominated by forcing from the deep ocean or by remotely generated shelf waves. Residual tidal currents are an important local effect, especially near Cape St. James and along the escarpment at the northern end of Hecate Strait. The model studies reported in this thesis concentrate on the effects of local wind forcing.

When the water column is stratified, a depth-averaged model is missing an important part of the dynamics. This does not mean that the model results can not be used to suggest interpretations of the observations. However one should be careful.

Chapter 3

Hecate Strait: Data for Model Comparison

The period chosen for direct comparison of the model results with current meter observations was January to April 1984. The winter conditions in Hecate Strait make a wind-driven, depth-averaged model a reasonable approximation: the winds are strong and the vertical stratification is weak. The winter season is when Pacific cod and English sole spawn and the winter currents are an important component of the larval advection problem discussed in the Introduction.

Drifter trajectories provide information about the circulation that is especially relevant to the study of larval advection and oil spills. Winter drifter studies are rare and there are none from the winter of 1984. Observations from all seasons are discussed.

The chapter is divided into 3 sections: calculation of wind stress from the observed winds; the winds and the currents; and drifter trajectories.

3.1 Calculation of Wind Stress

The wind stress is the tangential stress imposed on the ocean surface by the wind. It represents momentum transfer from the atmosphere to the ocean. In numerical ocean models the wind stress is calculated from a bulk formula of the form

$$\tau = \rho_a C_d |W|W \quad (3.1)$$

where τ is the surface wind stress, ρ_a is the density of air, C_d is the drag coefficient and W is the wind velocity. In general C_d depends on the sea state, the surface roughness, the

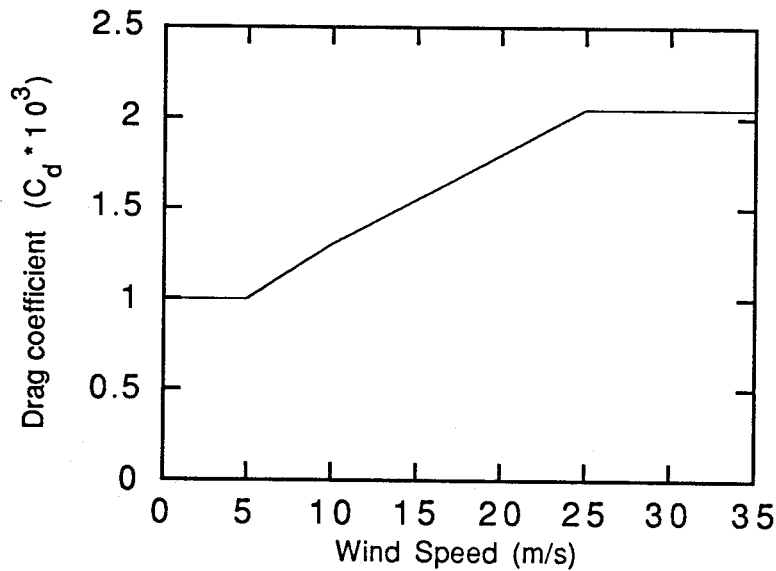


Figure 3.13: Dependence of drag coefficient C_d on wind speed for winds measured at 10 m and neutral atmospheric stability (Smith, 1988).

stability of the air over the ocean, the relative humidity and the height of the anemometer. For use with the regional model I have assumed that the atmosphere is neutrally stable and that the drag coefficient depends only on the wind speed. The dependence of the drag coefficient on wind speed measured at 10 m (Smith, 1988) is shown in Fig. 3.13. Conversion of winds measured at heights other than 10 m is done by interpolation on the tables in Smith (1988). The drag coefficient does not take into account the differences in effective drag when the wind is blowing with the waves and across the waves (Large and Pond, (1981). Incorporating such effects into a numerical model would require either a parameterization based on changes in the wind direction or that the model contained information about the wave heights and sea state.

The drag coefficient C_d increases when the atmosphere is unstable and decreases when the atmosphere is stable. The stability is measured by the sea-air potential virtual temperature difference, an adjusted version of the difference between the sea surface temperature and the air temperature at 10m (see Smith 1988 for details). For a wind

speed of 10 m s^{-1} and sea-air potential virtual temperature differences of $(-2, 0, 2)^\circ \text{C}$, the drag coefficients are $C_d = (1.21, 1.30, 1.35) \times 10^{-3}$. The stability of the atmosphere can make a difference, although it is ignored in this thesis.

Most of the wind velocity data for the test period was from land stations – airports and lighthouses. There was only one ocean-based anemometer: W4S located near current meter W04 in Fig. 3.14. The results of Smith (1988) are valid only for wind measurements made over the ocean. The time series used to drive the regional model for the winter of 1984 comparison was computed from observations at W4S. For the drifter comparisons the wind observations were taken from the nearest Atmospheric Environment Service weather buoy.

There does not exist a systematic method for converting winds measured at a lighthouse station to surface wind stress over the ocean. An approximate wind stress can be computed by using (3.1) and choosing a reasonable value for the drag coefficient. This means that when lighthouse winds are used to drive a numerical model there is an arbitrary scale factor - the drag coefficient.

There are logistical problems related to trying to compute surface wind stress from observed winds. Lighthouse wind measurements are usually biased by blockage due to trees or a hill. Winds measured from moored anemometers can have problems when the waves get high and the anemometer is alternating exposed and blocked. These effects are not accounted for here.

3.2 Wind and Current Fluctuations

The discussion of the wind and current fluctuations in Hecate Strait is organized as follows. The first section looks at the dominant spatial patterns (mode 1) of the wind and current fluctuations. The main results are that the mode 1 currents and winds

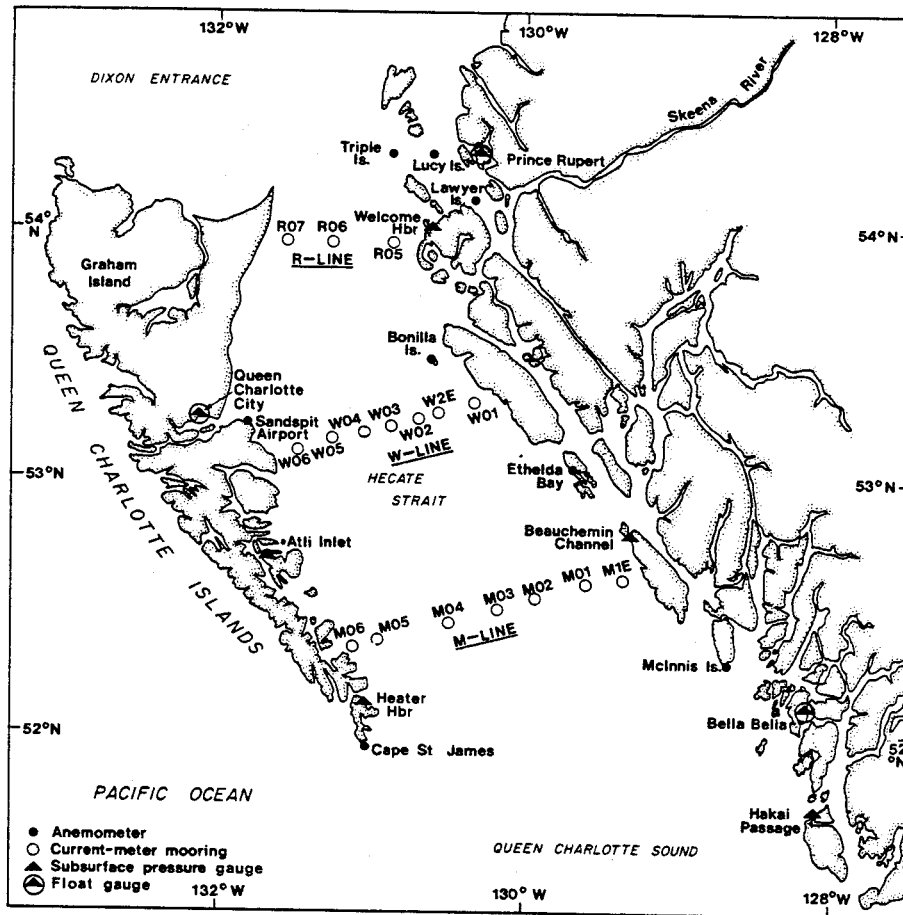


Figure 3.14: Locations of current meters, pressure gauges and anemometers in Hecate Strait from Jan - April 1984. Fig. 1 from Crawford et al. (1985, with permission).

represent fluctuations in magnitude (not direction) about the mean currents and winds. The next section looks at the relationship between the transport fluctuations and the wind and the cross-strait pressure gradients. In this context *transport* is the net flow rate through Hecate Strait. The two sections are based on the work of Crawford, Huggett and Woodward (1988, hereafter CHW88) and Crawford, Tyler and Thomson (1990, hereafter CTT90). In the final section I propose that the mode 1 current fluctuations and the transport fluctuations are closely related. This has implications for the use of transport time series in the study of larval advection and fisheries stock-recruitment prediction (Tyler and Crawford, 1991).

The collection of the current meter data is discussed by CHW88. The geographic locations are shown in Fig. 3.14. Meters W05, W06, R06, R07 failed during the Jan to Apr 1984 deployment and are not included in any of the analysis.

The tidal and inertial currents were removed from the observations with a 2-d low pass filter. The filter used was an 8th order Butterworth low-pass filter with half power at 40 hr and 98% transmission at 48 hr. The price paid for this elegant filter (steep transition zone and minimum ringing) is a wide footprint. Five days must be trimmed from each end of every time series to eliminate end effects (Appendix C).

The work of CHW88 and CTT90 used the complete data set from 20 January to 4 April 1984. Many of these results are discussed in this section. The comparison of the observed and modelled currents in this thesis was carried out for the period 25 January to 30 March 1984. The current meter data was re-constructed from the original data files and much of the analysis repeated for both the 20 Jan to 4 Apr time period and the 25 Jan to 30 Mar period. Changes in the results of the analysis due to the shorter time series were minor and these changes are noted. The character of the results do not change. Only selected wind time series were re-constructed.

All the times series mentioned in this section were filtered with the same filter as the

currents. The discussion is concerned with time scales of days to weeks.

For ease of plotting the time series I have used Julian day notation on the time axis. The Julian day is the ordinal number of the day of the year: 1 January is day 1 and noon on 1 January is day 1.5. The period 25 January to 30 March 1984 corresponds to days 25 to 91, 1984.

3.2.1 Spatial Patterns

In their analysis of the winter 1984 current meter observations in Hecate Strait, CTT90 made three observations: 1) there was a flow in Moresby Trough against the dominant wind direction; 2) the mean currents and mode 1 current fluctuations were generally in the same direction; and 3) the mean and mode 1 current fluctuations were wind driven.

The mode 1 currents are the spatial pattern associated with the first mode found by applying empirical orthogonal function (EOF) analysis to the data. In brief, EOF analysis finds coherent patterns in the fluctuations of the data. The data is reduced to a set of modes, where each mode has three components: an eigenvalue, an eigenvector, and a time series of modal amplitude. The eigenvalue is a measure of the total energy contained in the mode and is a measure of the mode's overall importance. The eigenvector contains the spatial character of the mode. The time series of modal amplitude records the fluctuations of the mode. EOF analysis is a statistical technique and interpretation of the patterns in terms of physical processes is a separate issue. The details of EOF analysis are discussed in Appendix B.

The pattern of the EOF mode 1 currents and winds for the winter of 1984 are shown in Figure 3.15. The wind and current modes were computed separately. The mode 1 currents contain 23% of the energy and the mode 1 winds contain 49% (CTT90). When interpreting the patterns, the magnitude of a vector is the RMS amplitude of the fluctuations at that point (Appendix B). The whole pattern fluctuates in phase, with

Dates 1984	comments	scaled	# modes	Λ_1	Λ_2	Λ_3
20 Jan - 1 Apr	CTT90	yes	58	23 %	–	–
25 Jan - 31 Mar	without R05	yes	58	23%	11%	10%
25 Jan - 31 Mar	with R05	yes	60	25%	10%	9%
25 Jan - 31 Mar	with R05	no	60	25 %	10 %	9%
25 Jan - 31 Mar	depth averaged	no	26	39%	12%	11%
25 Jan - 31 Mar	depth averaged	yes	26	31%	12%	11%

Table 3.1: Statistics for the current EOF analysis for the winter of 1984. The Λ_i are the first three eigenvalues. Scaled refers to whether each time series was scaled by its standard deviation before EOF analysis.

the currents at each location directed along the line of the vector. The vectors do not rotate. The time history of the fluctuations is given by the associated time series of modal amplitude. I repeat, the wind and current modes shown in Figure 3.15 were computed separately and have different modal time series.

The current vectors generally lie in the same direction as the mean currents (Fig.2.8c), thus they represent fluctuations in magnitude not direction. The major exception are at M03 where the mean flow is to the west and the mode 1 fluctuations are NE/SW, and at W03 where the mean is to the north, along the strait, and the fluctuations are directed across the strait. The fluctuations are required to be in phase, thus when the northward flow at M01 and M02 increases so does the southwesterly flow at M04.

The mode 1 winds are an along-shore pattern and the vectors are generally in the same direction as the means. It is not completely unreasonable to approximate the mode 1 winds by a single vector.

CTT90 concluded that both the mean and mode 1 currents were predominately wind driven. Their conclusion was based on 1) the high coherence between the mode 1 winds and the mode 1 currents (greater than 0.75 for frequencies less than 0.5 cycles/day); 2) the similarity of the mean and mode 1 currents; and 3) the change in the mean currents from summer to winter when the winds change direction and character (Fig. 2.8).

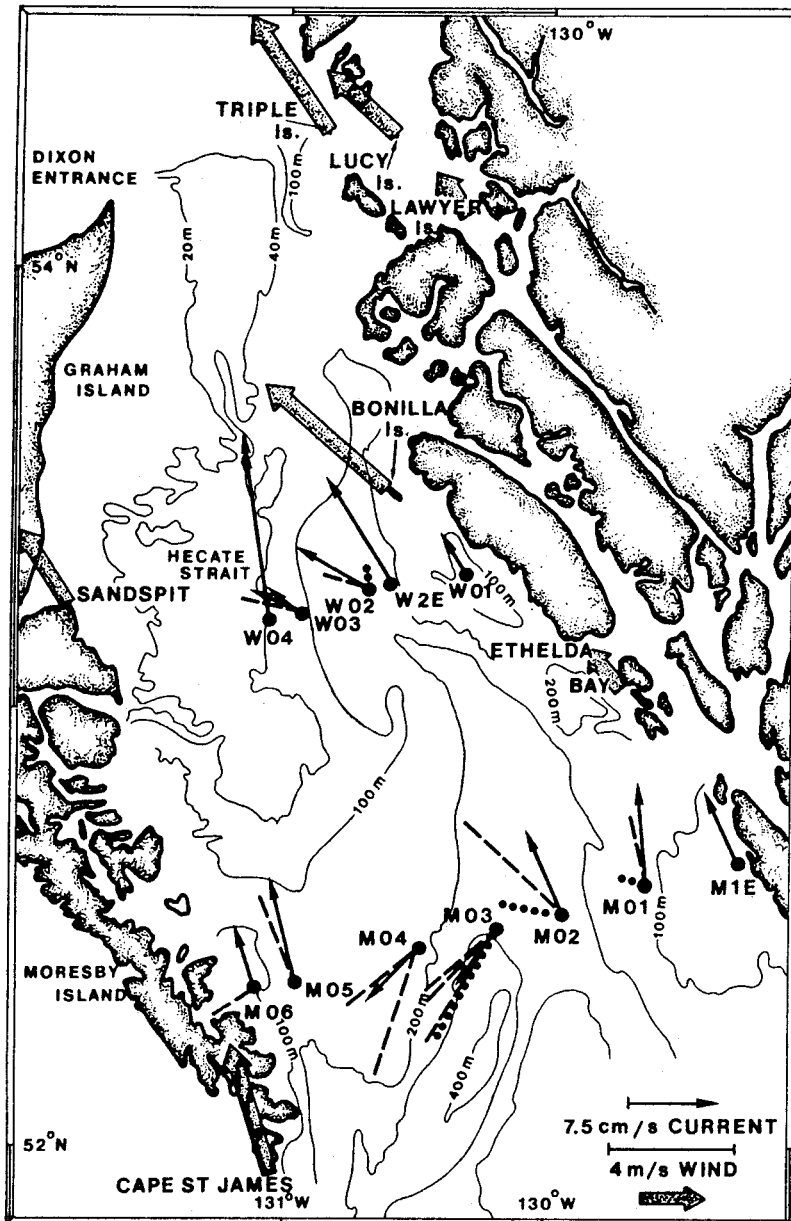


Figure 3.15: Vectors of the empirical orthogonal functions for the period 20 January-4 April, 1984. Fig. 8 from Crawford et al., 1990.

For comparison with the model, I depth-averaged the observations before the EOF analysis. The depth-averaging caused an increase in the relative importance of mode 1. Table 3.1 shows how the EOF statistics changed for minor changes in the analysis. The eigenvalues (Λ_i) are given in terms of the percentage of the total energy represented by that mode. There are only small changes associated with reducing the length of the time series and with adding the data from current meter R05 (not included in CTT90's analysis). The column labelled 'scaled' refers to whether the time series were divided by their standard deviation before analysis. Scaling the time series means that one energetic time series can not dominate the analysis. Table 3.1 shows that scaling has only a small effect on the eigenvalues. The spatial patterns, when plotted in dimensional form (Appendix B), were not greatly affected by the scaling. The EOF mode 1 spatial pattern computed from the depth-averaged currents has the same character as the pattern shown in Fig. 3.15 The pattern is plotted in Fig. 8.64 where it is compared with the model results.

3.2.2 Water Transport Through the Strait

The transport is the volume of water moving perpendicular to a line across Hecate Strait. In a steady-state situation the transport is the amount of water moving from one end of the strait to the other. The standard oceanographic unit of transport is the Sverdrup (Sv): $1 \text{ Sv} = 10^6 \text{ m}^3 \text{ s}^{-1}$.

The computation of the transport from the current meter observations is described by CHW88. The most reliable estimates were made at W-line (Fig. 3.14). The transport fluctuations (W-line) are compared with the along-shore wind stress fluctuations (W4S) in Fig. 3.16. The time series are obviously related, the peaks line up, but they are not identical. The time series were normalized by subtracting the mean and dividing by the standard deviation. The linear trend was also removed. The mean and standard

	Mean		Fluctuations			Correlation	
	dir. (deg)	magn. (m s ⁻¹)	maj. dir. (deg)	St. Dev.		magn.	lead (h)
				maj. (m s ⁻¹)	min. (m s ⁻¹)		
WINDS							
Cape St James	19	3.4	329	5.5	3.9	0.70	12
Sandspit	7	3.1	322	4.4	1.9	0.55	12
Bonilla Island	336	6.3	329	6.5	2.9	0.64	6
Ethelda Island	330	2.1	320	2.5	1.9	0.74	6
Lawyer Island	340	3.5	327	2.5	1.4	0.46	6
Lucy Island	331	4.7	318	5.5	1.6	0.41	6
Triple Island	341	5.6	333	5.9	3.4	0.65	6
W4S	342	5.3	326	5.7	2.8	0.58	6
	Mean		Fluctuations				
SPATIAL-AVERAGE WIND							
EOF 1		—		—		0.71	6
AIR PRESSURE		(kPa)		(kPa)			
[PRA + McI]/2 - SA		0.21		0.23		0.69	6
SUBSURFACE PRESSURE							
Beauchemin - Atli (B - A)		0.39		0.44		0.91	0
[PR + BB]/2 - QCC		-5.6		0.72		0.83	0
Prince Rupert (PR)		141.		0.69		0.85	0
Q. Charlotte C. (QCC)		141.		0.51		0.15	12
Bella Bella (BB)		131.		0.67		0.78	0
UPWELLING INDICES		(10 kg s ⁻¹ m ⁻¹)		(10 kg s ⁻¹ m ⁻¹)			
Bakun 51°N		-7.6		10.1		-0.78	12
Bakun 54°N		-11.3		11.5		-0.65	12
TRANSPORT		(10 ⁶ m ³ s ⁻¹)		(10 ⁶ m ³ s ⁻¹)			
R-line		0.29		0.30		0.89	0
W-line		0.33		0.31		1.00	0

Table 3.2: Characteristics of time series in winter, 20 Jan to 4 Apr, 1984. The last two columns give maximum correlations and phase leads in hours of a given time series with transport through W-line. EOF 1 is the lowest (first) mode of wind from the the empirical orthogonal function analysis. Table 1c in Crawford et al.(1988).

deviation of the transport and wind stress time series were (0.36 Sv, 0.30 Sv) and (0.13 Pa, 0.17 Pa) respectively.

The EOF mode 1 wind pattern (Fig. 3.15) represents along-shore fluctuations in the wind field. The results in Table 3.2 support the idea that the major wind fluctuations are parallel to the coast. At all stations the major axis of variance is directed along-strait (roughly 340°T). At most stations the mean wind is also directed along the strait (roughly 340°T). The exception is Cape St. James where the mean wind has a large cross-strait component.

The linear correlation between the transport (as measured at W-line) and the various wind time series range from very good at Ethelda Bay ($r=0.74$) to not very good at Lucy Island ($r=0.41$). The correlation with the wind EOF 1 time series was better than with most of the individual wind time series. This suggests that the basin wide winds are more important to the transport than the wind at any one location (CHW88).

The calculation of the transport based on discrete current meters is potentially limited by the density of current meters. High frequency spatial variations in the velocity field can cause problems. The transport estimated by the single current meter R05 in R-line agreed very well with the estimate from W-line (Table 3.2). This increases the confidence in the estimate. CHW88 regarded the estimated transport through M-line as untrustworthy because it was the small difference between large northward and southward flows (see Fig. 2.8 and Fig. 3.15).

The aim of CHW88 was to test time series that could be used as surrogates for the transport in studies of fisheries stock recruitment in Hecate Strait. The cross-strait pressure difference B-A (Beauchemin Channel minus Atli Inlet) was a very good indicator of transport (Table 3.2). The high correlation between the transport and the cross-strait pressure difference is an indication that the transport in the strait is in geostrophic balance (balance between the Coriolis force and the cross-strait pressure gradient). There

is speculation that the cross-strait pressure difference is a better indicator of transport than that estimated from the current meters (W.R. Crawford, pers. comm.).

The sub-surface pressure gauges at Beauchemin and Atli were in place for only a few years. Among the time series with long historical records, adjusted sea level at Prince Rupert (PR) and Bella Bella (BB) were good indicators as were some of the wind time series.

Part of the motivation for the regional model was the hindcasting of the oceanographic conditions (transport) in Hecate Strait. An important question for this work is, does forcing the model with local winds improve the ability of the wind to predict the transport through the strait? Since the model is driven with wind stress, an assessment of the model requires correlation of transport with wind stress. Otherwise an improvement attributed to the model could simply be due to the use of wind stress instead of wind speed.

The correlation between the transport and the along-shore component of the wind speed (W) has been repeated for the model test period (25 Jan to 30 Mar 1984) for 4 lighthouse stations and W4S (Table 3.3). The correlation increased markedly at Cape St. James (0.70 to 0.78) due to the shorter time series. The first and last 5 days were particularly poorly correlated. The correlations at the other stations stayed much the same. The changes in the lead of the wind over the transport were due to the change to hourly time series (from six hourly in CHW88). The correlation analysis was done for all stations using wind stress time series calculated from (3.1) and a constant drag coefficient (τ_1). The final calculation (τ_2) computed the wind stress at the ocean-based anemometer W4S using the method of Smith (1988). The stress calculations were done *before* the time series were filtered and the along-shore component computed.

The correlations were not strongly peaked. In most cases the correlation coefficient r_{max} was reduced by less than 0.02 up to four hours on either side of the maximum. The analysis of CHW88 indicated that a sample correlation of 0.7 was drawn from a

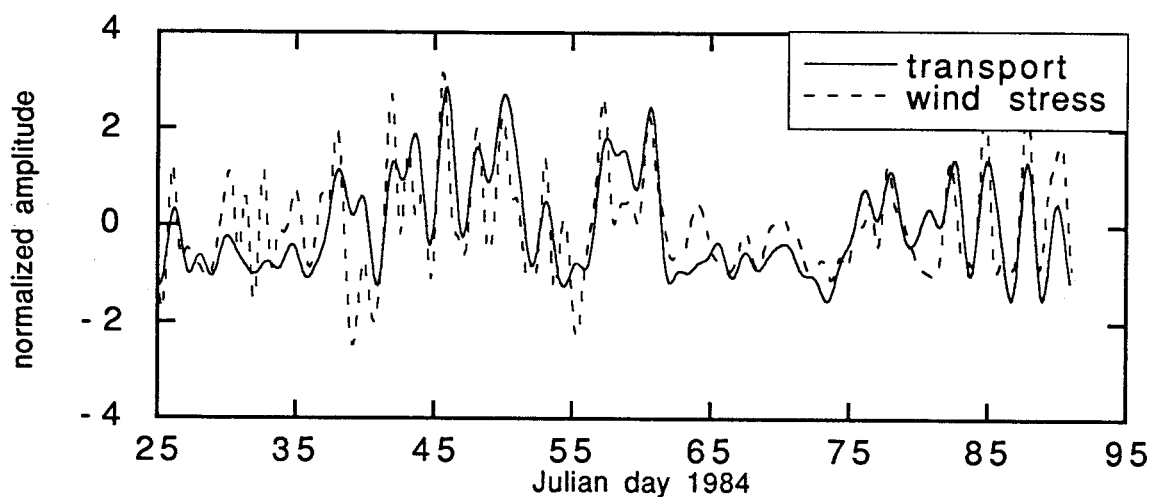


Figure 3.16: The observed transport and along-shore wind stress fluctuations in Hecate Strait from 25 Jan – 30 Mar 1984. Both time series have been normalized by subtracting the mean and dividing by the standard deviation.

Station	type	r_{max}	lead (h)
Cape St. James	W	0.78	9
	τ_1	0.78	9
Bonilla Island	W	0.68	5
	τ_1	0.74	3
Ethelda Island	W	0.77	5
	τ_1	0.77	5
Triple Island	W	0.67	4
	τ_1	0.69	4
W4S	W	0.62	8
	τ_1	0.72	8
	τ_2	0.70	7

Table 3.3: Correlation of transport with various wind time series for the period 25 Jan - 30 Mar 1984. The maximum correlation r_{max} was obtained for the lead given (lead of the wind with respect to the transport). Wind time series are the along-shore component of wind speed (W), wind stress using a constant drag coefficient (τ_1), and wind stress using Smith (1988) (τ_2).

population correlation in the range 0.5 - 0.8 (at 95% confidence limits). One should not place too much faith in the exact values of the correlation coefficients or the lags.

Using τ_1 rather than W did not increase r_{max} at Cape St. James, Ethelda Island, and Triple Island. The use of τ_1 gave a slight increase at Bonilla. The wind stress estimates τ_1 and τ_2 markedly increased r_{max} at W4S (from 0.6 to 0.7). τ_2 did not improve the correlation over τ_1 . The best correlations at each station came up to the same level. The square of the correlation coefficient is a measure of how well one time series explains the other. Based on r^2 , the local winds explain roughly 50% of the energy in the transport fluctuations. It is interesting to note that using the wind stress estimates had the largest effect at the two stations in central Hecate Strait.

3.2.3 Transport and the Mode 1 Currents

Tyler and Crawford (1991) provided evidence that the transport fluctuations in Hecate Strait are an important predictor of the fluctuations in the year-class strength of Pacific cod. No specific mechanism for the influence was proposed. CTT90 suggested that the mean and mode 1 current patterns were important for the advection of larvae in Hecate Strait. In hindsight an obvious question is, are the transport fluctuations and the mode 1 current pattern related?

The time series of the EOF mode 1 current fluctuations is compared with the transport fluctuations in Figure 3.17. To allow comparison the mean was removed from the transport and both time series were scaled by their standard deviation. They are almost the same time series. The correlation between the transport and the mode 1 currents is closer than the correlation between the transport and local winds ($r_{max} = 0.9$, compared with $r_{max} = 0.7 - 0.8$ for the winds). The current pattern shown in Fig. 3.15 is associated with the movement of water from one end of Hecate Strait to the other. For use in Fig. 3.17 the current meter data was normalized before the EOF modes were computed.

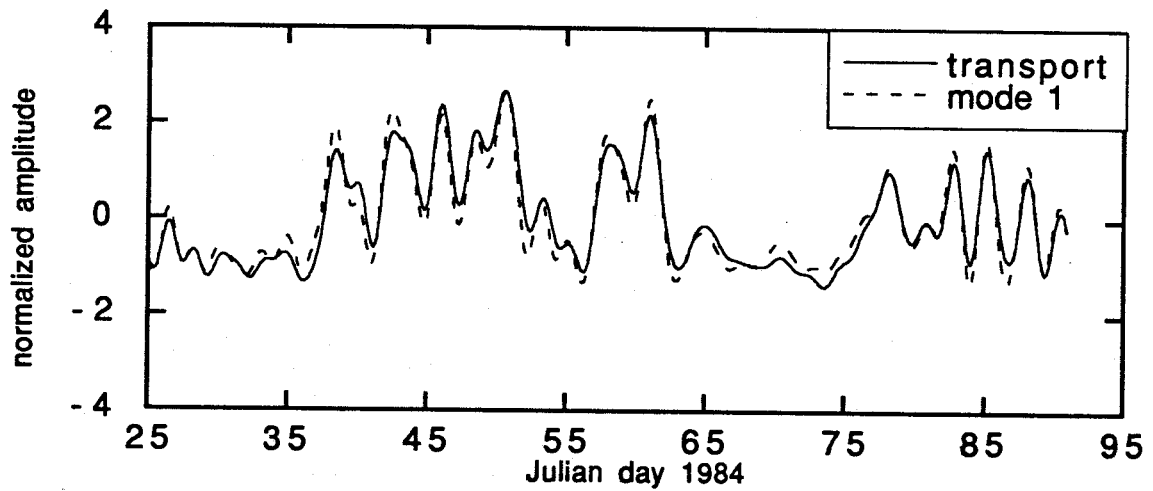


Figure 3.17: Comparison of the transport and mode 1 currents for the period 25 Jan - 31 Mar 1984. Both time series have been normalized by subtracting the mean and dividing by the standard deviation.

When the currents are not normalized before analysis, mode 1 current fluctuations and the transport fluctuations are identical.

The relationship between transport and the mode 1 currents implies that the winter transport fluctuations are associated with a particular current pattern. This provides some reason to believe that transport fluctuations are related to advection of fish eggs and larvae. On the other hand, the 75% of the energy in the current fluctuations not associated with mode 1 is not related to transport fluctuations. This places a hard limit on predicting advection patterns from transport (or surrogate transport) series. This relationship has not been tested for the summer and fall data sets.

3.3 Drifters

Most of the drifter observations have taken place in the summer, when the weather allows drifters to be recovered and redeployed. The drifters are intended to track the near surface waters. In general the drogue is a 5-m-high holey sock centered at 10 m. A few have drogues centered at 3 m.

For several years the drifter path shown in Fig. 3.18 represented most of the drifter data in Hecate Strait. The drifter was seeded to the east of Cape St James with the expectation that it would drift west past the Cape and get caught in an eddy. Instead it remained trapped in Queen Charlotte Sound for 6 weeks before escaping north through Hecate Strait and into Dixon Entrance. The winds during this first period (September and early October 1983) were variable. This drifter illustrates that the trapping of drifters in Queen Charlotte Sound near Cape St James is possible.

In late October the drifter travelled north along Hecate Strait under the influence of strong winds from the SE. The drifter entered Dixon Entrance at its eastern end and went in and out of Clarence Strait before moving west along Dixon Entrance and on into

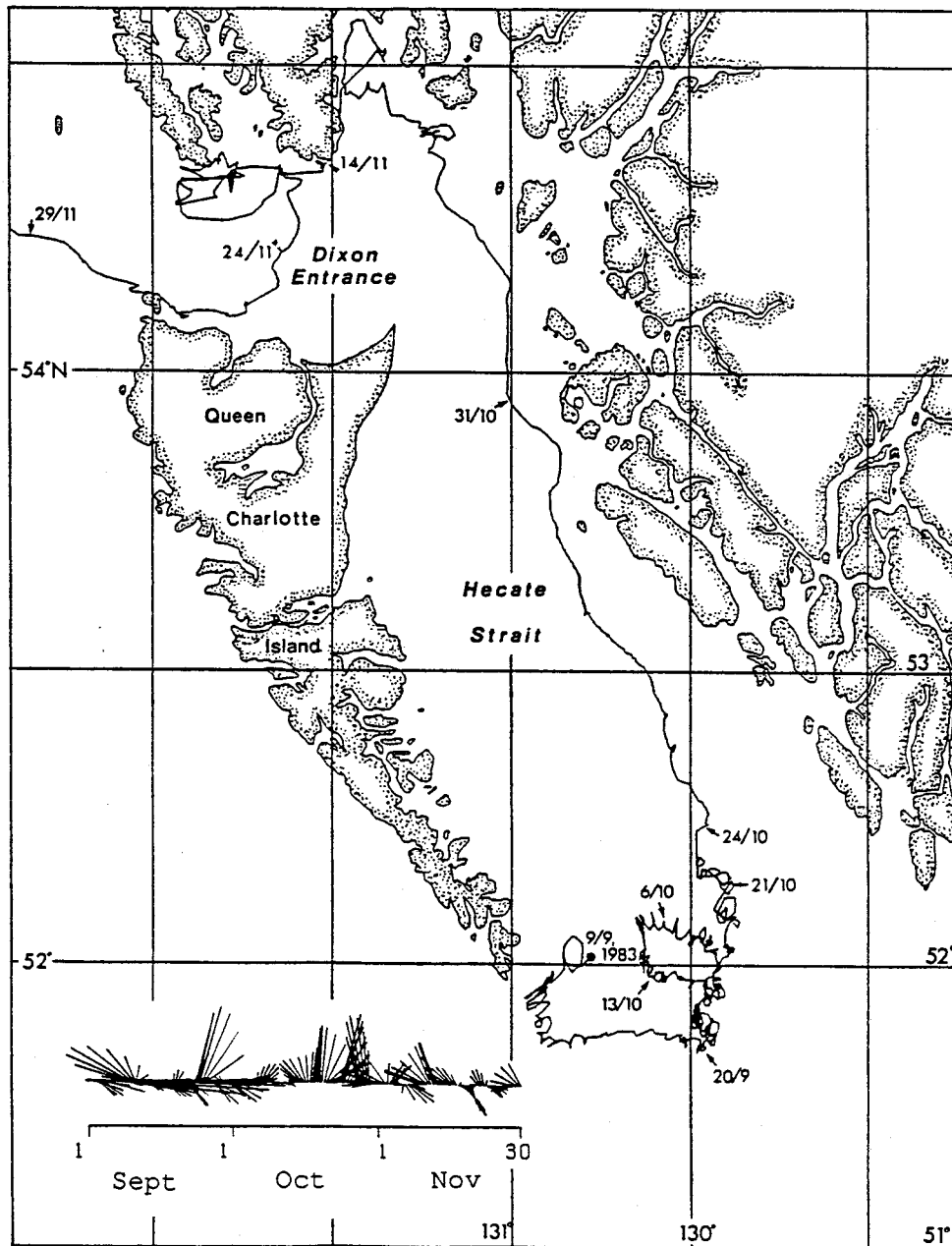


Figure 3.18: Path of satellite tracked drifter for 9 Sept – 29 Nov 1983. The winds at Cape St. James are shown in the lower left corner (1 day low-pass filtered). The free end of the wind vectors point in the direction the wind is blowing to. (Adapted from Fig.13 Hannah et al., 1991.)

the Pacific.

The drifters in Fig. 3.19 were part of an investigation into tidal rectification around Cape St James in March 1986 (Thomson and Wilson, 1987). The winds were generally from the south. The two drifters (1190, 1195) seeded near the coast on either side of the island travelled along the coastline in the direction of the wind. Drifters 1191 and 1193 escaped from Queen Charlotte Sound and illustrate the strong outflow near Cape St. James.

An important component of the overall project of which this thesis forms a part is an extensive program of near surface drifter studies. The first of these was conducted in southern Hecate Strait in the summer of 1990. The drifters in Fig. 3.20 are representative results from this deployment. The winds were generally from the northwest. The drifters were drogued at 10 m. Of the four drifters shown, three were seeded in the same area at different times and illustrate the variability in the flow. Drifters A and C illustrate the circulation up Moresby Trough against the wind and around the bank. These tracks are compatible with the summer mean currents in Fig 2.8. Drifter D, seeded later, went in the opposite direction. It moved to the north and then to the southwest where it followed a path similar to drifter B, which was seeded closer to Cape St James. These two drifters (B,D) travelled past Cape St James and across the shelf break and then looped back into the mouth of Queen Charlotte Sound. These two drifters indicate significant surface flows in and out of the mouth of Queen Charlotte Sound near Cape St James.

Strong outflow past Cape St James is often observed during NW winds. The outflow is believed to be driven by tidal rectification (Thomson and Wilson 1987) and estuarine outflow. The summer 1990 drifters confirm that the outflow is confined to an area very close to the Cape. Gray Rock is only 15 km southeast of Cape St. James and 10 of 12 drifters which escaped past Cape St James in July 1990 went between the Cape and Gray Rock. Drifters B and D were the only two to escape south of Gray Rock. The dynamical

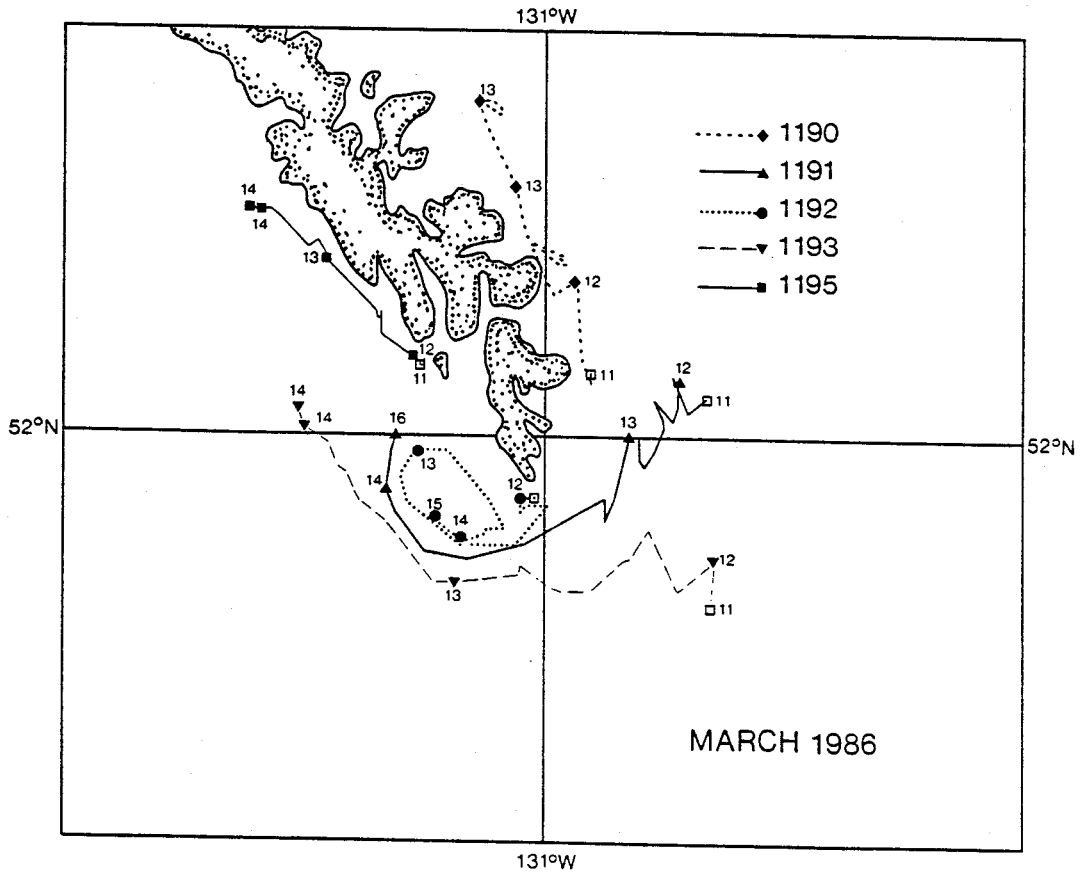


Figure 3.19: Drifter tracks near Cape St. James for the period 12–20 March 1986. (Adapted from Fig. 12a in Thomson and Wilson, 1987.)

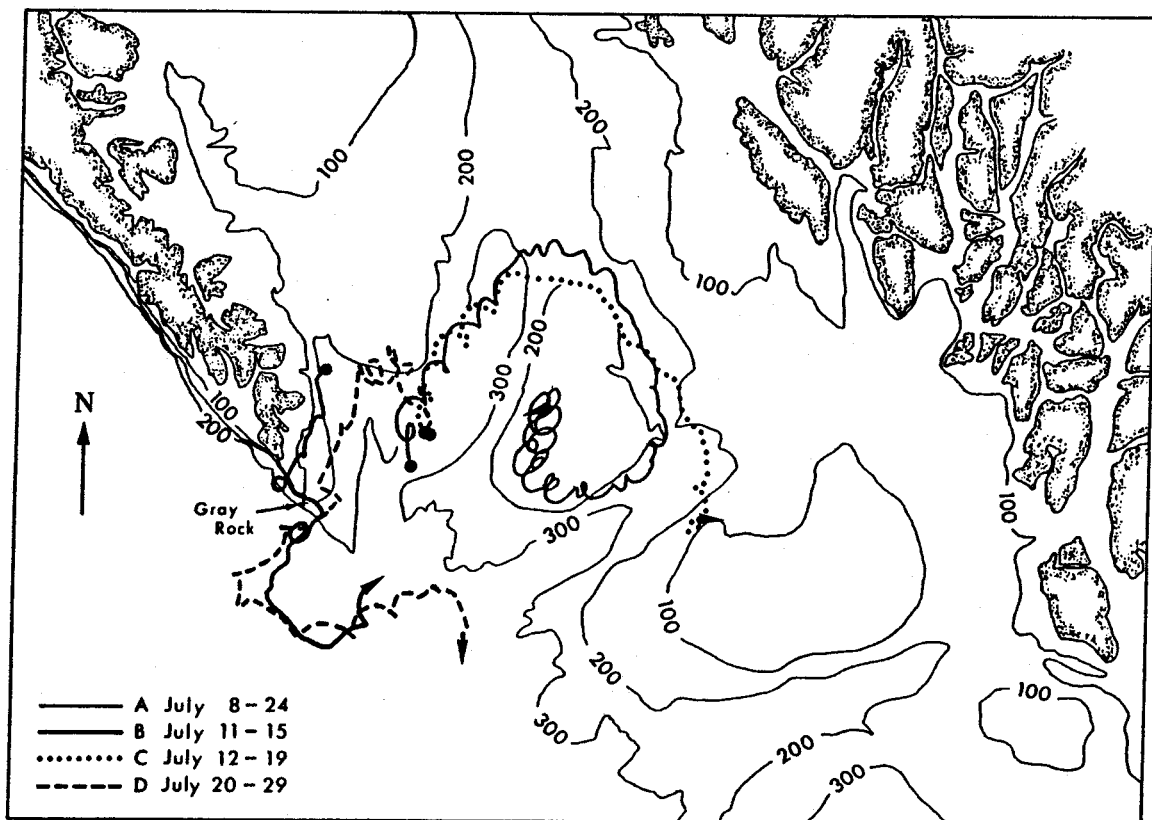


Figure 3.20: Drifter tracks in southern Hecate Strait from 8-29 July 1990. The winds were from the NW or N. (Adapted from Fig. 14 in Hannah et al., 1991.)

processes believed responsible for this outflow are not part of this model. Modelling this outflow feature is further complicated by its small spatial scale (15 km).

The tidal excursion at Cape St. James can be up to 10–15 km which makes drifter trajectories near the cape strongly dependent on tidal phase as the drifters approach it.

The two drifters shown in Fig. 3.21 along with the ones from March 1986 (Fig. 3.19) represent all of the winter drifter data in Hecate Strait. These satellite tracked drifters were seeded in January 1991 to provide some test data for the regional model. One drifter floated out of the mouth of Queen Charlotte Sound and travelled up the outside of the Queen Charlotte Island. This drifter made a short excursion into the mouth of Dixon Entrance. The other drifter stayed around Middle Bank and Moresby Trough for a long time until it grounded in a small inlet.

The drifter program in July 1991 concentrated on northern Hecate Strait. This region is most likely to be well described by a wind-driven, depth-averaged model as the water is shallow and well mixed even in the summer.

Fig. 3.22 shows selected drifter tracks that illustrate the character of the flow. The dramatic change in direction of three drifters (a35, b40, c22) corresponds to the change in direction of the wind around July 11. These drifters were all drogued at 3 m. The drifters in the deeper water actually turned around slightly later than the drifters in the shallow water (W.R. Crawford pers. comm., 1992). The fourth drifter, b32 (drogued at 10 m) was launched just after the wind shift.

Drifter c22 illustrates that the drifters tend to move along the steep escarpment extending NE from Rose Spit and that movement from Hecate Strait into Dixon Entrance tends to be confined to the region around Dundas Island. This behaviour was observed in other drifters as well.

The two drifters in Fig. 3.23 started at almost the same location and the same time. Drifter A was drogued at 3.5 m and B at 10 m. These drifters were put in place on July



Figure 3.21: Paths of two satellite tracked drifters from 19 January to 20 March 1991. The starting locations are marked by the two black dots east of Cape St. James. The winds were generally from the SE.

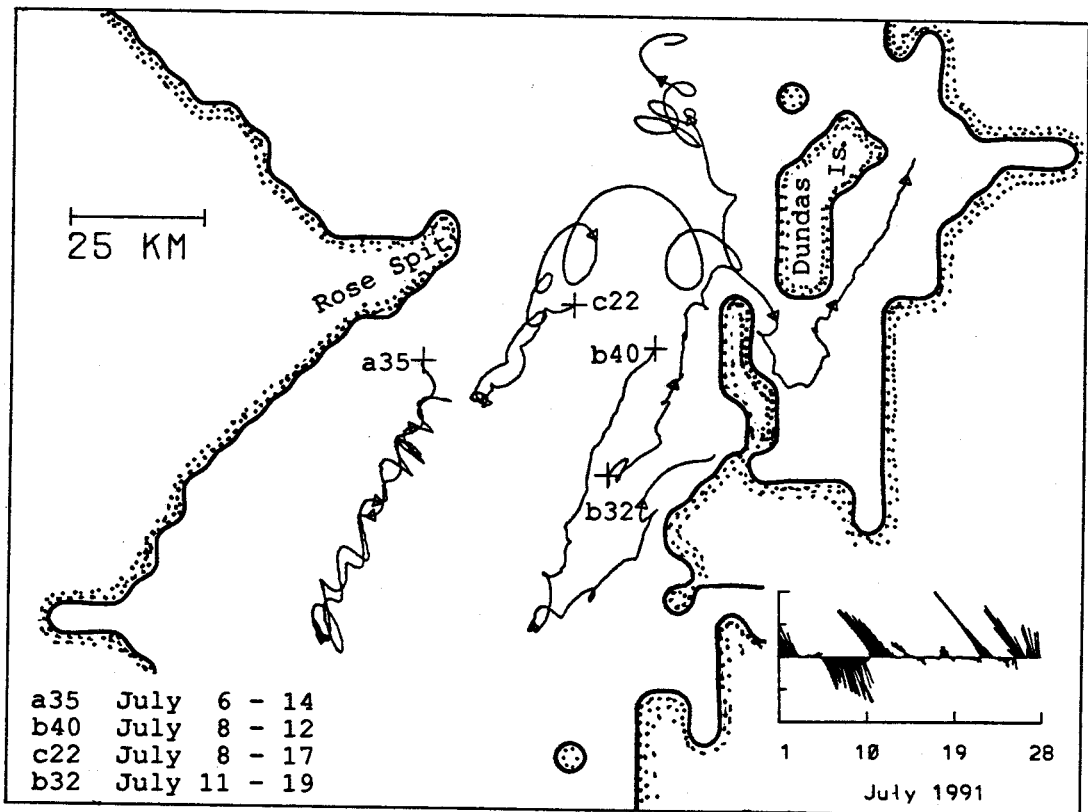


Figure 3.22: Drifters in northern Hecate Strait from July 1991. The abrupt change in direction displayed by drifters a35, c22, and b40 corresponds to the change in wind direction from NE to SE on July 10. Drifter b32 was launched after the wind changed direction. The arrows on the drifter paths mark 2 days elapsed time.

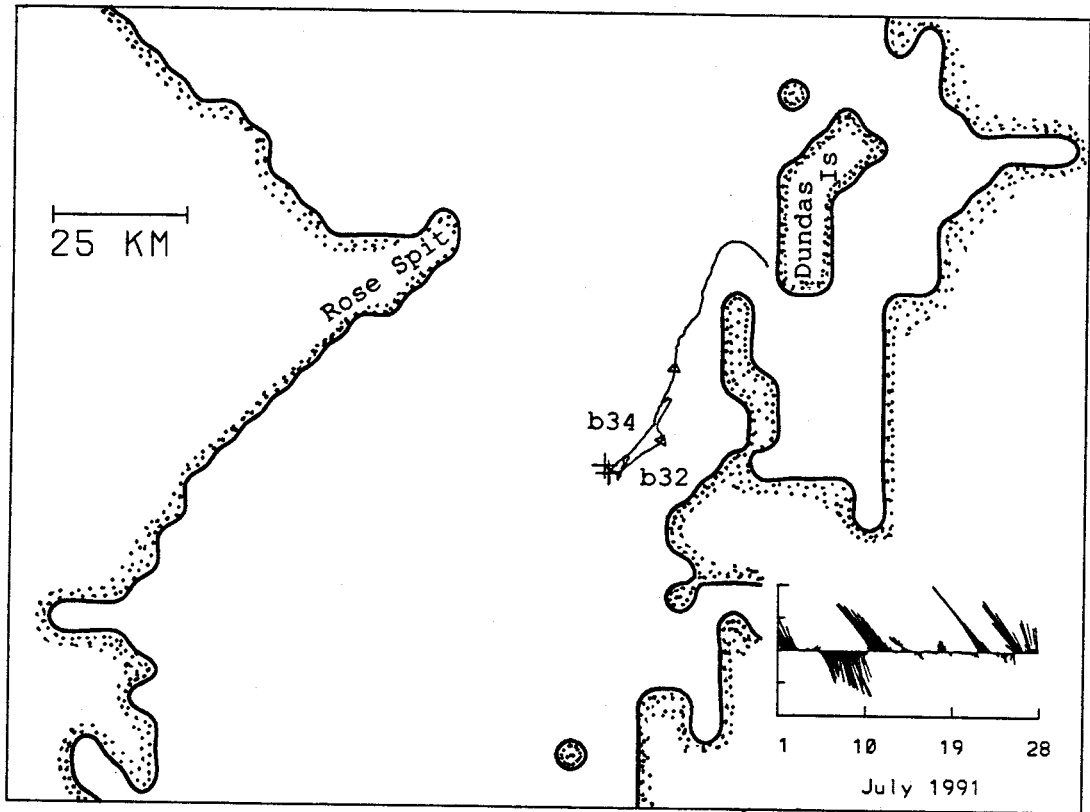


Figure 3.23: Two drifters in northern Hecate Strait from 11 to 13 July 1991. The drogue on drifter b32 was centred at 10 m, the drogue on b34 at 3.5 m. The two drifters were launched at the same time and b34 (shallow) travelled twice as far as b32 (deep). The arrows mark 1 day elapsed time.

11 just after the wind shifted to the southeast (Fig. 3.22). The difference in distance travelled over two the days was quite dramatic. The complete trajectory of drifter B is shown in Fig. 3.22 (drifter b32). These two drifters illustrate that there was vertical shear even through the water column was well mixed (W.R. Crawford, pers. comm.).

3.4 Summary

In Hecate Strait during the winter the local winds provide the primary mechanism for forcing velocity fluctuations with time scales of days to weeks. For the period January to April 1984 observation period, the 2-d low-pass filtered transport fluctuations were highly correlated with the local wind (filtered in the same manner). The mean velocity pattern is also believed to be wind-driven. In northern Hecate Strait the near-surface drifters reversed direction when the wind reversed.

The observations indicate that a model of the depth-averaged currents, forced by local winds, should simulate the transport fluctuations in Hecate Strait and capture the character of the current fluctuations. For the test period 20 January to 30 March 1984 the model should exhibit the following behaviour.

- The model should provide a good simulation of the transport fluctuations. The correlation between the simulated transport and the observed transport should be greater than $r = 0.7$, the maximum value of the correlation coefficient correlation between the winds at W4S (used to driven the model) and the observed transport.
- The model currents should capture the character of the mean and EOF mode 1 current pattern. In particular there should be a counter-current in the middle of M-line. The currents in the middle of M-line should be directed in the opposite direction to the currents at the edges of M-line and at R-line. This should be true of the mean currents and the EOF-mode-1 currents.

- The simulated transport fluctuations and EOF-mode-1 current fluctuations should be highly correlated, as they are in the observations.

It is difficult for a depth-averaged model to provide accurate simulation of drifter trajectories when even the well mixed water in northern Hecate Strait exhibits significant vertical current shear. However comparison of individual trajectories will be done for selected drifters from July 1990 and July 1991. A more general comparison of the simulated drifters with the general character of the observed drifters will also be carried out.

Chapter 4

Low Frequency Flow in Sea Straits

The purpose of this chapter is to develop the rotation-limited-flux model and apply it to Hecate Strait. Before delving into rotation-limited-flux, it is useful to introduce two important concepts: geostrophic balance and frictional adjustment. While the discussion takes place in the context of channel flow, both have wider application.

The sea strait under consideration is illustrated in Fig. 4.24 and Fig. 4.25. The strait has a flat bottom, uniform sides and the along-strait velocity is uniform in both the horizontal and vertical directions. The cross-strait velocity is ignored. The slope of the sea surface is exaggerated to emphasize the fact that the sea surface is not level in rotating channel flow: it slopes in both the cross-strait and along-strait directions. Two additional assumptions are made. Attention is restricted to low frequencies so that the assumption of cross-strait geostrophic balance can be made, and the velocities are assumed small enough so that linear models are appropriate.

4.1 Cross-strait Geostrophic Balance

One of the important force balances in oceanography is geostrophic balance: the balance between the Coriolis force and the pressure gradient. When studying the low frequency flow in sea straits, geostrophic balance is assumed to hold in the cross-strait direction. To first order, the cross-strait sea-surface slope balances the Coriolis force arising from

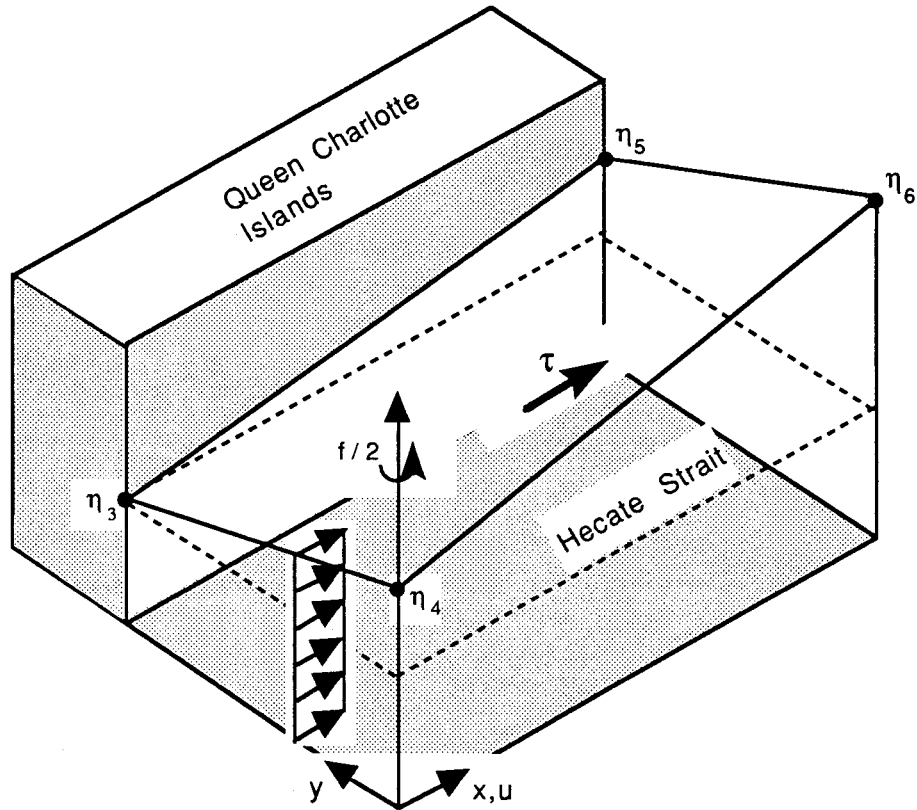


Figure 4.24: Schematic diagram of Hecate Strait.

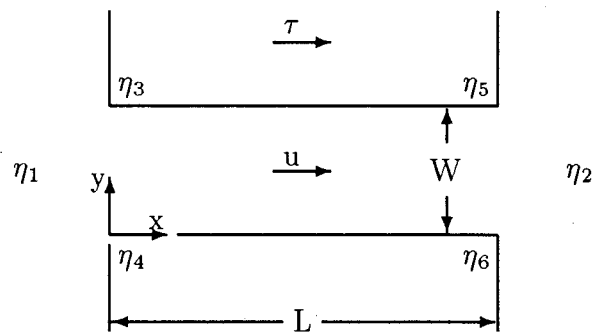


Figure 4.25: Plan view of the strait. η_1 and η_2 are the far-field sea level elevations. The other η_i are the sea levels at the respective corners. The corner labelling scheme is for the northern hemisphere.

the along-strait velocity:

$$fu = -g \frac{\partial \eta}{\partial y} \quad (4.2)$$

where f is the Coriolis parameter, u the along-strait velocity, g the acceleration due to gravity, η the departure of the sea surface from its mean level, and y the cross-strait coordinate. The cross-strait velocity is ignored. For a fluid of constant density, the sea surface gradient and the pressure gradient are equivalent: $\nabla(p/\rho) = g\nabla\eta$, where p is the pressure and ρ the density of water. The identity of the sea surface and pressure gradients is assumed throughout this thesis.

Cross-strait geostrophic balance means that flow through the strait affects the sea level at the coast. When looking in the direction of flow, the sea surface slopes up to the right and down to the left (in the northern hemisphere). In the southern hemisphere $f < 0$ and the sea surface slopes up to the left and down to the right. Cross-strait geostrophy is the reason for the correlation between the transport through Hecate Strait and the cross-strait pressure difference (Chapter 3).

4.2 Frictional Adjustment

Consider an infinite channel with uniform width and depth where the earth's rotation is ignored. The assumption of infinite length allows one to ignore along-strait pressure gradients. Let the depth-averaged, horizontally uniform, along-strait velocity be u and assume that the wind stress τ is parallel to the axis of the strait (Fig. 4.25). In the absence of along-strait pressure gradients, the dynamic balance is between the acceleration, the wind stress, and the bottom friction; a relationship of the form:

$$\frac{\partial u}{\partial t} + \lambda u = \frac{\tau}{\rho h} \quad (4.3)$$

where λ is a linear friction coefficient, h is the depth of the water, and ρ is the density of the water. This equation has some simple solutions.

Let the fluid start at rest, $u(0) = 0$. The solution for a constant wind stress τ_0 applied at $t = 0$ is

$$u(t) = u_\infty(1 - e^{-\lambda t}) \quad (4.4)$$

This is exponential relaxation to the steady state velocity $u_\infty = \tau_0/\rho h \lambda$ with e-folding time λ^{-1} . The time scale λ^{-1} is referred to as the relaxation time, the frictional adjustment time, the spin-up time, and the spin-down time. The solution (4.4) is also the solution for the velocity at the coast in a semi-infinite ocean, where the coastal boundary condition ($u=0$ at the coast) suppresses the Coriolis terms (Roed and Cooper, 1987).

The solution for an oscillating wind $\tau = \tau_0 \sin(\omega t)$ is

$$u(t) = \frac{u_\infty}{\sqrt{1 + (\omega/\lambda)^2}} \sin(\omega t - \phi) + \frac{\omega u_\infty}{1 + (\omega/\lambda)^2} e^{-\lambda t} \quad (4.5)$$

where $\tan \phi = \omega/\lambda$. The solution for $\tau_0/\rho h = 1$, $\omega = 1$, $\lambda = \omega/6$ is shown in Fig. 4.26. The parameters were chosen so that the two time scales were about the same ($\lambda^{-1} \sim T \approx 2\pi/\omega$). The initial overshoot is clearly visible.

The simplest model of flow in rotating straits assumes that frictional adjustment (4.3) holds in the along-strait direction and that geostrophic balance (4.2) holds in the cross-strait direction. What is ignored here is the along-strait gradient. The next section the along-strait pressure gradient is introduced. The frictional adjustment solution is recovered in the non-rotating limit or the limit of $W/L \rightarrow 0$.

4.3 Rotation-limited-flux

Rotation-limited-flux is a conceptual model of the influence of the finite length of the strait on the low-frequency flow. The work presented here is based on the original derivation by Garrett and Toulany (1982, hereafter GT) and the extension to include the local wind forcing by Hannah (1992a). The low frequency sea level response can be characterized in terms of two modes: a pressure-forced mode where the sea surface slopes down

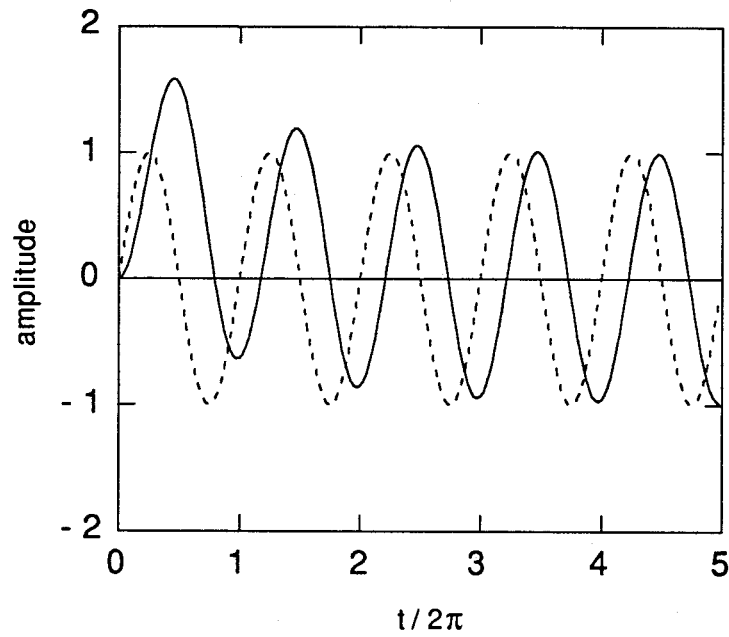


Figure 4.26: Frictional adjustment with sinusoidal forcing. The solid line is the velocity and the dotted line is the wind stress. The frictional scale $\lambda = \omega/6$.

in the direction of flow, and a wind-forced mode where the sea surface slopes up in the direction of flow. Both modes are assumed to be in geostrophic balance in the cross-strait direction, and therefore have cross-strait sea surface slopes. In the literature, the idea of rotation-limited-flux is also referred to as geostrophic control.

Hannah (1992a) compared the rotation-limited-flux model with an analytical model of flow in straits of finite length applied to Bass Strait (Middleton, 1991; Middleton and Viera (1991), hereafter MV). Their model deals explicitly with the ocean/strait coupling and the scattering of the Kelvin waves at the ends of the strait. For fluctuations with a period of 240 hours, the pressure-forced and wind-forced sea level responses derived from rotation-limited-flux were shown to be identical to those of MV.

The agreement between the rotation-limited-flux model and the results of MV arises from the following. When the width of the strait is less than one external Rossby radius (\sqrt{gh}/f), the low frequency (long wavelength) Kelvin waves have a uniform sea surface slope over the entire strait. When this is true, the primary assumption made in the derivation of rotation-limited-flux, that the derivatives in the equations of motion can be replaced by differences, is valid. In those cases, the rotation-limited-flux model provides useful insight into the low-frequency dynamics of the strait.

This section contains a brief derivation and a short discussion of the application to Hecate Strait. The details of the application to Bass Strait and the comparison with the results of MV are part of a paper in press (Hannah, 1992a). The original work, arising from this thesis, is the extension of the results of GT to include direct wind forcing, the demonstration that the rotation-limited-flux model is a valid long-wave approximation to the more sophisticated model of MV, and the application to Hecate Strait.

4.3.1 Derivation

Consider the same strait as before (Fig. 4.25) but now include the Coriolis force and both cross-strait and along-strait pressure (sea-level) gradients. The strait has length L , width W and uniform depth h . Assume that the strait connects two infinite oceans. The coordinate origin is the lower left corner (labelled η_4). Bottom friction is again parameterized by λu , where $\lambda = r/h$, and r is a friction coefficient. Following GT and MV, cross-strait geostrophic balance is assumed to hold and in the along-strait direction the local acceleration is balanced by the pressure gradient, friction, and wind stress. The model equations are

$$fu = -g \frac{\partial \eta}{\partial y} \quad (4.6)$$

$$\frac{\partial u}{\partial t} = -g \frac{\partial \eta}{\partial x} - \lambda u + F \quad (4.7)$$

where $F = \tau/(\rho h)$. The cross-strait velocity is ignored.

The cross-strait pressure difference is approximated by

$$\eta_4 - \eta_3 = \eta_6 - \eta_5 = -(f/g)uW \quad (4.8)$$

and the along-strait pressure difference is

$$\eta_5 - \eta_3 = -\frac{L}{g} \frac{\partial u}{\partial t} - \frac{L}{g} \lambda u + \frac{L}{g} F \quad (4.9)$$

The equation for the along-strait velocity, found by subtracting (4.8) from (4.9) and solving for u is

$$\frac{\partial u}{\partial t} + (\lambda + fW/L)u = \frac{g}{L}(\eta_4 - \eta_5) + F \quad (4.10)$$

This has the same form as the frictional solution (4.3). The strait responds to a suddenly imposed forcing with time-scale λ_1^{-1} , where $\lambda_1 = \lambda + fW/L$. The effect of the finite length of the strait disappears in the limit $fW/L \rightarrow 0$.

Consider the forced response to a single driving frequency, such that u , η , and F vary as $e^{i\omega t}$. It is useful to separate the flow into 2 parts: the pressure-driven flow and the wind-driven flow. Let $u = u_p + u_w$, where

$$u_p = \frac{\frac{g}{L}(\eta_4 - \eta_5)}{i\omega + \lambda + fW/L} \quad (4.11)$$

$$u_w = \frac{F}{i\omega + \lambda + fW/L} \quad (4.12)$$

The sea level difference $\eta_4 - \eta_5$ is an external forcing term, like the wind stress. It represents the pressure forcing due to the sea level difference between the two basins. All effects related to the difference in sea level between the two basins are associated with u_p . The effects of the local winds are contained in u_w . The ratio of the velocities is simply the ratio of the forcing terms.

In the limit $\omega, \lambda \ll fW/L$, the along-strait velocity can be written

$$u = u_p + u_w = \frac{\frac{g}{L}(\eta_4 - \eta_5) + F}{fW/L} \quad (4.13)$$

This is the maximum flow rate through the strait. The effect of friction and time variation is to further reduce the flux. This is the origin of the name rotation-limited-flux.

The steady-state limit ($\omega = 0$) of the wind mode is equivalent to that derived by Baines et al. (1991) for use in Bass Strait (their equation 14) and is subject to all the limitations discussed therein. The pressure mode corresponds to the result of GT, when η_4 and η_5 take on the appropriate far field values: $\eta_5 \rightarrow \eta_2$, $\eta_4 \rightarrow \eta_1$. The validity of this identification is part of the ocean/strait coupling. When dealing with observations one is not always able to distinguish between say η_1 and η_4 , and one is forced to use the available data.

Discussion of the ocean/strait coupling in the context of rotation-limited-flux (geostrophic control) can be found in GT, Toulany and Garrett (1984), Wright (1987), Rocha and Clarke (1987), Tang (1990), Pratt (1991), and Hannah (1992a). The coupling required

by rotation-limited-flux is consistent with that derived by MV. Therefore the rotation-limited-flux model is a consistent approximation to the more complete theory.

A consistent solution in the southern hemisphere ($f < 0$) can be derived by recognizing that η_4 and η_5 are the upstream points with respect to Kelvin wave propagation. Leave the coordinate system untouched (origin in the lower left corner) but interchange η_4 and η_3 and interchange η_5 and η_6 . With this labelling convention the along-strait velocity can be written

$$u = u_p + u_w = \frac{g}{L}(\eta_4 - \eta_5) + \frac{F}{i\omega + \lambda + |f|W/L} \quad (4.14)$$

which is valid for both hemispheres.

The sea level structure associated with each mode can be derived by assuming that the sea level varies linearly within the strait. Following the notation in MV, let wind-driven sea level be $\eta_w(x, y, t)$

$$\eta_w(x, y, t) = \alpha_1 N_w(x, y)$$

where

$$\alpha_1 = \tau L e^{i\omega t} / (\rho g h)$$

The sea level structure of the wind mode (in the northern hemisphere) can be written as

$$N_w = \Delta\eta_{along}(x/L) + \Delta\eta_{across}(y/W)$$

where $\Delta\eta_{along}$ is the along-strait sea level difference due to the local wind and $\Delta\eta_{across}$ is the corresponding cross-strait sea level difference. The along-strait sea level difference found by substituting (4.12) into (4.9) is

$$\Delta\eta_{along} \equiv (\eta_5 - \eta_3)_w = \alpha_1 \left(1 - \frac{i\omega + \lambda}{i\omega + \lambda + |f|W/L} \right) \quad (4.15)$$

which may be simplified by defining

$$(\eta_5 - \eta_3)_w = \alpha_1 K e^{-i\theta}$$

where

$$\begin{aligned}\theta &= \tan^{-1}\left(\frac{\omega}{\Gamma + \lambda}\right) \\ K &= \Gamma[(\Gamma + \lambda)^2 + \omega^2]^{-1/2} \\ \Gamma &= |f|W/L\end{aligned}$$

Γ is the rotation-limited-flux parameter.

The cross-strait sea level difference (substitute (4.12) into (4.8)) is equal to the along-strait pressure difference. This means that the diagonal pressure term $(\eta_4 - \eta_5)_w$ is identically zero. The *no pressure forcing* condition defines the coupling of the strait to the ocean for the wind mode and is consistent with the interpretation of u_p and u_w as pressure and wind modes. The sea level structure of the wind-driven mode is

$$N_w = K e^{-i\theta}(x/L - y/W) \quad (4.16)$$

The steady-state limit of the sea level response ($\alpha_1 N_w$) is equivalent to that derived by Baines et al. (1991) (their equation 13).

The sea level for the pressure mode is derived in a similar manner. Let

$$\eta_p(x, y, t) = \alpha_2 N_p(x, y)$$

where $\alpha_2 = (\eta_4 - \eta_5)e^{i\omega t}$. The sea level structure of the pressure mode is

$$N_p = 1 - (1 - K e^{-i\theta})(x/L) - K e^{-i\theta}(y/W) \quad (4.17)$$

The expressions for the sea level response structures in the southern hemisphere can be recovered with the substitution $y = 1 - y/W$ (Hannah, 1992a). The necessity for this is a consequence of the labelling convention for the southern hemisphere.

4.3.2 Wind and Pressure Driven Sea Level Responses

For the purposes of illustration consider the application of rotation-limited-flux to Hecate Strait. Parameter estimates are given in Table 4.4: the frequency corresponds to a period of 6 days. The parameter Γ is greater than ω and λ , but all three are of the same order of magnitude. For these parameters, the steady-state velocity is reduced by a factor of 4 compared with the non-rotating case: $\lambda/(\lambda + \Gamma) = 1/4$.

parameter	value
Coriolis parameter f	$1 \times 10^{-4} \text{ s}^{-1}$
frequency ω	$1 \times 10^{-5} \text{ s}^{-1}$
width W	50 km
length L	150 km
depth h	50 m
friction coefficient r	$5 \times 10^{-4} \text{ m s}^{-1}$
Rossby radius \sqrt{gh}/f	220 km
W/L	0.3
$\lambda = r/h$	$1 \times 10^{-5} \text{ s}^{-1}$
$\Gamma = f W/L$	$3 \times 10^{-5} \text{ s}^{-1}$
K	0.7
θ	14°

Table 4.4: Estimates of parameters for Hecate Strait

The phase lag θ is reasonably small and the sea level response modes can be discussed in steady state terms. For the wind mode (Fig. 4.27) the wind is blowing from left to right and the sea surface is tilted up in the direction of flow. This set-up is the defining characteristic of the wind mode. The pressure mode (Fig. 4.28) is characterized by tilting down in the direction of flow. By assumption, both modes are in geostrophic balance in the cross-strait direction. When looking in the direction of flow, they slope up to the right in the northern hemisphere and up to the left in the southern hemisphere.

The set-up character of the wind mode can be seen by considering the steady-state

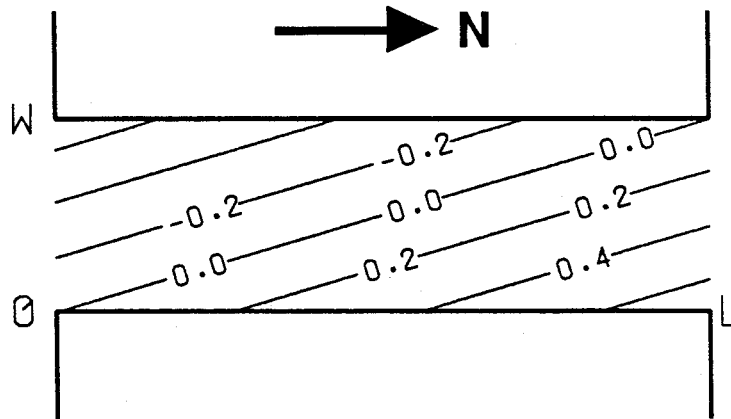


Figure 4.27: The sea level structure for the wind-driven mode, N_w .

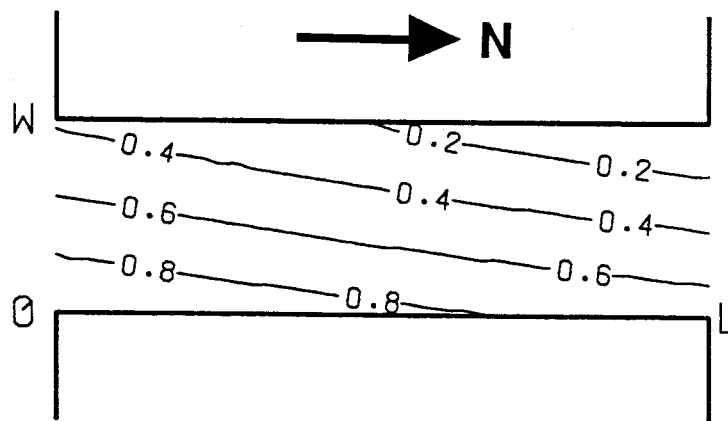


Figure 4.28: The sea level structure for the pressure-driven mode, N_p .

limit of the along-strait pressure difference (4.15)

$$(\eta_5 - \eta_3)_W = \alpha_1 \left(1 - \frac{1}{1 + \Gamma/\lambda} \right) \quad (4.18)$$

The first term is the pressure gradient, or set-up, that would arise if the down-wind end of the strait was closed. The second term is the reduction in the slope necessary to let the appropriate amount of water through. When the set-up is suppressed, the effect of rotation-limited-flux completely disappears and the frictional adjustment problem is recovered.

The along-strait structure can be hidden by combining the modes so that the along-strait gradients cancel and the combined sea level field looks like simple geostrophy. In the low frequency limit the condition is $\alpha_1/\alpha_2 = \lambda/\Gamma$. For Hecate Strait this would require that the pressure forcing be 5 times the wind forcing.

Hecate Strait is less than one Rossby radius wide (Table 4.4), so the rotation-limited-flux model should provide a useful description of the low-frequency sea level fluctuations.

4.3.3 Comparison with Observations in Hecate Strait

The work on rotation-limited-flux was motivated by the sub-surface pressure observations shown in Fig. 4.29. The data was filtered with the same 2-d low-pass filter as the currents and the time series were normalized before the EOF modes were computed. In both the fall and winter data, the first mode contained roughly 80-90% of the variance due to its large vertical excursion, and the second mode contained roughly 8%. In Table 4.5 each mode has two numbers listed for each station. The first is the component of the eigenvector corresponding to that station. This dimensionless number is a measure of the station's contribution to that EOF mode. For both seasons, all the stations contribute equally to mode 1 but some stations do not contribute to mode 2. The second number is the dimensional component plotted in Fig. 4.29 (see Appendix B for details).

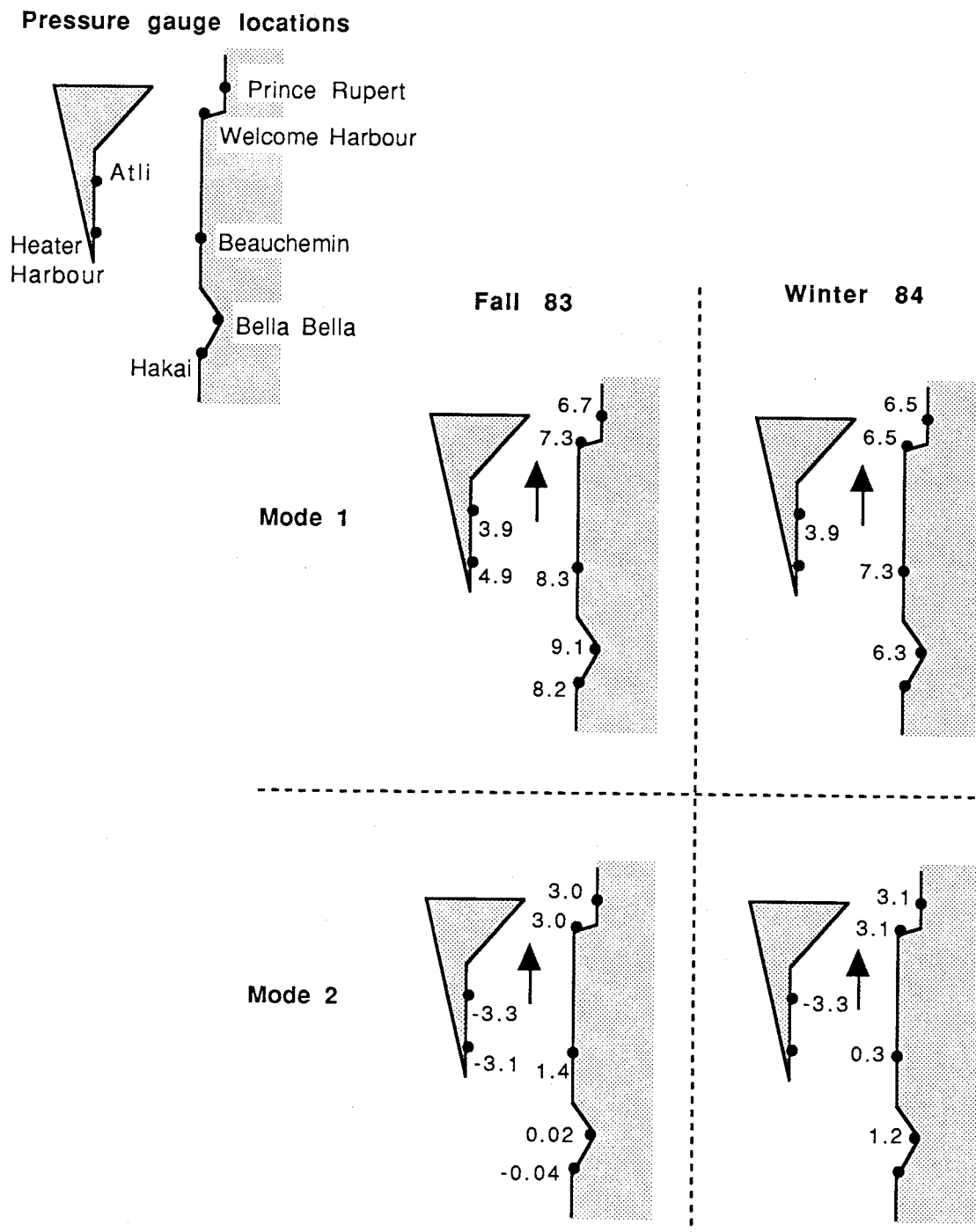


Figure 4.29: Spatial patterns of the observed sub-surface pressure fluctuations in Hecate Strait. Plotted are the first two modes of the empirical orthogonal function analysis for the fall of 1983 and the winter of 1984. The modal amplitudes are in cm of water. The arrow in Hecate Strait is the direction of the geostrophic current implied by the cross-strait pressure difference. The data are listed in Table 4.5.

Station	Fall 1983				Winter 1984			
	mode 1		mode 2		mode 1		mode 2	
		cm		cm		cm		cm
Prince Rupert	0.37	6.7	0.44	3.0	0.45	6.5	0.48	3.1
Welcome	0.38	7.3	0.41	3.0	0.45	6.5	0.48	3.1
Atli	0.41	3.9	-0.77	-3.3	0.41	3.9	-0.77	-3.3
Beauchemin	0.39	8.3	0.18	1.4	0.47	7.3	0.05	0.3
Heater Harbour	0.35	4.9	-0.58	-3.1	-	-	-	-
Bella Bella	0.39	9.1	-0.005	-0.04	0.45	6.3	0.20	1.2
Hakai	0.40	8.2	0.02	0.2	-	-	-	-
eigenvalues	6.3		0.9		4.4		0.89	

Table 4.5: Sub-surface pressure EOF modes in Hecate Strait. Each mode has two columns: the dimensionless eigenvector, and the eigenvector with units of cm of water. The eigenvalues are dimensionless. Fall 1983: 28 September to 20 December 1984. Winter 1984: 20 January to 4 April 1984. (Courtesy W.R. Crawford.)

After considerable studying of Fig. 4.29, two points emerge. For a given season, the modes have: 1) comparable cross-strait pressure differences and 2) comparable along-strait pressure differences. If one assumes that a cross-strait pressure differences implies an along-strait current in geostrophic balance, then the modes represent comparable currents. Mode 1 has the along-strait gradient in the direction of the implied current and mode 2 has the along-strait gradient opposing the implied current.

Mode 1 can be interpreted as a pressure-driven rotation-limited-flux mode. The aim of the work discussed in Section 4.3 was to learn if mode 2, with the along-strait pressure gradient opposing the flow, could be interpreted as a wind-driven mode. There are other possible explanations for the along-strait gradients. They could be artifacts imposed by the requirement that the modes be orthogonal, or they could be due to complex local effects.

When applied to Hecate Strait, rotation-limited-flux makes the following predictions about the qualitative structure of the sub-surface pressure modes. (The sea levels in Fig. 4.27 and Fig. 4.28 are equivalent to the observed sub-surface pressure fluctuations.)

The pressure mode (EOF mode 1) should have:

- an along-strait pressure gradient sloping down in the direction of the implied current.
- high correlation with the sub-surface pressure fluctuations at all the observation locations in Hecate Strait.
- the same sign at all locations. The sub-surface pressures rise and fall together.

The wind mode (EOF mode 2) should have:

- an along-strait pressure gradient opposing the implied current.
- a sign change across the strait. When the sub-surface pressure goes up on one side of the strait it should go down on the other.
- high correlation with the sub-surface pressure fluctuations at Atli and Heater Harbour (equivalent to location W in Fig.4.27).
- high correlation with the sub-surface pressure fluctuations at Welcome Harbour (location L in Fig.4.27).
- low correlation with the sub-surface pressure fluctuations at Beauchemin (equivalent to location 0); note the location of the zero line in Fig.4.27.

The observed modes have all these properties. Bella Bella and Hakai are outside of Hecate Strait.

The rotation-limited-flux model also predicts that both modes should be poorly correlated with the sub-surface pressure fluctuations in the north-west corner of Hecate Strait. This prediction can not be checked because there are no observations in that area.

Direct use of rotation-limited-flux as a model of the transport fluctuations in Hecate Strait raises some problems:

- Estimating the pressure forcing requires observations in the northwest corner in order to compute $\eta_4 - \eta_5$, and there are no observations there. In the Hecate Strait Model, the pressure forcing in the strait arises naturally as a consequence of movement of the sea surface over the whole Queen Charlotte Islands region.
- The estimate of the flux, $Q = Whu$, requires estimates of W and h . Given the strong bathymetric variations in Hecate Strait, the rotation-limited-flux model would contain 4 adjustable parameters: W , L , h , and λ . This is more adjustable parameters than are in the Hecate Strait Model.

Further application of rotation-limited-flux to Hecate Strait is limited to interpreting the results of the Hecate Strait Model.

Chapter 5

The Hecate Strait Model

The Hecate Strait Model is the first non-tidal model of the region. The decision made was to start with simple physics and create a model where the model was simpler than the real world and the assumptions were obvious rather than obscured by layers of numerics. To this end, the equations of motion were considered in their depth-averaged form which involves two restrictive assumptions:

- Density gradients do not contribute to the dynamics: the density field is replaced by the mean density.
- Vertical shear is ignored: the velocity vectors of the fluid elements in a column of water are replaced by a single vector.

These are important restrictions and they severely limit the practical application of the model. On the other hand, the restrictions make the problem tractable by reducing the size of parameter space. The model results can be used as a guide for more sophisticated models.

This chapter starts with a discussion of the shallow water equations which form the basis for the Hecate Strait Model. This is followed by a brief look at the finite differencing scheme. The balance of the chapter is devoted to an overview of the technical aspects of the model. Many of the details are contained in Appendix D.

The computer program that implements the numerical model is a modification of software provided by W.P. Budgell (Buckley and Budgell, 1988). My contributions to

the software development are discussed in Section 5.7.

5.1 The Depth-Averaged, Non-Linear Shallow Water Equations

The numerical model is based on the shallow water equations and these consist of statements of conservation of mass and momentum. The equations are used in depth-averaged or vertically integrated form. The coordinate system is defined in Fig. 5.30. The horizontal velocity vector \vec{v} has components (u, v) and the departure of the sea level from the average height (H), the sea level anomaly, is denoted η .

Conservation of mass, after integration over the fluid depth, is written

$$\nabla \cdot (\vec{v}h) = -\frac{\partial \eta}{\partial t} \quad (5.19)$$

where $h = H + \eta$ is the total depth and t is the time. A net influx of fluid into a control volume is accompanied by a rise in sea level.

Conservation of momentum in the horizontal, after depth-averaging, is written as

$$\frac{\partial \vec{v}}{\partial t} + \vec{v} \cdot \nabla \vec{v} = -f\hat{k} \times \vec{v} - g\nabla\eta + \vec{G} \quad (5.20)$$

where f is the Coriolis parameter, \hat{k} is the unit vector in the vertical direction, g is the gravitational constant, and $\vec{G}(x, y, t)$ represents the forcing and dissipation. Equation (5.20) is simply Newton's second law, with the acceleration of a fluid parcel being equal to the sum of the forces, which include the Coriolis term, pressure gradients, friction and body forces. The approximations, parameterizations, and outright fudges are restricted to the terms that make up \vec{G} .

The derivation of the shallow water equations from the Navier-Stokes equations in a rotating reference frame can be found in standard texts such as Pedlosky (1979). The fundamental assumption is that the horizontal scale of the motion is much greater than the vertical scale and the equations consider nearly horizontal motion: thus the shallow

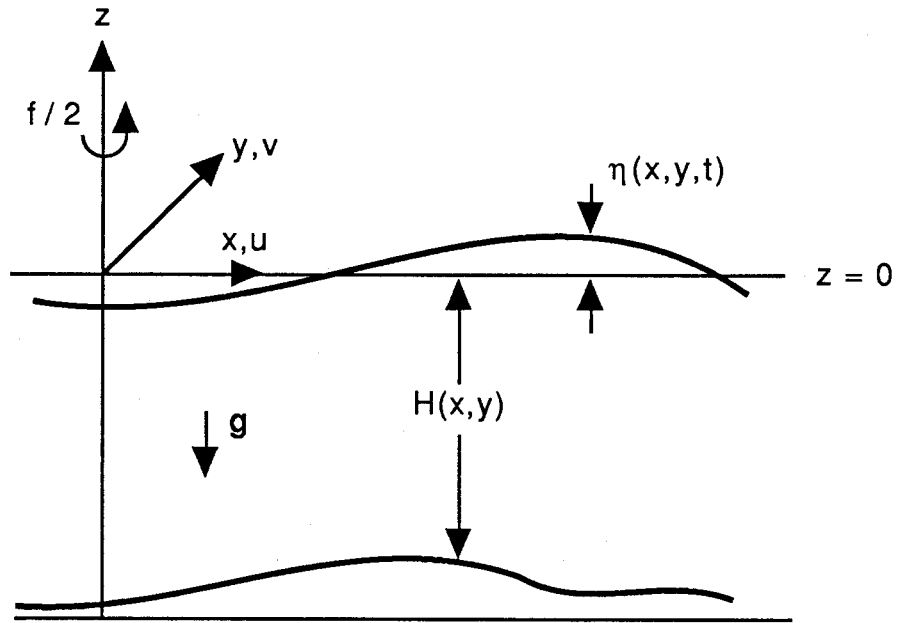


Figure 5.30: Sketch of the ocean defining the axis system.

water equations. Based on these scaling arguments, conservation of momentum is separated into vertical and horizontal components. In the vertical the assumption about the scales of the motion leads to the hydrostatic approximation, which reduces the vertical momentum equation to a balance between the vertical pressure gradient and the gravitational potential

$$\frac{\partial p}{\partial z} = -\rho g \quad (5.21)$$

where ρ is the density, p is the pressure and z the vertical coordinate (positive up). The hydrostatic approximation has been used to express the pressure in terms of the sea level anomaly η in the horizontal momentum equation (5.20).

The forcing and dissipation \vec{G} takes the form

$$\vec{G} = \frac{\vec{\tau}}{\rho h} - \frac{\vec{F}_b}{h} - \mu \vec{v} - \nu \nabla^2 \vec{v} \quad (5.22)$$

where $\vec{\tau}_s(x, y, t)$ is the wind stress and $\vec{F}_b(x, y, t)$ is the bottom friction. These surface stresses appear as body forces rather than boundary conditions because the flow is integrated over the water column. The last two terms represent internal frictional forces. The friction terms are discussed later in this chapter.

For the purposes of this thesis an f-plane model is applied, whereby the Coriolis parameter f is assumed constant over the model domain

$$f = 2\Omega \sin \phi = 1.15 \times 10^{-4} \text{ s}^{-1} \quad (5.23)$$

where $\Omega = 7.29 \times 10^{-5} \text{ s}^{-1}$, the rotation rate of the earth, and $\phi = 52.5^\circ \text{N}$ the latitude. Equations (5.19) and (5.20) are the depth-averaged, non-linear, shallow water equations on an f-plane.

5.1.1 Topographic Steering

Another view of the motion is found by taking the curl of (5.20) to form the vorticity equation:

$$\frac{\partial \zeta}{\partial t} - \frac{f}{h} \frac{\partial \eta}{\partial t} + (\vec{v}h) \cdot \nabla \left(\frac{f + \zeta}{h} \right) = \nabla \times \vec{G} \quad (5.24)$$

where the relative vorticity $\zeta = \hat{k} \cdot \nabla \times \vec{v}$ is the vertical component of the full relative vorticity vector. Equation (5.24) can be reorganized to yield

$$\frac{Dq}{Dt} = \left(\frac{\partial}{\partial t} + \vec{v} \cdot \nabla \right) \left(\frac{\zeta + f}{h} \right) = \frac{1}{h} \nabla \times \vec{G} \quad (5.25)$$

where the material derivative is

$$\frac{D}{Dt} = \left(\frac{\partial}{\partial t} + \vec{v} \cdot \nabla \right)$$

and the potential vorticity is defined by

$$q = (\zeta + f)h^{-1}.$$

Equation (5.25) is a statement of conservation of potential vorticity.

In the limit $\nabla \times \vec{G} \approx 0$ (no friction, no surface stresses), $\eta \ll H$, and $\zeta \ll f$ conservation of potential vorticity reduces to

$$\frac{D}{Dt}(f/H) = 0 \quad (5.26)$$

In the absence of other things, low frequency flow follows contours of f/H . When f is constant, the flow is parallel to the depth contours. This is called topographic steering.

5.1.2 Geostrophic Balance

The equations used to develop the conceptual models are simplifications of the shallow water equations. Consider the strait in Fig. 5.31, the same strait used in Chapter 4.

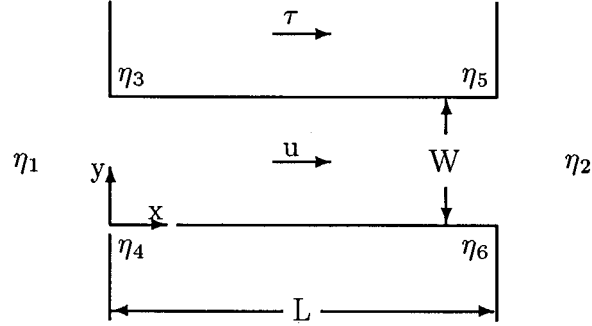


Figure 5.31: A sea strait

Let (u, v) be the along-strait and cross-strait velocities respectively. Let the wind be directed along-strait. Assume that the only friction is linear bottom friction and ignore the non-linear term. The horizontal momentum equation reduces to

$$\frac{\partial u}{\partial t} - fv = -g \frac{\partial \eta}{\partial x} + \frac{\tau}{\rho h} - \lambda u \quad (5.27)$$

$$\frac{\partial v}{\partial t} + fu = -g \frac{\partial \eta}{\partial y} - \lambda v \quad (5.28)$$

Under the further assumption that there is no significant cross-strait velocity (5.28) reduces to

$$fu = -g \frac{\partial \eta}{\partial x} \quad (5.29)$$

Equation 5.29 is an expression of geostrophic balance. The Coriolis force is balanced by the pressure gradient created by the sloping sea level. Looking in the direction of flow the sea level must be higher on the right-hand-side (in the northern hemisphere). This relationship, which is valid for low frequency flow in sea straits, is the reason for the high correlation observed between the transport through Hecate Strait and the cross-strait pressure difference (Chapter 3).

Equations 5.29 and 5.27 were used in the development of geostrophic control in Chapter 4.

5.2 Numerical Formulation

The numerical integration of the shallow water equations requires conversion of the continuous partial differential equations into discrete form. The technique chosen here is finite differences. There are many possible finite difference versions of the shallow water equations and each version has its own properties and problems (Mesinger and Arakawa, 1976; Haltiner and Williams, 1980). The scheme chosen follows Arakawa and Lamb (1981) for the spatial differencing and the leap-frog scheme for the time differencing.

5.2.1 Discrete Equations: Arakawa-Lamb, 1981

The scheme of Arakawa and Lamb (1981, hereafter AL81) is based on the idea that potential vorticity should be explicitly conserved in the finite difference form of the equations (5.20) and (5.19). The AL81 scheme guarantees conservation of mass, energy, momentum, and potential vorticity for the shallow water equations over arbitrarily steep topography. These conservation properties can hold only in the absence of the corresponding sources and sinks and the spatial discretization is specified for the unforced, frictionless, shallow-water-equations: $\vec{G} = 0$ in (5.20). The scheme is second order accurate in space. Details are given in Appendix D.

An important property of AL81 is the conservation of the domain integral of potential enstrophy, $hq^2/2$. The inaccuracies of finite difference versions of the non-linear shallow water equations tend to manifest themselves through the collection of energy at the smallest resolvable spatial scale: $2\Delta x$, where Δx is the grid size. AL81 attempts to control the transfer of energy to these small scales by conserving the domain integral of potential enstrophy. Restricting this spurious energy transfer means that 1) the model results will not change significantly when the grid resolution changes and 2) large viscous terms are not needed to soak up the small scale energy which would otherwise make the

model unstable.

5.2.2 Time Stepping: Leap-frog Scheme

Arakawa and Lamb (1981) specify the differencing of the spatial derivatives but not the time derivatives. The time stepping is done here using the leap-frog scheme. The friction terms are dealt with implicitly to avoid a well known instability (Mesinger and Arakawa, 1976).

Stability considerations require that the fastest wave can not cross a grid cell in less than one time step: the Cauchy- Fredricks-Levi or CFL criteria. For the numerical representation of the shallow water equations in two dimensions using the leapfrog scheme, the time step Δt must satisfy

$$\Delta t \leq \frac{\Delta s}{2\sqrt{2gh_{\max}}} \quad (5.30)$$

where Δs is the grid spacing and h_{\max} is the maximum depth in the model domain (Haltiner and Williams, 1980).

The leap-frog scheme introduces a computational mode which is filtered using a Robert (1966) filter. The filter has the form

$$\overline{s(n)} = s(n) + \gamma[s(n+1) - 2s(n) + \overline{s(n-1)}] \quad (5.31)$$

where s is the variable being filtered, n is the time index and the over-bar denotes a filtered value. The filter is applied to all three prognostic variables (u , v , η) at every grid point and every time step. A filter parameter of $\gamma = 0.01$ was used (Foreman and Bennett, 1988; Buckley and Budgell, 1988). The properties of this filter are discussed by Asselin (1972). There is a brief discussion in Appendix D.

5.3 Bathymetry, Grid Size and Time Step

The model domain is 450 km x 995 km with a grid spacing of 5 km (90 x 199 grid points). The domain is centered at 52.5°N, 131°W and rotated so that the shelf break is roughly perpendicular to the cross-shelf open boundaries. The map shown in Fig. 5.32 covers 90 x 150 grid points, the model domain extends 20 grid points (100 km) north and south of the area shown.

Although the ocean depths reach 3500 m in the model domain, the maximum depth in the model bathymetry is 2525 m. This permits a time step of $\Delta t = 10$ s and saves computation time. The depth limitation reduces the maximum Kelvin wave speed from 185 m s^{-1} to 157 m s^{-1} . This might limit the usefulness of this bathymetry as part of a tidal model since the meeting of the two arms of the tide in northern Hecate Strait is important. The effect on the results presented here is expected to be minimal.

Accurate representation of the bathymetry, or ocean topography, is important because topographic steering (the tendency of the flow to follow the depth contours) is an important part of the dynamics. The representation of the bathymetry is limited by the grid resolution. The choice of grid resolution requires balancing two competing considerations; the need for accurate bathymetry, and the need to limit the computational load. The computational load is linearly proportional to the number of grid points N and the number of time steps. Doubling the resolution increases the computational load by 8. There are 4 times as many grid points and twice as many time steps. The bathymetry, grid size, and time step are related through the CFL criteria (5.30). The grid size of 5 km was a compromise between 10 km (not enough resolution) and 3 km (too much computation).

Along-shore bathymetric variations were removed near the cross-shore open boundaries to suppress the generation of topographic waves near the cross-shore boundaries

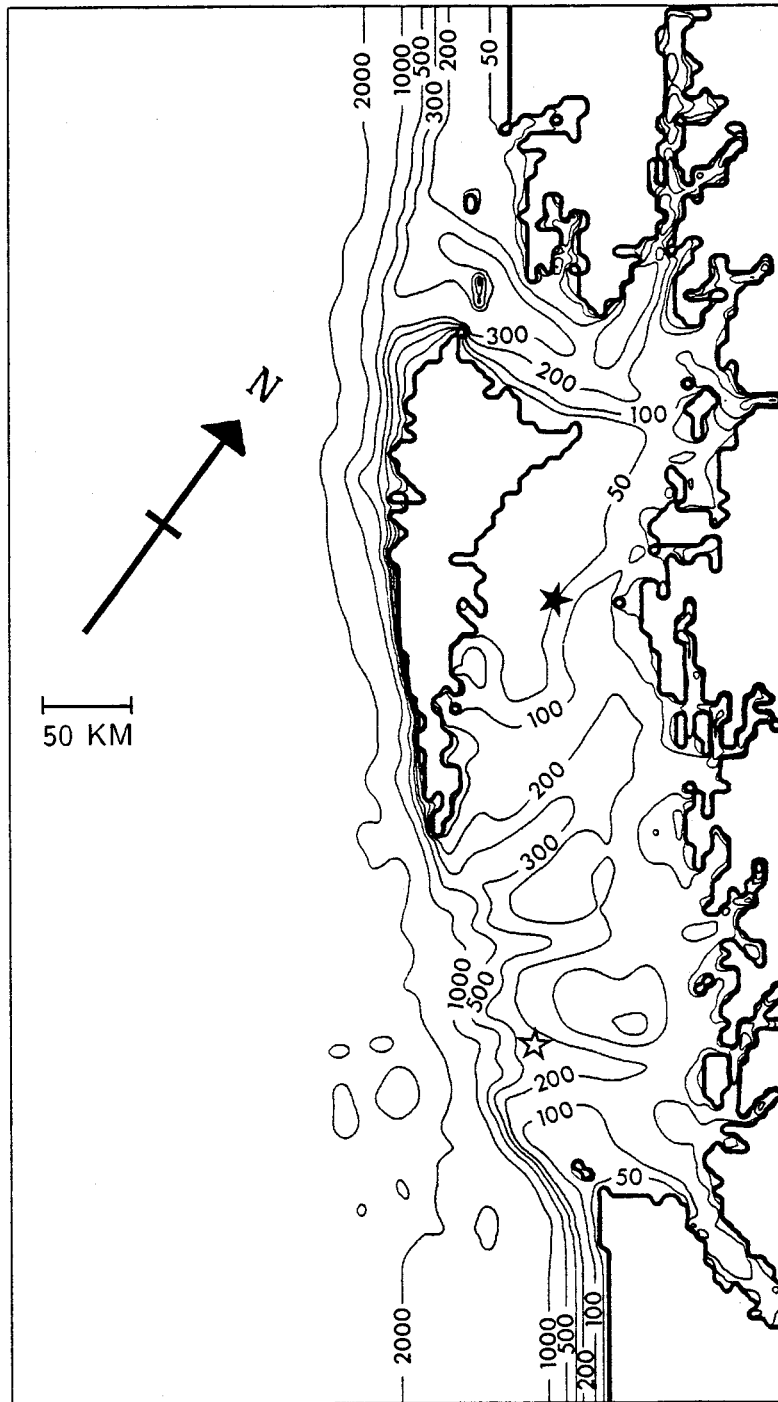


Figure 5.32: The model domain

and to accommodate the open boundary conditions discussed in Section 5.5. The uniform along-shore bathymetry extends 20 grid points (100 km) beyond the northern and southern ends of Fig. 5.32.

5.4 Energy Dissipation Mechanisms

Energy dissipation was parameterized in terms of the depth-averaged velocity. The form chosen was

$$\vec{F}_f = \frac{\vec{F}_b}{h} + \mu\vec{v} + \nu\nabla^2\vec{v} \quad (5.32)$$

These are the last three terms in \vec{G} (5.22) and they represent bottom friction, Rayleigh friction and eddy viscosity respectively. The primary mechanism for removing energy in the model is bottom friction. Additional dissipative effects due to the Robert (1966) filter are discussed in Appendix D.

Four bottom friction parameterizations were considered at early stages in the model trials:

$$\vec{F}_b = C_d(u_0^2 + |v|^2)^{1/2}\vec{v} \quad (5.33)$$

$$\vec{F}_b = k\vec{v} \quad (5.34)$$

$$\vec{F}_b = (ah_0/h)\vec{v} \quad (5.35)$$

$$\vec{F}_b = C_d v_{rms}(x, y)\vec{v} \quad (5.36)$$

These are referred to as quadratic friction, linear friction, h^{-2} linear friction, and spatially varying linear friction respectively. The first two forms are quite standard, the last two are not in common use.

Drag coefficients for quadratic friction (5.33) in depth-averaged models are usually in the range $C_d \approx 2 - 4 \times 10^{-3}$ (Murty, 1984). The spatially-invariant background velocity u_0 attempts to represent the effect of the missing tidal velocities by a single number.

The linear friction coefficient (5.34) can be derived by linearizing the quadratic friction with respect to a background velocity, $k = C_d u_0$. Tidal models indicate that the root mean square (rms) barotropic tidal velocities on the shelf range from 10 cm s^{-1} to over 40 cm s^{-1} (M.G.G. Foreman, IOS, pers. comm.). This gives k in the range $(0.3 - 1.6) \times 10^{-3} \text{ m s}^{-1}$.

The h^{-2} form (5.35) was discussed by Simons (1980), where it was suggested that $ah_0 \approx 0.1 \text{ m}^2 \text{ s}^{-1}$ in Lake Ontario. In this case, the use of (5.35) represents an attempt to have friction in the shallow water regions dominate the friction in the entire model. The choice of name comes from the fact that in the model equations \vec{F}_b/h has an h^{-2} dependence.

The form (5.36) was an attempt to improve the spatial distribution of bottom friction by using a spatially-variable tidal velocity when computing the linear friction coefficient. The rms tidal velocities ($v_{rms}(x, y)$) from the model described in Foreman et al. (1992) were used.

Linear friction is the standard bottom friction used in this thesis. The other forms are used to test the sensitivity of the model results to the bottom friction parameterization. The use of linear friction makes it easier to use the conceptual models presented in Chapter 4 to interpret the regional model results.

The depth dependence of the bottom friction means that it provides very little dissipation in deep water. The Rayleigh friction was introduced to provide dissipation in the offshore region. The parameter μ is important because it controls both the adjustment time and the steady-state velocity in the deep water.

The horizontal eddy viscosity ν was originally introduced to remove small scale retrograde shelf waves in a model of the Beaufort Sea (Buckley and Budgell, 1988). The eddy viscosity does not seem to affect the results in the Queen Charlotte Islands region. As reported by Hannah et al. (1991), tests with and without the eddy viscosity showed

that: 1) the model is stable when the eddy viscosity is removed ($\nu = 0$), and 2) the model results are not sensitive to the value of ν . The model usually runs with the horizontal eddy viscosity $\nu = 10 \text{ m}^2 \text{ s}^{-1}$.

5.5 Lateral Boundary Conditions

Regional ocean models have two types of lateral boundaries: side walls and open boundaries. Side walls are where the land and ocean meet. Open boundaries are arbitrary lines defining the limits of the regional model domain.

5.5.1 Side Walls

The side wall boundary condition used is: no flow through the boundary and free slip along the boundary. This is implemented by setting the normal velocity and the relative vorticity, ζ , equal to zero at the boundary. Neither the tangential velocity nor the sea level need to be specified at the land/ocean boundary (Appendix D). The reader should be aware that the real ocean does not have side walls, only a sloping bottom that intersects its surface.

5.5.2 Open Boundary Conditions

An open boundary is the arbitrary line drawn in the ocean that separates the known (the model domain) from the unknown (the rest of the ocean). Difficulties arise because the equations of motion contain spatial derivatives that require information from outside the domain when computing the solution at the open boundary. One way around this difficulty is to prescribe the solution along the boundary. This is the *only* way to get information into the model domain about events that occur outside the domain. This technique requires good information/observations about the solution along the open

boundary. In coastal tidal models and fjord models this is the only viable solution because the external forcing is of primary importance. In other cases one can make the approximation that all important events happen inside the domain – local forcing dominates. In these cases ‘...the purpose of the open boundary condition is to allow disturbances originating inside the model domain to leave without disturbing or deteriorating the solution in the interior.’ (Roed and Cooper,1987; hereafter RC87). In other words the numerical model must compute a solution along the open boundary which is transparent to all disturbances that reach the open boundary.

There is no general solution to the open boundary condition problem. As observed by Roed and Cooper (1987), ‘...the choice of OBC depends upon the particular application that modeler has in mind.’ In a regional model one cannot prove that an open boundary condition is fully satisfactory. The best that one can do is to demonstrate that it works in simple test cases and then carefully watch the numerical solution near the boundaries. Paranoia is a virtue.

For this model I assumed that the local winds provide the only important forcing mechanism. The only purpose of the open boundary conditions was to let disturbances out. External influences such as tides and shelf waves were ignored.

5.5.3 Implementation of the Open Boundary Conditions

The open boundary of the Queen Charlotte Island region can be thought of being composed of 3 pieces; northern and southern cross-shelf open boundaries and an offshore open boundary (Fig. 5.32).

Cross-shelf boundary

The cross-shore open boundary conditions used in this model are based on the flow relaxation scheme of Martinsen and Engedahl (1987). In this scheme the solution in the

interior of the domain is relaxed to a specified (exterior) solution at the open boundary in a relaxation zone. The cross-shore relaxation zones are not shown in Fig. 5.32. Each zone extends 100 km (20 grid points) beyond the edge of the figure. The discussion here refers to a single cross-shelf open boundary. The second one is dealt with in a similar manner.

The exterior solution chosen was a wind-forced solution: the solution to the equations of motion with all the along-shore gradients removed. This solution, which can be computed at the open boundary, does not permit the propagation of waves in the along-shore direction. The underlying assumption is that the shelf continues to infinity with the same topography. The exterior solution in the relaxation zone was computed during the model run using the same wind forcing as the rest of the model.

Relaxing the solution in the interior of the domain to the exterior solution means that waves propagating in the along-shore direction are damped and that there are no abrupt changes in mass fluxes near the open boundary. In the absence of wind the boundary condition reduces to a sponge layer: the exterior solution becomes a no-motion solution with $u = 0$, $v = 0$, and $\eta = 0$. As one might expect because the Ekman flux is handled correctly this open boundary condition is most successful when there is strong wind forcing.

The relaxation was done as follows. At all points not in the relaxation zone, the model solution equals the interior solution. At all points along the open boundary, the model solution equals the exterior solution. The model solution must then vary smoothly across the relaxation zone. At each time step and at each point in the relaxation zone a prognostic variable such as the along-shore velocity v is updated according to

$$v = \alpha v_1 + (1 - \alpha)v_2 \quad (5.37)$$

where v_1 is the exterior solution, v_2 is the interior solution, and the relaxation parameter α

varies only in the along-shore direction. At the open boundary $\alpha = 1$ and at 20 grid points from the open boundary $\alpha = 0$. Thus the relaxed variable v equals the exterior solution at the open boundary and the interior solution at the interior side of the relaxation zone. All of the experiments reported use α of the form

$$\alpha(i) = 1 - \tanh[(20 - i)/4], \quad i = 1, \dots, 20 \quad (5.38)$$

where $i = 1$ in the interior and $i = 20$ at the open boundary.

The choice of external solution means that the wind forcing is the only mechanism for forcing water through the cross-shore open boundaries. The other possible mechanism for forcing water through the boundaries is an along-shore pressure gradient. Since the external solution does not allow along-shore gradients, they are not part of the solution at the boundary. Techniques for handling outflow due to persistent pressure gradients near the open boundary are being developed (Lars Petter Roed, pers. comm., 1991).

Tests of the open boundary conditions are discussed in Appendix E

Off-shore Boundary

In their experiments ME87 use a relaxation zone along the off-shore boundary which is similar to the cross-shore one discussed. I am not convinced that a reasonable scheme exists for dealing with the fact that the cross-shore and off-shore relaxation zone intersect in the corners of the domain. Recall that in the cross-shore relaxation zone the solution has no along-shore gradients. In the off-shore relaxation zone the solution has no cross-shore gradients. In the corners these two solutions have to be combined.

The model used something simpler. The offshore boundary condition is a clamped sea level condition: $\eta = 0$ along the offshore boundary. This is the condition used in the boundary condition studies of Chapman (1985) and Roed and Cooper (1987).

5.6 Atmospheric Forcing Fields

5.6.1 Wind Stress

For the model simulations the wind stress field was constant in space and varied in time. The wind stress forcing was computed using winds measured by a sea-based anemometer close to the area of interest. For example the model verification tests in Hecate Strait were driven by winds measured at W4S in the middle of the strait.

The conversion of raw wind speeds to model wind stress was discussed in Chapter 3. For the simulations the wind stress time series were passed through a 1-day low pass filter to suppress inertial oscillations and other high frequency motion in the model. The wind stress in the model was updated hourly.

The fact that the conversion from wind speed to stress is non-linear means that it is important that the filtering be done after the conversion, not before. For the winter of 1984, filtering the wind velocities before converting to stress resulted in a four-fold decrease in the peak wind stress compared with filtering after. The more the winds are averaged before the conversion, the lower the peak wind stress. Using a larger effective drag coefficient does not recover the peaks.

The decision not to use lighthouse winds for calculating the wind stress to drive the model has an important consequence. It reduces the number of tunable parameters in the model. Recall that Smith (1988) has no free parameters whereas using lighthouse winds involves at least one, the drag coefficient. When both the wind stress and bottom friction are adjustable there is room for endless adjustment of parameters to try and improve the agreement between the model results and the observations. When only the bottom friction is adjustable the room for parameter adjustment is drastically reduced.

5.6.2 Pressure Gradients

Atmospheric pressure gradients were not used to force the model. In general, open boundary conditions do not react well to forcing with atmospheric pressure gradients. I have not developed a robust method of handling pressure gradients near the open boundaries. The effect of atmospheric pressure gradients on the circulation in this region has not been investigated.

5.7 Computer Program

The original version of the model software was provided by W.P. Budgell. The model was developed for use in the Beaufort Sea (Buckley and Budgell, 1988). The software has been extensively rewritten to make the program easier to use, easier to modify, and to fix a few bugs. These changes have been largely confined to the input, output and diagnostic routines. The code that implements the Arakawa and Lamb (1981) algorithm is untouched.

The code for the open boundaries was rewritten to implement the flow relaxation boundary conditions. The drifter module was modified to implement different time stepping algorithms and to check for drifters crossing land/ocean boundaries. The vorticity balance module was rewritten to improve the estimate. The input and output modules have been rewritten.

A combined user's manual and model documentation (Hannah, 1992b[37]) has been written to provide a new user with enough information to run the Hecate Strait Model and make minor changes to the software.

Chapter 6

Evolution from Rest to Steady State in the Hecate Strait Model

This chapter contains a short discussion of the behaviour of the Hecate Strait model as it evolves from a rest to a steady state: the model spin-up. The two important results are:

- The spin-up of the transport through Hecate Strait is dominated by 2 time-scales: a fast adjustment (4 h) and a slow adjustment (48 h). The fast adjustment is the response of the strait to the local wind forcing. The slow adjustment is the response to the along-shore pressure gradient which results from the spin-up of the rest of the model domain.
- The steady-state transport through the strait is only weakly dependent on the values of the friction parameters.

Other topics discussed are frictional adjustment, the selection of the friction parameters for the simulations in the next chapter, and a preview of the circulation patterns. The results presented here form the basis for the discussion in the next chapter, and the reader should at least browse through this chapter before continuing.

For the purpose of this thesis the phrase *numerical experiment* means that the model was forced with very simple forcing; a sinusoidal wind, for example. The word *simulation* means that model was forced by a time series computed from observed winds. The purpose of a numerical experiment is to learn about the inner workings of the model. The purpose of a simulation is to compare the model results with observations.

6.1 Frictional Adjustment

Numerical experiments reported in Appendix E show that frictional adjustment (4.4)

$$u = u_{\infty}(1 - e^{-\lambda t})$$

provides a good description of the along-shore velocity in a simple rectangular domain with uniform along-shore topography and realistic cross-shelf topography. In the Hecate Strait Model, the concept of frictional adjustment is important for three reasons: 1) it provides an upper bound on the adjustment time scale λ^{-1} , 2) the time-scales in the open-ocean portion of the model domain are determined by friction, and 3) the concept can be generalized to include effects such as geostrophic control (Chapter 4).

Linear friction (5.34) is the standard form for bottom friction in the Hecate Strait Model. From Chapter 4, the relaxation constant has the form

$$\lambda = k/h + \mu$$

where k and μ are constants and the total water depth h is variable. The dependence of the steady state velocity ($u_{\infty} = \tau/\rho h \lambda$) and frictional adjustment time (λ^{-1}) on total water depth h and Rayleigh friction μ are shown in Fig. 6.33 and Fig. 6.34 (for $k = 0.5 \cdot 10^{-3} \text{ s}^{-1}$). The general behaviour is that the frictional adjustment time increases and the steady-state velocity decreases as the depth of the water increases. Notice the wide range of adjustment time as a function of depth. For $\mu = 3 \cdot 10^{-7} \text{ s}^{-1}$ the adjustment time ranges from 1 day for $h = 50 \text{ m}$ to 21 days for $h = 2000 \text{ m}$.

In the limit $\mu = 0$, the steady state velocity is independent of the water depth and the spin-up time increases linearly. In the limit $k = 0$, both the steady state transport (vh) and the spin-up time are independent of water depth and the velocity decreases with water depth. For $k \neq 0$ and $\mu \neq 0$ the behaviour is a mixture of the two limiting cases.

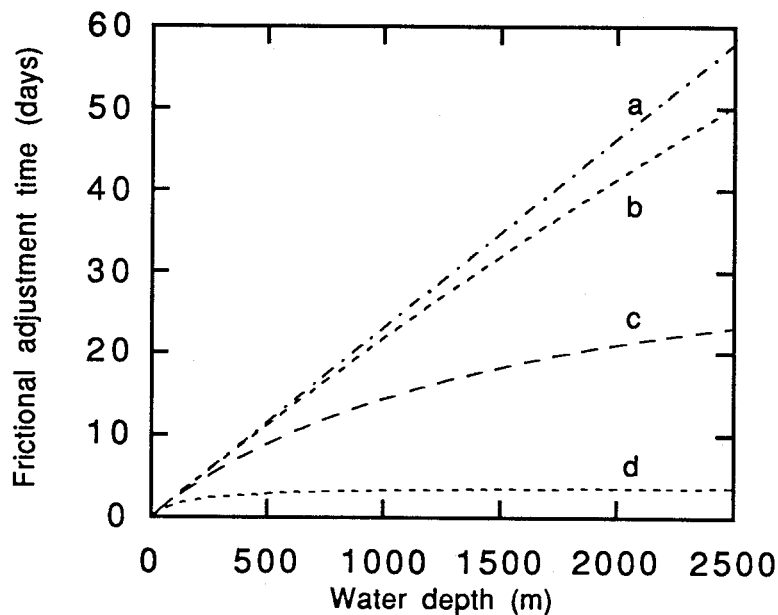


Figure 6.33: Frictional adjustment in a simple channel. Spin-up time as function of the water depth for $k = 0.5 \cdot 10^{-3} \text{ s}^{-1}$ and (a) $\mu = 0$; (b) $\mu = 3 \cdot 10^{-8} \text{ s}^{-1}$; (c) $\mu = 3 \cdot 10^{-7} \text{ s}^{-1}$; (d) $\mu = 3 \cdot 10^{-6} \text{ s}^{-1}$.

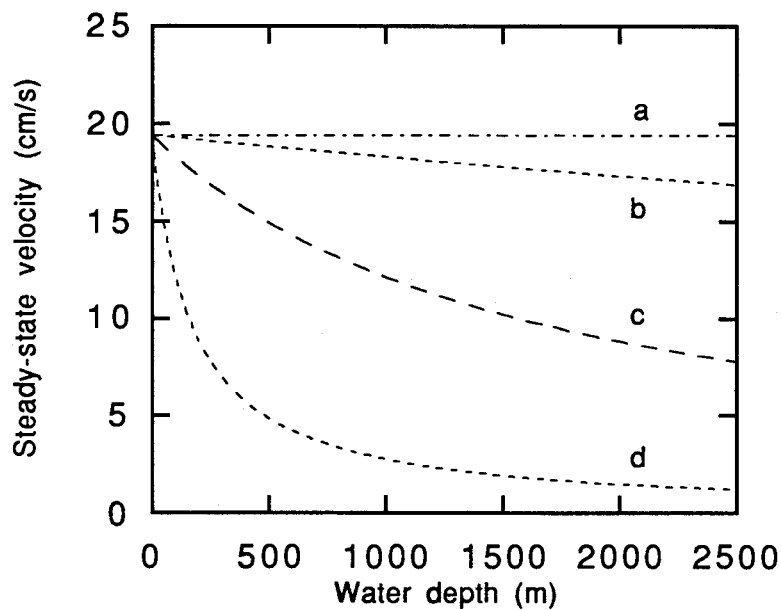


Figure 6.34: Frictional adjustment in a simple channel. Steady state velocity as a function of the water depth for $k = 0.5 \cdot 10^{-3} \text{ s}^{-1}$ and (a) $\mu = 0$; (b) $\mu = 3 \cdot 10^{-8} \text{ s}^{-1}$; (c) $\mu = 3 \cdot 10^{-7} \text{ s}^{-1}$; (d) $\mu = 3 \cdot 10^{-6} \text{ s}^{-1}$.

The along-shore velocity and the adjustment time are very sensitive to the value of the Rayleigh friction. The Rayleigh friction is a one-parameter model of the deep ocean. It was not intended to affect the shelf circulation. The dependence of the regional model results on both k and μ is investigated in the next section.

6.2 The Basic Experiment: Spin-up

A useful way to study the model is to watch it evolve from rest to a steady state: a spin-up experiment. In the basic spin-up experiment the ocean starts at rest ($u=0, v=0, \eta=0$) and a constant wind stress is applied at time $t=0$. The initial impulse excites a broad range of frequencies and allows observation of the relaxation (or adjustment) processes and the natural modes of the system (resonances). The spin-up experiment is the basic experiment conducted in this chapter. In cases where an impulsive start is not desired, the wind is started smoothly with a cosine ramp

$$\tau = \begin{cases} \tau_0(0.01 + 0.495(1 - \cos(\pi t/t_0))) & t < t_0 \\ \tau_0 & t \geq t_0 \end{cases} \quad (6.39)$$

where t_0 equals one or two days.

Most of the experiments in this chapter were forced with a uniform along-shore wind stress of $\tau_0 = 0.1$ Pa: a wind speed of roughly 8 m s^{-1} . Other directions are considered in later chapters. The wind stress was tapered linearly to zero at the off-shore boundary over the outer 25 grid points. The standard model parameters are listed in Table 6.6. Bottom friction is linear (5.34) unless explicitly noted. The Hecate Strait Model domain and the observation locations are shown in Fig. 6.35.

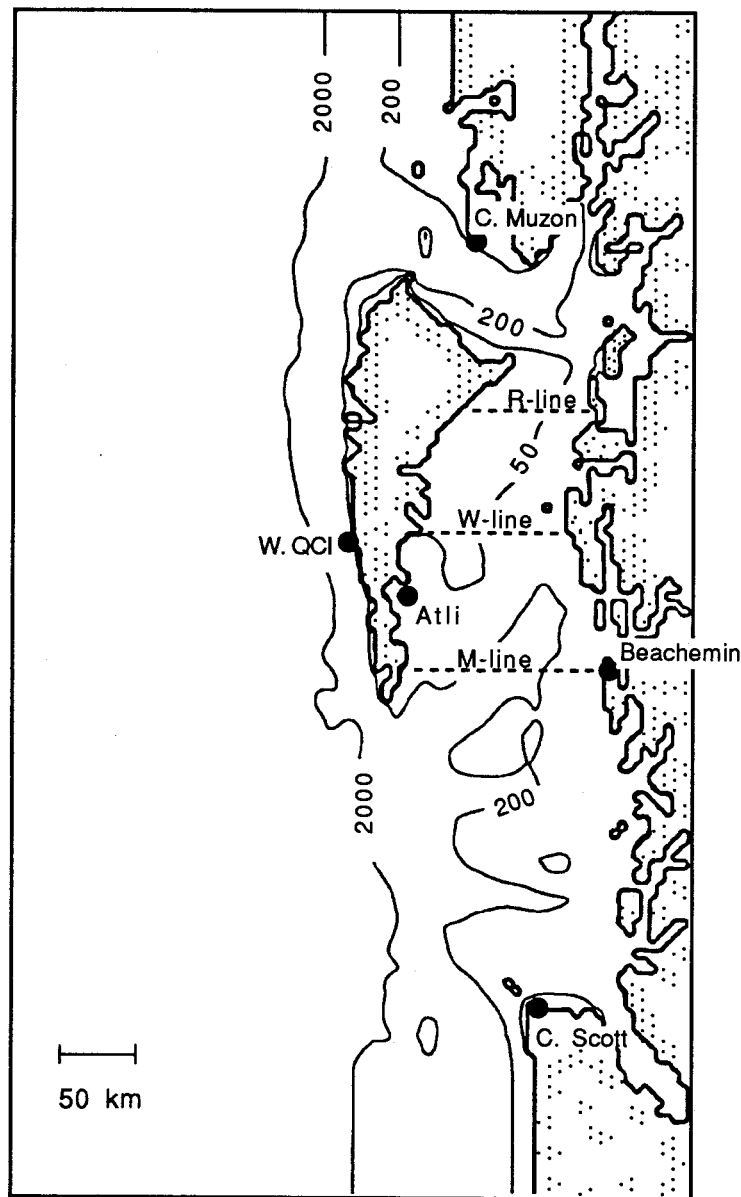


Figure 6.35: The standard model domain. The cross-shore flow relaxation zones are not shown; they extend 100 km off the top and bottom of the figure. The line on the left-hand side is the off-shore open boundary.

L	domain length	199 grid points
W	domain width	90 grid points
Δs	grid size	5 km
h_{max}	maximum depth	2525 m
Δt	model time step	10 s
f	Coriolis parameter	$1.15 \cdot 10^{-4} \text{ s}^{-1}$
k	friction parameter	$0.5 \cdot 10^{-3} \text{ s}^{-1}$
μ	Rayleigh friction	$3.0 \cdot 10^{-7} \text{ s}^{-1}$
ν	eddy viscosity	$10 \text{ m}^2 \text{ s}^{-1}$
γ	filter parameter	0.01
ρ	density of sea water	1030 kg m^{-3}
	relaxation zone width	20 grid points

Table 6.6: Standard regional model parameters.

6.3 Selecting Friction Parameters

The friction and dissipation mechanisms discussed in Chapter 5 are the only adjustable parameters in the model. The experiments reported here provide a basis for selecting parameter values. The selection criterion was that the steady-state transport be roughly 0.3 Sv for an along-shore wind stress of $\tau = 0.1 \text{ Pa}$, in rough agreement with the observations (Chapter 3). The parameter values chosen are used in the simulations in the next chapter. More important than the actual values selected is the fact that the model transport is only weakly dependent on the friction parameter values.

k (s^{-1})	μ (s^{-1})		
	0	$3 \cdot 10^{-7}$	$3 \cdot 10^{-6}$
$0.3 \cdot 10^{-3}$	0.34	0.33	0.24
$0.5 \cdot 10^{-3}$	0.27	0.26	0.22
$1.0 \cdot 10^{-3}$	0.19	0.19	0.17

Table 6.7: Linear friction. Steady state transport (Sv) for a range of k and μ . Along-shore wind stress $\tau = 0.1 \text{ Pa}$.

The first parameter that needed selection was the Rayleigh friction μ . Table 6.7 shows that the steady-state transport is insensitive to changes in μ for $\mu \leq 3 \cdot 10^{-7} \text{ s}^{-1}$. The

Rayleigh friction takes the value $\mu = 3 \cdot 10^{-7} \text{ s}^{-1}$ from this point on.

The transport is weakly dependent on the linear bottom friction coefficient k . Cutting k in half increases the transport by roughly 30%. For a steady-state transport of roughly 0.3 Sv, the linear friction parameter should be in the range $0.3 \cdot 10^{-3} < k < 0.5 \cdot 10^{-3}$ (assuming $\mu = 3 \cdot 10^{-7} \text{ s}^{-1}$). The value $k = 0.5 \cdot 10^{-3} \text{ m s}^{-1}$ was chosen as the standard value.

C_d	$u_0 \text{ (cm s}^{-1}\text{)}$		
	0	20	40
$1.3 \cdot 10^{-3}$	0.36	0.31	0.25
$2.5 \cdot 10^{-3}$	0.31	0.25	-
$5.0 \cdot 10^{-3}$	0.26	-	-

Table 6.8: Quadratic friction. Steady state transport (Sv) for a range of C_d and u_0 . Along-shore wind stress $\tau = 0.1 \text{ Pa}$. Rayleigh friction $\mu = 3.0 \cdot 10^{-7} \text{ s}^{-1}$.

For quadratic friction (5.33), an effective linear friction coefficient at each point was computed at each time step from

$$k^* = C_d(u_0^2 + |\vec{v}|^2)^{1/2}$$

where C_d and u_0 are constants and \vec{v} is the local velocity vector. Table 6.8 shows that a range of C_d and u_0 yields the required transport. The values chosen for the simulation were $C_d = 2.5 \cdot 10^{-3}$ and $u_0 = 0$.

For the spatially varying linear friction (5.36) the linear friction coefficient was computed at each point from

$$k^* = C_d v_{rms}(x, y)$$

where v_{rms} were the rms tidal velocities from a barotropic tidal model (M.G.G. Foreman, pers. comm., 1991). This frictional form is discussed further in Chapter 8 and Appendix F. For $C_d = (1.3, 2.5, 5.0) \cdot 10^{-3}$ the steady state transports were 0.42 Sv, 0.32 Sv, and 0.23 Sv, respectively. A value of $C_d = 2.5 \cdot 10^{-3}$ was selected.

The steady-state circulation pattern is previewed at the end of this chapter. As discussed in Chapter 8, the pattern is not sensitive to the choice of the functional form of the bottom friction.

6.4 Adjustment Time-Scales in Hecate Strait

This section describes the evolution of the model transport and coastal sea level during spin-up. The results are used to estimate the characteristic relaxation or adjustment time-scales in Hecate Strait. The standard model domain and parameters were used.

The transport through Hecate Strait as measured at R, W, and M lines is shown in Fig. 6.36. At all three sections the spin-up was dominated by two time scales: one of the order of several hours, the other of a few days. At W and M lines there was a third time scale, a high frequency oscillation. At the end of this section the oscillation is interpreted as a basin resonance. The oscillation disappeared when the wind stress was started smoothly using the cosine ramp with $t_0 = 1$ d.

After 9 days the transport had stopped growing but the sea level was still rising in Hecate Strait (Fig. 6.37) and on the outer coast (Fig. 6.38). The relationship between along-shore velocity and cross-shore pressure gradient (geostrophic balance) makes the coastal sea level sensitive to the open ocean currents. From Fig. 6.33 the frictional adjustment time for a depth of 2000 m is 21 days. The sea level was still rising because the open ocean currents were still growing. The dynamical variable of interest is sea-level gradients not absolute sea level. The cross-strait pressure (sea level) difference in Hecate Strait (Fig. 6.39) had the same spin-up characteristics as the transport.

A plausible explanation for the two adjustment time-scales in Hecate Strait is that the fast time-scale is the response to the local wind forcing and the slow time-scale is the response to an along-shore pressure gradient set up by processes outside of Hecate Strait.

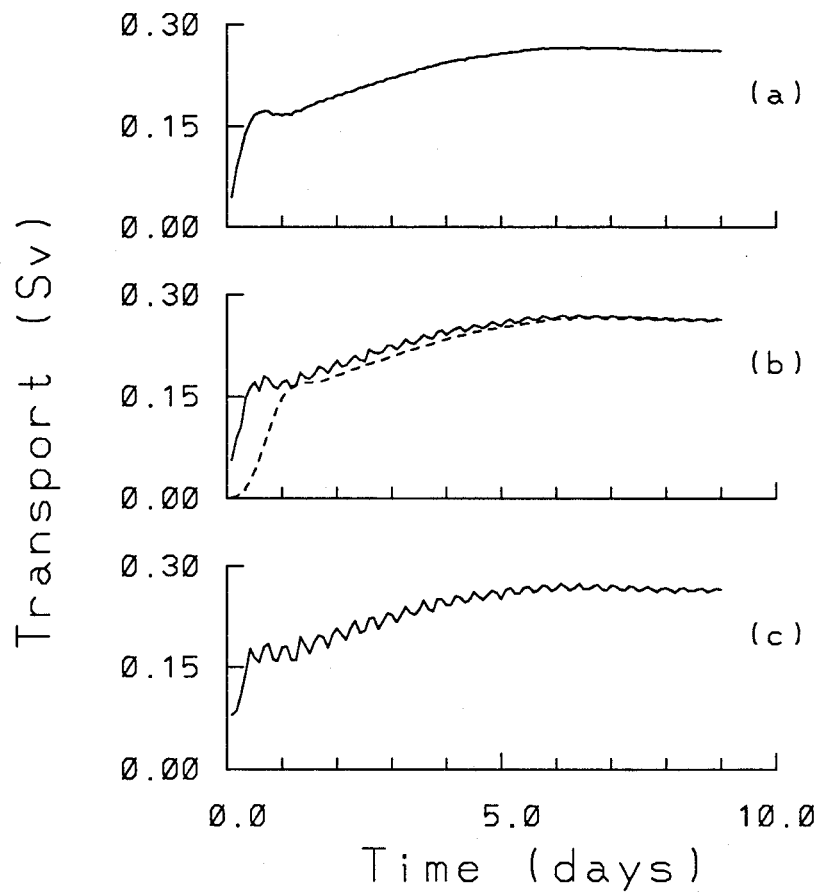


Figure 6.36: Spin-up test. Time series of transport through Hecate Strait for an impulsively started wind. (a) R-line, (b) W-line, (c) M-line. The dotted line in (b) is the transport when the wind was started smoothly (see text).

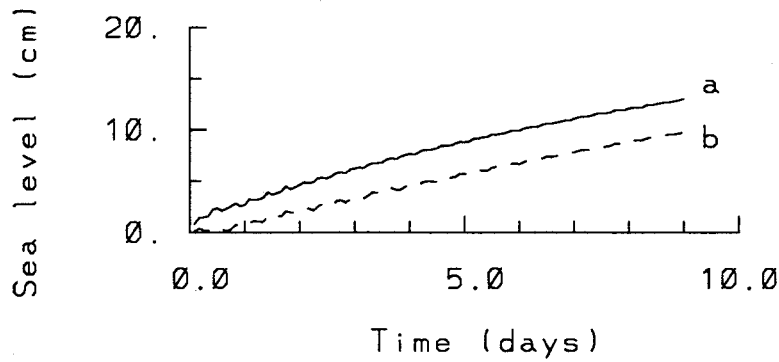


Figure 6.37: Spin-up test. Time series of sea levels in Hecate Strait. a) Atli and b) Beauchemin.

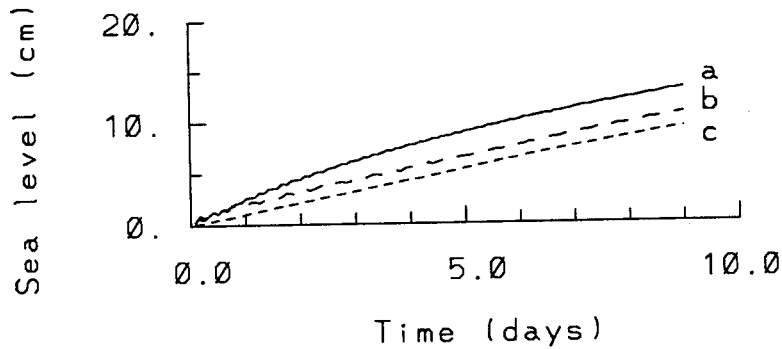


Figure 6.38: Spin-up test. Time series of sea levels on the outer coast. a) Cape Muzon, b) W. QCI, and c) Cape Scott.

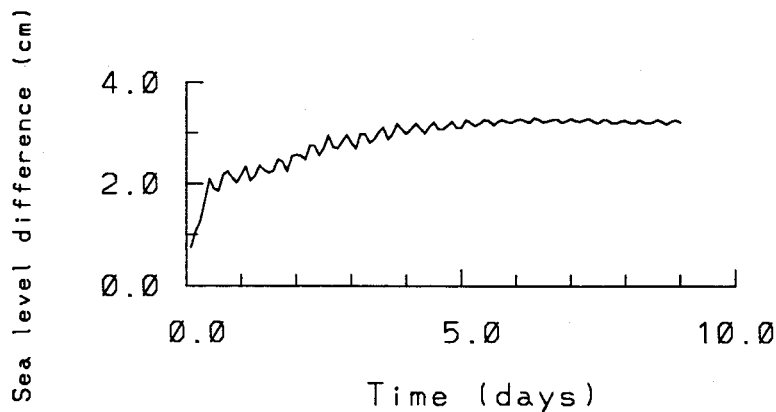


Figure 6.39: Spin-up test. Cross strait pressure difference Beauchemin minus Atli.

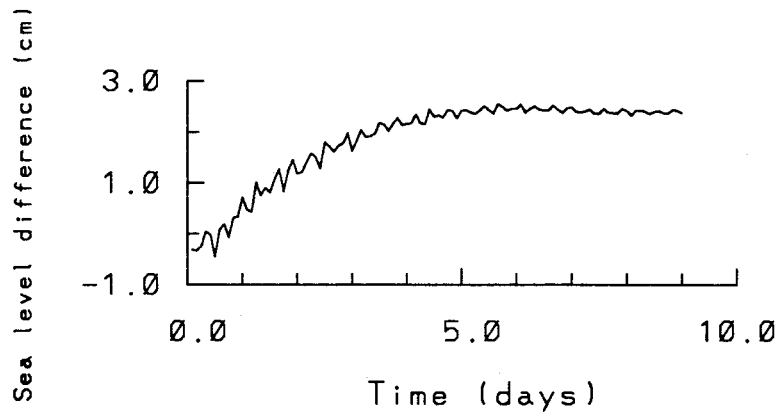


Figure 6.40: Spin-up test. Along-shore pressure difference Cape Scott minus Cape Muzon.

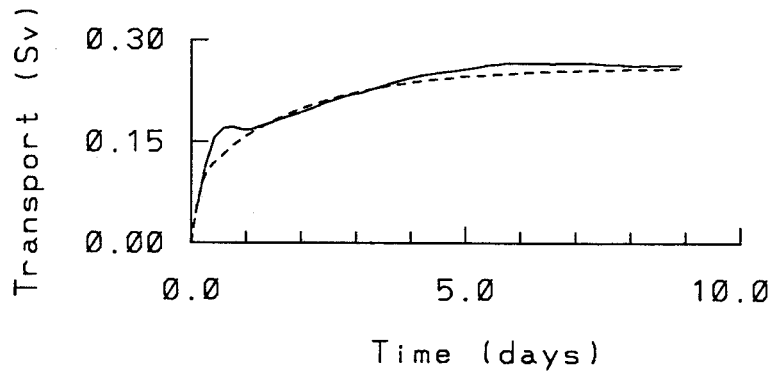


Figure 6.41: Spin-up test. Comparison of transport through R-line with a two component adjustment.

The sea level difference between Cape Scott and Cape Muzon (Fig. 6.40), a measure of the along-shore pressure gradient, has an adjustment time scale similar to that seen in the transport (Fig. 6.36). The analysis and experiments reported in Appendix F support this explanation and suggest the following simple relationship for the transport Q

$$Q(t) = 0.13(1 - e^{-\lambda_1 t}) + 0.13\beta(1 - e^{-\lambda_2(t-0.5)}) \quad (6.40)$$

where the locally wind-driven response has an e-folding time of $\lambda_1^{-1} = 4$ h, the pressure forced response has an e-folding time of $\lambda_2^{-1} = 48$ h, and $\beta = 0$ if $t < 0.5$ d and $\beta = 1$ otherwise. The pressure-forced component is suppressed for the first 1/2 day because computing a robust estimate of the e-folding time scale from the sea level difference Cape Scott minus Cape Muzon required trimming the first 1/2 day from the time series, suggesting a time delay. This simple relationship is in good agreement with the transport in the regional model (Fig. 6.41). The only characteristic not reproduced is the bump during the first day. The amplitudes of the two components were set equal based on a long look at the spin-up in Fig. 6.36. Other choices are certainly possible.

Given the assumption that the adjustment time scales are determined by friction, one can compute the depth that is controlling the flow from

$$\lambda = k/h + \mu$$

Using the values of k and μ (Table 6.6) yields $h_1 = 7$ m and $h_2 = 90$ m from λ_1 and λ_2 respectively. Since there are no significant regions in Hecate Strait, or anywhere in the model, with depths less than 10 m, this suggests that something other than friction is determining the value of λ_1 . The contribution of the Rayleigh friction μ to the adjustment time-scales is insignificant.

6.4.1 Basin Resonance

The high frequency oscillation seen in the basic spin-up experiment can be separated from the underlying adjustment processes spin-up by subtracting the transport at W-line from that at R-line. Figure 6.42 shows a decaying oscillation with approximately three cycles per day. The power spectrum (Fig. 6.43) reveals that the dominant mode has a frequency of $\omega = 0.133 \pm 0.004$ cph (cycles per hour) and a period of 7.5 ± 0.5 h. This is very close to the resonance mode found by Foreman et al. (1992) with $\omega = 0.128$ cph. This is the half wavelength mode of a resonance set up between the shelf break in the mouth of Queen Charlotte Sound and the shelf break in the mouth of Dixon Entrance, analogous to a double open-ended organ pipe. The peak at $\omega = 0.258$ cpd is the one wavelength mode.

6.5 Circulation Patterns: A Preview

The through-strait transports calculated in this chapter have an associated transport vector field $\vec{v}^* = \vec{v}h$, where \vec{v} is the velocity field. The pattern of the steady-state transport field (Fig. 6.44) develops quickly. In the spin-up experiments, the underlying velocity pattern is established between Day two and three (Chapter 8).

The important characteristics of the steady-state transport pattern in Hecate Strait are:

- The pattern is constrained by the topography.
- There is an up-wind counter flow in the south-central strait opposite to the direction of net transport. The flow is along the north slope of Moresby Trough.
- At the southern end, the net northward transport is the small difference of large northward transports at the edges and a large southward transport in the center.

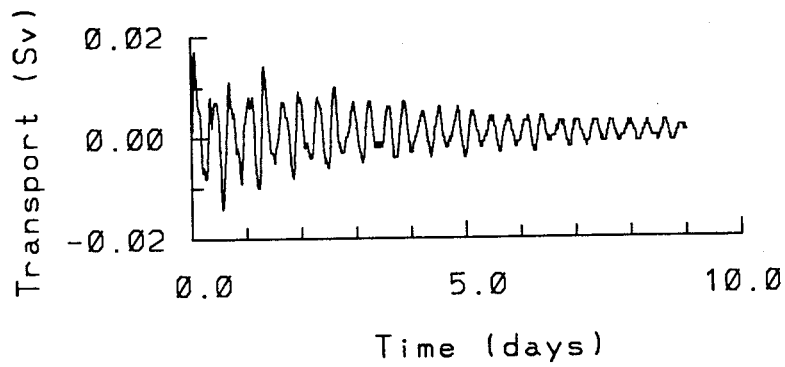


Figure 6.42: The high frequency oscillation at W-line.

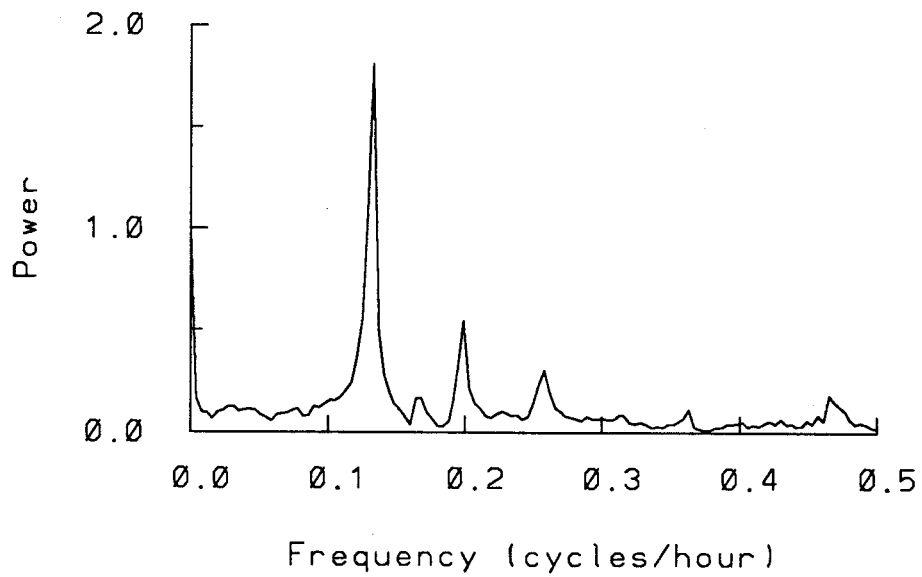


Figure 6.43: The power spectrum of the oscillation at W-line.

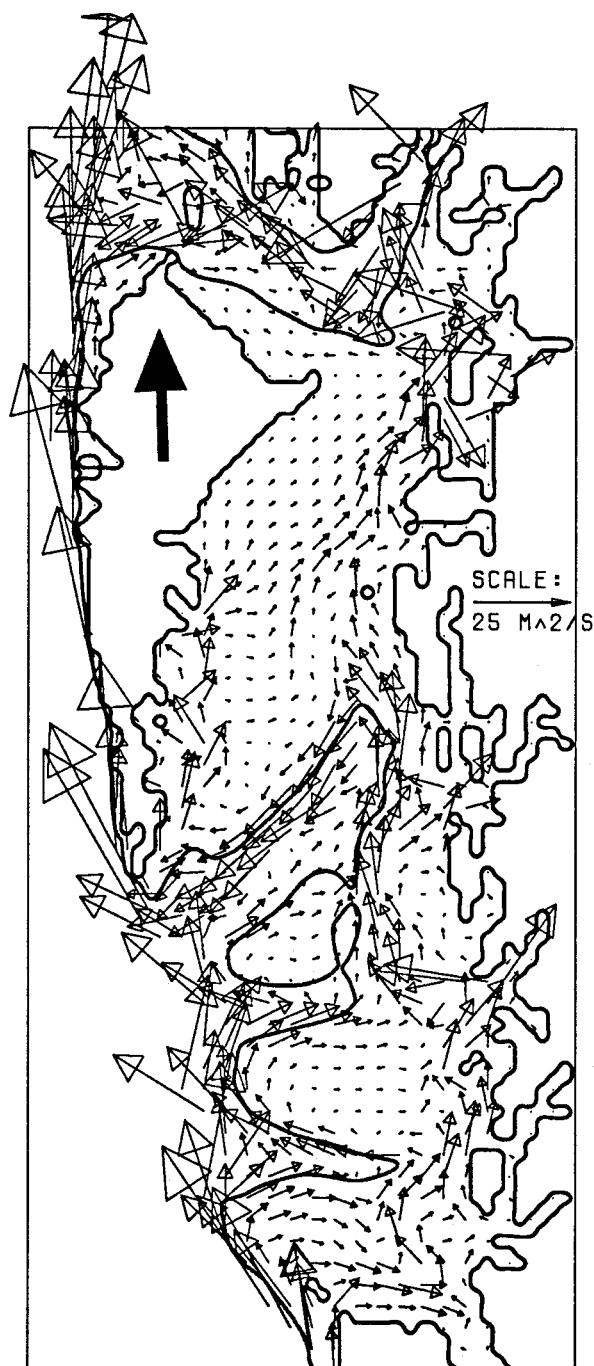


Figure 6.44: Steady-state transports with a uniform SE wind. The wind direction is indicated with an arrow on Graham Island. The 200 m contour is the heavy dark line. Only 1/4 of the vectors are plotted. The vectors were suppressed for depths greater than 500 m.

- At the northern end, the transport is concentrated in the deep water on the eastern side.
- There are regions of low transport in the northwest corner and in the center of the strait.

The validity of the steady-state picture as a guide to the time-varying model results is discussed in Chapter 8.

6.6 Force Balance

Force balances were computed in Hecate Strait during the spin-up experiments. These computations show that the primary cross-strait force balance is between the pressure gradient and the Coriolis force (geostrophic balance). The wind stress enters the balance at the northern end, where the axis of the strait makes a large angle with the grid lines. The along-strait force balance at southern end (M-line) is between the wind stress, pressure gradient and the Coriolis force. The friction is negligible except in the shallow water at the edges. At the northern end (R-line), by Day 2, the acceleration term is important only in the deep water on the eastern (right hand) side. Over the rest of the line, the wind stress is balanced by the bottom friction and the pressure gradient (Fig. 6.45). In the southern end of the strait, the along-strait and cross-strait components of the forces were resolved along the grid lines. At R-line, in the northern end of the strait, the forces were resolved parallel and perpendicular to the local velocity. This removes the Coriolis term from the along-strait force balance in Fig. 6.45.

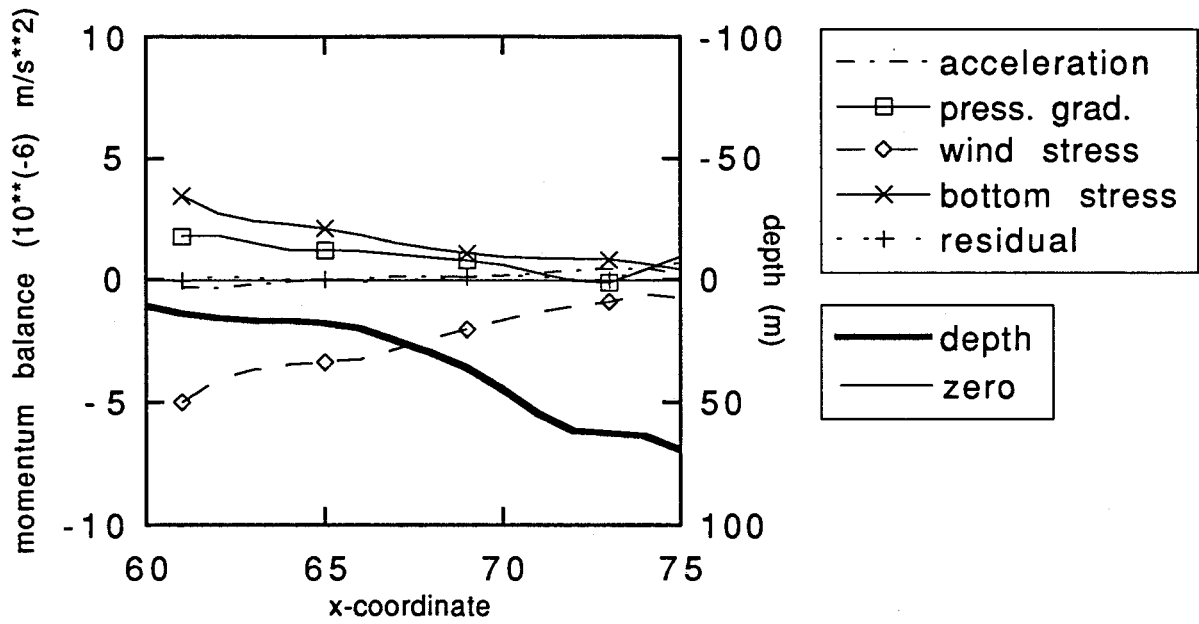


Figure 6.45: The along-strait force balance at R-line after two days of steady along-shore SE wind.

Chapter 7

Rotational Limitations on the Water Transport Through Hecate Strait

This chapter concentrates on the transport of water through Hecate Strait, starting with a comparison of the simulated and observed transport time series for the winter of 1984. The Hecate Strait Model transport is shown to be a good representation of the observed transport. The model is then used to explore the relationship between the friction parameters, the Coriolis parameter, and the transport. The purpose is to understand why the magnitude of the transport fluctuations in the simulations are not very sensitive to the friction parameters. Rotation-limited-flux provides an explanation.

7.1 Winter 1984

In this section the observed transport through Hecate Strait is compared with simulated results for the period 25 Jan to 30 Mar 1984 (Day 25 to 91). The simulations were forced by the wind stress time series shown in Fig. 7.46. The wind was predominantly along-shore and from the SE. The computation of the wind stress from the observed winds at W4S was discussed in Chapter 3 and Chapter 5. The cosine ramp (Chapter 6) was used for the first two days to avoid the high frequency oscillations seen in the test cases.

The model has done a reasonable job of simulating the observed transport. Comparison of the observed time series with that from a simulation using the standard model parameters (E501a in Table 7.9) shows that the peaks line up but that there is disagreement about the magnitude of many of them (Fig 7.47). There were two periods of persistent poor simulation: Day 30 to 40 and Day 75 to 85. There were also some short

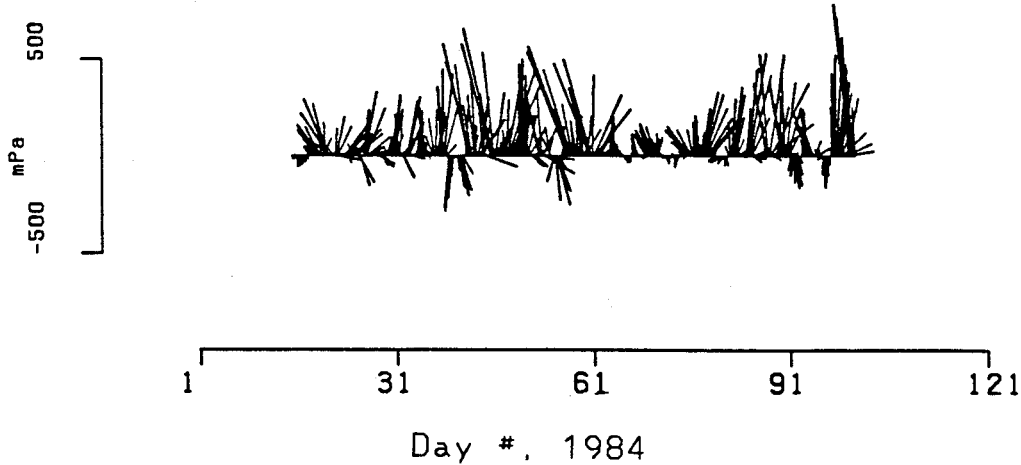


Figure 7.46: The wind stress time series used to drive the verification experiments. The vectors are oriented to conform to the orientation of the model domain; up represents a SE wind. The winds were measured at W4S.

Experiment	Friction type	Parameter values
E501a	linear	$k = 0.5 \cdot 10^{-3} \text{ s}^{-1}$
E501b	linear	$k = 1.0 \cdot 10^{-3} \text{ s}^{-1}$
E502a	quadratic	$C_d = 1.3 \cdot 10^{-3}, u_0 = 0$
E502b	quadratic	$C_d = 2.5 \cdot 10^{-3}, u_0 = 0$
E503	rms	$C_d = 2.5 \cdot 10^{-3}$

Table 7.9: Model verification experiments.

events that were poorly simulated; near Day 62, for example.

A series of simulations were conducted to test the sensitivity of the modelled transport to the bottom friction (Table 7.9). The statistics computed from the transport time series were not very sensitive to the bottom friction (Table 7.10). The mean transport varied, but the magnitude of the fluctuations did not change very much. The time series themselves were very similar.

The observed transport is more highly correlated with the simulated transport ($r_{max} = 0.77$) than with the along-shore wind stress ($r_{max} = 0.70$). This shows that using the winds to drive the model provides a better estimate of the transport than using the winds alone. Using the model brings the predictive ability of the winds measured at W4S up to

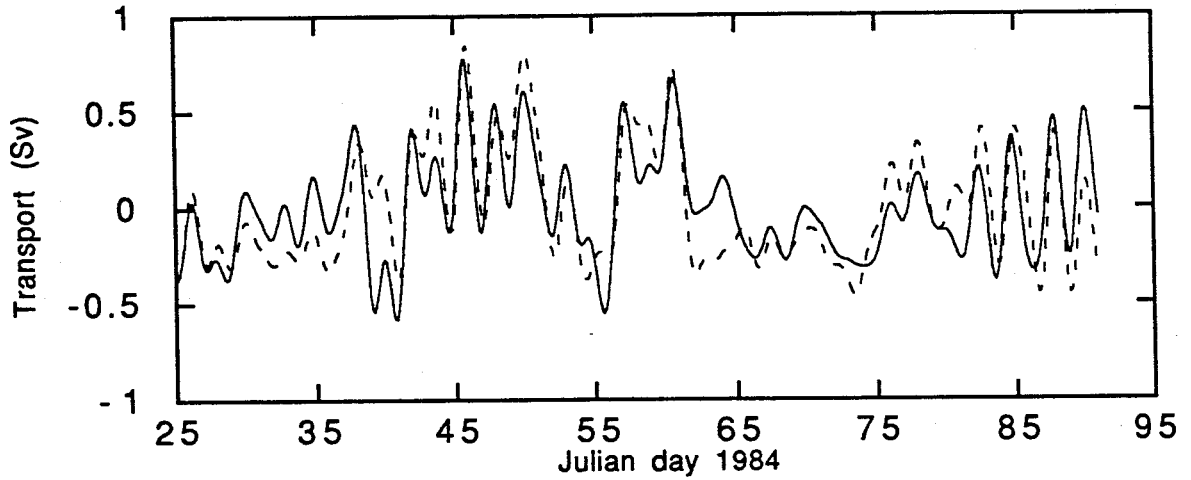


Figure 7.47: Transport through W-line from 25 Jan - 30 Mar 1984. Comparison of simulation E501a (solid) and the observations (dotted).

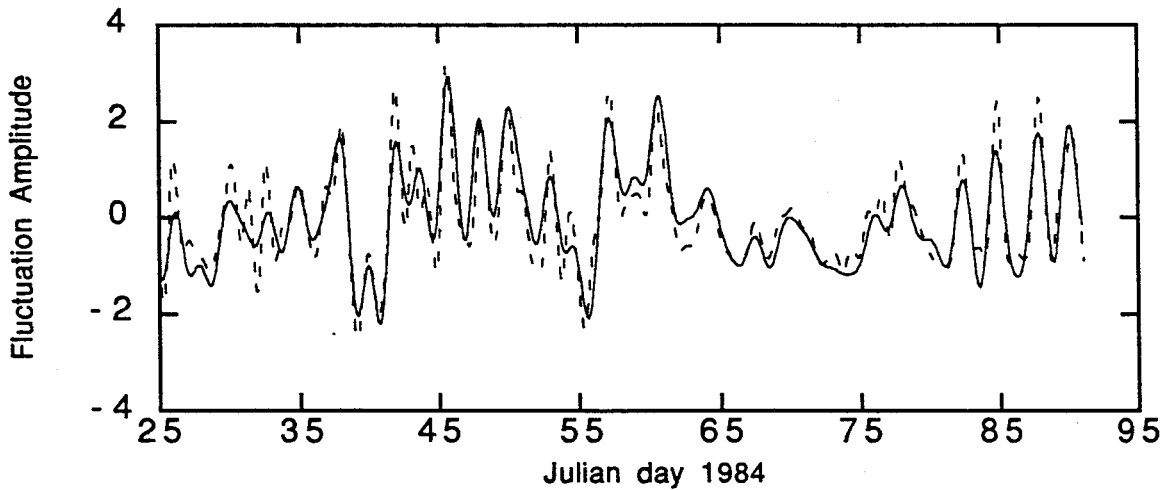


Figure 7.48: Time series of along-shore wind stress (dotted) and simulated transport (solid) in Hecate Strait from 25 Jan - 30 Mar 1984. Both time series have been normalized.

Experiment	Transport		Correlation	
	mean (Sv)	st. dev. (Sv)	wind	obs. transport
E501a (linear)	0.30	0.26	0.90	0.78
E501b (linear)	0.23	0.22	0.92	0.77
E502a (quadratic)	0.37	0.26	0.90	0.78
E502b (quadratic)	0.33	0.24	0.91	0.77
E503 (RMS)	0.44	0.27	0.85	0.76
observations	0.36	0.30	0.70	–

Table 7.10: Model verification. Comparison of the simulated and observed transport through Hecate Strait for the period 25 Jan - 30 March 1984. The correlations are the maximum linear correlation coefficients of the transport time series with the along-shore wind stress and with the observed transport.

the level of the best of the lighthouse winds (Table 3.3). A word of warning: the analysis of CHW88 indicates that for the observed transport, the sample correlation is drawn from a population correlation in the range 0.53–0.82 (95% confidence limits). Therefore, the improved correlation is not statistically significant.

The model underestimates the magnitude of the observed transport fluctuations (standard deviation). The results in Table 7.10 indicate that it is difficult to increase the magnitude of the fluctuations by adjusting the bottom friction. This is supported by the results in Chapter 6. The fluctuation could be brought up to the level of the observations by increasing the wind stress estimate by 10%. One could use the uncertainties inherent in the calculation of the wind stress from the wind speed to justify such an *ad hoc* increase. Nevertheless, this would not improve the overall simulation since the model already over-estimates the transport near Days 30 and 63.

Improvements in the transport simulation require improved atmospheric forcing. Comparison of the along-shore wind stress fluctuations with the transport fluctuations (Figure 7.48) shows that the transport tracks the wind stress very closely. This is the meaning of a correlation coefficient $r = 0.9$. There is nothing in the model dynamics that allows the transport to depart significantly from the wind forcing. Comparison of Fig. 7.47 and

Fig. 7.48 shows that the model performed well when the winds were strong (Day 40 to 60) and not as well when the winds were weak (Day 25 to 40). This suggests a non-local effect, perhaps an along-shore atmospheric pressure gradient or a wind field not well represented by a single vector.

In CHW88 three surrogate transport series were constructed from the sub-surface pressure observations: Beauchemin minus Atli (B-A), Prince Rupert, and the linear combination (Prince Rupert plus Bella Bella)/2 minus Queen Charlotte City (PBQ). In the simulations, B-A and PBQ were well correlated with the transport ($r_{max} > 0.95$). Prince Rupert was a poor predictor, $r_{max} = 0.71$. The poor performance of Prince Rupert in the model is related to the absolute sea-level problem discussed in Chapter 6.

The comparison of the observed and simulated cross-strait sea level difference is shown in Fig. 7.49. The model under-estimates the magnitude of many of the large peaks. If, as mentioned in Chapter 3, the cross-strait sea level difference Beauchemin minus Atli (B-A) is a better indicator of the transport through Hecate Strait than that computed from the currents, then the model is under-estimating the peak transport.

7.2 Friction, Coriolis Parameter, and Transport

Rotation-limited-flux provides a plausible explanation for the observation that the simulated transport through Hecate Strait is relatively insensitive to changes in the bottom friction parameter (Section 7.1 and Chapter 6). The rotation-limited-flux equation for the along-strait velocity (4.14)

$$u = \frac{\frac{g}{L}(\eta_4 - \eta_5) + F}{i\omega + \lambda + fW/L} \quad (7.41)$$

suggests that the steady-state transport through a flat-bottomed channel, $Q_0 = Whu$, can be written

$$Q_0 = \frac{A}{\lambda + fW/L} \quad (7.42)$$

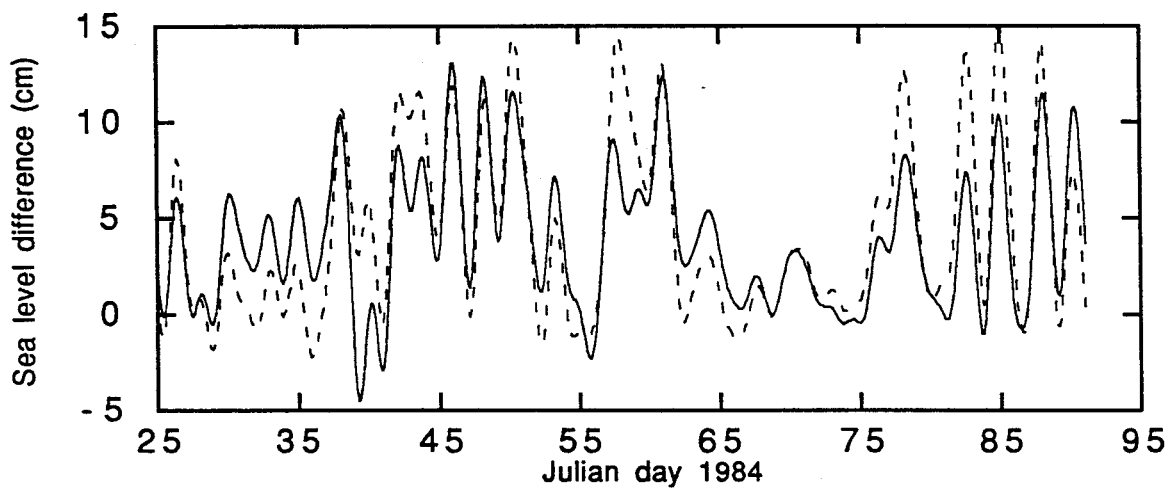


Figure 7.49: Cross-strait sea level difference Beauchemin minus Atli for the period 25 Jan - 30 Mar 1984. Comparison of E501a (solid) with the observations (dotted).

where A represents the forcing terms. The estimates from Table 4.4 of $\lambda = 1 \cdot 10^{-5} \text{ s}^{-1}$ and $fW/L = 3 \cdot 10^{-5} \text{ s}^{-1}$ indicate that the effect of rotation is to decrease the steady-state transport by a factor of 4 ($\lambda/(\lambda + fW/L) = 1/4$). Further the steady-state transport should not vary linearly with λ^{-1} . In fact the transport should have a weak dependence on λ . For time varying flow the presence of the $i\omega$ term in (7.41) further weakens the dependence on λ .

To test the idea that rotation-limited-flux is important in Hecate Strait a series of spin-up experiments were conducted. In these experiments the spin-up of the water transport through the strait was monitored for different values of the Coriolis parameter f and the bottom friction coefficient k . The standard model domain (Fig. 6.35) and linear bottom friction were used throughout.

The discussion is split into two parts. In the first part the steady-state results are used to estimate the parameter W/L which plays an important role in rotation-limited-flux. A reasonable estimate of $W/L \approx 0.2$ is obtained. In the second part estimates of the spin-up time scale are used to estimate both W/L and λ . The analysis of the spin-up data is more sensitive to the limitations of rotation-limited-flux than the steady-state data.

The relationship between the steady-state transport in the model and the Coriolis parameter shown in Fig. 7.50 is in agreement with (7.42). The transport increases as $f \rightarrow 0$ and decreases as $f \rightarrow \infty$. For large f the effect of the difference in the bottom friction coefficient disappears and the two curves converge. These experiments were done with an along-shore wind localized over Hecate Strait. As shown later in Fig. 7.52, the transport spin-up exhibits only one time scale when the model is forced by such a wind. This represents the local wind-driven response; the forcing due to along-shore pressure gradients, $\eta_4 - \eta_5$ in (7.41) is minimized. One process has been isolated.

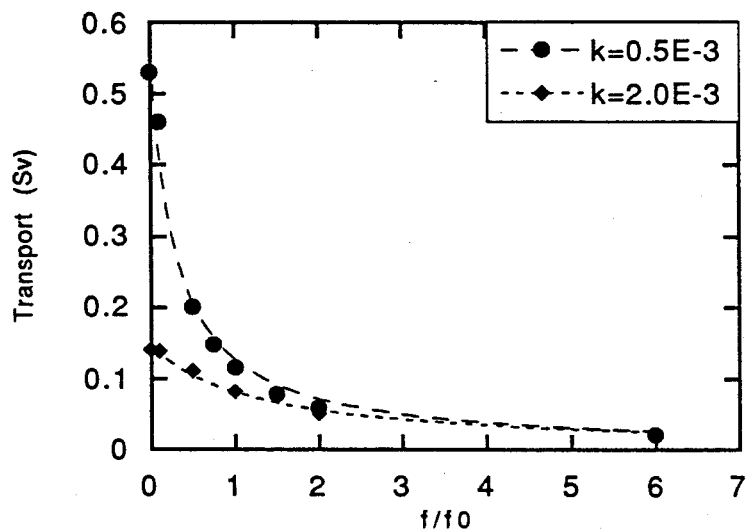


Figure 7.50: Steady state transport as a function of Coriolis parameter for a wind localized over Hecate Strait. The Coriolis parameter has been normalized with $f_0 = 1.1 \times 10^{-4} \text{ s}^{-1}$.

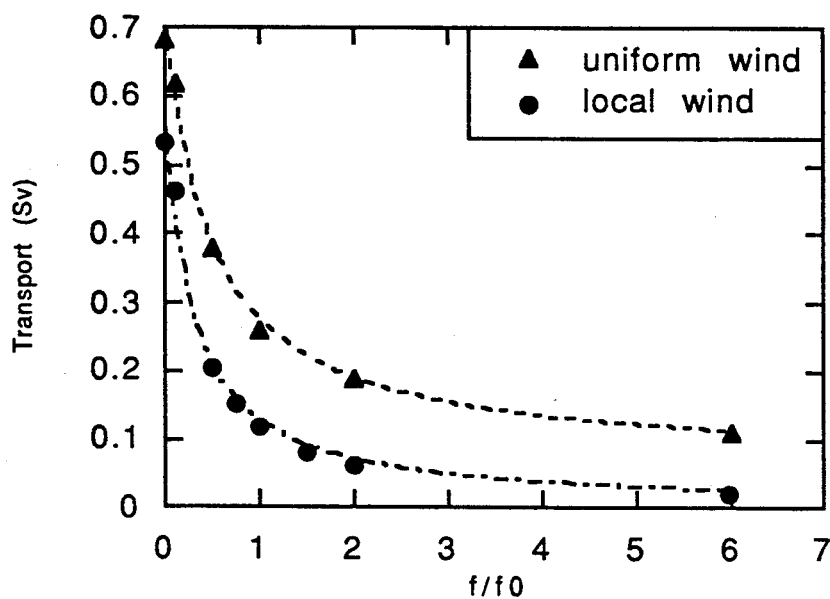


Figure 7.51: Steady-state transport as a function of Coriolis parameter for a uniform along-shore wind stress (triangle) and for a wind stress localized over Hecate Strait. In both cases $k = 0.5 \cdot 10^{-3} \text{ s}^{-1}$. The Coriolis parameter has been normalized with $f_0 = 1.1 \times 10^{-4} \text{ s}^{-1}$.

Estimating W/L from Fig. 7.50 is non-trivial. In (7.42) A , λ and W/L are all unknowns and curve fitting to estimate all three leads to unstable estimates since the variables are highly correlated: increases in A can be balanced by increases in λ and W/L . A stable form for curve fitting is

$$Q = \frac{B}{1 + Cf/f_0} \quad (7.43)$$

where $B = A/\lambda$ and $C = Wf_0/L\lambda$. The smooth curves in Fig. 7.50 are the best fits of the data to an equation of this form. The data and fit parameters are listed in Appendix G. Unfortunately the parameter $W/L = C\lambda/f_0$ cannot be estimated directly from the fit because λ is unknown. There are three unknowns A , W/L and λ and only two fitted parameters.

One way to estimate λ is to make an independent estimate of the effective depth. From the transport vector field in Fig. 6.44 a depth of $h^* = 70$ m is a reasonable estimate of the mean depth corresponding to the region of maximum transport in northern Hecate Strait. Using this value and the known form of the friction in the model ($\lambda = k/h + \mu$) yields estimates of W/L in the range 0.2 – 0.3. The estimates vary linearly with $(h^*)^{-1}$.

The experiments in Fig. 7.50 used a localized wind to limit the forcing in the strait to local wind forcing only. The character of the results did not change appreciably when the uniform wind was re-introduced. The steady state transports for the uniform along-shore wind and the localized along-shore wind are compared in Fig 7.51. To a first approximation the curves are offset by a constant. As described in Appendix G an estimate of $W/L = 0.15$ was obtained from the uniform wind data.

These dynamical estimates of $W/L \approx 0.2$ are reasonable. From Fig. 6.35 the width of Hecate Strait is 70 km and the length is roughly 250 km; $W/L = 0.3$. The steady-state transport vector field (Fig. 6.44) suggests that the effective width and length are quite different from the geographic width and length. A width of 20 km and length of 120

km yields $W/L = 0.2$. Both estimates are in reasonable agreement with the dynamical estimates.

Rotation-limited-flux provides a reasonable explanation for the fact that the transport through Hecate Strait is relatively insensitive to changes in the friction parameters. Estimates for the ratio W/L range from 0.15 to 0.3 depending on the friction parameter values and the method of forcing the strait. The rest of this section is devoted to extracting estimates of W/L and λ from the spin-up data. The discussion of the results points out the limitations of rotation-limited-flux in a complex environment. The reader can skip to the end of the section without missing any important concepts.

The derivation of rotation-limited-flux suggests that the response of the transport to an impulsively started wind should resemble frictional adjustment. Equation (4.10) can be written

$$\frac{\partial u}{\partial t} + \lambda_1 = F \quad (7.44)$$

where $\lambda_1 = \lambda + fW/L$ and F is the forcing term. For the experiments with the localized wind, the spin-up time series should be well approximated by a curve of the form

$$Q(t) = Q_0(1 - e^{-\lambda_1 t}) \quad (7.45)$$

where Q is the transport through Hecate Strait. The two spin-up examples shown in Fig. 7.52 are well approximated by (7.45).

The form of λ_1 suggests a method for estimating W/L and λ . W/L is the slope of the best fit straight line through a plot of λ_1 versus f , and λ is the y-intercept. The spin-up data from the localized wind experiments (Fig. 7.53) yields estimates of W/L equal to 0.5 and 0.6 for $k = 0.5 \cdot 10^{-3} \text{ s}^{-1}$ and $k = 2.0 \cdot 10^{-3} \text{ s}^{-1}$, respectively. These results imply a wider channel than the previous estimates. To bring the previous estimate of $W/L \approx 0.2$ in line with the new estimate would require an effective depth of 20 to 30 m. This is much too shallow.

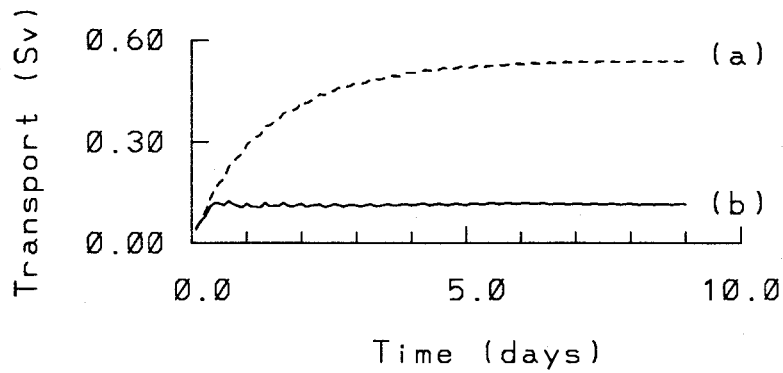


Figure 7.52: Transport spin-up for an along-shore wind localized over Hecate Strait for $k = 0.5 \cdot 10^{-3} \text{ s}^{-1}$. (a) $f = 0$ and (b) $f = 1.1 \cdot 10^{-4} \text{ s}^{-1}$.

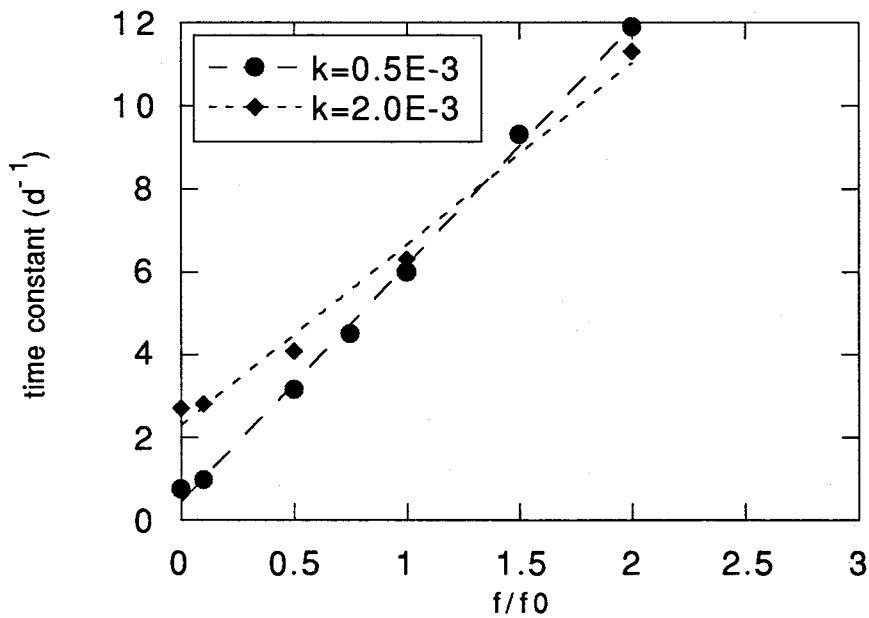


Figure 7.53: Relaxation time as a function of Coriolis parameter for a wind localized over Hecate Strait. a) $k = 0.5 \cdot 10^{-3} \text{ s}^{-1}$, b) $k = 2.0 \cdot 10^{-3} \text{ s}^{-1}$.

Effective depths for the bottom friction can be obtained from the estimates of λ using the known form of the bottom friction $\lambda = k/h + \mu$, and $\mu = 3 \cdot 10^{-7} \text{ s}^{-1}$. For $k = 0.5 \cdot 10^{-3} \text{ s}^{-1}$, the adjustment time $\lambda = 0.4 \text{ d}^{-1}$ and the effective depth $h^* = 100 \text{ m}$. Similarly, for $k = 2.0 \cdot 10^{-3} \text{ s}^{-1}$, $\lambda = 2.3 \text{ d}^{-1}$ and $h^* = 76 \text{ m}$. These estimates of the effective depth are consistent with the *ad hoc* estimate of $h^* = 70 \text{ m}$. No purpose would be served by using these effective depths to refine the estimates of W/L made from the steady-state data. For both data sets in Fig. 7.53 the estimate of λ , and thus h^* , is sensitive to which data points are used to compute the best fit straight line. In both cases the estimate of λ decreased when the point at $f = 0$ was not included in the fit. For $k = 0.5 \cdot 10^{-3} \text{ s}^{-1}$ the estimated λ was less than μ , which implies a negative effective depth. The estimate of the slope, and thus W/L , was robust.

The differences in the estimates of W/L obtained with the two methods is an indication that rotation-limited-flux has limitations when applied to a real channel. The biggest limitation is the fact that Hecate Strait is not a flat-bottom channel. As $f/f_0 \rightarrow 0$ the flow is not constrained to follow contours of f/h since it is no longer true that $f \gg \zeta$, where ζ is the relative vorticity. I believe that the fact that the bathymetric gradients cut diagonally across the strait causes the effective geometry of the strait to change as $f/f_0 \rightarrow 0$. A close look at the data in Fig. 7.50 suggests that the curves flatten out for small f/f_0 . For both curves, a straight line through the data with $f = 0$ and $f = 0.1$ removed had a similar slope but a much smaller y-intercept.

At the other end of the spectrum, there were problems estimating the time constant as f increased and the transport decreased. The noise in the spin-up which was only a minor annoyance in Chapter 6 when the steady-state transport was 0.26 Sv became a major factor as the steady-state transport decreased. This affected all the results for $f/f_0 \geq 1$ and made the estimate for $f/f_0 = 6$ worthless.

Given the acknowledged limitations of rotation-limited-flux, the analysis was not pursued any further. Appendix G.3 contains a brief discussion of the validity of the assumption of a flat bottom.

7.3 Frequency Response

The experiments with an impulsively started wind provide one view of the model's behaviour. A complementary view is provided by the frequency response: the model's response to sinusoidal forcing.

The frequency response was computed using a spatially uniform wind with sinusoidal time variation $\tau(x, y, t) = \tau_0 \sin \omega t$, where $\tau_0 = 0.1$ Pa. The test variable was the transport through Hecate Strait. The amplitude spectrum of the response (Fig. 7.54) is well approximated at any frequency by the transport in the basic spin-up experiment (Fig. 6.36) at time $t = T/4$ where T is the period. The flat portion of the amplitude spectrum (Fig. 7.54) between $0.1 < \omega < 0.7$ cpd (periods between 1.5 and 10 days) corresponds to the knee or flat-spot in the spin-up response from day 0.5 to 1.5.

The lag of the transport behind the wind (Fig. 7.55) has a range of 5 to 15 h over most of the spectrum. This is consistent with the lags of 5 to 12 h obtained from the correlation analysis of the winds and the observed transport in Chapter 3, where they are reported as the lead of the wind over the transport.

In Chapter 6 the basic transport spin-up time series was shown to be reasonably approximated by the sum of two friction adjustment processes with time scales $\lambda_1 = 4$ h and $\lambda_2 = 48$ h. In analogy with the frictional adjustment solution (4.5), an approximate amplitude spectrum $Q(\omega)$ was computed from

$$Q^2(\omega) = A^2 + B^2 + 2AB \cos(\phi_1 - \phi_2) \quad (7.46)$$

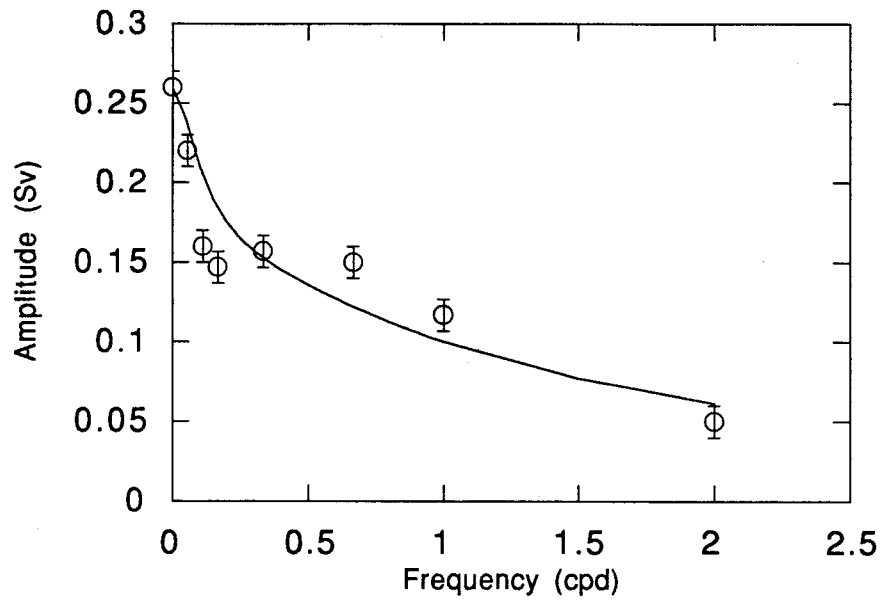


Figure 7.54: Amplitude spectrum computed from the response of the transport through Hecate Strait to oscillating winds (data points). The solid line is an approximate spectrum (see text).

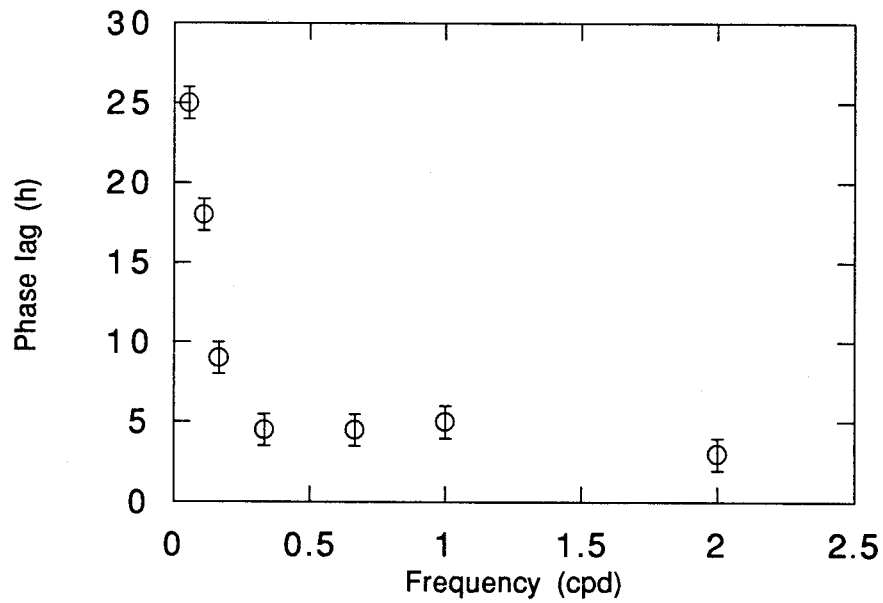


Figure 7.55: Phase spectrum computed from the response of the transport through Hecate Strait to oscillating winds.

where $\tan \phi_i = \omega/\lambda$,

$$A = \frac{(K_1)}{\sqrt{1 + (\omega/\lambda_1)^2}}$$

$$B = \frac{(K_2)}{\sqrt{1 + (\omega/\lambda_2)^2}}$$

and the K_i are the amplitudes of the two components. The amplitude spectrum for the case $K_1 = K_2 = 0.13$ is shown in Fig. 7.54. The approximate spectrum looks like a smooth curve through the regional model's spectrum, it lacks the broad flat section. For the frequency range of interest, periods in the range 1 to 20 days, the knee in the spin-up (Fig. 6.36) is important.

The idea that the amplitude spectrum should be well approximated by a frictional adjustment style process has its basis in Fig. 7.56. The model's transport response to an oscillating wind looks very much like the frictional adjustment solution with sinusoidal wind forcing shown in Fig. 4.26.

The amplitude spectrum was not sensitive to the value of the friction parameters for periods in the range 3 - 9 days. The most noticeable effect of larger friction was to increase the phase lag and to reduce the height of the transient peak in Fig. 7.56.

7.4 Summary

The rotation of the earth reduces the transport through Hecate Strait compared with a non-rotating earth. The effect is consistent with the rotation-limited-flux model with parameter $W/L \approx 0.2$. For the numerical experiments discussed, the rotation of the earth ($f = 1.1 \cdot 10^{-4} \text{ s}^{-1}$) reduced the steady-state transport by a factor between 2 and 5 depending on the friction parameter and the method of forcing the strait.

The character of the response of Hecate Strait to an impulsive wind changes when the rotation of the earth is neglected. After half a day the transport spin-up curves for the

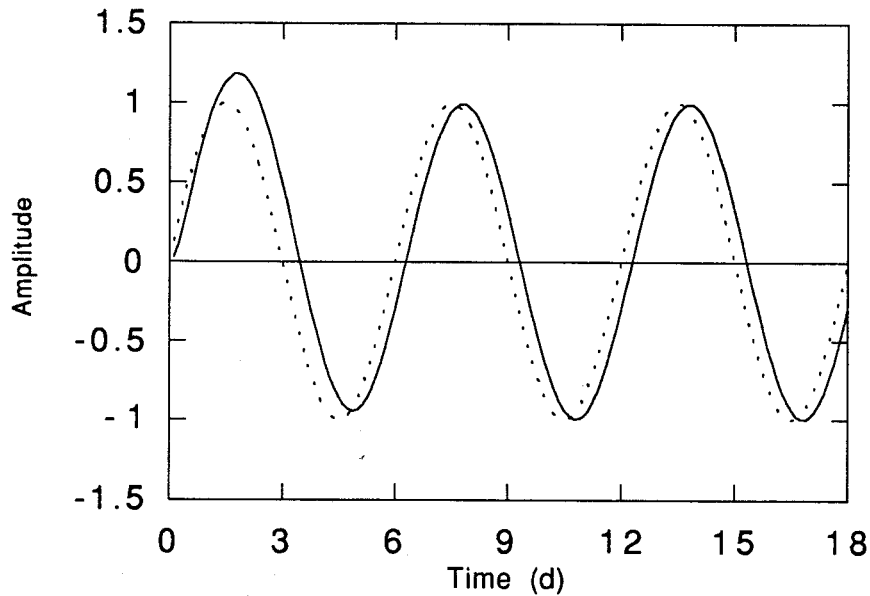


Figure 7.56: Transport time series for an oscillating along-shore wind with period 6 days. The solid line is the transport, the dotted is the wind forcing. Both time series have been normalized by the amplitude of the respective sine waves (0.15 Sv, 0.1 Pa).

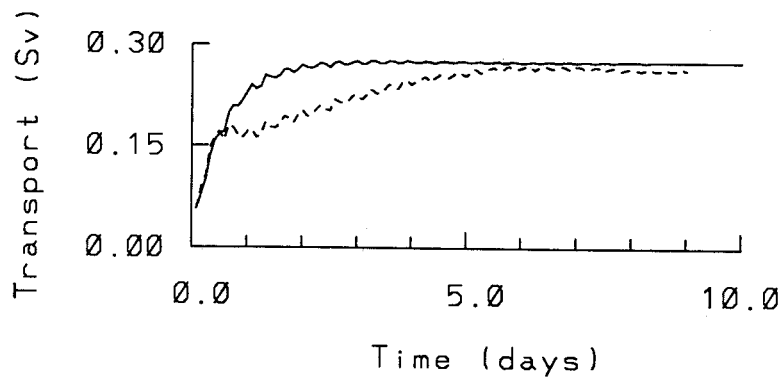


Figure 7.57: The transport spin-up in Hecate Strait for a non-rotating (solid) and rotating (dashed) version of the model. For the non-rotating case $k = 1.3 \cdot 10^{-3} \text{ m s}^{-1}$ and for the rotating case $k = 0.5 \cdot 10^{-3} \text{ m s}^{-1}$. The bottom friction for the non-rotating case was chosen so that the steady-state transports were similar.

rotating earth and non-rotating earth (Fig. 7.57) are very different. The major difference is that the non-rotating response has one time scale, while the rotating case has two. The bottom friction values were selected so that the steady-state transports were similar.

In the Hecate Strait Model, the water is forced through Hecate Strait not only by the local wind forcing but also by the along-shore pressure gradients established by the currents in other parts of the model. When the rotation of the earth is turned off, topographic steering and geostrophic balance disappear from the dynamics. This affects the circulation both inside and outside Hecate Strait.

The bottom friction in a non-rotating model can be chosen so that the non-rotating and rotating models give similar results for short time scales. The results in this chapter show that the bottom friction will be larger in the non-rotating case and that the results will be sensitive to the friction parameter value. The use of quadratic friction in a non-rotating model may give very different results from linear friction. In the rotating version of the Hecate Strait Model, the results were only weakly dependent on the bottom friction parameters.

Chapter 8

Wind-Driven Flow Patterns in Hecate Strait

This chapter presents a comparison of the observed flow patterns with the patterns from the Hecate Strait Model. The model results support a new interpretation of the observed currents in southern Hecate Strait. The discussion is divided into three sections: 1) the basic flow patterns from the Hecate Strait Model, 2) direct comparison of model simulations with the observations, and 3) the regional circulation patterns.

The discussion of the basic flow patterns (circulation) starts with a look at the spin-up of the velocity field under a SE wind. The observed counter-current in south-central Hecate Strait is seen to play a major role in the model circulation. Then the model is used to show how the character of the velocity pattern changes when the rotation of the earth is ignored. Finally, the pattern in southern Hecate Strait is shown to be independent of the details of the flow in northern Hecate Strait.

Comparison of the observed and simulated velocities from 25 January to 30 March 1984 shows that the Hecate Strait Model captures many of the features of the observations. In particular, the counter-current in southern Hecate Strait is present in the model results. Comparison of observed and simulated drifter trajectories from July 1990 and July 1991 demonstrates that the model can provide useful information about trajectory directions, but the simulated drifters significantly under-estimate speed of near-surface drifters. The model does not provide good information in the vicinity of Cape St. James.

Drifter trajectories from the winter 1984 simulation show that the steady-state wind-driven flow pattern provides a useful picture of the overall flow pattern. These drifters

emphasize that the model currents are strongly constrained by the topography (topographic steering). The model results indicate that the counter-current is part of a pattern that (under SE winds) takes water flowing north along the eastern side of Hecate Strait to the western side of the strait.

8.1 Basic Patterns

The evolution of the velocity field during a spin-up experiment exhibits a fast response and a slow response, analogous to the transport (Fig. 6.36). The first part of the domain to respond to the wind is the shallow water in northern and western Hecate Strait (Fig. 8.58a; Day 1). This pattern corresponds to the fast transport response. By the end of the Day 2 (Fig. 8.58b), one can see the beginning of a southwest flowing counter-current in south-central Hecate Strait and a current developing along the coast from northern Vancouver Island to northern Hecate Strait. The fully developed pattern (Fig. 8.59a; Day 8) has the same character as that seen on Day 2. The pattern has simply become more intense. In interest of clarity only one vector in four has been plotted. This is true of all the plots of the velocity and transport vector fields.

The northward transport of water through Hecate Strait is complicated by the southwest flowing counter-current along the north flank of Moresby Trough (represented by the 200 m contour in south-central Hecate Strait). Water which starts out flowing north along the mainland coast in Queen Charlotte Sound can either continue to hug the coast and continue north through Hecate Strait and into Dixon Entrance or it can turn to the SW and follow the north flank of Moresby Trough towards Cape St. James. Once at the cape, the water can either escape to the open ocean or remain in Hecate Strait and flow north along the western side of Hecate Strait. The currents along the eastern and western sides of the strait eventually recombine in the northeastern corner of Hecate

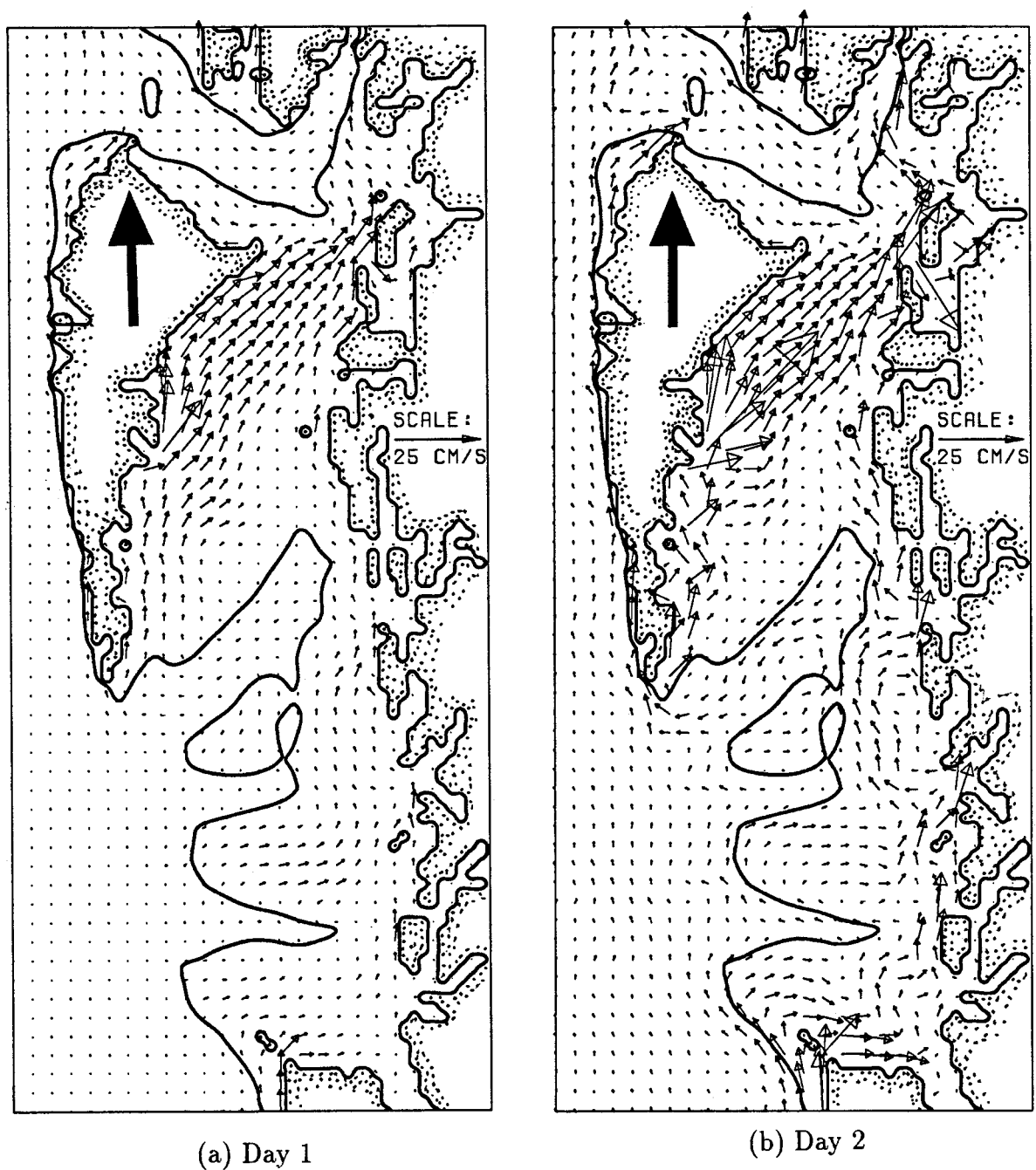


Figure 8.58: Evolution of the velocity field with a steady SE wind. The wind direction is indicated with an arrow on Graham Island. The 200 m contour is the heavy dark line. Only 1/4 of the vectors are plotted.

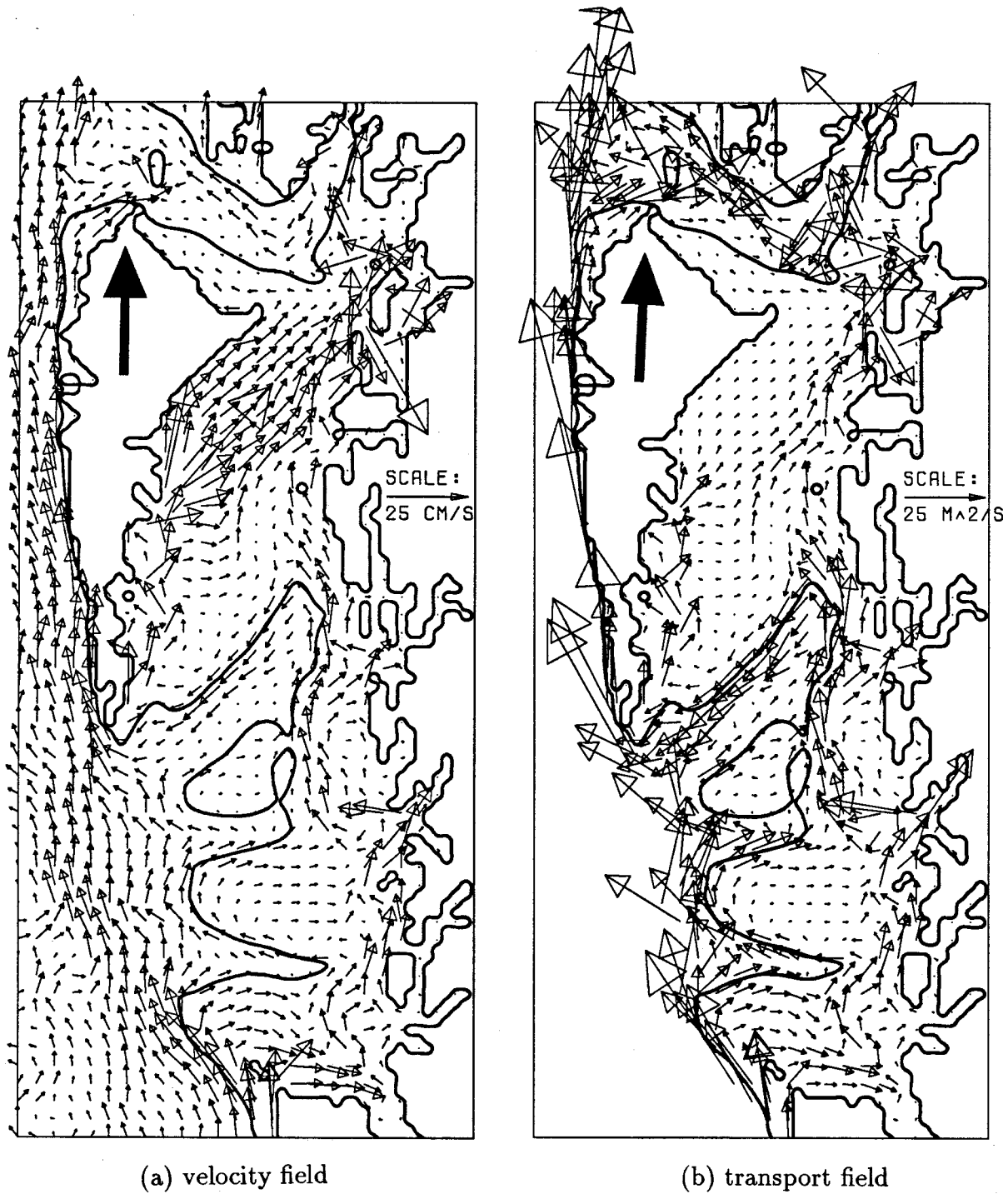


Figure 8.59: The velocity field and transport vector field at Day 8, with a steady SE wind - typical winter storm winds. On the shelf the velocities have reached a steady state. In the deep ocean the velocities are still adjusting, but this does not affect the velocity field on the shelf. The 200 m contour is shown.

Strait.

The relationship between the flow pattern and the topography is clear: the steady-state currents follow the topography. This is topographic steering, where the conservation of potential vorticity creates a tendency for the low-frequency flow to follow the local isobaths (lines of constant depth; equation 5.26 in Chapter 5). The steady-state velocity pattern (Fig. 8.59a) is the basic pattern that the reader should remember. The velocities in the northern part of the Hecate Strait are in the direction of the wind and there is a large flow against the wind in the south-central portion of the strait. This is in agreement with the observations (Chapter 3).

The steady-state velocity pattern and the steady-state transport pattern (Fig. 8.59b) are very similar. Topographic steering is the dominant factor in both patterns. The most noticeable difference is in the shallow water of northwestern Hecate Strait where the large velocities transport very little water.

In Queen Charlotte Sound the near-shore flow is parallel to the coast and there are large flows into and out of the sound near Cape Scott. In the central portion of the sound the currents are parallel to the local isobaths. The pattern is consistent with that of the principal axes of variance of the observed near-surface current fluctuations (Fig. 2.9). Topographic steering provides an organizing principle for the currents in the central sound which were described by Crawford et al. (1985) as 'weak and disorganized'.

In Dixon Entrance there is no evidence of the eddies seen in the observations. The strong flow along the northern side is consistent with the historical view of the wind-driven flow (Chapter 2). The model velocity pattern in Dixon Entrance is sensitive to the details of the topography at the mouth of Dixon Entrance, especially at Langara Island (Appendix F).

On the western side of Hecate Strait, about half way along the Queen Charlotte Islands, there are several very large velocities (Fig. 8.59a). A simulation of the winter

1984 with $k = 0.3 \cdot 10^{-3} \text{ s}^{-1}$ failed when these currents exceeded 8 m s^{-1} . Linear friction has limitations. Notice also the large velocity vector at the one grid point that connects Chatham Sound and Hecate Strait (the northeast corner of the strait).

The steady-state pattern for an along-shore wind from the NW is shown in Fig. 8.60a. Reversing the wind reverses the pattern. The pattern for a cross-shore wind is shown in Fig. 8.60b. The pattern for a wind direction between the along-shore and cross-shore directions is a linear combination of the basic along-shore and cross-shore patterns.

The circulation patterns are robust. The character of the patterns did not change when quadratic friction and spatially varying linear friction were used. The magnitude of the vectors and minor details changed when the parameter values were changed but the pattern remained. Velocity fields corresponding to quadratic friction and spatially varying linear friction are shown in Appendix F.

Given that the model does not represent a stratified fluid very well the circulation in Queen Charlotte Sound and Dixon Entrance was not investigated in more detail.

8.1.1 Vorticity Balance

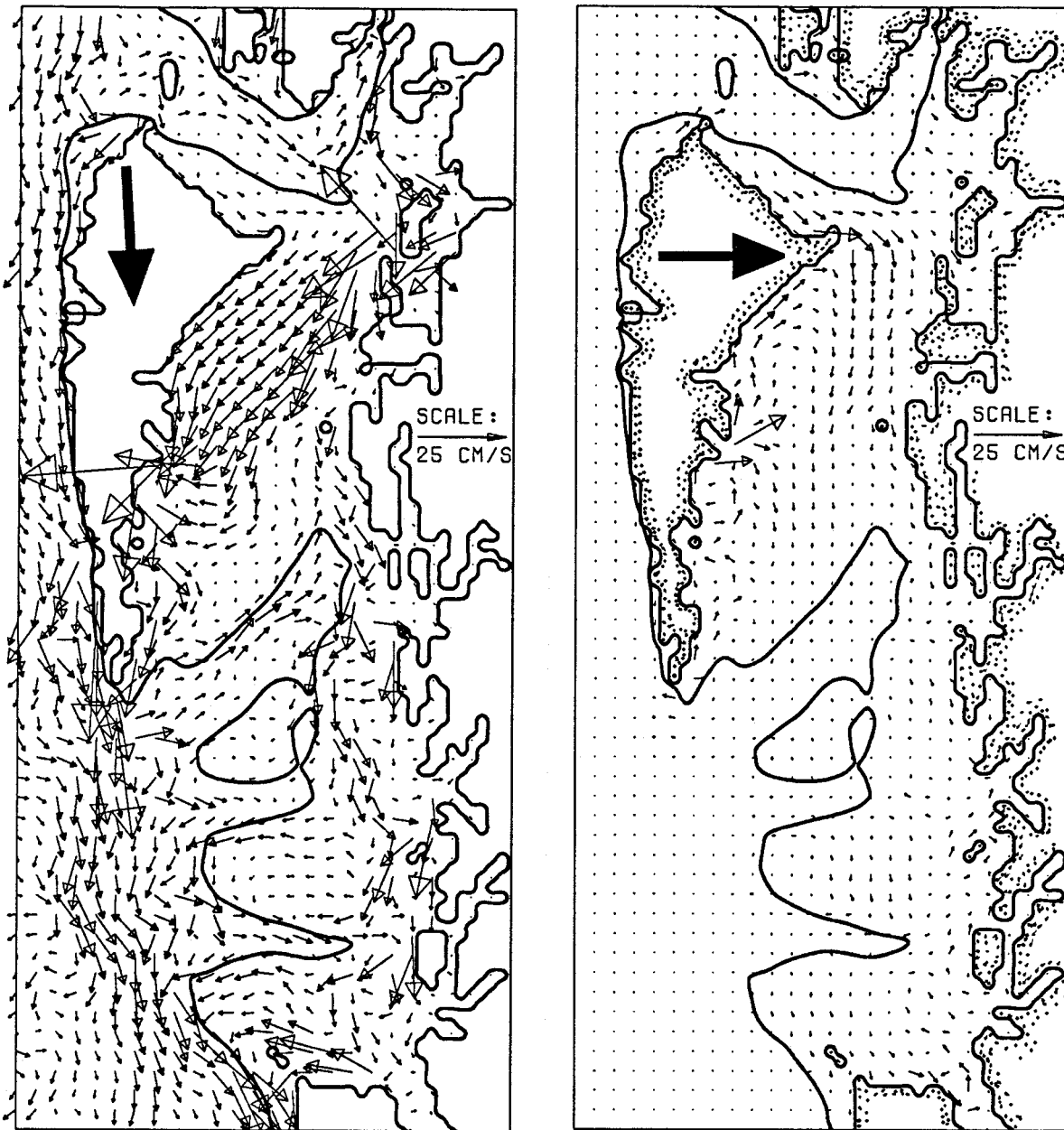
During the spin-up run, diagnostic vorticity balances were calculated at three sections across Hecate Strait: at M-line in the south, at W-line in the middle, and at R-line in the north. The results of these calculations are discussed here.

Recall from Chapter 5 that the vorticity balance can be written

$$\frac{\partial \zeta}{\partial t} - \frac{f}{h} \frac{\partial \eta}{\partial t} + (\vec{v}h) \cdot \nabla \left(\frac{f + \zeta}{h} \right) = \nabla \times \left(\frac{\vec{\tau}}{\rho h} - \vec{F}_f \right) \quad (8.47)$$

where τ is the wind stress and \vec{F}_f represents the friction and dissipation terms discussed in Chapter 5.4.

The term $(\vec{v}h) \cdot \nabla(f/h)$ is the vortex stretching term. In the Hecate Strait Model, where f is a constant, it represents the movement of water across depth contours. When



(a) along-shore wind

(b) cross-shore wind

Figure 8.60: Steady-state velocity fields for two different wind directions.

a parcel of water is moved from one depth to another, the vortex column is stretched or compressed. When the vortex stretching term is small, the water is flowing parallel to the local depth contours; thus topographic steering.

When a wind stress is imposed on a motionless fluid, the water starts to move down-wind without regard for the topography. This generates a large vortex stretching term. In the initial stages the balance is between the time rate of change of the relative vorticity and the vortex stretching

$$\frac{\partial \zeta}{\partial t} \sim (\vec{v}h) \cdot \nabla(f/h) \quad (8.48)$$

with a small contribution from the curl of the wind stress. Relative vorticity (shear) is generated and the flow reorganizes itself to minimize vortex stretching. In most regions of Hecate Strait the reorganization is successful and the flow is parallel to the local depth contours. In Hecate Strait, the regions of cross-isobath flow tend to occur where the constraints imposed by the coastline and the bathymetry force the water to change depth; at the edges of the strait and over most of the northern Hecate Strait. The steady-state vorticity balance in these areas is

$$(\vec{v}h) \cdot \nabla\left(\frac{f}{h}\right) \approx \nabla \times \left(\frac{\vec{\tau}}{\rho h} - \vec{F}_f\right) \quad (8.49)$$

with a contribution from the advection of relative vorticity. The curl of the bottom stress is an important factor in the vorticity balance.

Before moving on to the specifics of the vorticity balance, three useful results:

- The surface wind stress τ was spatially uniform. However the $1/h$ dependence creates a wind stress curl. In the spin-up experiments, $\vec{\tau} = (0, \tau^y)$ and the wind stress curl was

$$\nabla \times \left(\frac{\vec{\tau}}{\rho h}\right) = -\frac{\tau^y}{\rho h^2} \frac{\partial h}{\partial x}$$

Only the cross-strait depth gradients couple with the along-strait wind stress to generate vorticity.

- The curl of the bottom friction makes an important contribution. For linear bottom friction

$$\nabla \times \left(\frac{k\vec{v}}{h} \right) = \frac{k\zeta}{h} - \frac{k}{h^2} \left[u \frac{\partial h}{\partial y} - v \frac{\partial h}{\partial x} \right]$$

Thus the bottom friction contributes through both the relative vorticity ζ and the interaction of the velocity with the bottom slope.

- The term $(f/h)(\partial\eta/\partial t)$ was always very small and is ignored in this discussion.

At R-line the steady-state vorticity balance was established within the first day. The balance was between vortex stretching and the curl of the wind stress and bottom stress (8.49). There was a small contribution from the advection of relative vorticity. The time rate of change $\partial\zeta/\partial t$ was very small after the first 12 hours of integration.

The evolution of the vorticity balance at M-line and W-line was slower than at R-line. The balance between the time rate of change and the vortex stretching (8.48) dominated for the first two days of the spin-up, with a small contribution from the curl of the wind stress. By Day 4 the two dominant terms had decreased by an order of magnitude and the vorticity balance required all the terms, except $(f/h)(\partial\eta/\partial t)$.

By Day 8, the vorticity balance involved all the terms. The magnitudes were very small. For example, the maximum value of $\partial\zeta/\partial t$, which occurred in the middle of M-line, was

$$\frac{\partial\zeta}{\partial t} \approx 10^{-11} \text{s}^{-2}$$

This represented an increase in the shear between two neighbouring grid points of 0.05 cm s⁻¹ per day. While the vorticity was still changing in one small region, the pattern was essentially the steady-state pattern. The primary regions of cross-isobath flow (vortex stretching) were the eastern and western edges of the strait. In these regions, both the curl of the wind stress and the curl of the friction terms were important factors in the vorticity balance.

In northern Hecate Strait, the flow pattern with the velocity roughly parallel to the isobaths is established very quickly. After a short initial start-up period, the fluid parcels do not feel the strong topographic gradients because they are constrained to flow parallel to depth contours. This might explain why rotation-limited-flux (with its flat bottom) provided a good explanation for the steady-state transport results but not for the spin-up time results (Chapter 7 and Appendix G). In the initial spin-up, the vorticity dynamics play a large role as the flow is forced to align with the depth contours. After the flow is aligned, the importance of the sloping bottom diminishes and rotation-limited-flux becomes a useful concept.

8.1.2 Effect of Rotation

The steady-state circulation patterns are clearly governed by topographic steering. However it has been suggested that the counter-current along the north flank of Moresby Trough is not due to topographic steering but due to a back-pressure induced by the constriction at the northern end of the strait: that the narrowing and shallowing of the strait causes water to pile up at the northern end of the strait, and the resulting pressure gradient forces water to flow back down the strait and around Cape St. James. The numerical model is well suited to investigating this possibility.

The steady-state velocity pattern when rotation is absent (Fig. 8.61) is qualitatively different from the basic rotating pattern (Fig. 8.59a). The non-rotating pattern consists of broad sweeping currents which flow across the topographic features, not around them: topographic steering is absent when there is no rotation. The broad current out of Queen Charlotte Sound and around Cape St. James may be due to the constriction in northern Hecate Strait. However this current is not the concentrated counter-current seen in the basic pattern.

To further test the idea that the counter-current is independent of the details of

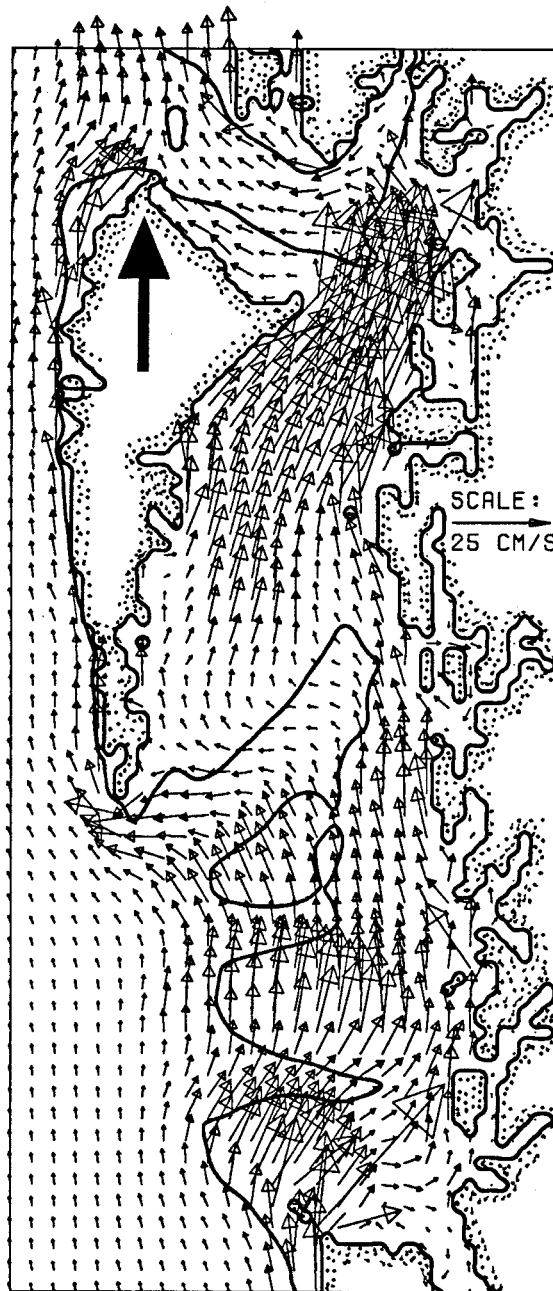


Figure 8.61: Steady-state velocity field for a SE wind and a non-rotating earth ($f = 0$).

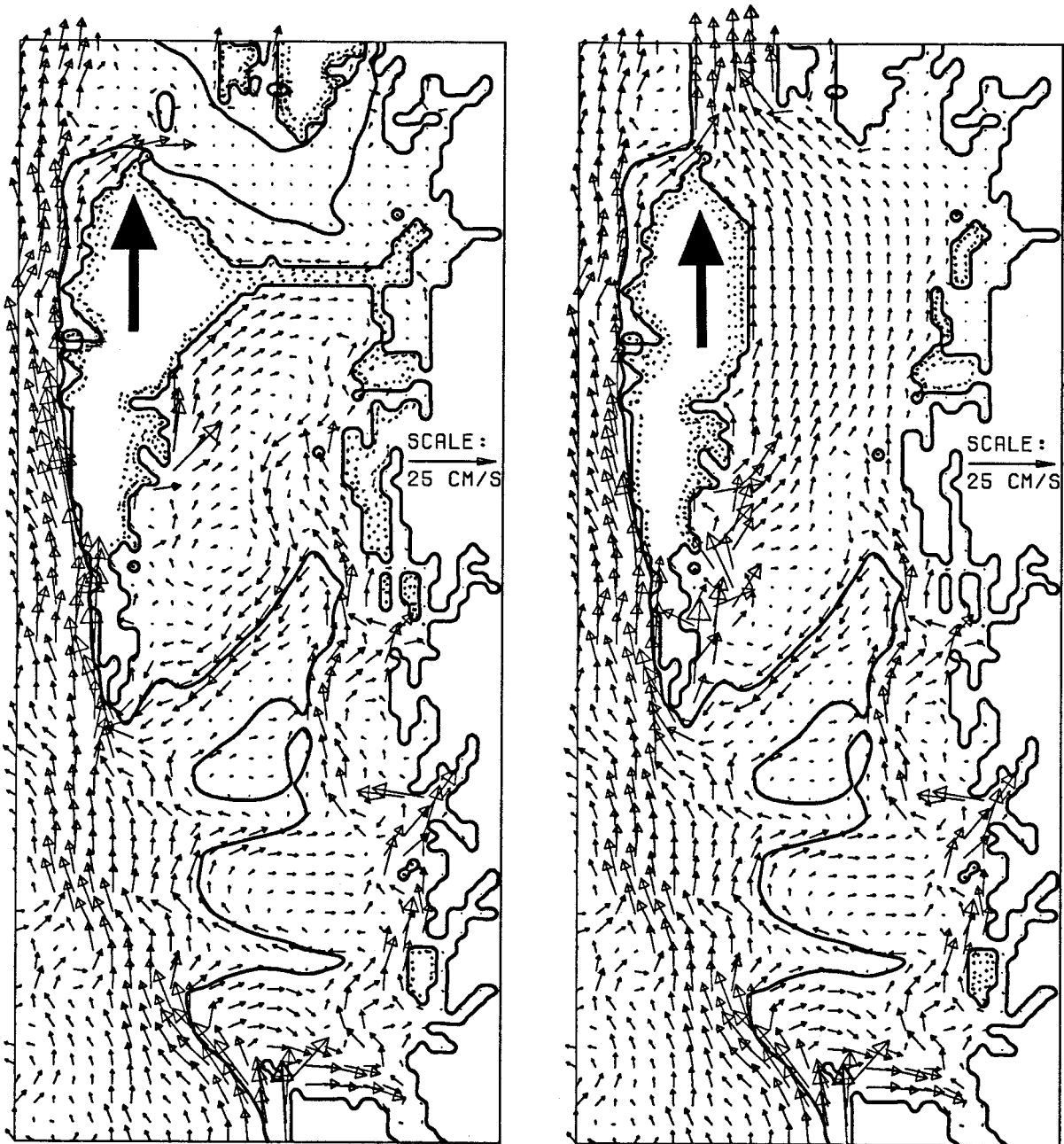


Figure 8.62: Steady-state velocity field when: (a) northern Hecate Strait is blocked off; (b) the constriction at the northern end of Hecate Strait is removed (see text). This was for a SE wind and a rotating earth, $f = 1.1 \times 10^{-4} \text{ s}^{-1}$.

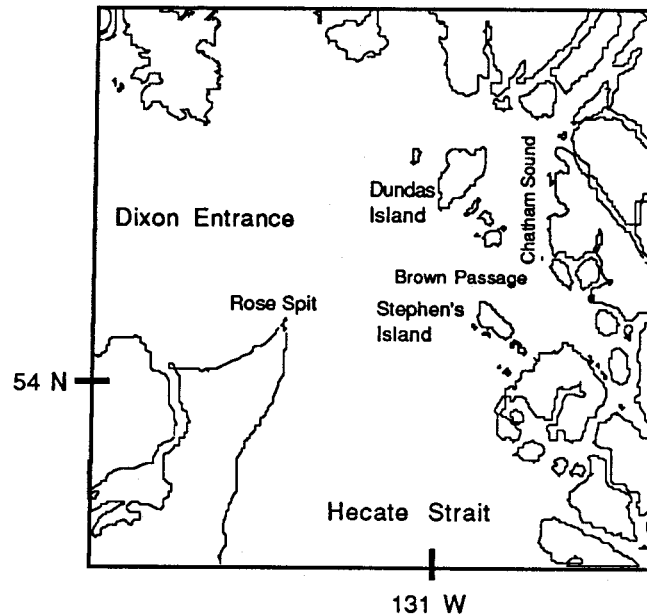


Figure 8.63: Close up of the northeast corner of Hecate Strait.

the flow in northern Hecate Strait, two experiments were conducted with altered model bathymetry. In the first, the northern end of Hecate Strait was blocked off (Fig. 8.62a). In the second, the northern end of Hecate Strait was widened and all the depths in northern Hecate Strait and Dixon Entrance were set to 80 m (Fig. 8.62b). In both cases the pattern in southern Hecate Strait and Queen Charlotte Sound were not affected by the changes in northern Hecate Strait. The steady-state pattern is dominated by topographic steering and the counter-current in Moresby Trough is independent of the details of the flow at the northern end of Hecate Strait.

8.1.3 Chatham Sound Diversion

Brown Passage, which connects Chatham Sound to Hecate Strait, looks like a wide channel (Fig. 8.63) but it is actually quite shallow and the portion deeper than 10 m is narrow. During preliminary experiments I noticed that during SE winds most drifters moving north along Hecate Strait made a hard right turn into Brown Passage. The

drifters then proceeded north along Chatham Sound and into Dixon Entrance. I assumed that this was wrong and closed the Brown Passage down to 1 grid point.

Narrowing Brown passage did not change the drifter tracks. Further investigation found that 30-50% of the transport through Hecate Strait was diverted through Brown Passage and into Chatham Sound (recall the large velocity vector in Fig. 8.59). The smaller the friction, the larger the diversion. A related problem was experienced by Crean et al., 1988 in the Strait of Georgia. They found that large friction parameters were needed to get reasonable tidal velocities in narrow poorly-resolved passages. They introduced a spatially varying friction coefficient to deal with the problem.

At the time of the writing of this thesis it is not known whether a significant fraction of the transport through Hecate Strait is actually diverted through Chatham Sound on its way into Dixon Entrance. Analysis of the observations from the 1990-1992 field program should provide some insight. The drifters from the July 1991 drifter deployment (Fig. 3.22 and Fig. 3.23) indicate that there is surface flow into Chatham Sound via Brown Passage during SE winds.

8.2 Comparison with Observations in Hecate Strait

In this section the model is tested by comparison of model simulations with the observations in Hecate Strait. In the first part the mean and EOF mode 1 velocity patterns are compared for the period 25 January to 30 March 1984. This is the same period as the transport comparison in Chapter 7. In the second part simulated drifter trajectories are compared with observations from July 1990 and July 1991.

8.2.1 Currents: Winter 1984

The simulations of the winter of 1984 discussed here are the same simulations that were used in the transport comparison in Chapter 7. The model results plotted in the figures in this section were taken from simulation E501a which used linear friction ($k = 0.5 \times 10^{-3} \text{ s}^{-1}$) and the standard parameters (Table 6.6). The results from the other simulations (Table 8.11) were very similar and are not shown.

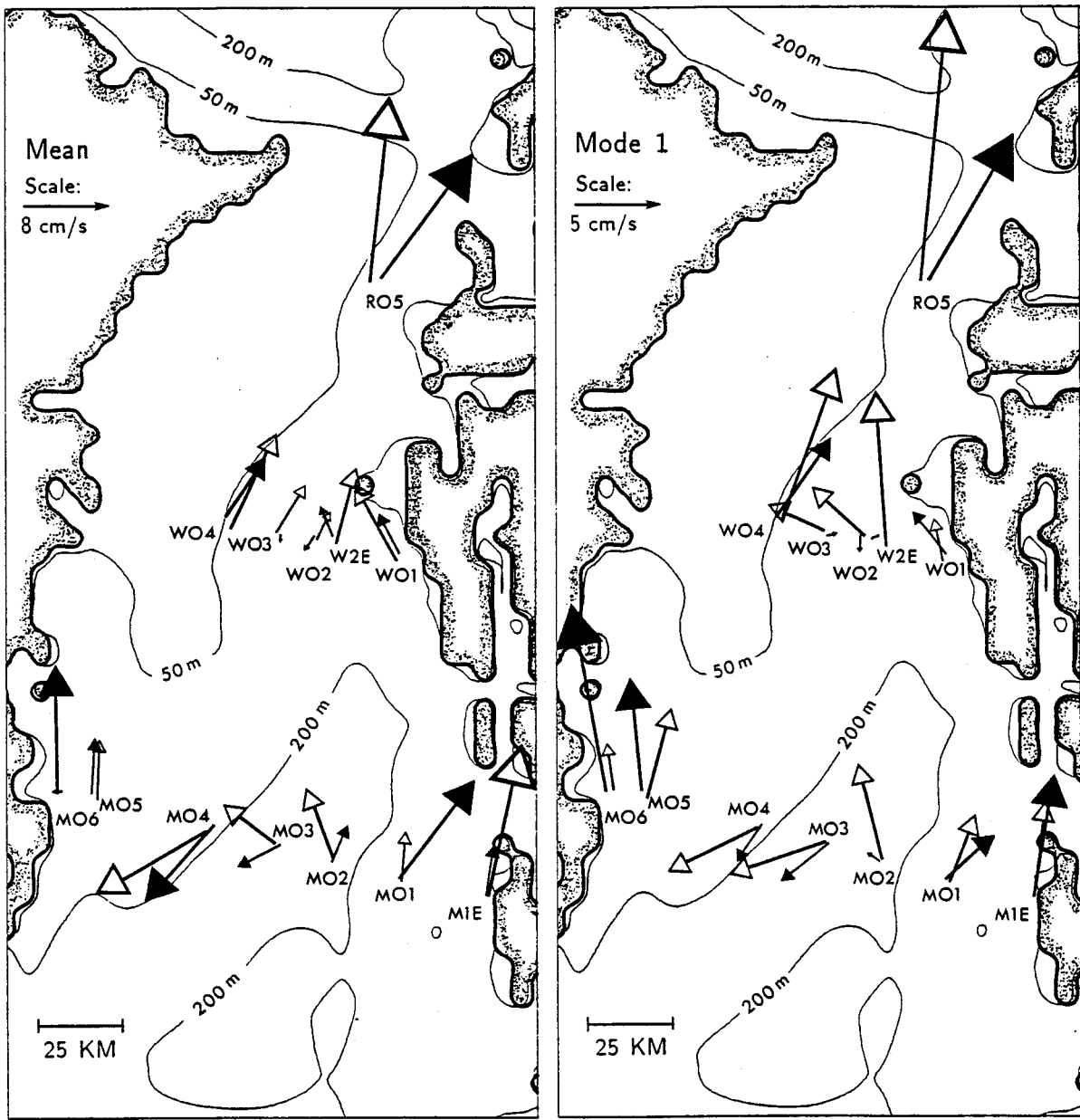
experiment	Λ_1 ($\text{cm}^2 \text{ s}^{-2}$)	Λ_2 ($\text{cm}^2 \text{ s}^{-2}$)
E501a (linear)	374 (0.67)	82 (0.15)
E502a (quadratic)	359 (0.72)	56 (0.11)
E503 (RMS)	395 (0.69)	110 (0.19)
depth averaged observations	633 (0.39)	192 (0.12)
observations reported in Chapter 3	1231 (0.28)	605 (0.14)

Table 8.11: The first two eigenvalues from the EOF analysis of the simulated and observed velocities for the period 25 January - 30 March 1984. Each eigenvalue, Λ_i , is represented by two values; its magnitude and the fraction of total energy that this represents (in brackets).

The simulated mean currents have the same character as the observations (Fig. 8.64a). The flow is to the SW in the middle of M-line, to the NE at R05 and W04, and confused in the middle of W-line. Notable exceptions are the strong cross-isobath velocities observed at M03 and the small mean velocity observed at M06. The simulated velocities at W02 and W03 are much too small and go the wrong way. At R05 the observed velocity has a strong cross-isobath component, absent in the simulated velocity.

The model current meters were placed at the grid point closest to the actual meter. The differences in location can be seen by the location of the tails of the vectors in (Fig. 8.64).

The time series were not scaled by their standard deviation before EOF analysis.



(a) mean currents

(b) mode 1 currents

Figure 8.64: Model verification. Comparison of the simulated (E501a) and observed currents in Hecate Strait from 25 January to 30 March 1984. The depth-averaged observations are shown with open arrow heads; the simulated currents with solid arrow heads. The model was driven with winds measured near W04.

Therefore the eigenvalues reported in Table 8.11 have units of $\text{cm}^2 \text{s}^{-2}$ and are a direct measure of the energy. The eigenvalues from the simulations are smaller than those from the observations. This is consistent with the results in Chapter 7 where the simulated transport fluctuations were too small. In the simulations mode 1 (Λ_1) represents 70% of the energy, whereas in the observations it represents 30% to 40%. The higher modes contain much more energy in the observations than they do in the simulations. This reminds us that there are significant processes in the ocean that are not represented in this model (Chapter 2).

The simulated EOF mode 1 velocity pattern captures the character of the observed pattern (Fig. 8.64b; note the scale change between the mean and mode 1 currents). The model reproduces the gyre structure in M-line with the velocity fluctuations in the deep water in the opposite direction to those in the shallower water and in the opposite direction to the fluctuations at R05. There are problems, however. At M-line the fluctuations in the deep water are too small compared with those in the shallow water. The fluctuations at M06 are much too large. At R05 the velocity is too small and seems overly constrained by the topography. The velocities in the middle of W-line exhibit the same problem as the mean velocities – too small and in the wrong direction.

The velocities at W-line are sensitive to the details of the friction. The velocities in the middle of W-line (W2E, W02, W04) are at the northern end of the counter-current in Moresby Trough. When the friction coefficient is increased, these small southward velocities become small northward velocities (see Fig. 6 in Hannah et al., 1991).

At M-line the major problem is that the velocities in the deep water are too small with respect to the velocities in the shallow water. This is especially true in the mode 1 velocities. It is conceivable that the observations do not accurately represent the depth-averaged flow. In the middle of M-line (M01 to M05) the upper current meter was 50 m below the surface. At M1E and M06 the upper meters were at 21 m and 25 m respectively.

A significant fraction of the water in the upper 50 m might move in the direction of the wind. This would decrease the depth-averaged velocity in the region where the water flows against the wind. Blaming the observations is a time-honoured excuse of numerical modellers.

The velocity patterns from the other experiments reported in Table 8.11 are very similar to those shown. The eddy viscosity had a negligible effect on the results. Removing it resulted in an overall energy level increase of less than 2%.

The time series of modal amplitudes for the observed and simulated EOF-mode-1 velocities are compared in Fig. 8.65. The differences between the modal amplitudes are mirrored in the differences between the observed and simulated transports (Fig. 7.47). Recall that in the observations, the mode 1 velocities represented the transport of water through the strait (Chapter 3). The same is true of the simulation results.

The observed and simulated EOF mode 2 time series (not shown) bear no resemblance to each other.

Discussion

Changing the friction parameters has more impact on the velocities in the shallow water than in the deep water. Therefore the friction could be increased to improve the pattern across the M-line and in the middle of W-line. Such an increase in friction would decrease the transport and the velocity at R05. This could be compensated by increasing the wind stress estimate. Trying to force the model to fit the observations by this *ad hoc* technique has drawbacks. Nothing within the range of the model dynamics will change M06 from a strong along-strait velocity to a weak on-shore velocity. Trying to reduce the velocity at M06 ($h=100$ m) while increasing the velocity at R05 ($h= 55$ m) is unlikely to be successful.

Using the rms tidal velocities to compute a spatially varying friction coefficient was

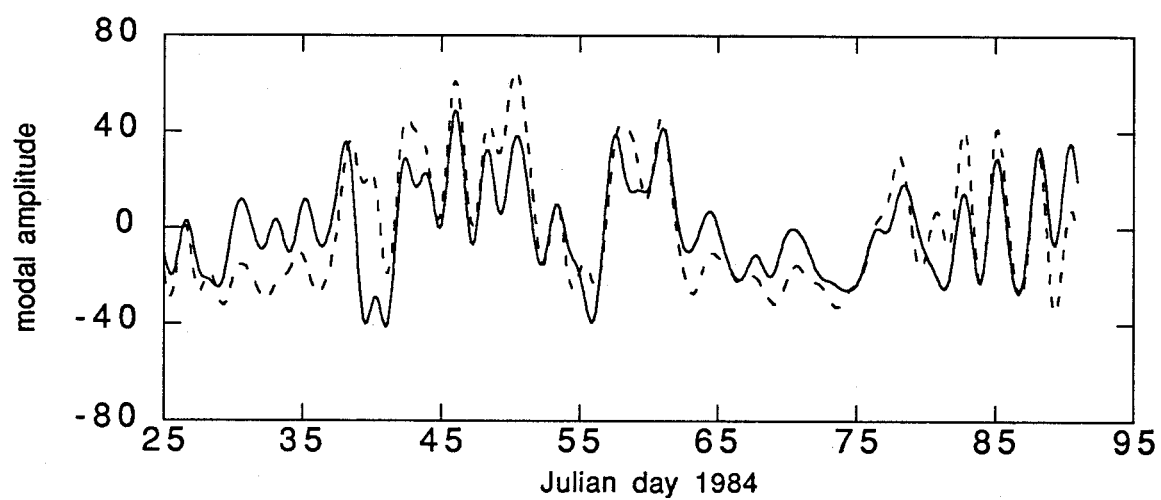


Figure 8.65: Time series of modal amplitudes of the EOF-mode-1 velocities. Comparison of simulation E501a (solid) with the observations (dotted) in Hecate Strait from 25 January to 30 March 1984.

an attempt to redistribute the friction in a physically realistic manner. The lack of significant improvement in the results indicates that friction is not the key to improved simulations.

These results indicate that minor changes in the bottom friction formulation are unlikely to improve the simulations. One possible improvement is the scheme of Hunter and Hearn (1990) which removes the constraint that the mean velocity and the bottom stress be parallel. This might be important and the results would be instructive.

8.2.2 Drifters

Tests showed that the simulated drifters travelled much more slowly than the real near-surface drifters. To demonstrate that the simulated drifters had the proper behaviour albeit a bit slow, the following was done. Simulated drifters were started at regular intervals along the observed drifter track. The simulated drifters were then followed for several days to illustrate the model behaviour. In many cases the simulated drifter trajectories were very sensitive to the exact location of the drifter and extra drifters are used to show this.

July 1990

The July 1990 drifter study took place in southern Hecate Strait. Two simulations are shown. The observed drifters are near-surface drifters with drogues centred at 10 m. The observed trajectories contain the tidal motions, while the simulated ones do not. The winds used in these simulations were measured at an Atmospheric Environment Service (AES) weather buoy located 150 km SE of Cape St. James.

In Figure 8.66 the observed drifter started near the mouth of Moresby Trough and proceeded in a clockwise loop around the shallow bank to the south (Middle Bank).

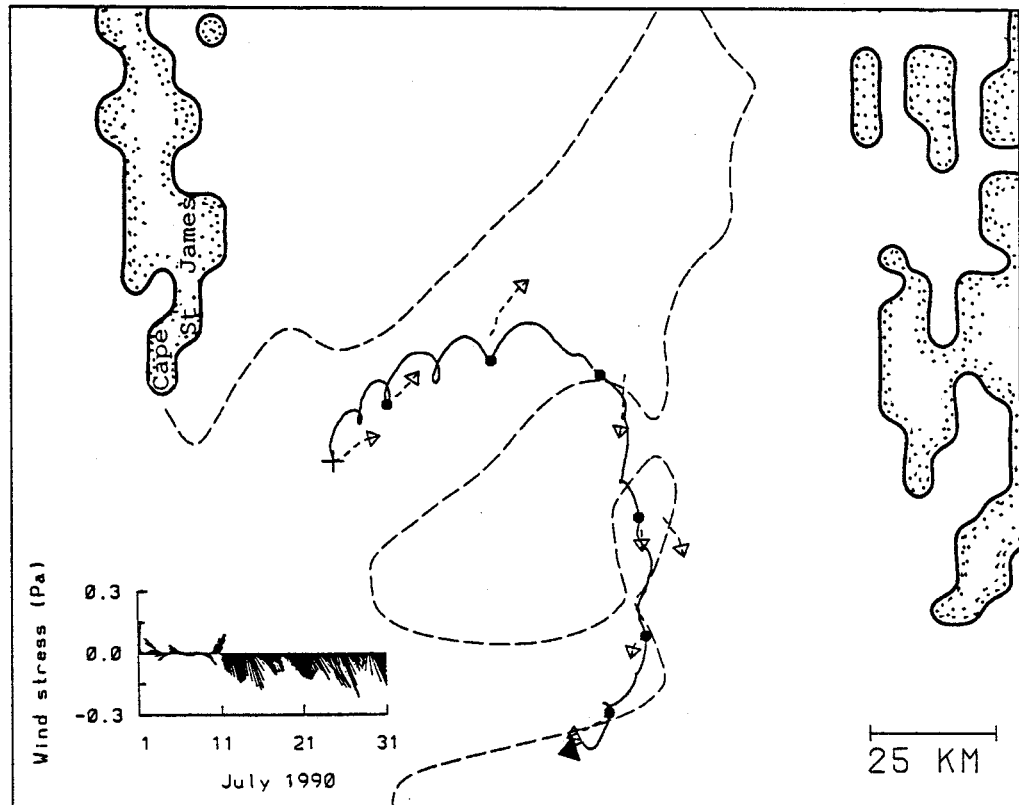


Figure 8.66: Comparison of an observed drifter trajectory and simulated drifters in Moresby Trough from 12 to 18 July 1990. The observed drifter (solid) started at the cross. Simulated drifters (dashed) were started at daily intervals (circles) along the observed drifter trajectory. The simulated drifter trajectories are 4 days long. In cases where the simulated drifter did not move very far an extra drifter was started 1 grid point away. The winds were measured at a weather buoy located 80 km below the bottom of the figure (see text). The wind stress time series is shown in the lower left corner. The free end of the wind vectors indicates the direction the wind is blowing to. The 200 m contour is shown for reference.

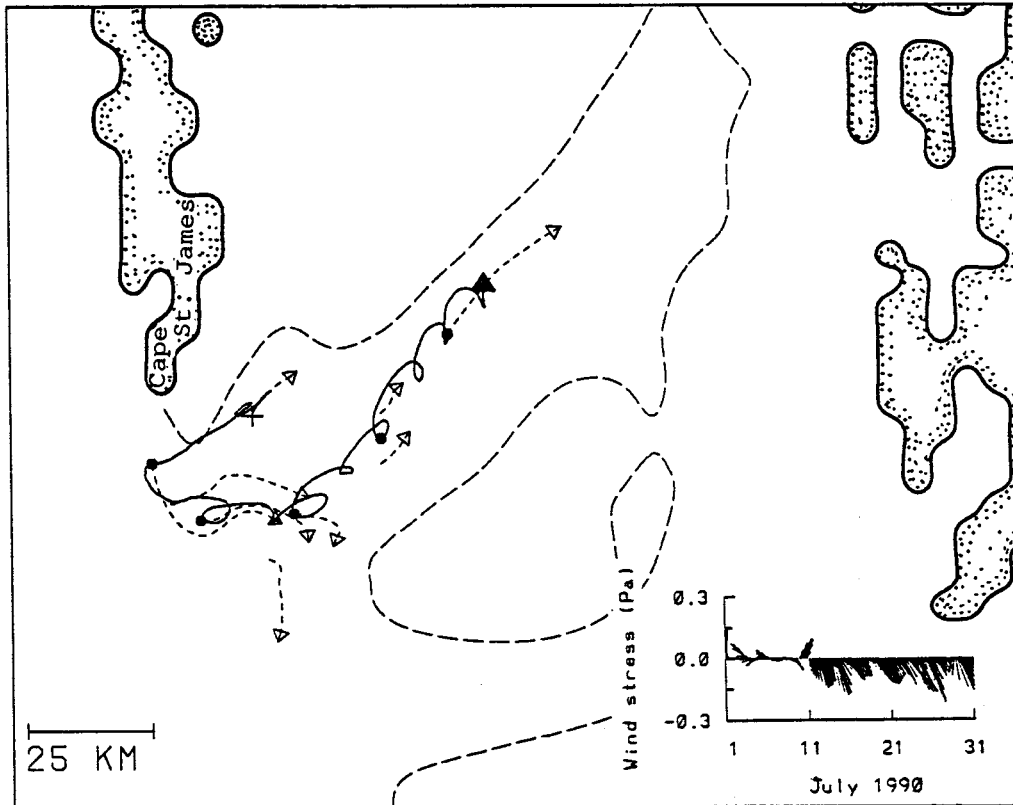


Figure 8.67: Comparison of an observed drifter trajectory and simulated drifters near Cape St. James from 21 to 26 July 1990. See Fig. 8.66 for details.

The simulated drifters were started at daily intervals and were followed for 4 days. The observed drifter trajectory was 6 days long (12 July to 18 July).

In Figure 8.67 the observed drifter started to the east of Cape St. James and travelled west past the cape before it looped back into Moresby Trough. The observed trajectory was 5 days long and the simulated drifters were followed for 4 days. The model did not allow the drifters to move out past the cape. However it did bring the drifter at day 2 back into Moresby Trough.

In both cases, the simulated drifters were much too slow, generally 1/4 to 1/10 the speed of the observed drifters. Nevertheless the simulated drifters were good indicators of the direction of travel of the near-surface drifters, except in the vicinity of Cape James. The results shown are representative of simulations of other drifters from the same deployment.

July 1991

The July 1991 drifter study took place in northern Hecate Strait. Two simulations are shown. Again the observed trajectories contain the tidal motions, while the simulated ones do not. The winds used in these simulations were measured at an AES weather buoy whose location is shown in the figures with the drifters.

The observed drifter in Fig. 8.68 was launched just after the wind abruptly shifted from northwesterly to southeasterly. The drifter was driven north along Hecate Strait and then turned into Chatham Sound. The trajectory was 8 days long. The drifter had a drogue centred at 10 m and it drifted at half the speed of a drifter launched at the same place and time with a drogue centred at 3.5 m (see Fig. 3.23).

The simulated drifters, started at daily intervals and followed for 4 days, do a good job of tracking the observed drifter when the winds were strong. The velocities are about 1/4 the observed values. When the wind died down (about the time the drifter

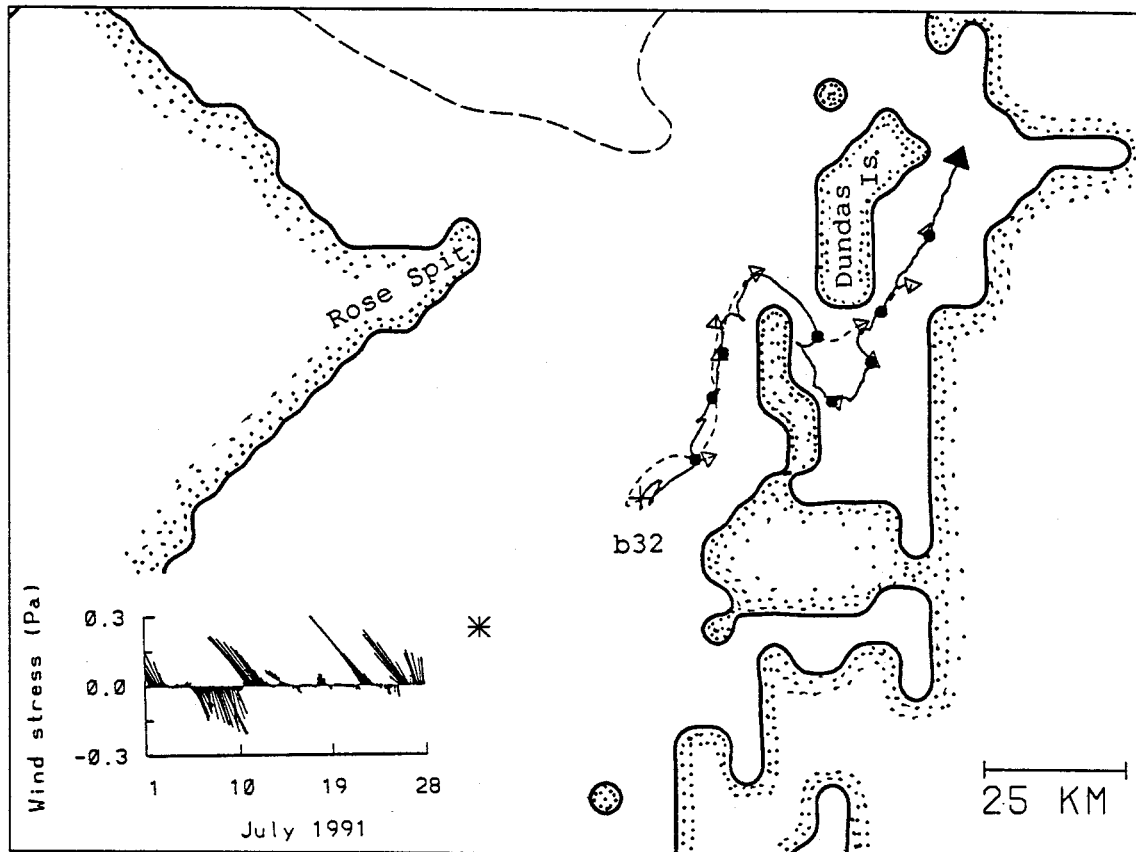


Figure 8.68: Observed and simulated drifter trajectories in northern Hecate Strait from 11 to 19 July 1991. Drifter b32 was launched shortly after the winds changed direction on July 10. The wind stress time series shown in the lower left corner was measured at the * in the center of the strait. The free end of the wind vectors indicates the direction the wind is blowing to.

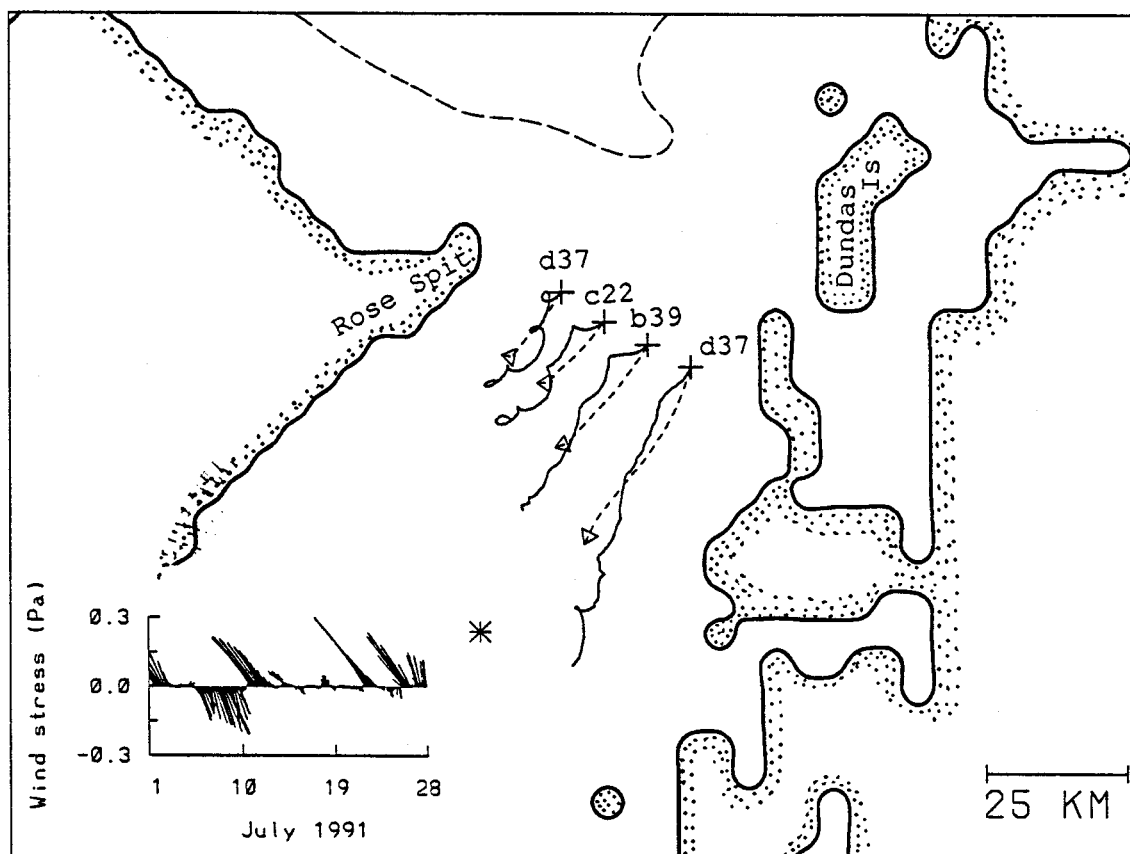


Figure 8.69: Observed and simulated drifter trajectories in northern Hecate Strait from 8 to 10 July 1991. All the trajectories are 2 days long. During this time the wind was steady and from the NW. The end of the trajectories corresponds to the change in wind direction near July 10. The wind stress time series shown in the lower left corner was measured at the * in the center of the strait.

entered Chatham Sound) the simulated drifters did not move far enough to give a sense of direction.

In the second test four drifters were launched in a line across northern Hecate Strait (within 2 hours of each other). The drogues were centred at 3.5 m. All the trajectories are two days long (observed and simulated) and no extra drifters were used (Fig. 8.69). The simulated drifters travel in the right direction and at about 1/2 to 3/4 the speed of the observed drifters.

A marked feature of the observed drifters from this deployment was that the drifters tended not to cross the steep escarpment that separates Hecate Strait from Dixon Entrance (see drifter c22 in Fig. 3.22). Drifters tended to work their way along the escarpment and cross at the eastern end. This is also a feature of the simulated drifters. Simulation of particular drifters was unsatisfactory.

8.3 Regional Circulation Patterns

The drifter trajectories from the winter of 1984 simulation (E501a) provide a clear illustration of the model's circulation pattern. The near-shore drifters in Fig. 8.70 and Fig. 8.71 trace out the historical winter flow pattern. Under winter (SE) winds, the water flows into Queen Charlotte Sound at Cape Scott and then follows the coastline north through Hecate Strait and Dixon Entrance and then into the Pacific Ocean. During the simulation the winds were consistently from the SE.

The effect of topographic steering is clearly illustrated by the drifters in Queen Charlotte Sound (Fig. 8.71). Simulated drifters do not cross the 200 m contour: offshore drifters stay offshore and inshore drifters stay inshore. None of the drifters show any tendency to flow out of the mouth of Queen Charlotte Sound as one was observed to do in the winter of 1990.

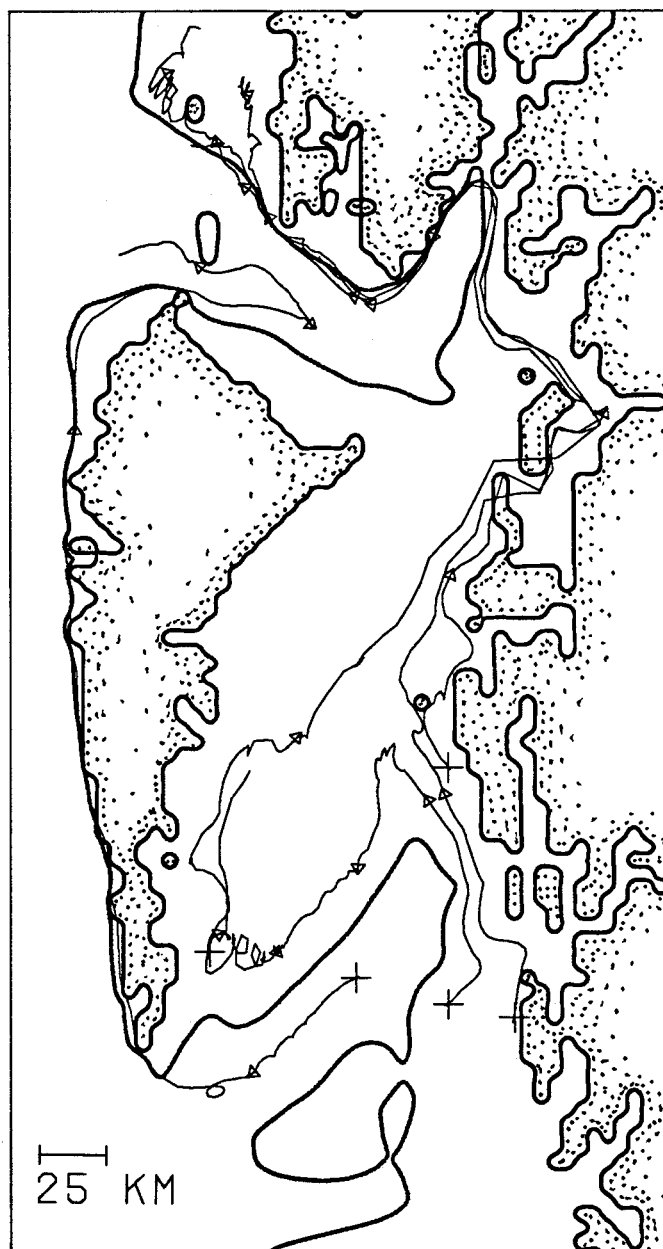


Figure 8.70: Simulated drifters in the northern half of the model domain for 20 Jan to 30 Mar 1984. The starting location of each drifter is marked by a cross. The drifter trajectories are marked with arrows at 20 d intervals.

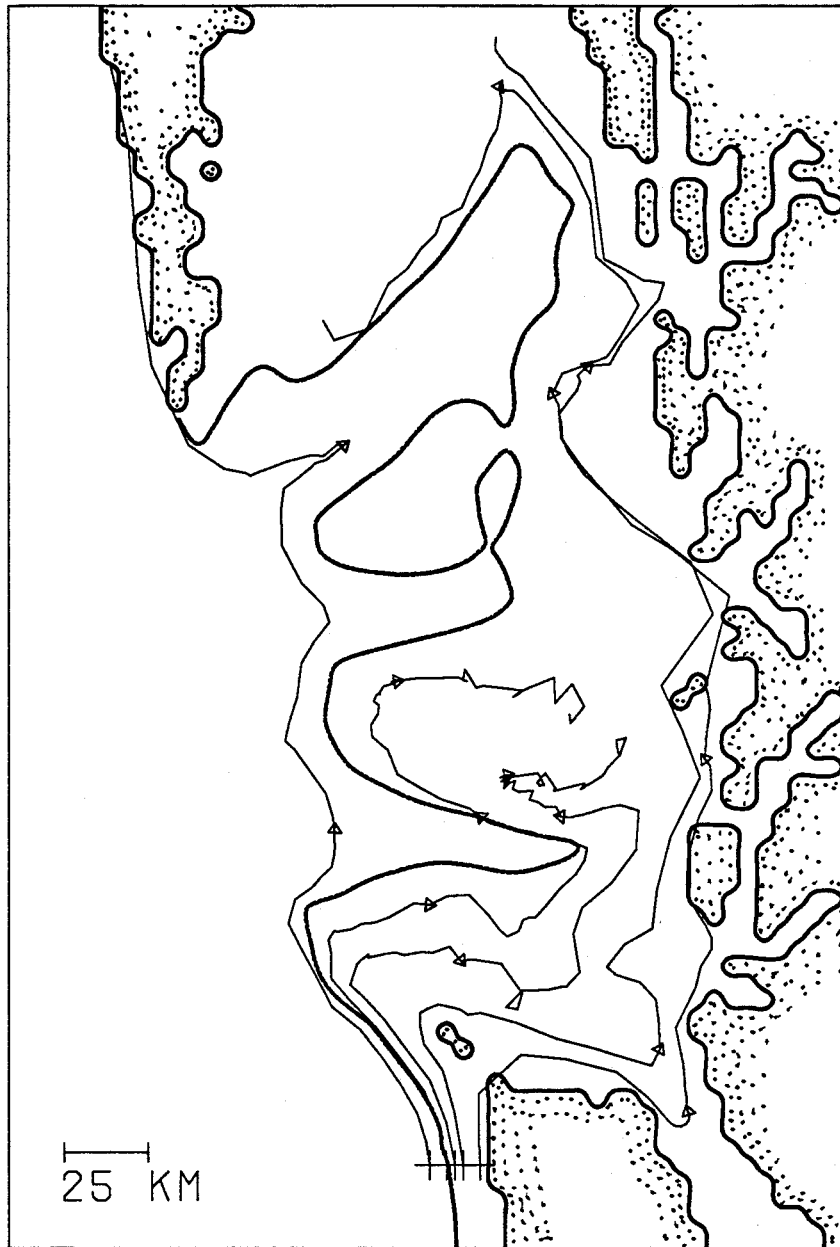


Figure 8.71: Simulated drifters in Queen Charlotte Sound for 20 Jan to 31 Mar 1984. The starting location of each drifter is marked by a cross. The drifter trajectories are marked with arrows at 20 d intervals.

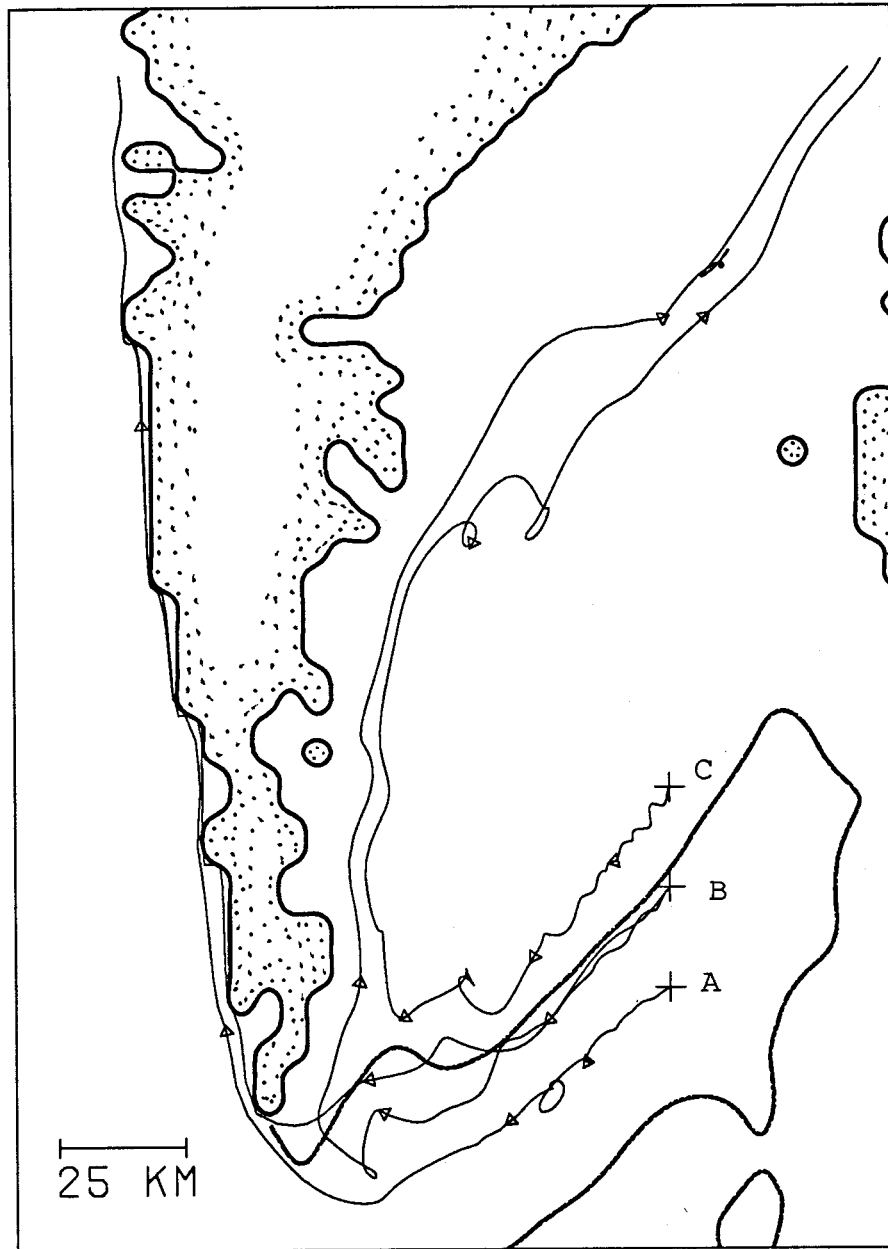


Figure 8.72: Simulated drifters near Cape St. James. The starting location of each drifters is marked by a cross. The drifter trajectories are marked with arrows at 20 d intervals.

The counter-current in south-central Hecate Strait shows clearly with the drifters travelling to the SW along the north slope of Moresby Trough. Along the mainland coast there is a fine line between those drifters which continue to hug the coast and those which turn to the SW towards Cape St. James.

The drifter trajectories have some details in common with the observed trajectories:

- Drifters in northeast Dixon Entrance make a loop into and out of Clarence Strait on their way to the Pacific (compare with Fig. 3.18).
- Under SE winds, many drifters travelling from Hecate Strait to Dixon Entrance do so by detouring through Chatham Sound rather than floating directly into Dixon Entrance.
- The drifter in Fig. 8.70 that goes into and out of the mouth of Dixon Entrance near Langara Island is similar to that seen from the winter of 1990 (compare with Fig. 3.21).

The fate of a drifter caught in the counter-current depends on the details of the flow as the drifter nears Cape St. James. The drifter trajectories shown in Fig. 8.72 illustrate the variability of the simulated flow near Cape St. James. The starting locations represent one of the regions where English sole are believed to spawn. Drifters were started every 5 days at each location and selected ones plotted. All the drifters started at location A escaped past Cape St. James into the open ocean. All the drifters started at location C travelled close to Cape St. James and then moved north along Hecate Strait and into Dixon Entrance. The fate of the drifters started at location B was less predictable. Some drifters escaped past Cape St. James and some remained in Hecate Strait (and travelled into Dixon Entrance). The details of the flow at Cape St. James are crucial in determining the fate of drifters travelling SW along Moresby Trough.

In this simulation the 200 m contour defines a region that separates those locations where the drifters always escaped past Cape St. James and those locations where the drifters remain in Hecate Strait. The exact position of this critical region depends on the bottom friction parameterization.

The overall circulation pattern revealed by the drifters in Fig. 8.70 and Fig. 8.71 is consistent with the pattern of the steady-state currents in Fig. 8.59. The time variation of the winds affects the details such as the fate of individual drifters near Cape St. James but not the overall circulation pattern. This is consistent with the idea that the EOF-mode-1 currents represent fluctuations in magnitude (not direction) about the mean velocities. The features discussed in this section were evident in all the simulations and do not depend on the friction parameterization.

All of the drifter trajectories shown in this section were computed during the simulation runs except for the drifters in Fig. 8.71 which were computed using the daily currents saved during the simulation. This technique is discussed in Appendix D and Appendix F.

8.3.1 Southern Hecate Strait

The model results presented above suggest the following winter circulation pattern in southern Hecate Strait. Water from Queen Charlotte Sound enters Hecate Strait along the mainland coast on the eastern side. Some of the water hugs the coastline and continues north. The rest of the water flows southwest along Moresby Trough to Cape St. James where some water escapes around the cape into the open ocean and some flows north along the western side of Hecate Strait (Fig. 8.73). This pattern is consistent with the observations.

The new idea is the S-shaped path from the eastern side of Hecate Strait to Cape St. James and then north along the western side of the strait. The S-shaped path has

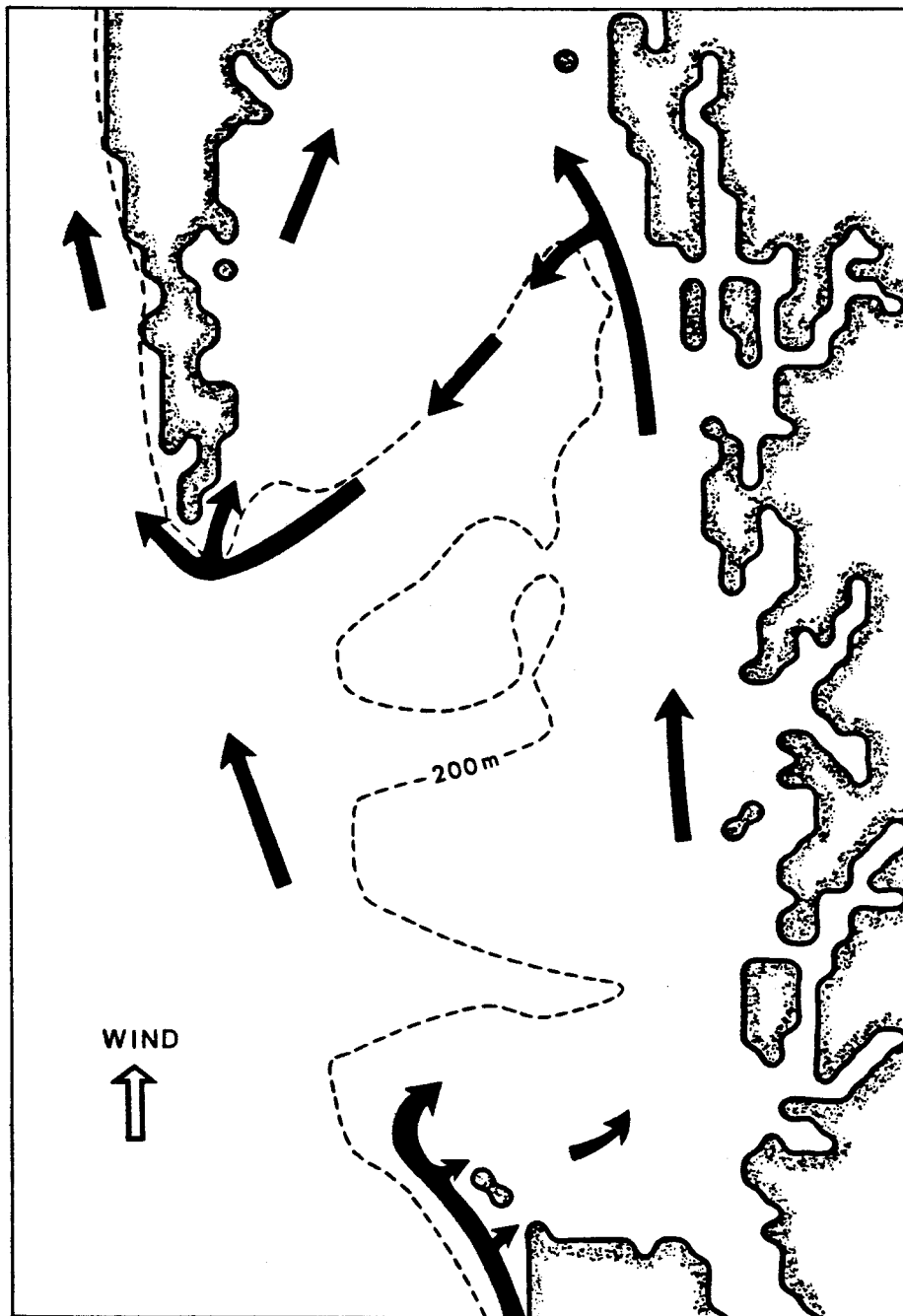


Figure 8.73: Sketch of the circulation in Hecate Strait and Queen Charlotte Sound under a SE wind.

implications for the larval advection problem and differs from the interpretation of the mean and mode 1 current patterns proposed by Crawford, Tyler and Thomson (1990). They speculated that the observed current pattern at M-line represented the north end of an eddy that closed somewhere to the south. This eddy was invoked as a mechanism to ‘...recirculate a significant fraction of the larvae in the Strait, increasing their residence time sufficiently to allow settling out, thus enhancing recruitment.’ The S-shaped path would also increase the residence time of the larvae. The proposed path is also supported by a remark made by Crawford, Tyler and Thomson (1990):

Fish eggs and larvae in the Strait tend to be concentrated on the western side, putting them in a position to be retained by the eddy. They seem equally abundant in the northern and southern halves rather than concentrated to the south where the eddy seems most evident (Mason et al., 1981c).

The pattern proposed in Fig. 8.73 would concentrate larvae in a narrow band along the west side of Hecate Strait. If the S-shaped circulation pattern is correct then the advection of English sole larvae from the spawning grounds in southern Hecate Strait to the nursery in the northwest corner depends on the details of the flow near Cape St. James.

8.4 Summary

The Hecate Strait Model, a depth-averaged model driven by local winds, is a useful model of the flow patterns in Hecate Strait. The simulations showed that:

- The model does a good job of simulating the winter transport and mode 1 velocity fluctuations in Hecate Strait.

- The model currents capture the character of the spatial patterns of the observed mean and mode 1 velocities.
- The model drifters generally give a good indication of near-surface drifter direction but under-predict the velocity.
- The steady-state current pattern (Fig. 8.59) provides good prediction of the model drifter trajectories and is a reasonable guide to the circulation patterns in the region.
- The simulated drifters do not perform well near Cape St. James.
- The results were best when the wind was strong, which indicates that other forcing becomes important when the winds are weak.

The model results in southern Hecate Strait are summarized in Fig. 8.73. The pattern is consistent with the observations and differs from a previous interpretation of the observations.

Chapter 9

Conclusion

A regional model of the depth-averaged currents was successfully applied to the winter circulation in Hecate Strait, British Columbia. Simulations using the Hecate Strait Model demonstrated:

- good agreement between the observed and simulated water transport through Hecate Strait for January to March 1984.
- qualitative agreement between the observed and simulated current patterns for the same period.
- reasonable prediction of the direction of travel of near-surface drifters, but not their speeds.

The physical insights provided by this study indicate that the earth's rotation has a significant impact on the water transport in Hecate Strait. The interaction of the rotation with the finite length of the strait creates an extra impedance, which behaves like a linear friction term. The simulated transport through Hecate Strait was found to be consistent with the rotation-limited-flux model. In numerical experiments with a non-rotating earth, the linear bottom friction had to be increased by roughly three times to be equivalent to the effects of rotation.

The circulation pattern in the Hecate Strait Model depended strongly on the rotation of the earth. This was interpreted as the effect of topographic steering – the tendency for the low-frequency flow in a rotating fluid to be parallel to the local isobaths. In particular

the counter-current in south-central Hecate Strait was a consequence of topographic steering and independent of the details of the flow in northern Hecate Strait.

The analysis of the observations and the model results led to three insights of lasting value:

- For the winter of 1984, the observed fluctuations in water transport through Hecate Strait were highly correlated with the EOF-mode-1 currents. In fact, the EOF-mode-1 current pattern is the pattern that moves water from one end of Hecate Strait to the other. The remaining 75% of the energy in the current fluctuations is related to redistribution of water within Hecate Strait.
- The counter-flow in south-central Hecate Strait is part of an S-shaped flow pattern that moves water from the eastern side of Hecate Strait to the western side, rather than the northern edge of an eddy. This has implications for the larval advection problem and makes the details of the flow near Cape St. James extremely important.
- The rotation-limited-flux model is a valid long-wave approximation to a more complete theory. This means that: 1) rotation-limited-flux provides useful insight into the low-frequency sea-level fluctuations in sea straits; and 2) the rotation of the earth is important even for straits where the width is less than one external Rossby radius ($W < \sqrt{gh}/f$).

This study was limited in scope. The Hecate Strait Model was the first circulation model of the region and the assumption was made that the water velocity and density were vertically homogeneous. This restricted the application of the model to Hecate Strait. Even within Hecate Strait these assumptions severely limit the application of the model to practical problems such as oil spill trajectory prediction and larval advection problems.

Despite these restrictions, the Hecate Strait Model has been a useful tool for understanding the circulation in the Queen Charlotte Islands region. Predictions such as the proposed circulation pattern in southern Hecate Strait were used as working hypotheses for planning the 1990 to 1992 field program. The steady state velocity pattern was used in planning the July 1990 and July 1991 drifter programs. The inevitable discrepancies that will arise between the new observations and the predictions of the Hecate Strait Model will provide fertile ground for future modelling studies.

9.1 Future Work

There is room to improve the Hecate Strait Model. The areas for model improvement fall into three main categories: 1) atmospheric forcing, 2) open boundary information, and 3) model dynamics. The first two categories reflect the fact that the circulation in Hecate Strait is affected by processes outside the strait. The greatest improvement in the transport simulations would come from including these non-local effects. Improvement in the simulated currents requires improved model dynamics.

Improvements in atmospheric forcing can be easily incorporated into the model. The major hurdle is the construction of reliable forcing fields. At this time good information on the spatial variability of the winds is not available. The construction of a meso-scale climatology would be very useful.

The effects of the baroclinic and thermohaline circulation are beyond the reach of this numerical model. Nevertheless information about the vertical shear could be included by the addition of a spectral model in the vertical (Davies, 1985 and 1987; Forristall, 1974). This would provide useful information about velocity profiles and provide insight into the reasons for the differences between the simulated and observed currents at M-line. The near-bottom currents could be used to improve the bottom stress estimate.

Improving the open boundary information is a very large task. The open boundary conditions could be modified to include the tides, but I am not sure that doing so would improve our understanding of the circulation. Incorporating remotely generated shelf waves into the regional model requires improved information along the open boundaries. Before this is done, there are many interesting process studies that could be done to illustrate the effect of shelf waves on the circulation. Accurate representation of the shelf waves probably requires a model that supports density variations, but useful studies can be done with the depth-averaged model.

The most difficult area for improvement is the impact of the deep ocean circulation on the model region. Very little is known about the impact of water mass intrusion, along-shore pressure gradients, and eddies. These are beyond the scope of the model presented here.

Improvement and modification to the Hecate Strait Model may not be the best route for future work. A suite of finite element models have been adapted to the north coast region by M.G.G. Foreman at the Institute of Ocean Sciences (IOS), Sidney, B.C. The models range from a barotropic tidal model (Foreman et al., 1992) to a three-dimensional diagnostic model (the density field is fixed). A complete three-dimensional model is being developed. These models permit the investigation of the circulation using a range of physics and complexity while maintaining a consistent numerical framework. As well, a full three-dimensional model based on the Princeton model (Blumberg and Mellor, 1987) is being developed by P.C. Cummins at IOS.

This thesis has concentrated on the response to local wind forcing. Very little is known about how events outside the Queen Charlotte Islands region affect the circulation in Hecate Strait. Shelf waves are an important mechanism for transmitting information about remote events. The understanding of the shelf circulation in the Queen Charlotte Islands region would benefit from understanding the impact of remotely generated shelf

waves. In particular: 1) Is Brooks Peninsula a barrier to shelf wave propagation? and 2) What happens as the shelf wave passes by the mouth of Queen Charlotte Sound? The depth-averaged regional model could be used for such a study. However more reliable results would be obtained from a model that allowed some density stratification, which would improve the shelf wave dispersion relation.

Bibliography

- J.S. Allan, J.A. Barth, and P.A. Newberger, 1990: On intermediate models for barotropic continental shelf and slope flow fields. Part II: Comparison of numerical model solutions in doubly periodic domains. *Journal of Physical Oceanography*, 20, 1044–1076.
- J.S. Allen, 1980: Models of wind-driven currents on the continental shelf. *Ann. Rev. of Fluid Mech.*, 12, 389–433.
- A. Arakawa and V.R. Lamb, 1981: A potential enstrophy and energy conserving scheme for the shallow water equations. *Monthly Weather Review*, 109, 18–36.
- R. Asselin, 1972: Frequency filter for time integrations. *Monthly Weather Review*, 100, 487–490.
- P.G. Baines, G. Hubbert, and S. Power, 1991: Fluid transport through Bass Strait. *Continental Shelf Research*, 11, 269–293.
- W.H. Bell, 1963: Surface current studies in the Hecate Model. MS Rep. Ser. (Oceanogr. and Limnol.) 159, Fisheries Research Board Canada.
- W.H. Bell and N. Boston, 1962: The Hecate Model. MS Rep. Ser. (Oceanogr. and Limnol.) 110, Fisheries Research Board Canada.
- W.H. Bell and N. Boston, 1963: Tidal calibration in the Hecate Model. *J. Fish. Res. Board Canada*, 20, 1197–1212.
- J.R. Bennett and A.H. Clites, 1987: Accuracy of trajectory calculation in a finite-difference circulation model. *Journal of Computational Physics*, 68, 272–282.
- A.F. Blumberg and G.L. Mellor, 1987: A description of a three-dimensional coastal ocean circulation model. In *Three-Dimensional Coastal Ocean Models*, pages 1–16. American Geophysical Union.
- M.J. Bowman, A.W. Visser, and W.R. Crawford, 1992: The Rose Spit Eddy in Dixon Entrance: Evidence for its existence and underlying dynamics. *ATMOSPHERE-OCEAN*, 30, 70–93.
- J.R. Buckley and W.P. Budgell, 1988: Meteorologically induced currents in the Beaufort sea. Unpublished manuscript. Copy in IOS library.

- D.C. Chapman, 1985: Numerical treatment of cross-shelf open boundaries in a barotropic coastal ocean model. *Journal of Physical Oceanography*, 15, 1060–1075.
- W.R. Crawford and P. Greisman, 1987: Investigation of permanent eddies in Dixon Entrance, British Columbia. *Continental Shelf Research*, 7, 851–870.
- W.R. Crawford, W.S. Huggett, and M.J. Woodward, 1988: Water transport through Hecate Strait, British Columbia. *ATMOSPHERE-OCEAN*, 26, 301–320.
- W.R. Crawford, W.S. Huggett, M.J. Woodward, and P.E. Daniel, 1985: Summer circulation of the waters in Queen Charlotte Sound. *ATMOSPHERE-OCEAN*, 23, 393–413.
- W.R. Crawford and R.E. Thomson, 1984: Diurnal period continental shelf waves along Vancouver Island: A comparison of observations and numerical models. *Journal of Physical Oceanography*, 14, 1629–1646.
- W.R. Crawford, A.V. Tyler, and R.E. Thomson, 1990: A possible eddy retention mechanism for ichthyoplankton in Hecate Strait. *Can. J. Fish. Aquat. Sci.*, 47, 1356–1363.
- P. B. Crean, 1967: Physical oceanography of Dixon Entrance. Bulletin 156, Fisheries Research Board of Canada.
- P.B. Crean, T.S. Murty, and J.A. Stronach, 1988: *Mathematical modelling of tides and estuarine circulation: the coastal seas of southern British Columbia and Washington State*. Springer-Verlag, 471 pp.
- A. M. Davies, 1987: Spectral models in continental shelf oceanography. In *Three-Dimensional Coastal Ocean Models*, pages 71–106. American Geophysical Union.
- A.M. Davies, 1985: On determining the profile of steady wind-induced currents. *Appl. Math. Modelling*, 9, 409–418.
- J.W. Deardorff, K. Ueyoshi, and Y-J. Han, 1984: Numerical study of terrain-induced mesoscale motions and hydrostatic form drag in a heated growing mixed layer. *Journal of Atmospheric Sciences*, 41, 1420–1441.
- D.P. Dempsey and R. Rotunno, 1988: Topographic generation of mesoscale vortices in mixed layer models. *Journal of Atmospheric Sciences*, 45, 2961–2978.
- A. J. Dodimead, 1980: A general review of the oceanography of the Queen Charlotte Sound - Hecate Strait - Dixon Entrance Region. Manuscript Report 1574, Canadian Fisheries and Aquatic Sciences.

- B. Engquist and A. Majda, 1977: Absorbing boundary conditions for the numerical simulation of waves. *Mathematics of Computation*, 31, 1–24.
- M.G.G. Foreman, 1987: An accuracy analysis of selected finite difference methods for shelf waves. *Continental Shelf Research*, 7, 773–803.
- M.G.G. Foreman and A.F. Bennett, 1988: On no-slip boundary conditions for the incompressible Navier-Stokes equations. *Dynamics of Atmospheres and Oceans*, 12, 47–70.
- M.G.G. Foreman, R.F. Henry, R.A. Walters, and V.A. Ballantyne, 1992: A finite element model for tides and resonance along the north coast of British Columbia. *Journal of Geophysical Research*, submitted.
- G.Z. Forristall, 1974: Three-dimensional structure of storm generated currents. *Journal of Geophysical Research*, 79, 2721–2729.
- H.J. Freeland, W.R. Crawford, and R.E. Thomson, 1984: Currents along the Pacific coast of Canada. *ATMOSPHERE-OCEAN*, 22, 151–172.
- C.J.R. Garrett and B. Toulany, 1982: Sea level variability due to meteorological forcing in the northeast Gulf of St. Lawrence. *Journal of Geophysical Research*, 87, 1968–1978.
- G.E. Halliwell, Jr. and J.S. Allen, 1984: Large scale sea level response to atmospheric forcing along the west coast of North America, summer 1973. *Journal of Physical Oceanography*, 14, 864–886.
- G.E. Halliwell, Jr. and J.S. Allen, 1987: Wave number-frequency domain properties of coastal sea level response to along-shore wind stress along the west coast of North America, summer 1980–1984. *Journal of Geophysical Research*, 92, 11761–11788.
- G.J. Haltiner and R.T. Williams, 1980: *Numerical Prediction and Dynamic Meteorology*. Wiley, 477 pp.
- C.G. Hannah, 1992a: Geostrophic control with wind forcing, Application to Bass Strait. *Journal of Physical Oceanography*, accepted.
- C.G. Hannah, 1992b: The Hecate Strait Model, Users guide and documentation. Unpublished manuscript. Contact W.R. Crawford at the Institute of Ocean Sciences, Sidney, BC.
- C.G. Hannah, P.H. LeBlond, W.R. Crawford, and W.P. Budgell, 1991: Wind-driven depth-averaged circulation in Queen Charlotte Sound and Hecate Strait. *ATMOSPHERE-OCEAN*, 29, 712–736.

- J.R. Hunter and C.J. Hearn, 1991: On obtaining the steady-state solutions of the linearized three-dimensional hydrodynamic equations. *Appl. Math. Modelling*, 15, 200–208.
- M. Israeli and S.A. Orszag, 1981: Approximation of radiation boundary conditions. *Journal of Computational Physics*, 41, 115–135.
- B.M. Jamart and J. Oser, 1986: Numerical boundary layers and spurious residual flows. *Journal of Geophysical Research*, 91(C9), 10621–10631.
- K.S. Ketchen, 1956: Factors influencing the survival of lemon sole (*Parophrys vetulus*) in Hecate Strait, British Columbia. *Fish. Res. Bd. Canada*, 13, 647–694.
- W.G. Large and S. Pond, 1981: Open ocean momentum flux measurements in moderate to strong winds. *Journal of Physical Oceanography*, 11, 324–336.
- E.A. Martinsen and H. Engedahl, 1987: Implementation and testing of a lateral boundary scheme as an open boundary condition in a barotropic ocean model. *Coastal Engineering*, 11, 603–627.
- C.R. Mechoso, A. Kitoh, S. Moorthi, and A. Arakawa, 1987: Numerical simulations of the atmospheric response to a sea surface temperature anomaly over the equatorial eastern Pacific ocean. *Monthly Weather Review*, 115, 2936–2956.
- F. Mesinger and A. Arakawa, 1976: Numerical methods used in atmospheric models. GARP Publication Series No. 17.
- J.F. Middleton, 1991: Coastal trapped wave scattering into and out of straits and bays. *Journal of Physical Oceanography*, 21, 681–694.
- J.F. Middleton and F. Viera, 1991: The forcing of low frequency motion within Bass Strait. *Journal of Physical Oceanography*, 21, 695–694.
- T.S. Murty, 1984: *Storm Surges: meteorological ocean tides*. Can. Bull. Fish. Aquat. Sci. 212. Ottawa, 879 pp.
- L.A. Mysak, 1980: Recent advances in shelf wave dynamics. *Reviews of Geophysics and Space Physics*, 18, 211–241.
- G.D. Newton, 1985: Computer programs for common map projections. Bulletin 1642, U.S. Geological Survey, 33 pp.
- I. Orlanski, 1976: A simple boundary condition for unbounded hyperbolic flows. *Journal of Computational Physics*, 21, 251–269.

- J. Pedlosky, 1979: *Geophysical Fluid Dynamics*. Springer-Verlag, 624 pp.
- L. J. Pratt, 1991: Geostrophic versus critical control in straits. *Journal of Physical Oceanography*, 21, 728–732.
- R.W. Preisendorfer, 1988: *Principal Component Analysis in Meteorology and Oceanography*. Elsevier, 425 pp.
- A.J. Robert, 1966: The integration of a low order spectral form of the primitive meteorological equations. *Journal of the Meteorological Society of Japan, Ser. 2*, 44, 237–245.
- C.A. Rocha and A.J. Clarke, 1987: Interaction of ocean tides through a narrow single strait and multiple narrow straits. *Journal of Physical Oceanography*, 17, 2203–2218.
- L.P. Roed and C. Cooper, 1987: A study of various open boundary conditions for wind-forced flow barotropic numerical ocean models. In J.C.J. Nihoul and B.N. Jamart, editors, *Three dimensional models of marine and estuarine dynamics*, pages 305–335. Elsevier.
- L.P. Roed and O.M. Smedstad, 1984: Open boundary conditions for forced waves in a rotating fluid. *SIAM J. Sci. Stat. Comput.*, 5, 414–426.
- R. Shapiro, 1970: Smoothing, filtering, and boundary effects. *Reviews of Geophysics and Space Physics*, 8, 359–387.
- T.J. Simons, 1980: *Circulation models of lakes and inland seas*. Can. Bull. Fish. Aquat. Sci. 203. Ottawa.
- S.D. Smith, 1988: Coefficients for sea surface wind stress, heat flux, and wind profiles as a function of wind speed and temperature. *Journal of Geophysical Research*, 93, 15467–15472.
- B. Tang, 1990: Fluctuating flow through straits of variable depth. *Journal of Physical Oceanography*, 20, 1077–1086.
- R.E. Thomson, 1981: *The Oceanography of the British Columbia coast*. Can. Spec. Publ. Fish. Aquat. Sci., Bull 56. Ottawa.
- R.E. Thomson, 1989: The Queen Charlotte Islands physical oceanography. In G.G.E Scudder and N. Gessler, editors, *The Outer Shores*, pages 27–63.
- R.E. Thomson and W.J. Emery, 1986: The Haida current. *Journal of Geophysical Research*, 91, 845–861.

- R.E. Thomson, P.H. LeBlond, and W.J. Emery, 1990: Analysis of deep-drogued satellite tracked drifter measurements in the Northeast Pacific. *ATMOSPHERE-OCEAN*, 28, 409–443.
- R.E. Thomson and R.E. Wilson, 1987: Coastal countercurrent and mesoscale eddy formation by tidal rectification near an oceanic cape. *Journal of Physical Oceanography*, 17, 2096–2126.
- B. Toulany and C.J.R. Garrett, 1984: Geostrophic control of fluctuating barotropic flow through straits. *Journal of Physical Oceanography*, 14, 649–655.
- A.V. Tyler and W.R. Crawford, 1991: Modeling of recruitment patterns in Pacific cod (*Gadus macrocephalus*) in Hecate Strait, British Columbia. *Can. J. Fish. Aquat. Sci.*, 48, 2240–2249.
- A.V. Tyler and S.J. Westrheim, 1986: Effects of transport, temperature, and stock size on recruitment of Pacific cod (*Gadus macrocephalus*). In *INPFC Bull.* 47, pages 175–190.
- C.J. Walters, C.G. Hannah, and K. Thomson, 1992: A microcomputer program for simulating effects of physical transport processes on fish larvae. *Fisheries Oceanography*, 1, 11–19.
- D-P Wang, 1982: Effects of continental slope on the mean shelf circulation. *Journal of Physical Oceanography*, 12, 1524–1526.
- West Coast Offshore Exploration and Environmental Assessment Panel. *Offshore Hydrocarbon Exploration: Report and Recommendations of the West Coast Offshore Exploration and Environmental Assessment Panel*, April 1986.
- D.G. Wright, 1987: Comments on Geostrophic control of fluctuating barotropic flow through straits. *Journal of Physical Oceanography*, 17, 2375–2377.
- T. Yao, H.J. Freeland, and L.A. Mysak, 1984: A comparison of low-frequency current observations off British Columbia with coastal-trapped wave theory. *Journal of Physical Oceanography*, 14, 22–34.

Appendix A

List of symbols

f	Coriolis parameter
\vec{F}_b	bottom friction
g	acceleration of gravity
\vec{G}	forcing and dissipation
H	mean depth
h	total depth, $h = H + \eta$
k	friction parameter
\hat{k}	unit vector in vertical direction
K	kinetic energy
L	length of the strait; length of domain
q	potential vorticity, $(f + \zeta)/h$
r	linear correlation coefficient
t	time
\vec{v}	horizontal velocity vector
(u,v)	components of the horizontal velocity vector
W	width of the strait; width of domain
x, y	horizontal coordinates
z	vertical coordinate
γ	time domain filter parameters
ζ	the relative vorticity, $\nabla \times \vec{v}$
η	departure from mean sea level, the sea level anomaly
λ	friction coefficient
Λ	eigenvalue
μ	Rayleigh friction
ν	eddy viscosity
ρ	density of sea water
σ	standard deviation
τ	wind stress
ϕ	latitude
Φ	gravitational potential
ω	frequency
Ω	rotation rate of the earth, $7.29 \times 10^{-5} \text{ s}^{-1}$
∇	horizontal gradient operator
Δs	grid size
Δt	time step size

Table A.12: List of symbols used.

Appendix B

Empirical Orthogonal Function Analysis

Empirical orthogonal function (EOF) analysis is a statistical technique that attempts to reduce large amounts of data to some understandable numbers and patterns. The technique looks for patterns in the fluctuations of the data – it is analysis of variance. EOF analysis is a statistical technique, therefore interpretation of the patterns in terms of physical processes is a separate issue. Preisendorfer (1988) provides an excellent introduction to this field.

Consider a set of M observation stations, which each contribute a time series of length N . Assume that the time series are synchronous. For the moment assume that the time series are scalars. The data is reduced to a set of M modes, where each mode has 3 components; an eigenvalue, an eigenvector, and a time series. The eigenvalue measures the amount of the variance of the original data that is contained in the mode and is a measure of the mode's importance. The eigenvector contains the spatial character of the mode: a spatial pattern which fluctuates in phase. The i th element of the eigenvector is a measure of the contribution of time series i to that mode. The time series of modal amplitude records the time history of the mode.

The original time series can be reconstructed from the eigenvectors and the time series. If most of the variance is contained in a few dominant modes, then the original data is well represented by a few modes. Sometimes the patterns can be shown to have physical significance and insight is gained.

The calculation is very simple. Consider M time series each of length N , organized as

a matrix $z'(t, x)$, $t = 1, \dots, N$; $x = 1, \dots, M$. The time series are the columns of z' . The variable t is an integer label for the elements of the time series. Time itself ranges from 0 to $(N - 1)\Delta t$, where Δt is the sampling interval. The variable x is an integer label for the time series. x is used to suggest that the time series are recorded at separate locations – this need not be so. The first step is to compute and remove the mean of each time series,

$$z(t, x) = z'(t, x) - \overline{z(x)} \quad (\text{B.50})$$

$$\overline{z(x)} = N^{-1} \sum_{t=1}^N z'(t, x) \quad (\text{B.51})$$

Deterministic trends can also be removed at this point. Linear trends were removed in the analysis reported in this thesis. The scatter matrix (in this case the covariance matrix) is defined as

$$S(x, x') = \sum_{k=1}^N z(t, x)z(t, x') \quad (\text{B.52})$$

The spatial patterns are the eigenvectors of the scatter matrix ($e_i(x)$, $i = 1, \dots, M$). The modes are ranked by their eigenvalues (Λ_i , $i = 1, \dots, M$). Each eigenvector has one element for each time series and the number of eigenvectors is equal to the number of time series.

The computation of the EOF modes can be done without removing the mean of each time series. However, then one is not analysing the variance (or fluctuations) in the data.

The time series of the amplitudes of the modes are computed as follows

$$a_i(t) = \sum_{x=1}^M z(t, x)e_i(x) \quad (\text{B.53})$$

The original data can be reconstructed as follows.

$$z(t, x) = \sum_{i=1}^M a_i(t)e_i(x) \quad (\text{B.54})$$

When most of the variance is contained in the first few modes, the sum can be truncated and the important character of the data is retained.

When the eigenvalues are distinct (no two equal) then the eigenvectors are orthonormal and complete. In the case of one or more sets of multiple eigenvalues one can construct a complete orthonormal basis set. The existence of a complete, orthogonal set of basis vectors guarantees that the calculation of the amplitudes makes sense and that the reconstruction of the data works (Preisendorfer, 1988).

For analysis where the time series have different units (e.g. velocity and pressure) it is necessary to remove the scaling problem caused by the choice of units. A standard choice is to divide each time series by its standard deviation. The scatter matrix is then formed from the normalized time series. The rest of the analysis proceeds in the same manner. In this case the eigenvalues and the time series are dimensionless.

Dividing the time series by their standard deviation is a useful way to prevent one or two energetic time series from dominating the analysis.

For two-dimensional vectors the obvious thing is to do the analysis using complex numbers. Unfortunately, information is lost in the complex formalism (Preisendorfer, 1988, p 182-186). In the real-valued case the eigenvectors can be multiplied by ± 1 . In the complex case the eigenvectors can be multiplied by any complex number with length 1 ($e^{i\theta}$). Thus the pattern can not only be reversed, it can be rotated by any angle – the orientation of the pattern in space is arbitrary. We are interested in the relation of the velocities to the topography, therefore orientation is important.

The preferred method is to treat each vector component as a separate time series (Preisendorfer, 1988; Crawford et al., 1990). The analysis is done in the same manner and then the vectors reconstructed at the end. The eigenvectors are only indeterminate by a factor of ± 1 . For ease of analysis and interpretation, the two components of the vector occupy adjacent locations in the data array (k vectors generate $2k$ time series).

For interpretation and plotting it is useful for the eigenvectors to have the same units as the original time series. To do this the eigenvector is scaled by the square root of the

eigenvalue. If the time series have been normalized then the value at each location must also be scaled by the standard deviation of the appropriate time series. For scalars the dimensional value of eigenvector i at location x is

$$b_i(x) = \Lambda_j^{1/2} \sigma_x e_j(x) \quad (\text{B.55})$$

If the time series were normalized by dividing by the standard deviation then σ_x is the standard deviation of time series x , otherwise $\sigma_x = 1$.

For the vector data the dimensional velocity (u_i, v_i) of mode i at location x is

$$u_i(x) = \lambda_j^{1/2} \sigma_x e_j(x) \quad (\text{B.56})$$

$$v_i(x) = \lambda_j^{1/2} \sigma_{x+1} e_j(x+1) \quad (\text{B.57})$$

This vector represents the root mean square velocity fluctuations (associated with mode i) about the mean current at location x . A large vector represents large fluctuations (in time) along the line of the vector. A valid pattern (eigenvector) is obtained by reversing *all* the vectors. This is the meaning of the ± 1 indeterminacy of the eigenvectors.

The dimensionless mode has a useful interpretation. If all the components of an eigenvector are of similar magnitude then all the time series are contributing to the mode. Components much smaller than the others indicate time series that are not contributing to the mode.

Time series $a_i(t)$ can reveal cyclic or episodic behaviour. The time series can be used to correlate with other time series of interest in a search for a physical interpretation of the mode. CTT90 use the close correlation of the time series of the mode 1 winds with the mode 1 currents to claim that the mode 1 current pattern is wind driven.

A dimensional vector can be recovered by scaling each element of the vector by the appropriate standard deviation.

Appendix C

Butterworth Filter: End Effects

From Fig. C.74 it is clear that about 5 days must be trimmed off the ends of the records to remove the end effect of the filter. The 5 day trimming was evident for both 15 minute and hourly time series.

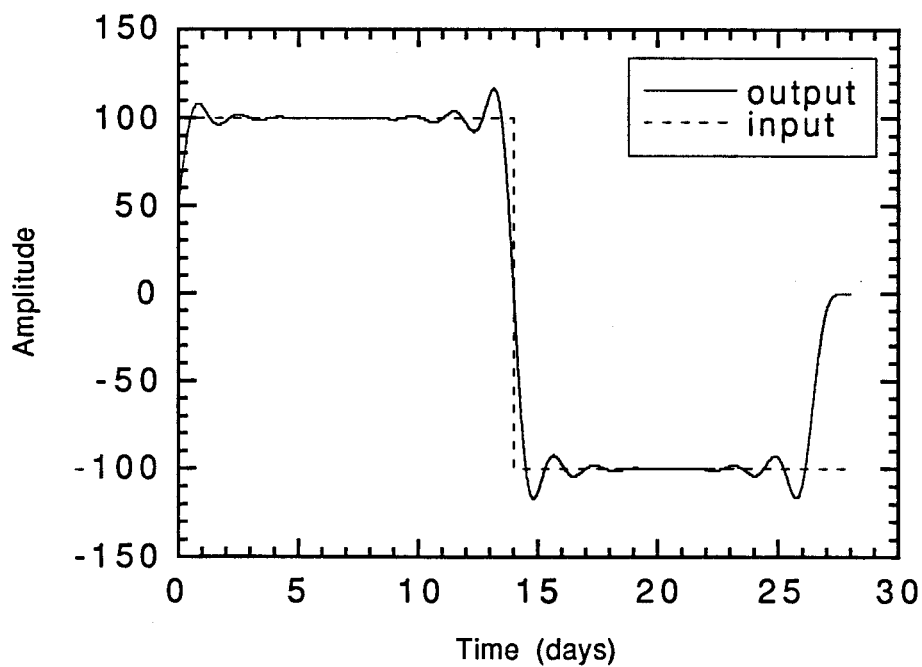


Figure C.74: The end effect of the Butterworth filter used to filter the time series data. The filter was an 8-th order filter with 1/2 power at 40 h. The time step was 15 m. The solid line is the filter output and the dashed line is the input.

Appendix D

Hecate Strait Model: Details

D.1 Numerical formulation

The scheme of Arakawa and Lamb (1981, hereafter AL81) is based on the idea that potential vorticity should be explicitly conserved in the finite difference form of the shallow water equations (5.20) and (5.19). AL81 guarantees potential vorticity conservation for the non-linear shallow water equations (SWE) over arbitrarily steep topography, as well as conservation of energy, mass and momentum.

Many finite difference schemes conserve mass, energy and momentum. Conservation of potential vorticity in the non-linear equations over steep topography is more difficult. Steep topography means large changes in depth over a few grid points, as is found near Cape St. James and Rose Spit.

The conservation of energy, mass, momentum, potential vorticity and potential enstrophy hold only in the absence of the corresponding sources and sinks. With $\vec{G} = 0$, (5.20) and (5.19) can be written in vector invariant form as

$$\frac{\partial \vec{v}}{\partial t} = -q\hat{k} \times \vec{v}^* - \nabla(K + \Phi) \quad (\text{D.58})$$

$$\frac{\partial h}{\partial t} = -\nabla \cdot \vec{v}^* \quad (\text{D.59})$$

where $\vec{v}^* = v \cdot h$ is the volume transport, $K = 1/2v^2$ the kinetic energy per unit mass and Φ is the gravitational potential energy. All the symbol definitions are collected together in Appendix A.

For our purposes $\Phi = g\eta$, where η is the sea level anomaly. However in the derivation of AL81 $\Phi = g(h + h_s)$, where h is the total fluid depth and h_s is the distance from an arbitrary reference surface to the bottom of the ocean. Recall that $h(x, y, t) = H(x, y) + \eta(x, y, t)$ where H is the mean depth. It turns out that $H + h_s$ is a constant and $\nabla\Phi = g\nabla\eta$. The reference level formulation is used to get a consistent form for energy conservation.

AL81 provide a spatial discretization for the unforced, inviscid shallow water equations. That is a scheme for differencing the right-hand-sides of (D.58) and (D.59). The time stepping method is left to the user. The regional model uses the leap-frog scheme, which is discussed later.

D.1.1 Arakawa and Lamb, 1981

I present here the details of the Arakawa and Lamb (1981) scheme for the spatial differencing of the inviscid, unforced shallow equations. The wind stress and friction terms are discussed at the end.

The spatial differencing is done on the C-grid, a staggered grid, where the variables u , v , η , and q are defined at different points (Fig. D.75). The properties of this grid and others are discussed in Mesinger and Arakawa (1976). The C-grid is the standard grid used in numerical models of the continental shelf.

Let the grid resolution be d . The grid is defined at the q points (D.75), that is the grid indices take integer values at the q point $(q_{i,j})$. Following this scheme the other variables are $u_{i,j+1/2}$, $v_{i+1/2,j}$ and $h_{i+1/2,j+1/2}$.

The continuity equation (D.59), defined at the h points, is written as:

$$\frac{\partial}{\partial t} h_{i+1/2,j+1/2} + (\nabla \cdot \vec{v}^*)_{i+1/2,j+1/2} = 0 \quad (\text{D.60})$$

where the finite difference form of the transport divergence is

$$(\nabla \cdot \vec{v}^*)_{i+1/2,j+1/2} = \frac{1}{d} [u_{i+1,j+1/2}^* - u_{i,j+1/2}^* + v_{i+1/2,j+1}^* - v_{i+1/2,j}^*] \quad (\text{D.61})$$

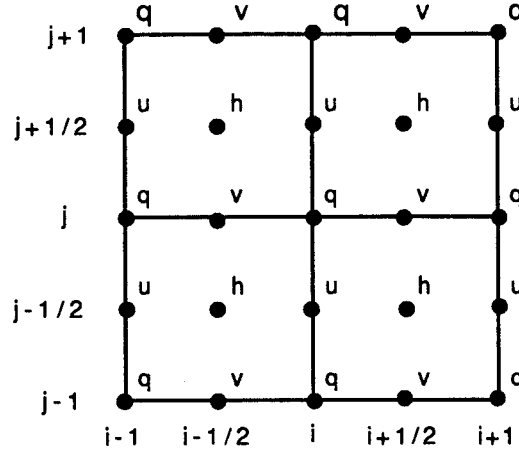


Figure D.75: The C-grid.

The volume transports, defined at the u and v points, are

$$u_{i,j+1/2}^* = [h^u]_{i,j+1/2} \quad (\text{D.62})$$

$$v_{i+1/2,j}^* = [h^v]_{i+1/2,j} \quad (\text{D.63})$$

and the corresponding depths are defined in terms of the depths given at the h points:

$$h_{i,j+1/2}^u = (h_{i-1/2,j+1/2} + h_{i+1/2,j+1/2})/2 \quad (\text{D.64})$$

$$h_{i+1/2,j}^v = (h_{i+1/2,j+1/2} + h_{i+1/2,j-1/2})/2 \quad (\text{D.65})$$

The differencing of the momentum equations (D.58) was done in the most general form possible by writing all the spatial derivatives in terms of the primitive variables and arbitrary weights. The weights are determined by applying the constraints (conservation of mass, energy, potential vorticity, and potential enstrophy). In the end the weights at a

given grid point are linear combinations of the potential vorticity at neighbouring points.

The scheme is second order accurate in space.

The momentum equations are defined at the appropriate velocity points

$$\begin{aligned}
0 = & \frac{\partial}{\partial t} u_{i,j+1/2} - \alpha_{i,j+1/2} v_{i+1/2,j+1}^* \\
& - \beta_{i,j+1/2} v_{i-1/2,j+1}^* - \gamma_{i,j+1/2} v_{i-1/2,j}^* - \delta_{i,j+1/2} v_{i+1/2,j}^* \\
& + \epsilon_{i+1/2,j+1/2} u_{i+1,j+1/2}^* - \epsilon_{i-1/2,j+1/2} u_{i-1,j+1/2}^* \\
& + d^{-1}[(K + \Phi)_{i+1/2,j+1/2} - (K + \Phi)_{i-1/2,j+1/2}]
\end{aligned} \tag{D.66}$$

$$\begin{aligned}
0 = & \frac{\partial}{\partial t} v_{i+1/2,j} + \gamma_{i+1,j+1/2} u_{i+1,j+1/2}^* \\
& + \delta_{i,j+1/2} u_{i,j+1/2}^* + \alpha_{i,j-1/2} u_{i,j-1/2}^* - \beta_{i+1,j-1/2} u_{i+1/2,j-1/2}^* \\
& + \phi_{i+1/2,j+1/2} v_{i+1/2,j+1}^* - \phi_{i-1/2,j-1/2} v_{i-1/2,j-1}^* \\
& + d^{-1}[(K + \Phi)_{i+1/2,j+1/2} - (K + \Phi)_{i+1/2,j-1/2}]
\end{aligned} \tag{D.67}$$

The momentum weighting coefficients are:

$$\epsilon_{i+1/2,j+1/2} = \frac{1}{24} [q_{i+1,j+1} + q_{i,j+1} - q_{i,j} - q_{i+1,j}] \tag{D.68}$$

$$\phi_{i+1/2,j+1/2} = \frac{1}{24} [-q_{i+1,j+1} + q_{i,j+1} + q_{i,j} - q_{i+1,j}] \tag{D.69}$$

$$\alpha_{i,j+1/2} = \frac{1}{24} [2q_{i+1,j+1} + q_{i,j+1} + 2q_{i,j} + q_{i+1,j}] \tag{D.70}$$

$$\beta_{i,j+1/2} = \frac{1}{24} [q_{i,j+1} + 2q_{i-1,j+1} + q_{i-1,j} + 2q_{i,j}] \tag{D.71}$$

$$\gamma_{i,j+1/2} = \frac{1}{24} [2q_{i,j+1} + q_{i-1,j+1} + 2q_{i-1,j} + q_{i,j}] \tag{D.72}$$

$$\delta_{i,j+1/2} = \frac{1}{24} [q_{i+1,j+1} + 2q_{i,j+1} + q_{i,j} + 2q_{i+1,j}] \tag{D.73}$$

Notice that $\beta_{i,j+1/2} = \gamma_{i-1,j+1/2}$ and $\gamma_{i,j+1/2} = \alpha_{i-1,j+1/2}$ so that there are only 4 sets of momentum weighting coefficients to compute.

The kinetic energy, defined at the h points, is:

$$K_{i+1/2,j+1/2} = \frac{1}{2}(u_{i,j+1/2}^2 + u_{i+1,j+1/2}^2 + v_{i+1/2,j}^2 + v_{i+1/2,j+1}^2) \quad (\text{D.74})$$

and the gravitational potential Φ is

$$\Phi_{i+1/2,j+1/2} = g\eta_{i+1/2,j+1/2} \quad (\text{D.75})$$

The potential vorticity q and relative vorticity ζ are defined as

$$q_{i,j} = \frac{(f + \zeta)_{i,j}}{h_{i,j}^q} \quad (\text{D.76})$$

$$\zeta_{i,j} = d^{-1}[u_{i,j-1/2} - u_{i,j+1/2} + v_{i+1/2,j} - v_{i-1/2,j}] \quad (\text{D.77})$$

The depth at the q point, $h_{i,j}^q$ is simply the average of the depths at the neighbouring depth points

$$h_{i,j}^q = \frac{1}{4}(h_{i+1/2,j+1/2} + h_{i-1/2,j+1/2} + h_{i-1/2,j-1/2} + h_{i+1/2,j-1/2}) \quad (\text{D.78})$$

As defined the scheme does not contain forcing or friction. They were implemented as follows. The components of the wind stress vector were placed on the same staggered grid as the velocities. Since there was no differencing involved they were simply included on the right-hand-sides of on the RHS of (D.66) and (D.67). All the friction coefficients (bottom friction, Rayleigh friction and eddy viscosity) were defined at the depth points and appropriate averages taken to get the values at the u and v points.

Atmospheric pressure gradients were not used in this thesis. Nevertheless the model does contain provision for atmospheric pressure gradients. They are defined at the h points and included with Φ .

The time stepping was done by the standard leapfrog scheme. This means that all the momentum weighting coefficients, pressure gradients, and wind forcing were evaluated at the n time level. The friction terms were dealt with implicitly because the leapfrog scheme is unstable with respect to friction terms. This suffices to define the numerical scheme to advance the velocities from the $n - 1$ time level to the $n + 1$ time level.

D.1.2 Discussion

The AL81 scheme has not been heavily used in either the oceanographic or atmospheric communities. It has been used in atmospheric studies of flow over topography (Dempsey, 1988; Deardorff, 1984) and a version with fourth-order accuracy has been used in the UCLA general circulation model (Mechoso, 1987). I know of no examples of the use of the AL81 scheme in a regional oceanographic model. The most recent application was as the ground truth in a comparison of approximations to the shallow water equations (Allen et al., 1990).

The perceived drawbacks are the complexity of the differencing scheme and the heavier computational load. I admit that the scheme looks complicated, however it is relatively easy to turn into computer code since all the variables are explicitly specified. The heavier computational load may or may not be a factor. The leapfrog version of the model is slower than a standard version of the shallow water equations. However the computer code optimizes very well and respectable results are obtained on the newer workstations. A version written by W.P. Budgell using a semi-implicit scheme for the time stepping involves no time penalty at all.

The most serious drawback is related to the way AL81 achieves its conservation properties. As described by Foreman (1987) the scheme has a large footprint. When computing the derivatives at $u_{i,j+1/2}$ (D.66), information is drawn from an area 3 grid points wide (i index) and 2 grid points high (j index). Consider the sequence: 1) the original depths are averaged to obtain h^q , 2) h^q is used to compute q , 3) q is used to compute the weighting coefficients, 4) the weighting coefficients are used to compute derivatives. The conservation of potential vorticity in the presence of steep topography is achieved by averaging the depths.

Now consider what happens when land is introduced. The presence of an island

directly influences the computation up to 3 grid points away. What is q on land? This was dealt with as follows. Define a minimum depth h_{min} . At a land point $q = f/h_{min}$. A value $h_{min} = 5$ m was used. Experiments by W.P. Budgell and by myself have shown that the results are not sensitive to the value of h_{min} in the range 1 to 20 m. In most atmospheric problems the topography does not break the surface and the problem does not arise.

An annoying feature arises when computing diagnostic vorticity balances. Precise balances of the form

$$\frac{\partial q}{\partial t} + \mathbf{v} \cdot \nabla q = \frac{1}{h} \nabla \times \vec{G} \quad (\text{D.79})$$

can be obtained. However, dividing the left-hand-side into the classical form represented by (5.24) is much less precise. The model thinks of q as a single entity not as separate components.

Care is required when linearizing the momentum equations. In the vector invariant form (D.58) the non-linear term $(\vec{v} \cdot \nabla \vec{v})$ contributes in two places: the kinetic energy K and through the relative vorticity ζ which appears in q . This is not a big deal it just requires some care.

D.1.3 Leap-frog Scheme

Arakawa and Lamb (1981) specify the differencing of the spatial derivatives but not the time stepping method. The model discussed in this thesis used the leap-frog scheme. As a simple example consider the equation

$$\frac{\partial u}{\partial t} = F(u, t); \quad u = u(t) \quad (\text{D.80})$$

Think of moving everything except the time derivative to the right hand of (D.58). Using the leap-frog scheme (D.80) is differenced as

$$u^{n+1} - u^{n-1} = 2\Delta t F^n \quad (\text{D.81})$$

where n is the time index, $t = n\Delta t$. F^n is the known value of $F(u, t)$ at time step n . This provides enough information to advance u from the $n - 1$ time level to the $n + 1$ time level. The leapfrog scheme is second order accurate in time (Haltiner and Williams, 1980).

The leap frog scheme has a small problem. The underlying differential equation (5.20) is first order in time. The difference equation is essentially second order in time (it uses 3 time levels). This introduces a second solution called the computational (or parasitic) mode. There are many ways to deal with the computational mode. The method chosen here is the Robert (1966) filter.

D.1.4 The Robert Filter

The Robert (1966) filter is a very weak three-point time domain filter. It is applied to all three prognostic variables u , v , η at every grid point and every time step. The filter looks like

$$\overline{u(n)} = u(n) + \gamma[u(n+1) - 2u(n) + \overline{u(n-1)}] \quad (\text{D.82})$$

where n is the time index and the over-bar represents a filtered value. The properties of the filter are discussed in the context of the leapfrog scheme by Asselin (1972). Minor complications are introduced because the filter is recursive – old filtered values are used to compute new values. Asselin showed that for small filter parameter, $\gamma < 1/3$, the amplitude response of the filter is very close to that of the standard centered filter

$$\overline{u(n)} = u(n) + \gamma[u(n+1) - 2u(n) + u(n-1)] \quad (\text{D.83})$$

Table D.13 shows the amplification factor for several different frequencies with a filter parameter of $\gamma = 0.01$ and a time step of $\Delta t = 10$ s. The amplification factor is very close to one, and the damping is very small, for time scales longer than a day.

period T	$\Delta t/T$	amplification	
		per Δt	per day
20 s	0.5	0.995	1.5×10^{-19}
60 s	0.17	0.9993	3.0×10^{-3}
1 hr	2.8×10^{-3}	–	$1 - 1.6 \times 10^{-3}$
1 day	1.2×10^{-4}	–	$1 - 3 \times 10^{-6}$
7 day	1.6×10^{-5}	–	$1 - 6 \times 10^{-8}$
28 days	4.1×10^{-6}	–	$1 - 4 \times 10^{-10}$

Table D.13: Amplitude response of the time domain filter for sinusoidal input. For periods of an hour or more the amplification factor is very close to 1 and is written in the form $1 - \epsilon$, where ϵ is a small number. $\Delta t = 10$ s and $\gamma = 0.01$.

D.2 Model Bathymetry

Accurate representation of the bathymetry, or ocean topography, is important because topographic steering is an important part of the dynamics. The representation of the bathymetry is limited by the grid resolution. The choice of grid resolution requires balancing two competing considerations; the need for accurate bathymetry, and the need to limit the computational load. The computational load is linearly proportional to the number of grid points N and the number of time steps. Doubling the resolution increases the computational load by 8. There are 4 times as many grid points and the time step is halved. The bathymetry, grid size, and time step are related through the CFL criteria.

How large does the model domain have to be? At the very least the model domain must extend from northern Vancouver Island to the northern side of Dixon Entrance (Fig. 1.1), and from the mainland coast to an offshore boundary west coast of the Queen Charlottes. The question of the size of the model domain becomes a question of location of the open boundaries (one offshore boundary and two cross-shore boundaries).

My philosophy on open boundaries is simple – move them as far away as possible. The grid has grown with the increase in computer power. My initial design decision was that I was willing to spend roughly half the computational effort on the open Pacific

west of the Queen Charlottes. In the end roughly 3/4 of the grid is outside the region of interest defined by Cape Scott to Dixon Entrance and the mainland to the west coast of the Queen Charlottes.

The grid resolution chosen was 5 km. This represents a compromise between 10 km (not enough resolution) and 3 km (too much computation). The standard model domain is 90 x 199 grid points. The whole domain has been rotated by 30 degrees from a north-south orientation to conform to the general trend of the coastline (Fig. 5.32). This reduces the number of wasted land points in the NE corner and makes the shelf-break roughly perpendicular to the cross-shelf open boundaries. The latter feature reduces the amount of energy incident on the open boundaries at oblique angles: recall that most of the flow is constrained to flow parallel to the isobaths.

After the best possible depths (Section D.2.1) were obtained the whole domain was filtered to remove the two-grid-space variations (often called $2\Delta x$ noise) from the bathymetry (Shapiro, 1970). The rationale being, if you cannot resolve it, remove it! As mentioned earlier, any non-linear, finite difference model tends to accumulate energy at the smallest resolvable scale $2\Delta x$. The presence of $2\Delta x$ noise in the bathymetry enhances this cascade of energy to small scales. The AL81 scheme restricts the spurious energy cascade but I did not think I was doing the model any favours by including unresolved bathymetric features.

I made one exception to this rule. Learmonth Bank which dominates the mouth of Dixon Entrance is a ridge 1 grid cell wide and 4 long and was removed in the filtering. In this case I put my faith in Arakawa and Lamb and the bank was put back in by hand. The effect of Learmonth Bank on the model circulation in Dixon Entrance is discussed in the next chapter. A feature which was not put back was the long narrow seamount just to the northwest of Cape St. James.

Smoothing the bathymetry is still an open question. On one hand the AL81 scheme is

designed to deal with the problem of unresolved topography and the analysis of Foreman (1987) showed that the scheme actually smooths the topography. On the other hand I do not think that the model results would benefit from a lot of small scale bathymetric variations.

As a final step, along-shore bathymetric variations were removed within 40 grid points of the cross-shore open boundaries to suppress the generation of topographic waves near the cross-shore boundaries and accommodate the open boundary conditions.

As part of the open boundary condition tests, larger domains are used. The depths in the extended regions were filled by extending the boundary values of the standard domain.

D.2.1 Creating the Bathymetry

The sources for the bathymetry data and the procedure used to massage the different sources onto a common grid is discussed.

The sources for the bathymetry were

- Canadian coastal waters – Energy, Mines and Resources Canada (EMR) topographic data base (nominally 1 km resolution) and Canadian Hydrographic Service charts.
- American coastal waters – National Oceanic Atmospheric Administration (NOAA) charts.
- Offshore waters – taken from the ETOPO5 data base which was compiled by the National Geophysical Data Center in Boulder Colorado and is available on the central computer at the Institute of Ocean Sciences, Sidney, BC. The resolution is quite good; the 1/12 degree resolution is roughly 5 km x 10 km at 52° N. However, the depths in the coastal waters are inaccurate.

- Coastline – taken from the high resolution coastline contained in the World Data Base 2. The data base was compiled by the CIA and is available on the central computer at the Institute of Ocean Sciences, Sidney, BC.

The latitude and longitude coordinates were converted to cartesian coordinates using a Universal Transverse Mercator (UTM) projection with the central meridian at 131° W. The UTM projection has a maximum scale error of 1/2500 within $\pm 3^\circ$ of the central meridian. This covers most of the area of interest. The conversion algorithms were taken from Newton (1985).

There are three coordinate systems to consider in what follows: 1) latitude, longitude; 2) UTM; and 3) model coordinates. Recall that the model domain was rotated by 30° from north-south.

Step 1: Choose a model grid.

Choose the grid resolution (5 km) and the model domain size (90x199). Choose the central location about which to rotate the model domain (52.5° N, 131° W). Choose the model coordinate which corresponds to the central point (96, 56). The last was chosen after much experiment.

Step 2: Generate a coastline.

Map the grid points defined in Step 1 to latitude, longitude coordinates. This requires two coordinate transformations. Plot the high resolution coastline and the grid points on the same chart. Choose the digitized coast line by hand. Many of the large fjords and inlets were included even though they do not affect the circulation.

Step 3: Get the EMR and ETOPO5 data onto the same grid.

The two digitized bathymetry data bases were mapped onto a 1 km x 1 km UTM

grid using the nearest neighbour technique. The ETOPO5 values were only used in the deep water and American open coastal waters. It was not used where there was valid EMR data.

Step 4: Reduce the 1 km data to 5 km.

The dense part of the array was reduced to 5 km resolution by averaging over the 9 nearest neighbours. Only valid water points were used in the average. Locations where the coast-line data conflicted with the depth data were flagged and dealt with by hand. Some mythical islands in the EMR data were discovered this way.

The sparse part of the array was mapped on to the grid as follows: if one of the 4 nearest 1 km grid points has a value use it. Otherwise flag it and fill by hand.

Step 5: Alaska.

The ETOPO5 data is inaccurate in coastal waters and the EMR data goes only to the Canada/US border. The Alaskan coastal waters were digitized in a similar manner to the coastline. The grid points were plotted to chart scale and the NOAA charts digitized by hand and eye.

Step 6: Final check.

The grid was plotted to chart scale and the depths compared directly with recent Canadian Hydrographic Service charts. Discrepancies were noted and changes made to the model bathymetry.

D.3 Drifter Algorithm

Computing simulated drifter trajectories on the C-grid presents a problem in addition to the usual problems of interpolation in space and time. The model's velocity components are not defined at the same points on the grid (Fig. D.75). The velocities must be

interpolated just to create a valid field. The algorithm used to define the velocity field (Bennett and Clites, 1987) has the following properties:

- The velocities are interpolated onto the q points (Fig. D.75).
- Only wet points are used in the interpolation.
- Bilinear interpolation is used to compute the velocity field between q points.

This approach ensures that that drifters do not get trapped in corners or slow down as they approach the coast (caused by using zero velocities for the land points in the interpolation). The algorithm has an interesting quirk; drifters can travel up to one grid-space onshore from an apparent land boundary. This is not serious except on those occasions when a drifter crosses a narrow (one grid-space wide) island or peninsula. The fix consists of checking the location of every drifter at every time step to see if it is on land. Grounded drifters are either moved back into the ocean or removed. An elegant fix does not seem to exist (David L. Schwab, GLERL, pers. comm., 1990).

The drifters move with the depth-averaged flow. No windage (impact of the wind directly on the drifter) has been added because the objective is to study the movement of the water not to track the wind.

D.3.1 Trajectory Computations

During the model runs the drifter trajectories were computed using the full Bennett and Clites (1987) algorithm, with the checks to see if drifters had grounded. A scheme using a fourth-order Runge-Kutta algorithm has also been used, but it used too much computation time.

Often it was only in hindsight that proper drifter placement was evident. In order to allow rapid evaluation of drifter trajectories the following procedure was developed. For

each experiment the model domain was seeded with a reasonable number of drifters in different areas and these drifters were tracked during the model run. During the model run, the current data at all grid points was saved at regular intervals (usually once a model day). After the model run was completed, a twin experiment was conducted with the new drifter trajectories being computed from the saved current records. If the twin trajectories were very close then additional drifter trajectories were computed using only the saved currents. The time integration of the drifter paths was done using a fourth order Runge-Kutta algorithm.

The technique worked best when the winds were from one direction. Daily currents and even twice-daily currents were found to be insufficient to resolve the changes in the currents due to the rapid changes in wind direction seen in the summer simulations. For this thesis the sampled-current-technique was used to find out what the drifters were doing. The proper simulation was then repeated with drifter locations and start times determined from the experiments using the the sampled-current-technique. This worked very well. The only drifters shown in this thesis that were computed using the sampled-current technique are the drifters in Fig. 8.71, which illustrate the flow in Queen Charlotte Sound.

D.4 Lateral Boundary Conditions

D.4.1 Side Walls and Boundary Layers

The model reported on in this thesis uses free slip boundary conditions at side walls. Figure D.76 shows a land/ocean boundary on the C-grid. Free slip boundaries are a natural on the C-grid. Only the normal velocity and the vorticity (q) appear on the land/sea boundary. A free slip boundary is implemented by setting the normal velocity equal to zero at the boundary and setting the relative vorticity ζ equal to zero the

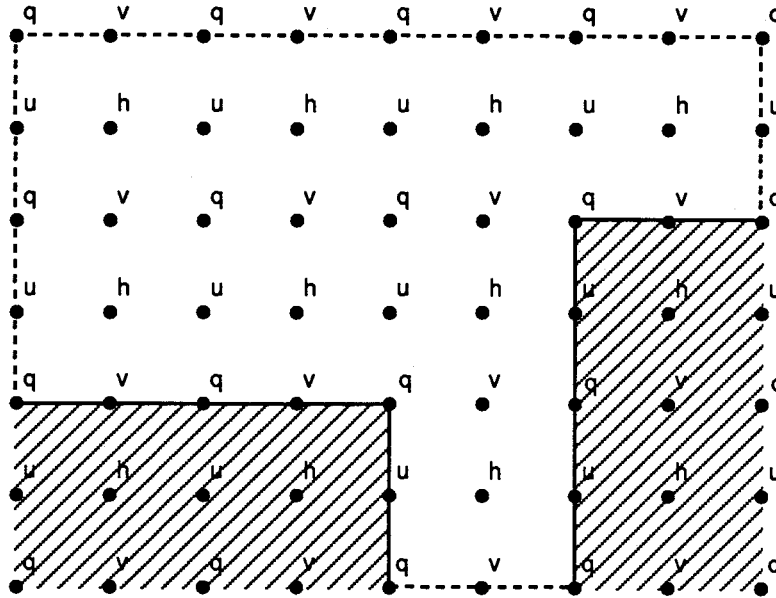


Figure D.76: Boundaries in the C-grid.

boundary. Setting $\zeta = 0$ means no shear at the boundary. Neither the tangential velocity nor the sea level need to be specified at the land/ocean boundary.

The proper fluid dynamics boundary condition for the interface between a fluid and a solid is *no flow through the interface* and *no slip along the interface*. In the Hecate Strait Model the *no slip* part was ignored. The no-slip boundary condition is most applicable when either the eddy viscosity is an important part of the model dynamics or the model resolves both the spatial scales and the important physics in the boundary layer. Not resolving the natural width of the boundary layer means that the viscous region gets too

wide. The Hecate Strait Model ignores the coastal boundary layer and uses the free-slip condition at the side walls.

Even no-flow through the boundary can cause problems. In 3-D models the question arises as to whether the no-flow condition should be imposed at each vertical grid point or only in the depth-average sense. The two choices give different solutions. Imposing no-flow through the boundary at each grid point creates a strong coastal jet (Jamart and Ozer, 1986). Nothing is ever simple.

D.4.2 Open Boundary Conditions

An open boundary is the arbitrary line drawn in the ocean that separates the known (the model domain) from the unknown (the rest of the ocean). For this thesis I assumed that the local winds provide the only important forcing mechanism. External influences such as tides and shelf waves were ignored. Therefore the only purpose of the open boundary conditions was to let disturbances out.

The use of open boundary conditions in regional models is one of the black arts of numerical modelling. In general all open boundary conditions are bad. The true art lies in picking the one that is least bad for the given application.

The number of open boundary conditions that have been developed is enormous. Most boundary conditions can be grouped into the following categories:

- no flow normal to the open boundary
- clamping the sea level
- zero gradient condition
- sponge layers
- radiation conditions

- relaxation schemes

‘No flow normal to the open boundary’ means what it says. Turn the ocean into a lake by putting a wall around the domain, which reflects waves back into the domain.

Clamping the sea level means that the sea level fluctuation (η) is set to zero everywhere along the open boundary: water can flow through, but sea level variations are reflected.

The zero gradient condition means that there is no gradient in sea level across the open boundary. This simple condition is effective in many situations (Roed and Cooper, 1987; hereafter RC87).

Sponge layers are regions of high energy dissipation that soak up energy propagating towards the boundary. They can be used to reduce the reflection from closed or clamped boundaries or combined with radiation conditions (Isreali and Orzag, 1981).

Radiation conditions are the most commonly used family of boundary condition in regional modelling. They assume that the dominant process near the open boundary is wave propagation and attempt to make the boundary transparent to waves propagating out of the domain. The success of the radiation condition at the boundary depends on the ability to accurately compute the dispersion relation of the outgoing waves. This is easily done in one dimension with systems that only have one family of waves (one dispersion relation). The presence of waves with different dispersion relations creates problems, as do waves hitting the boundary at oblique incidence.

In relaxation schemes the solution in the interior of the domain is forced to a specified (exterior) solution at the open boundary in a relaxation zone. If the exterior solution is ‘no motion’ then the relaxation zone becomes a sponge layer. The trick with relaxation schemes is choosing the exterior solution (Martinsen and Engedahl 1987).

Hybrid conditions can be formed by combinations of the above.

Intercomparisons of open boundary conditions in depth-averaged models were carried

out by RC87 and by Chapman (1985). The comparisons were done with an ideal shelf, a clamped offshore boundary and the OBC to be tested used on the cross-shore open boundaries. RC87 concluded that radiation conditions can work well when the forcing near the boundary is weak, and sponges can work well when the forcing near the boundary is weak or variable. Both types have difficulties when the forcing near the boundary is strong and persistent.

Sponge layers do not work well with strong forcing near the boundary because the sponge inhibits mass flow through the boundary. If the wind forcing near the boundary is strong or persistent then the low mass flux corrupts the solution in the interior.

The problem with the radiation condition is more subtle. In general radiation conditions are created by extracting free wave solutions from the equations of motion and assuming that all disturbances satisfy this condition. Most radiation conditions are based on a variant of the one dimensional wave equation

$$\phi_t + c\phi_x = 0$$

where c is the wave speed. This can work quite well. Strong forcing near the open boundary creates problems when the forced solution is incompatible with the radiation condition. Small scale waves are generated which can contaminate the solution in the interior (Enquist and Madja, 1977, see Remark #2). Satisfying the compatibility condition requires that the wind forcing be tapered to zero near the boundary which can cause a new set of difficulties. Strong topographic variations near the open boundary can cause similar problems.

Roed and Smedstad (1984) attempted to get around the compatibility problem by separating the solution near the boundary into a forced solution and a free wave solution and dealing with them separately. The results have been mixed (RC87).

The flow relaxation scheme proposed by Martinsen and Engedahl (ME87) approaches

the problem from a different perspective. They assume that the dominant process near the open boundary is wind forcing. Thus the important quantities are the along-shore and cross-shore mass fluxes. They chose the exterior solution to be the model equations with the along-shore gradients removed, there are no abrupt changes in mass fluxes near the open boundary and waves propagating in the along-shore direction are damped. In the absence of wind the boundary condition reduces to a sponge layer; the exterior solution becomes a no-motion solution ($u = 0, v = 0, \eta = 0$). As one might expect, because the Ekman flux is handled correctly this open boundary condition is most successful when there is strong wind forcing. This method is used here (Chapter 5).

D.4.3 Cross-shelf Boundary

Several radiation conditions including Orlanski (1976) and Roed and Smedstad (1984) were tested on the cross-shelf boundary. The results were consistently plagued with accumulation of energy trapped along the northern boundary (downstream with respect to propagation of Kelvin waves). The results became unstable with time-varying winds.

The flow relaxation scheme of Martinsen and Engedahl (ME87) has had very few problems. Tests and anecdotes are reported in Appendix F.

D.4.4 Off-shore Boundary

The offshore boundary condition chosen was a clamped sea level condition. The reasons are discussed in Chapter 5. Because of concerns about reflection off this boundary a sponge layer was created along the off-shore boundary. The sponge layer uses high eddy viscosity to dampen the short wavelengths and depth-independent linear friction to dampen the long wavelengths. The sponge region was 30 grid points wide and the viscosity and friction were ramped up with a parabolic profile. Tests showed no difference

in the solutions with and without the sponge layer. The sponge was not used in any of the experiments reported in this thesis.

Appendix E

Tests in Rectangular Domains

This appendix reports on tests of the cross-shore open boundary conditions in simple tests cases. Results of the tests of the open boundary conditions in the full Hecate Strait Model are reported in Appendix F.

The cross-shore open boundary condition used was the flow relaxation scheme of Martinsen and Engedahl (1987). This scheme was discussed in Chapter 5 and Appendix D. The offshore boundary condition was the clamped sea level condition: $\eta = 0$ along the off-shore boundary. The sponge layer was not used.

The test reported here are tests in an idealized domain: a rectangular box. The first two tests are done with a flat-bottomed box and replicate the tests of Roed and Cooper (1987), hereafter RC87. The final set of tests were done using the same box but with a sloping shelf and other parameters characteristic of the regional model. The sloping shelf provides a test of the model and the open boundary conditions in an environment similar to the Hecate Strait Model. The test case is used to illustrate frictional adjustment on a sloping shelf and to test the model since the frictional adjustment solution is known.

E.1 Flat Bottom

The model domain was a section of coastline in the semi-infinite ocean $x < 0$ (Fig E.77). For this appendix the x-axis, the index i , and velocity u denote cross-shelf quantities, while the y-axis, the index j , and velocity v denote along-shore quantities. The model parameters for the flat-bottom tests are listed in Table E.14

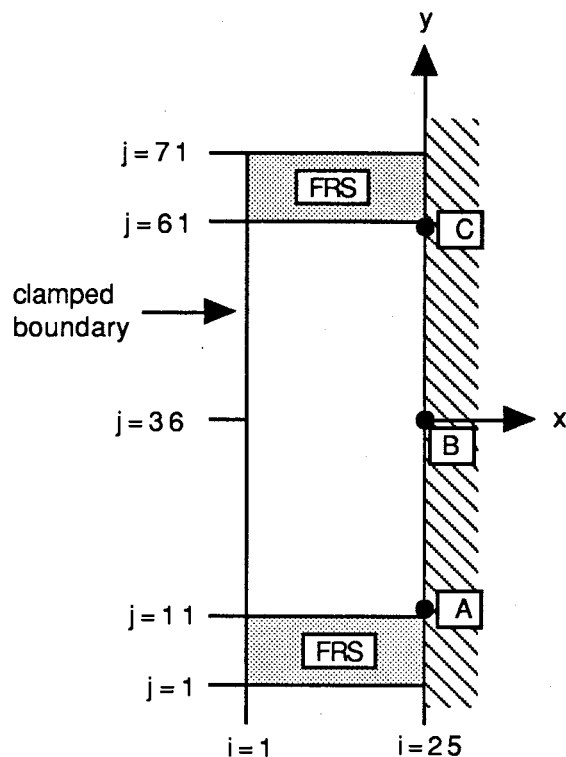


Figure E.77: Model domain for the open boundary condition tests. The flow relaxation zones are marked by cross hatching.

L	domain length	1000 km
W	domain width	500 km
Δs	grid size	20 km
f	Coriolis parameter	$1.2 \times 10^{-4} \text{ s}^{-1}$
k	friction parameter	$2.4 \times 10^{-3} \text{ s}^{-1}$
μ	Rayleigh friction	0
Δt	time increment	300 s
H	equilibrium depth	50 m
	relaxation zone width	200 km
		10 grid cells

Table E.14: Parameters for open boundary condition tests with a flat bottomed ocean

E.1.1 Uniform Along-Shore Wind

The first test uses a uniform along-shore wind to test the open boundary conditions with persistent forcing at the boundaries. The wind stress is a positive along-shore wind stress which decays off-shore.

$$\begin{aligned}\tau^x &= 0 \\ \tau^y &= \tau_0 \exp(ax)\end{aligned}$$

where the maximum wind stress $\tau_0 = 0.1$ Pa, the decay scale $a^{-1} = 200$ km, and $x < 0$ inside the model domain. The wind stress at the off-shore boundary is 8% of the maximum. The fluid starts at rest and the wind starts impulsively at $t = 0$.

The linearized equations are used to correspond with Roed and Cooper (1987), hereafter RC87. Interestingly there is no complete solution to this problem (see RC87 for details). At the coast, the along-shore velocity

$$v(0, y, t) = v_\infty(1 - e^{-kt/H})$$

and the steady state velocity

$$v(x, y) = v_\infty e^{ax}$$

where $v_\infty = \tau_0/(\rho H k) = 4.06$ cm/s and e-folding time scale $(k/H)^{-1} = 5.8$ hr. The Rayleigh friction was set to zero to correspond with RC87. In Chapter 4 the along-shore velocity was denoted u , here it is v to correspond with the choice of co-ordinate axes.

The model handles this case very well. The time series at sites A, B, C are identical and correspond to the analytical solution (Fig. E.78). Figure E.79a,b show the steady state sea levels and currents over the whole domain. There are no surprises; the sea level contours and the velocity vectors are parallel to the coast.

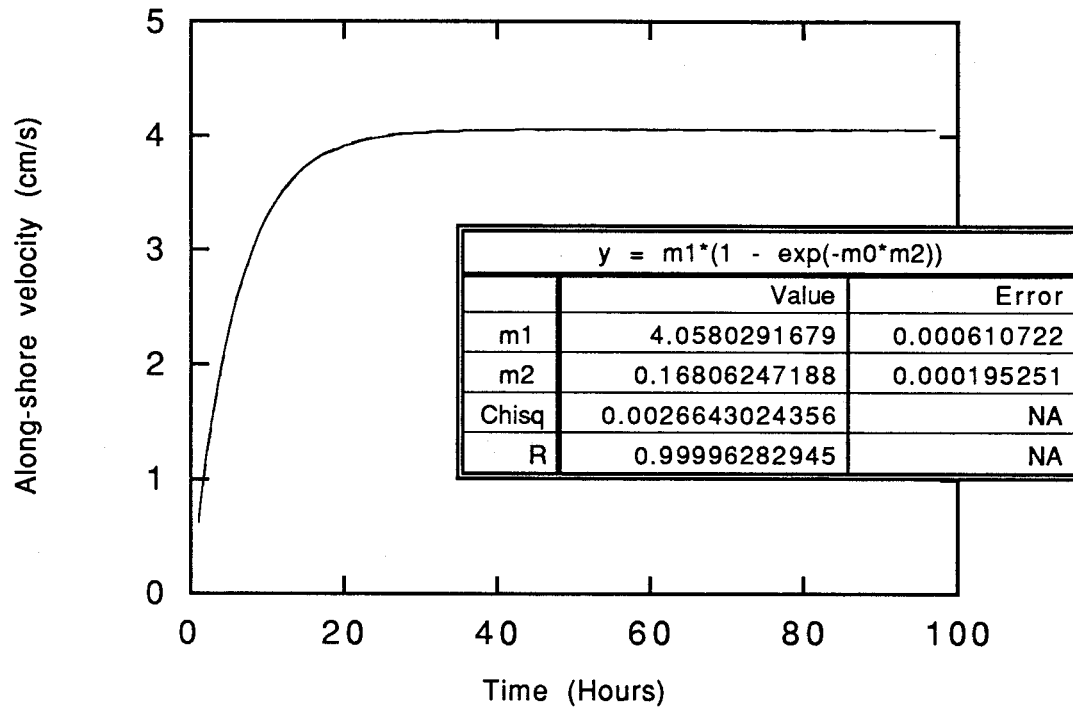


Figure E.78: Uniform along-shore wind experiment. Time series of along-shore velocity at the coast (site B). The time series at sites A,C are identical.

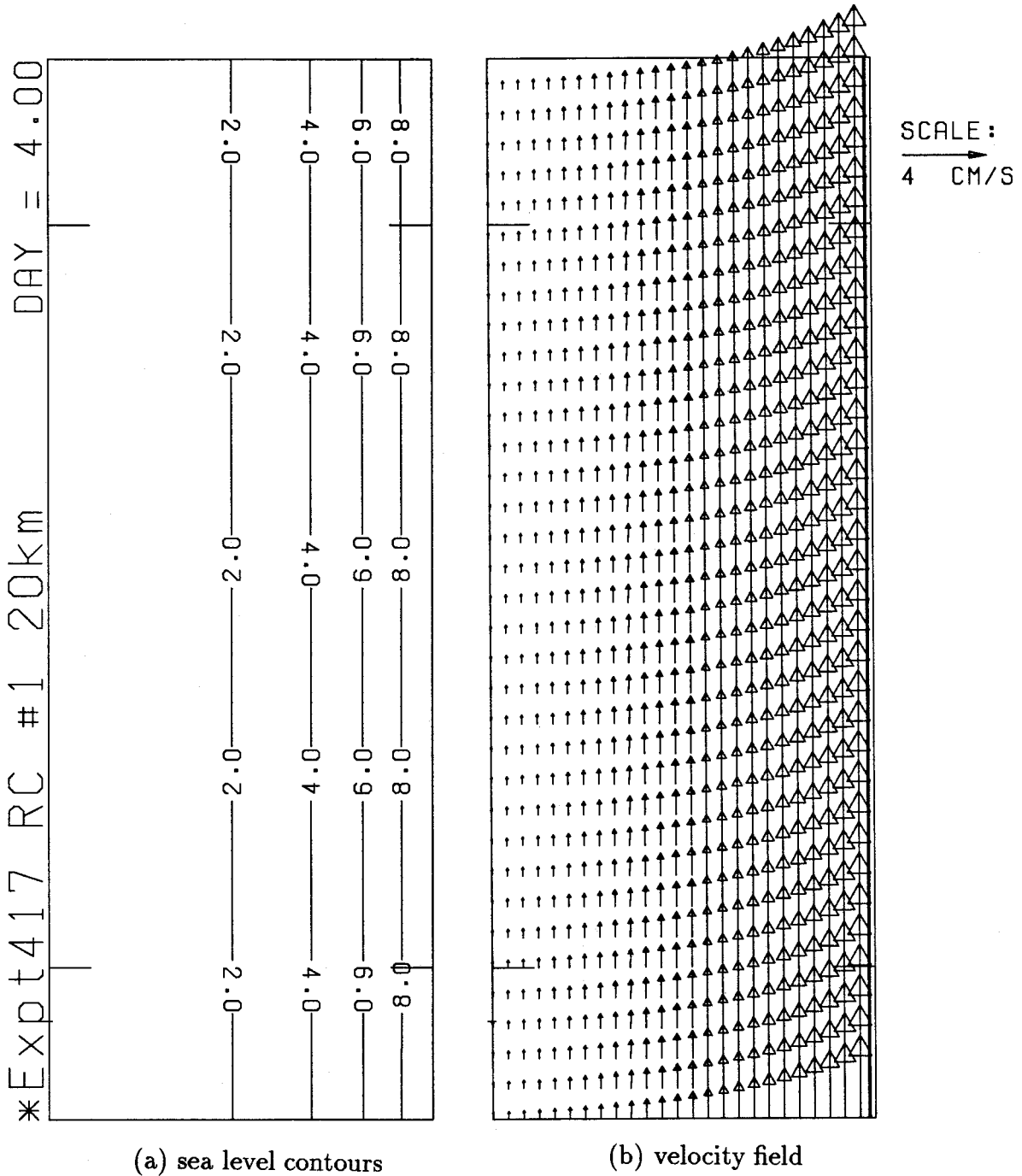


Figure E.79: Uniform along-shore wind experiment. The steady state a) sea level contours (cm), and b) velocity vectors.

E.1.2 Bell-Shaped Wind

A wind stress with a bell-shaped or Gaussian along-shore profile was used to test the open boundary conditions (OBC) with strong forcing in the interior and weak forcing at the boundaries.

The wind is turned on at $t = 0$ and off at $t = 48$ hr.

$$\tau^y = \begin{cases} \tau_0 \exp(-a^2 y^2) \exp(ax) & \text{for } t \leq 48 \text{ hr} \\ 0 & \text{for } t > 48 \text{ hr} \end{cases}$$

where the maximum wind stress $\tau_0 = 0.1$ Pa, the decay scale $a^{-1} = 200$ km, and $\tau^x = 0$. The wind stress at the cross-shore boundaries is 0.2% of the maximum. Figure E.80 shows the sea levels in the test domain after 40 hours. These are in good agreement with RC87.

Lacking an analytic solution for this case, I followed RC87 and added 4000 km to each end of the domain. This guarantees that waves reflecting off the end of the domain can not interfere with the solution before the end of integration (96 hours). This is referred to as the extended domain. Figure E.81 shows the time series of the along-shore velocities. The results are in excellent agreement with the extended domain case (and RC87). Site B exhibits the wind forced solution and the spin-down is a mirror image of the spin-up. At the downstream site one can see the Kelvin waves generated by the wind's start-up and shut-down pass by at roughly 9 and 57 hours (Fig. E.81, site C). There is a small discrepancy in the velocities at site C after hour 10 and this is seen in the excess mass (Fig. E.82). The excess mass is the average value of the sea level η over the domain.

E.2 Sloping Shelf

This test case uses the same rectangular domain as before, however the cross-shelf topography is taken from the northern end of the regional model domain (Fig. E.83). The

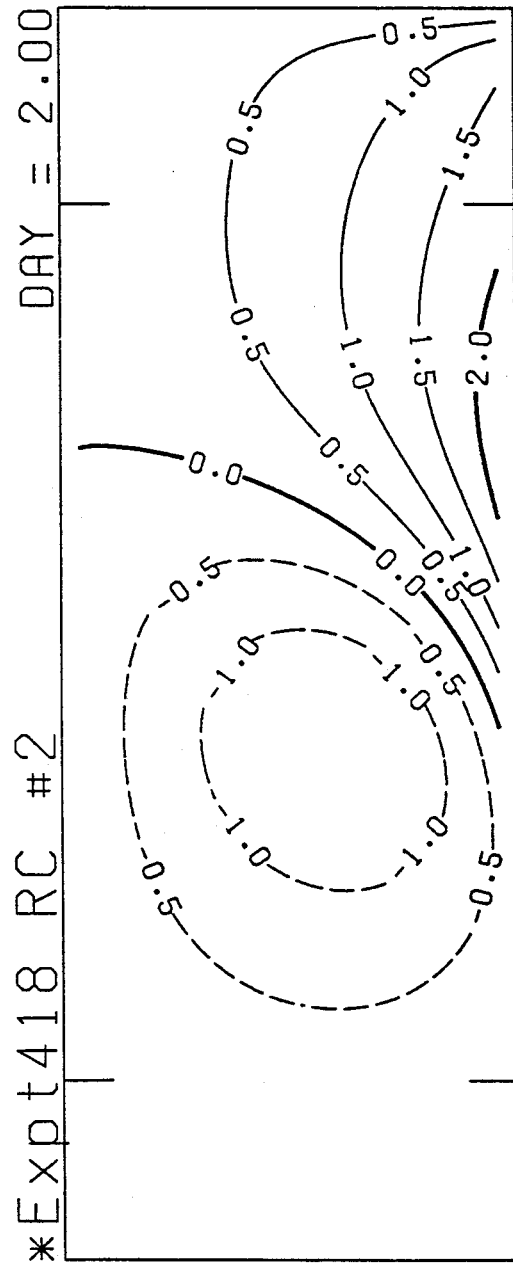


Figure E.80: Bell-shaped wind experiment. Sea level after 48 hours. The contour interval is 0.5 cm.

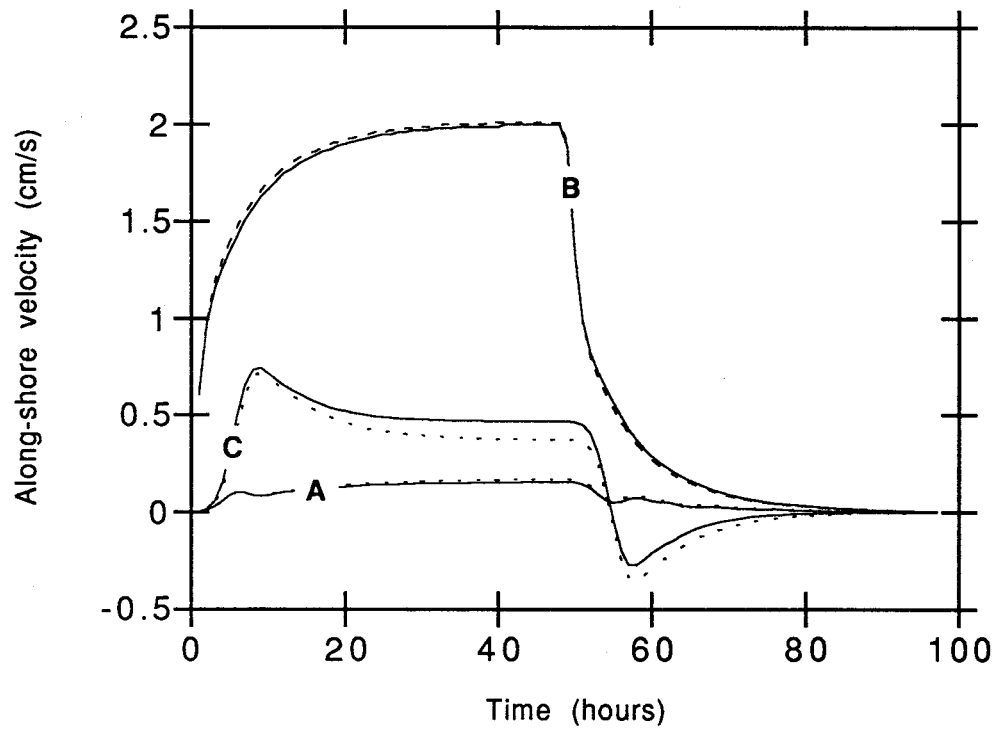


Figure E.81: Bell-shaped wind experiment. Time series of along-shore velocity at sites A, B, C. Data from the test domain is plotted as solid lines and data from the extended domain is plotted as dotted lines.

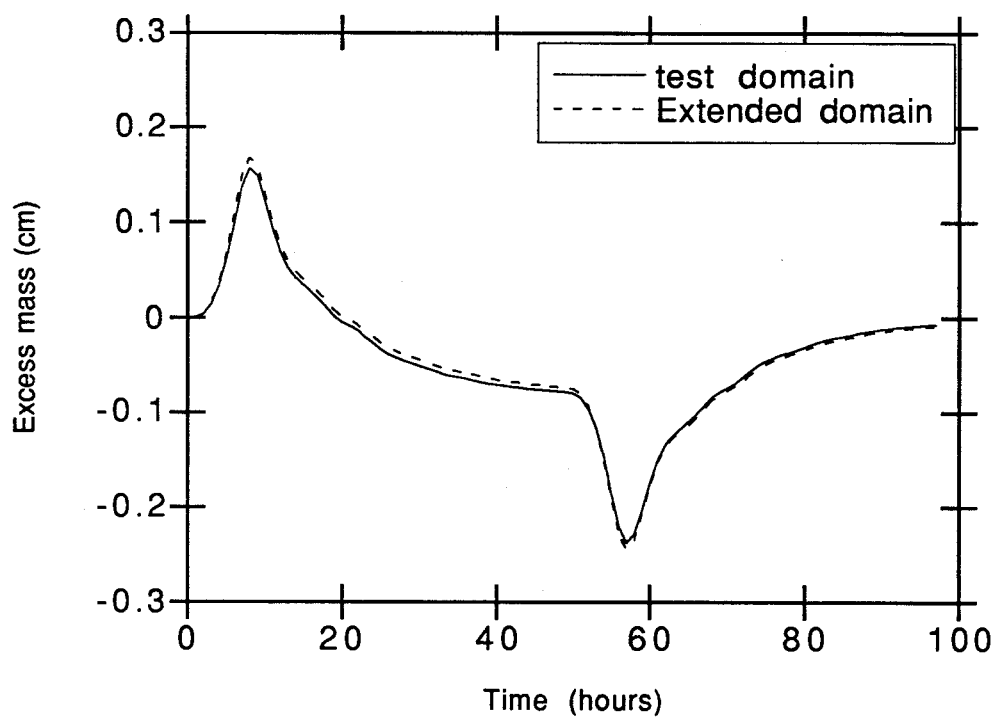


Figure E.82: Bell-shaped wind experiment. Time series of excess mass. Data from the test domain is plotted as solid lines and data from the extended domain is plotted as dotted lines.

topography does not change in the along-shelf direction. The non-linear equations are used and the other physical parameters (including grid size and friction) are taken from the Hecate Strait Model (Table E.15). Once again the x-axis, the index i , and velocity u denote cross-shelf quantities, while the y-axis, the index j , and velocity v denote along-shore quantities (Fig E.77).

L	domain length	250 km
W	domain width	100 km
Δs	grid size	5 km
f	Coriolis parameter	$1.1 \times 10^{-4} \text{ s}^{-1}$
k	friction parameter	$0.5 \times 10^{-3} \text{ s}^{-1}$
μ	Rayleigh friction	variable
Δt	time increment	12 s
	relaxation zone width	50 km
		10 grid cells

Table E.15: Parameters for open boundary condition tests with a sloping shelf

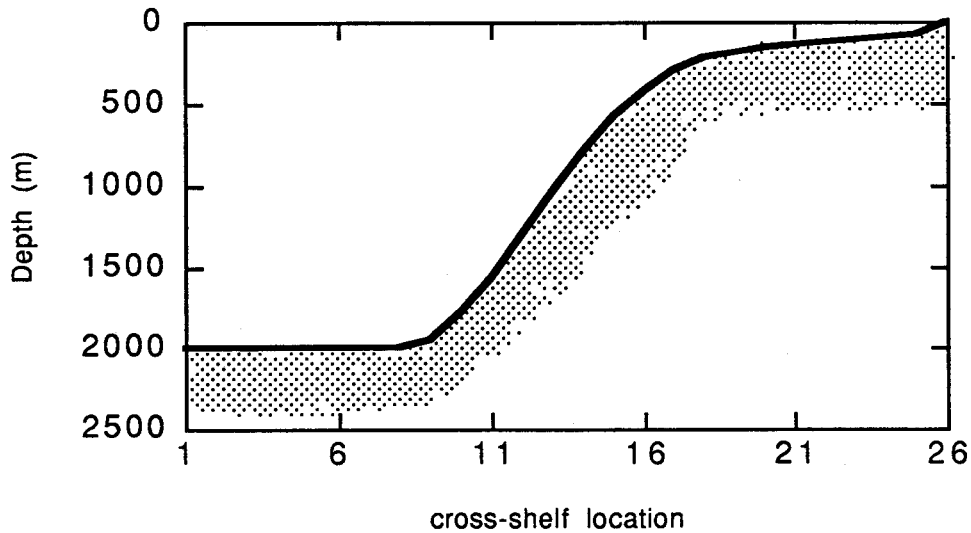


Figure E.83: Cross-section of the sloping shelf. Topography taken from regional model.

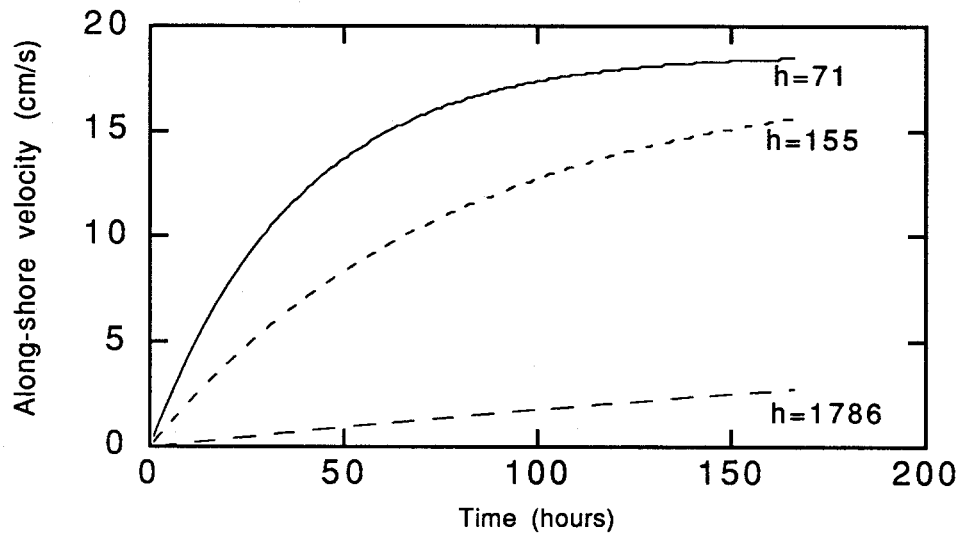


Figure E.84: Sloping shelf experiment. Time series of along-shore velocity at three different depths. The depth $h = 77$ m corresponds to location $(i,j) = (25,36)$. The depths $h = 155$ m and $h = 1786$ m correspond to $(i,j) = (20,36)$ and $(10,36)$ respectively.

The wind field is a uniform along-shore wind. In this case there is no offshore decay, the imposed wind stress is the same everywhere. The fluid starts from a state of rest.

The along-shore velocity time series at three different depths are shown in Fig. E.84. The time series show the increase in frictional adjustment time as the water gets deeper. After 196 hours of integration the two deeper locations have not reached the steady state (discussed further in the next section). The time series were taken from the following three locations: 1) at the coast, $(i,j) = (25,36)$ and $h = 77$ m; 2) 5 grid points off-shore, $(i,j) = (20,36)$ and $h = 155$ m; 3) 15 grid points offshore, $(i,j) = (10,36)$ and $h = 1786$ m.

The sea level and velocity fields are shown in Fig E.85. The jet structure is simply due the long adjustment times in the deep water. There are no surprises and no obvious kinks in the fields. Figure E.86 is a plot of along-shore velocity as function of along-shore location at three distances off-shore. There is a *very* small decrease in the along-shore velocity in the down-wind direction.

E.3 Frictional Adjustment on a Sloping Shelf

The sloping shelf test case provides an opportunity to test the model, particularly our understanding of the friction terms. The spin-up time series in Fig. E.84 look like frictional adjustment. This can be made more rigorous by comparing the steady-state velocities and e-folding times with the theoretical values.

A series of experiments were conducted for several different values of the Rayleigh friction coefficient μ . The along-shore velocities were monitored at the same three locations as before (depths of 71 m, 155 m, and 1786 m) and the best fit curves of the form

$$v(t) = v_{\infty}(1 - e^{-t/t_0})$$

were computed. The values of v_{∞} and $t_0 = \lambda^{-1}$ are compared with the theoretical values

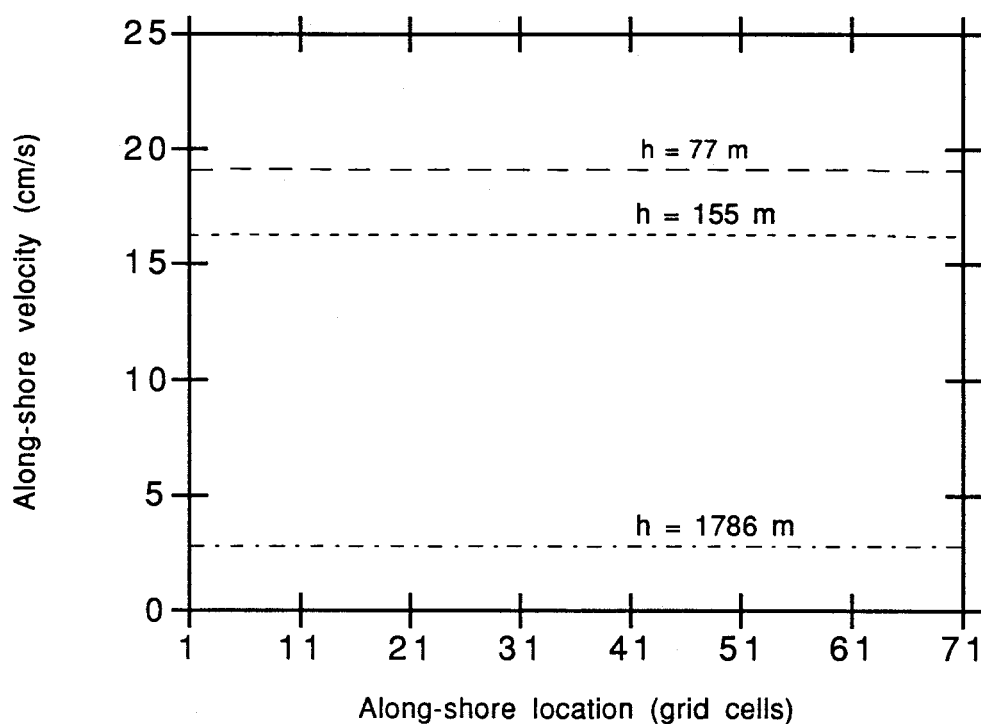


Figure E.86: Sloping shelf experiment. Along-shore velocity as a function of along-shore position. The velocity field was sampled at 3 distances off-shore, corresponding to depths of 77 m, 155 m, 1786 m. The model was forced with a uniform along-shore wind $\tau = 0.1$ Pa and the Rayleigh friction $\mu = 0$. The velocity field was sampled after 6.5 days of integration. The flow relaxation zones occupy along-shore locations 1 to 11 and 61 to 71. There are no kinks in the velocity field but there is a slight downward slope in the in the down-wind direction (from left to right).

		theory		model result	
μ (s ⁻¹)	h (m)	v_∞ (cm s ⁻¹)	t_0 (hr)	v_∞ (cm s ⁻¹)	t_0 (hr)
0.0	71	19.5	39.4	19.5	39.5
	155	19.5	86.1	19.5	86.9
	1786	19.5	922	–	1000.
$3.0 \cdot 10^{-8}$	71	19.4	39.3	19.4	39.4
	155	19.3	85.3	19.4	86.2
	1786	17.6	896	–	909
$3.0 \cdot 10^{-7}$	71	18.7	37.8	18.7	37.8
	155	17.8	78.8	17.8	79.5
	1786	9.4	479	–	483
$3.0 \cdot 10^{-6}$	71	13.7	27.7	13.7	27.6
	155	10.1	44.6	10.1	45.0
	1786	1.7	84.7	–	85.5

Table E.16: Frictional adjustment. Comparison of theoretical frictional adjustment times and the steady state velocity with the model results. The model results were fit to $v = v_\infty(1 - e^{-t/t_0})$. Fits were computed using time series of length 167 hours. Wind stress $\tau = 0.1$ Pa. Density $\rho = 1025$ kg m⁻³.

in Table E.16. The theoretical values were computed from

$$v_\infty = \frac{\tau}{\rho h \lambda}$$

$$\lambda = k/h + \mu$$

For $h = 1786$ m, the time scale t_0 was so long that the steady state velocity and the adjustment time-scale could not be estimated at the same time. For this depth steady-state velocity v_∞ was set to the theoretical value and only t_0 was estimated.

The good agreement between theory and the numerical experiments indicates that there are no hidden dissipation mechanisms in the model. The results also suggest that frictional adjustment provides a good model of the spin-up of the water in the open ocean portion of the Hecate Strait Model domain.

E.4 Stories

The reason for the going overboard here is because of my experience with open boundary conditions. Things always go wrong and one or two figures do not tell the whole story.

My first experience with this was when I was testing the Orlanski radiation condition. In a simple uniform wind test case I found that the sea levels looked fine but the velocity field reversed in the last few grid points near the outer boundary. After talking to many people working in the field I found that this is a common problem. When testing open boundary conditions, nobody ever publishes the velocity field.

My second war story relates to the flow relaxation boundary condition. After coding and initial testing it seemed to be working correctly. Eighteen months later, while tracking down a small problem near the northern open boundary, I found a bug. The exterior solution at the current time step was being relaxed with the interior solution at the *previous* time step. The solutions are only 10 s apart so this should not matter very much, right? Wrong!. The time step is chosen so that the fastest wave almost crosses a grid cell in one time step (almost but not quite). Combining different time levels in the relaxation scheme is a big problem. The problem was masked in the RC87 test cases because of the large friction, but it showed up in the real topography case as a large kink in the along-shore velocity in the relaxation zone.

Appendix F

Hecate Strait Model: Tests and Experiments

F.1 Open Boundary Condition Tests

In any limited-area or regional model, there is concern about the effect that the limited domain size has on the solution. In the Hecate Strait Model it is a fact of life that the interior knows that the boundaries are there. For the standard domain (Fig. 6.35) the travel time of shallow water waves from one end to the other and back is 3.5 h in the deep water. The external Rossby radius in 2000 m of water is 1300 km, and the distance from Cape St. James to the off-shore open boundary is 200 km (40 grid points). Therefore, a Kelvin wave travelling along the shelf break has a significant amplitude at the off-shore open boundary. The boundaries can not be moved far enough away.

Experiments were conducted for a range of domain sizes within computational reach. The larger domains were obtained by extending the depths at the boundaries. The results show that the flow relaxation boundary conditions (FRS) at the cross-shore boundaries work well (Table F.17). The steady-state transport changed slightly with the increase in domain size. There were significant changes when the boundaries were closed. The difference between the solution using the FRS and using closed boundaries manifested itself in the long time scale part of the spin-up, the behaviour after the first day or two (Figure F.87). The initial spin-up was identical. The time series for the standard domain (E310) lies on top of that for the long domain (E321) for the FRS open boundary condition. The standard parameters were used (Table 6.6).

expt	domain name	size	OBC	Transport (Sv)
E302b	small	90 x 160	FRS	0.26 (.259)
E310	standard	90 x 199	FRS	0.26 (.262)
E320	long	90 x 499	closed	0.21 (0.209)
E321	long	90 x 499	FRS	0.26 (0.263)
E300b	big	199 x 317	closed	0.20 (0.196)
E300c	big	199 x 317	FRS	0.27 (0.265)

Table F.17: Steady state transport in domains of different size with an along-shore wind ($\tau = 0.1$ Pa) and the standard friction parameters. Domain sizes are given in grid points. The open boundary conditions (OBC) are the flow relaxation scheme (FRS) and closed boundaries. The results for standard, big, and long were the same for FRS zone widths of 20 and 40 grid cells.

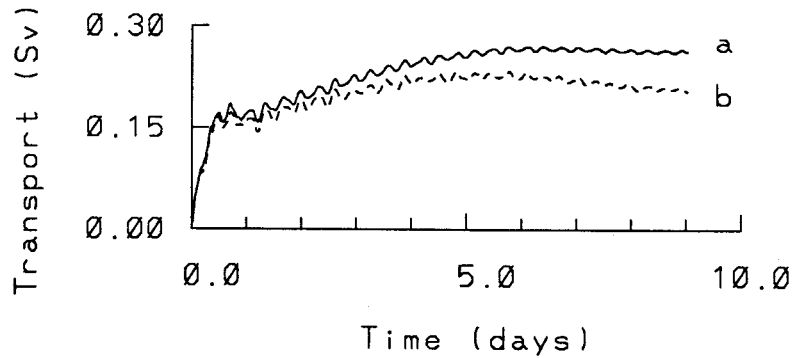


Figure F.87: Comparison of the transport through W-line for two different open boundary conditions: (a) flow relaxation method (E321, solid); and (b) closed (E320, dashed). The domain is the long domain.

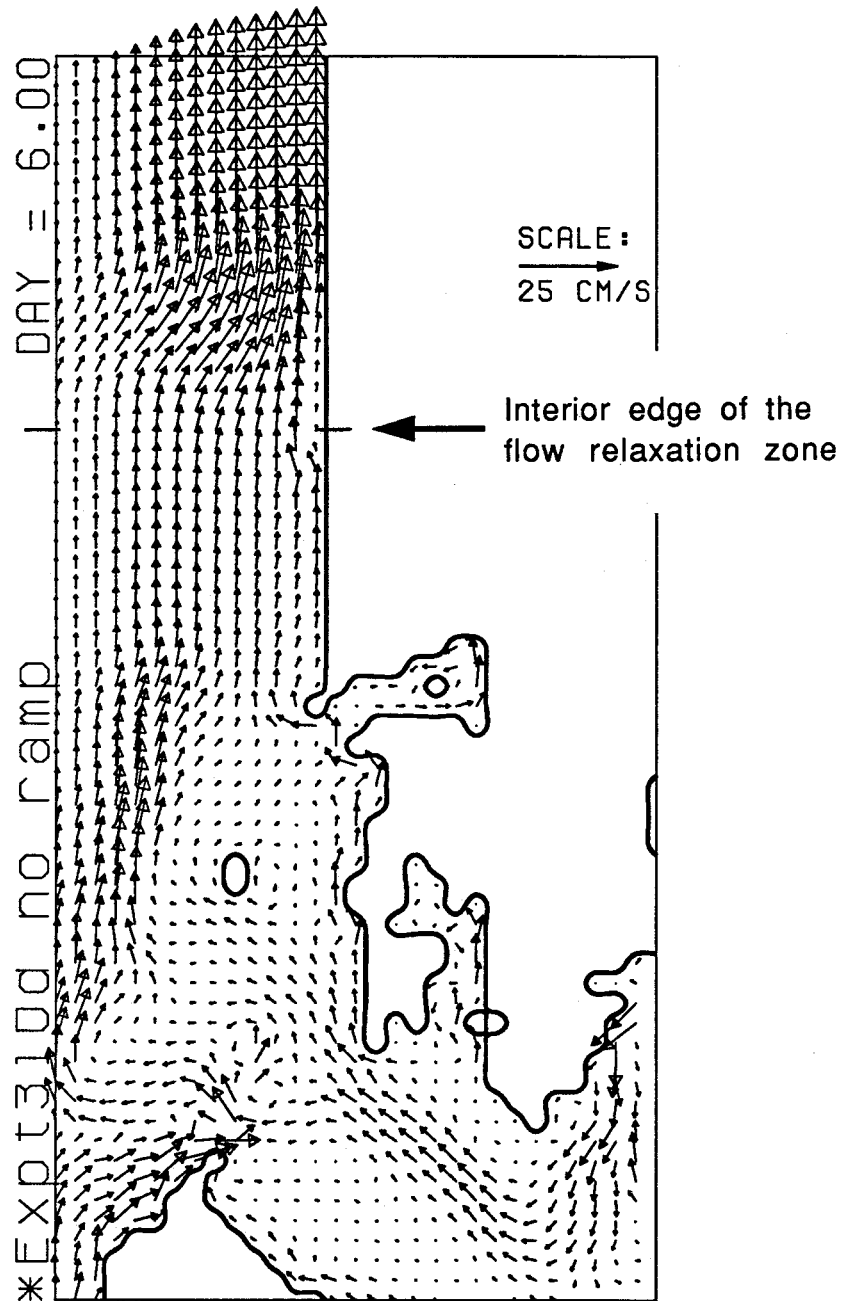


Figure F.88: The velocity field after 6 days near the northern cross-shore boundary. The top of the figure is the open boundary. All of the vectors are shown.

Two flow relaxation zone widths were tried: 20 and 40 grid cells. For the standard and larger domains there were no differences in the steady state results. For the standard domain, the extra FRS zone width was acquired by letting the FRS move further into the model domain: the overall domain size remained the same (90x199). The only significant effect of the larger relaxation zone was a reduction in the amplitude of the high frequency oscillation. This indicated that the open boundary condition was affecting the solution in Hecate Strait. Unless otherwise stated the flow relaxation zone width used in this thesis was 20 grid cells.

The impact of the open boundary conditions is illustrated in Fig. F.88. In the relaxation zone, the jet structure off the west coast of the Queen Charlotte Islands is merged with the wind forced solution at the open boundary in dramatic fashion. The velocity pattern in the mouth of Dixon Entrance and around Forrester Island did not change when the open boundary was moved 750 km downstream (E321). However the jog in the velocity field did move downstream.

I was concerned about reflections from the clamped off-shore boundary. To reduce the reflections a 30-grid-point-wide sponge layer was created along the off-shore boundary. This was done by increasing the Rayleigh friction and the eddy viscosity near the boundary. To date I have not been able to detect any difference in the solutions on the shelf with and without the sponge layer. The sponge layer was not used in this thesis.

For now accept that open boundary conditions are not having an enormous impact on the shelf circulation.

F.2 Adjustment Time-Scales in Hecate Strait

As discussed in Chapter 6, a plausible explanation for the two adjustment time-scales in Hecate Strait is that the fast time-scale is the response to the local wind forcing and the

slow time-scale is the response to an along-shore pressure gradient set up by processes outside of Hecate Strait. The purpose of this section is to take a closer look at this idea.

The steady-state velocity field for a wind localized over Hecate Strait is shown in Fig. F.89. The wind forcing was an along-shore wind that tapered to zero at the edges of the strait. The iso-lines of the wind stress are shown. The velocity pattern, after 8 days, looks like the pattern from the uniform wind experiment at Day 1 (Fig. 8.58a; note the velocity scale change). There are large currents in northern and western Hecate Strait and not much anywhere else. A tiny southwesterly flow along the north side of Moresby Trough is visible.

The picture changes dramatically when the model is forced with a wind localized over central Queen Charlotte Sound (Fig. F.90). In southern Hecate Strait the pattern is similar to the uniform wind pattern, and not at all like the velocity pattern with the wind localized over Hecate Strait. A very similar pattern is obtained when the model is forced by an along-shore wind localized near the southern open boundary (not shown).

The combination of Fig. F.89 and Fig. F.90 contains all of the important elements of the velocity pattern with a uniform wind (Fig. 8.59). On this basis, I proposed that the flow pattern in Hecate Strait is due to both local wind forcing and remote pressure forcing. The pattern due to local wind forcing is Fig. F.89, which also corresponds to Day 1 in Fig. 8.58. The pattern due to pressure forcing is Fig. F.90.

The transport time series for the uniform wind and the two localized winds are shown in Fig. F.91. The initial response from the wind localized over Hecate Strait has the same response time as the uniform wind. A curve of the form

$$Q(t) = Q_0(1 - e^{-\lambda t})$$

was fit to the transport time series for the wind localized over Hecate Strait (Fig. F.92). From the legend in the figure, the relaxation constant is $m_2 = 6.06 \text{ d}^{-1}$. An e-folding

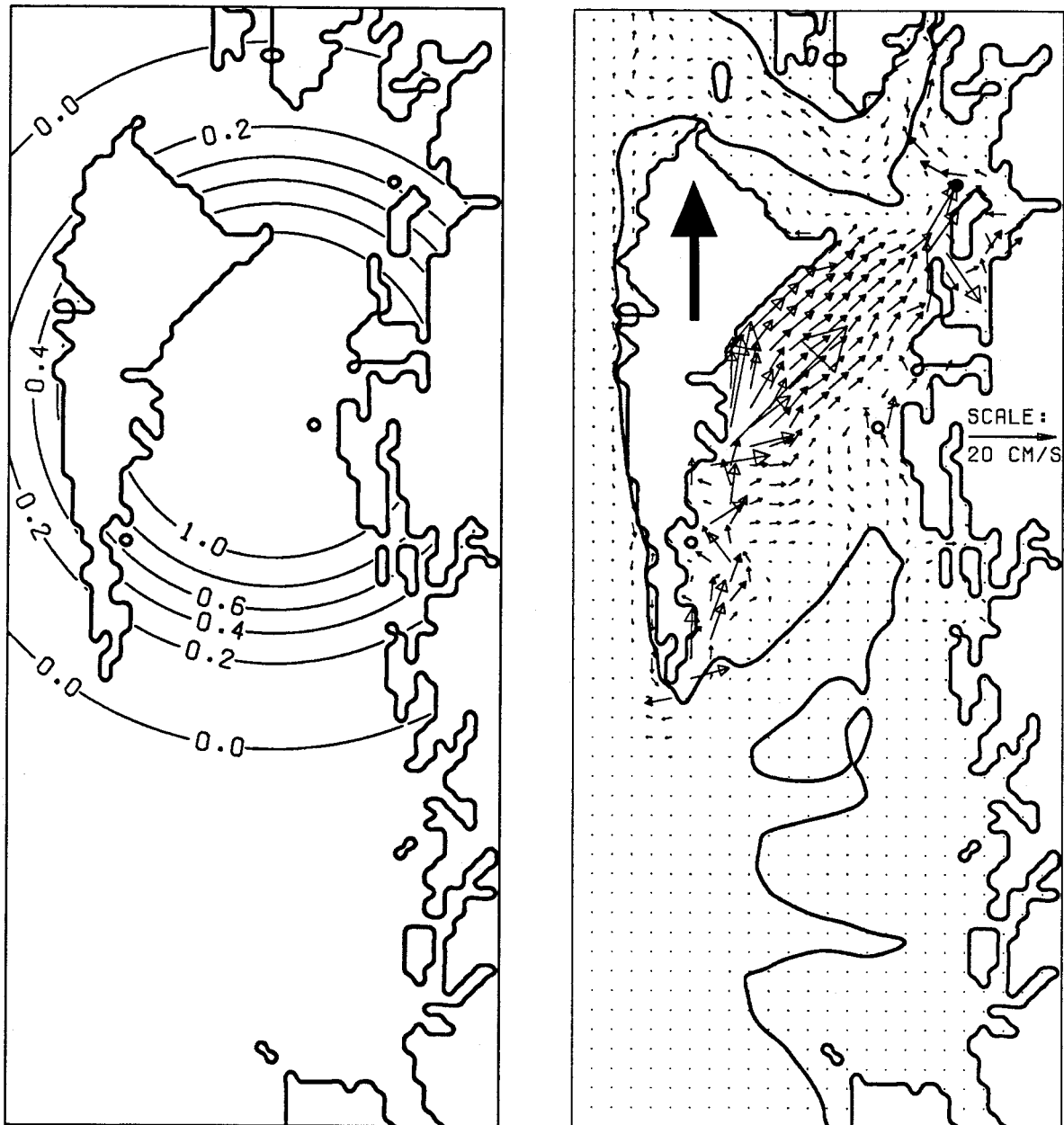


Figure F.89: The steady state velocity field forced by an along-shore wind localized over Hecate Strait. The maximum wind stress is 0.1 Pa.

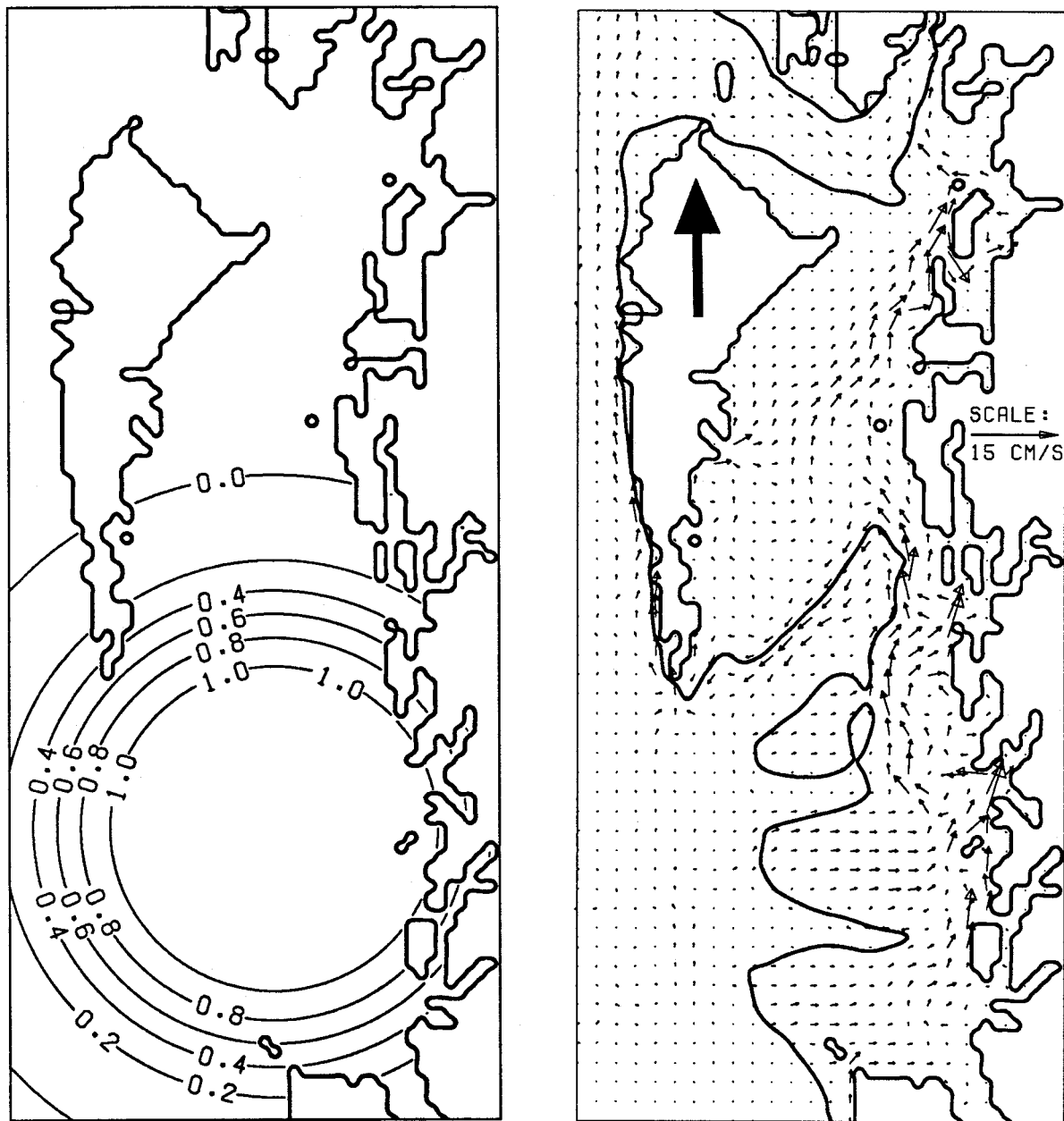


Figure F.90: The steady state velocity field forced by an along-shore wind localized over central Queen Charlotte Sound. The maximum wind stress is 0.1 Pa.

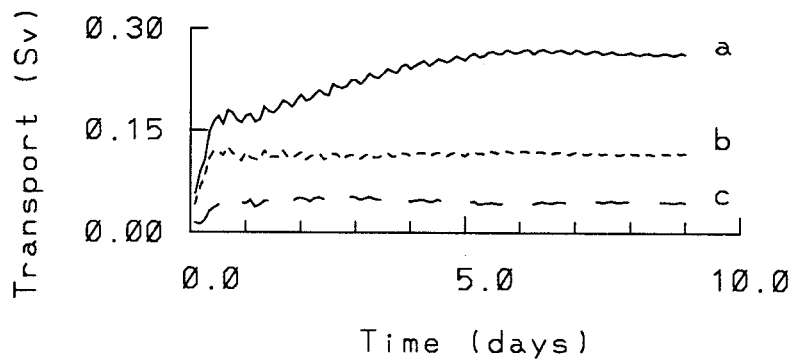


Figure F.91: Comparison of the transport spin-up for three along-shore wind scenarios: (a) spatially uniform, (b) localized over Hecate Strait and (c) localized over Queen Charlotte Sound. The maximum wind stress is 0.1 Pa.

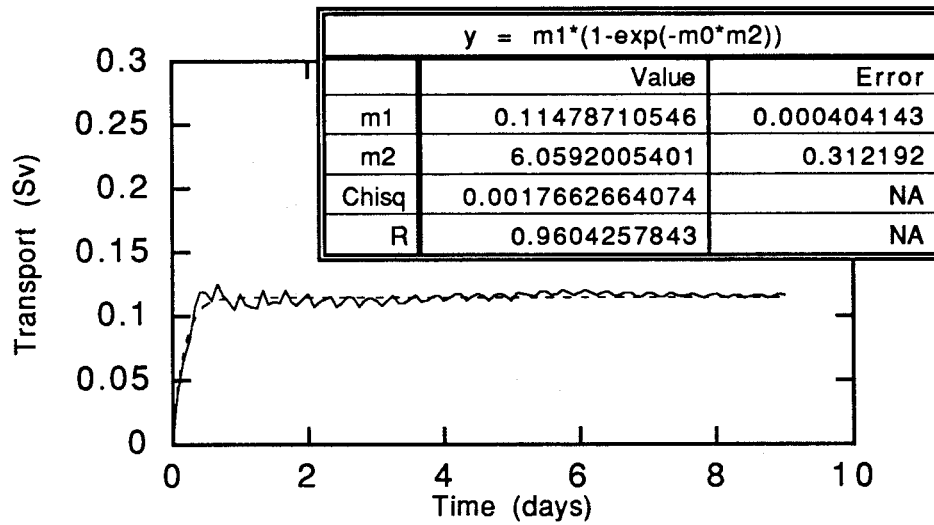


Figure F.92: Curve fit to the transport time series for a wind localized over Hecate Strait.

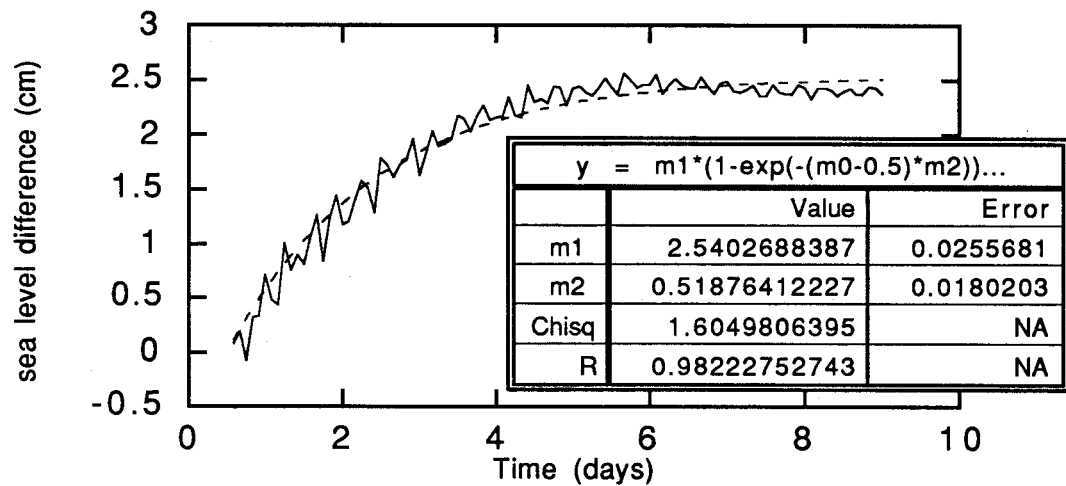


Figure F.93: Curve fit to the time series of sea level at Cape Scott minus sea level at Cape Muzon. The wind forcing was the standard spatially uniform wind.

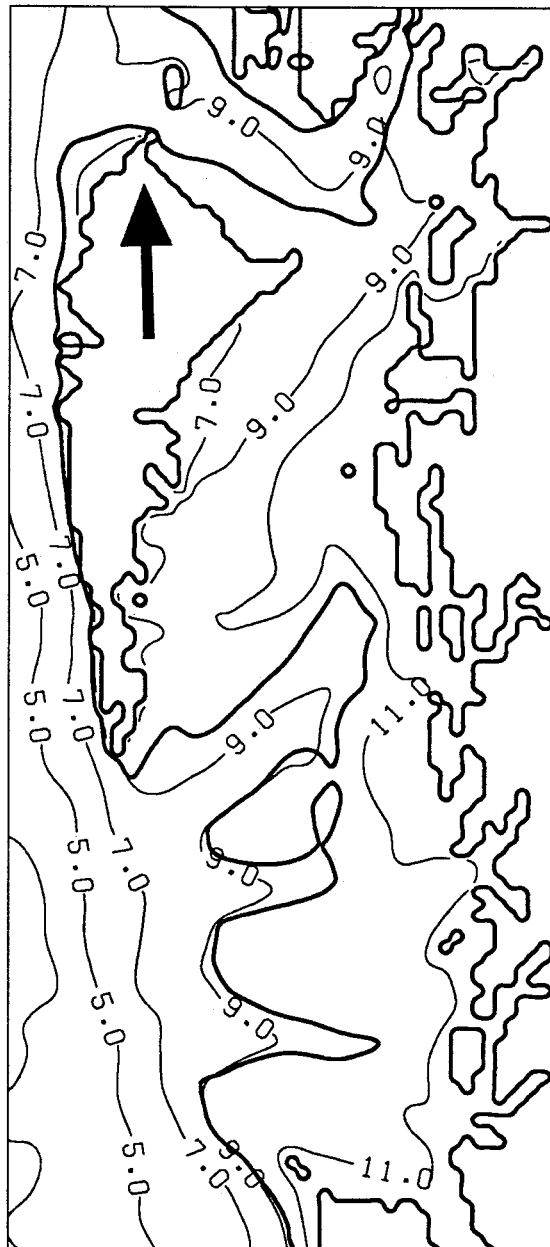


Figure F.94: The sea level field for a spatially uniform along-shore wind ($\tau = 0.1$ Pa). The contours are labelled in cm.

time of $\lambda_1^{-1} = (m_2)^{-1} = 4$ h was used in Chapter 6.

For the pressure forcing, the e-folding time was computed from the time series of the sea level difference between Cape Scott and Cape Muzon (from the uniform wind experiment reported in Chapter 6). A curve of the form

$$b(t) = b_0(1 - e^{-\lambda(t-t_0)})$$

was fit to the time series. The first 0.5 days were trimmed from the record before analysis: thus $t_0 = 0.5$ d. The fit is shown in Fig. F.93. From the legend the relaxation time constant is $m_2 = 0.52$ d⁻¹. An e-folding time of $\lambda_2^{-1} = (m_2)^{-1} = 48$ h was used in Chapter 6.

The reason for trimming the sea level difference time series is evident from the plot of the complete time series in Fig. 6.40. For the first half day the high frequency oscillation dominates the record. The exponential relaxation does not appear until Day 1 or so. Curve fits to the complete record yielded very poor results.

The sea level field for an along-shore spatially uniform wind is shown in Fig. F.94. Notice that the on-shore Ekman transport has raised the sea level everywhere. The sea level difference between Cape Scott and Cape Muzon is roughly 2 cm. The pressure, or sea level forcing, in Hecate Strait might be as much as 3 or 4 cm. Recall from Chapter 4 that the pressure forcing term $\eta_4 - \eta_5$ roughly corresponds to the sea level difference between Beauchemin and Rose Spit. Rose Spit is the northeast corner of the Queen Charlotte Islands and Beauchemin is located in the southeast end of Hecate Strait (under the 0 in the 11.0).

F.3 Steady State Velocity Fields

F.3.1 Bottom Friction

This section takes a second look the steady-state velocity field. Of interest is whether the patterns seen in Fig. 8.59 are robust to changes in the bottom friction formulation and the model topography.

The steady state velocity field resulting from quadratic bottom friction (5.33) is shown in Fig. F.95 for the case $C_d = 2.5 \times 10^{-3}$ and $u_0 = 0.0$. The rms tidal velocity field used to compute the spatially varying linear friction coefficient is shown in Fig. F.96. At each point, the linear friction coefficient was computed from

$$k^*(x, y) = C_d v_{rms}$$

where v_{rms} is the value of the rms velocity field at location (x,y) and C_d is the drag coefficient. The resulting steady state velocity field (Day 8) is shown for the case $C_d = 2.5 \times 10^{-3}$. The choice of the drag coefficients was discussed in Chapter 6.

In both cases the patterns are not significantly different from the linear friction pattern (Fig. 8.59). This indicates that bottom friction does not play an important role in determining the flow patterns.

F.3.2 Bathymetry

The generation of the coastline and bathymetry required many subjective decisions with respect to narrow features. To assess the impact of these decisions, the following changes were made to the bathymetry

- All the fjords and inlets were removed and the narrow passages closed.
- Rose Spit and Langara Island were cut back.

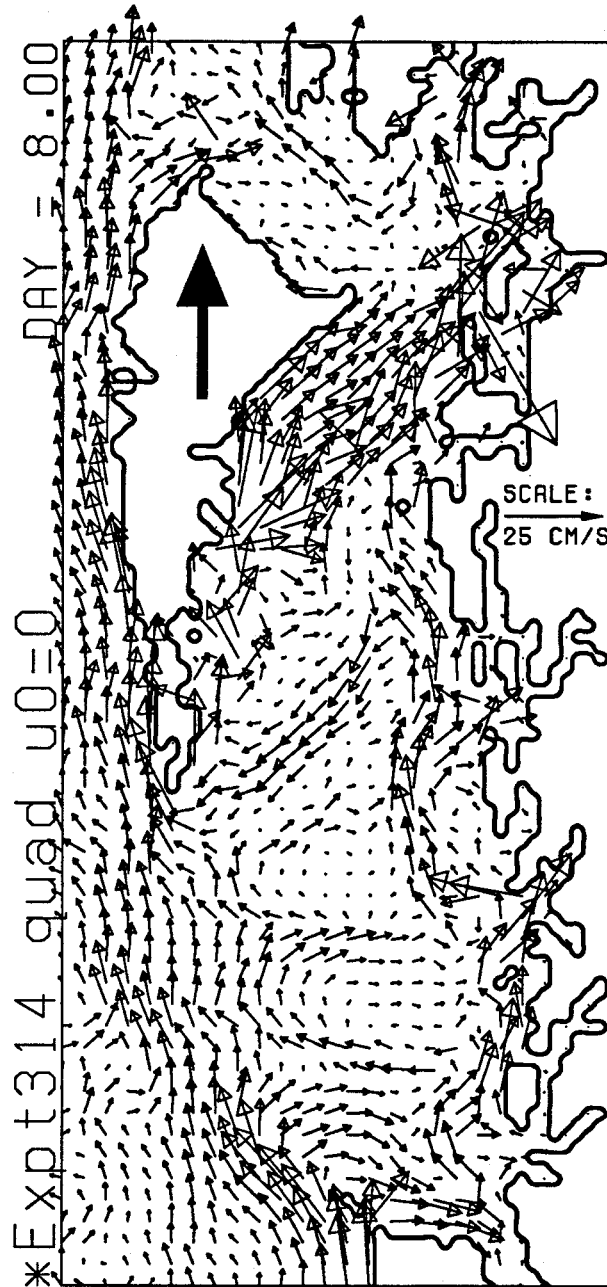


Figure F.95: Quadratic friction experiment. The steady state velocity field for a spatially uniform along-shore wind. The drag coefficient $C_d = 2.5 \times 10^{-3}$ and the background velocity $u_0 = 0/0$. The wind stress $\tau = 0.1$ Pa.

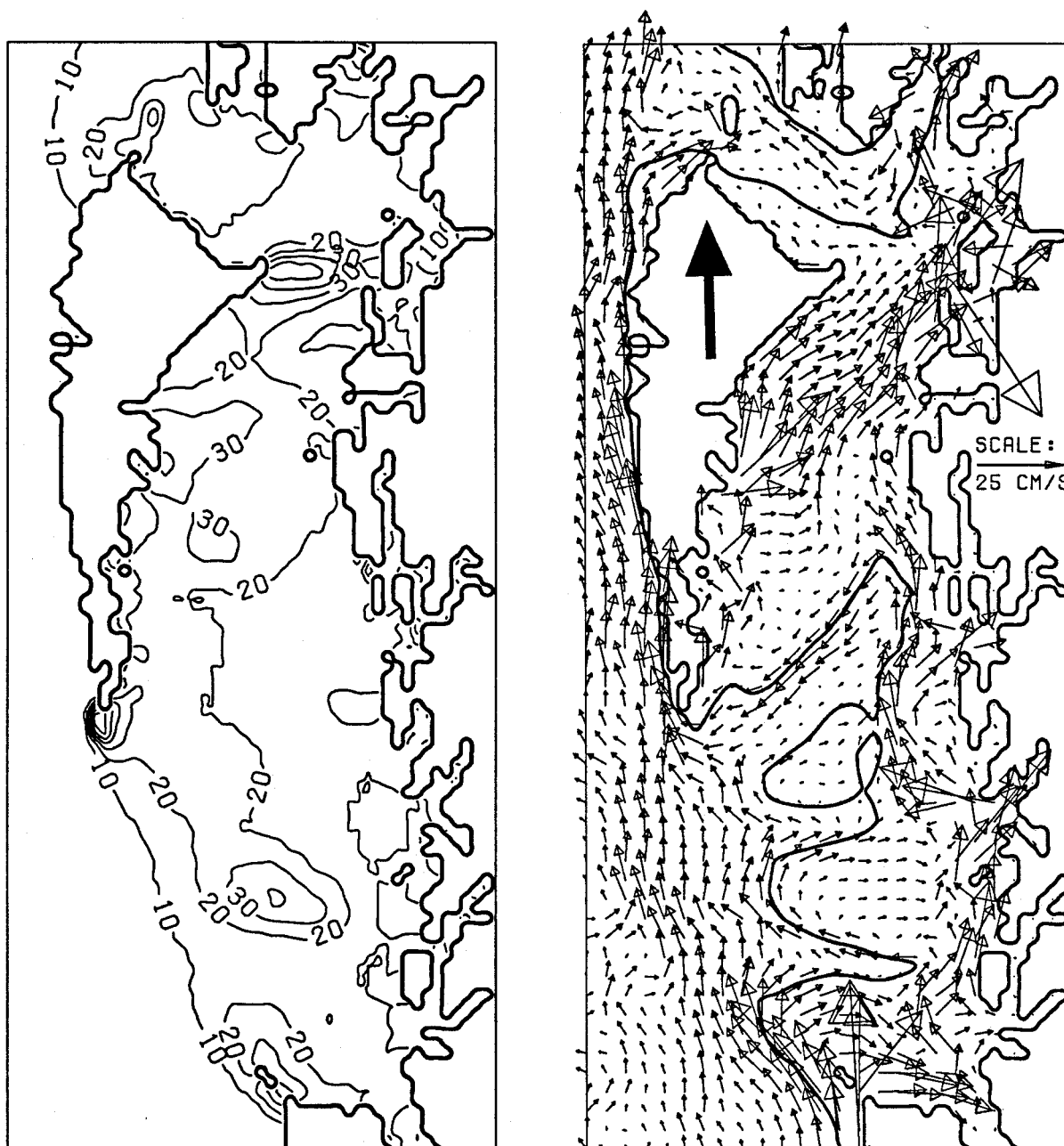


Figure F.96: Spatially varying linear friction experiment. The rms tidal velocity field (cm/s) and the resulting steady state velocity field from the Hecate Strait Model. The wind stress was spatially uniform with $\tau = 0.1$ Pa.

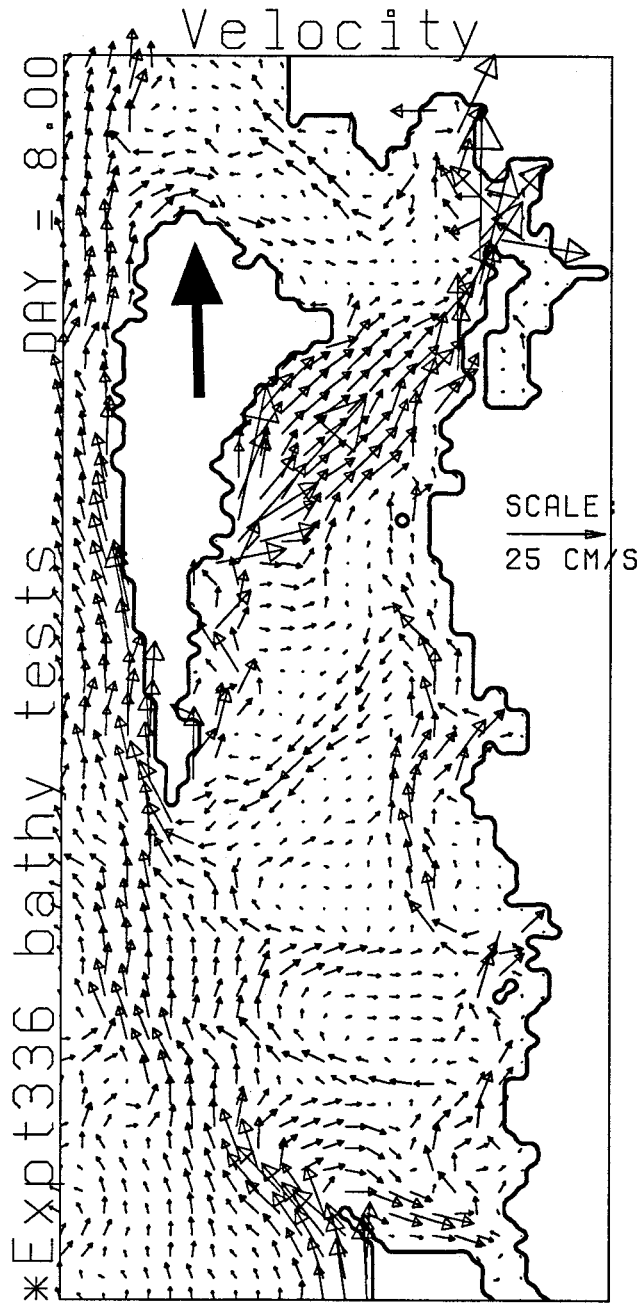


Figure F.97: Velocity field with altered bathymetry. The wind stress was spatially uniform with $\tau = 0.1$ Pa. Standard linear friction was used.

- Learmonth Bank was removed.

The steady-state circulation pattern is shown in Fig. F.97. In Queen Charlotte Sound and Hecate Strait the changes are confined to within a few grid points of the bathymetry changes. Closing Brown Passage resulted in larger velocities along the west side of Dundas Island and a 10% reduction in the steady state transport through Hecate Strait.

In Dixon Entrance there are structural changes. Cutting back Langara Island and letting water flow around the corner has changed the currents along the southern side of Dixon Entrance. The constraints of the depth-averaged dynamics makes the flow in Dixon Entrance sensitive to the depths near Langara Island. One pattern is obtained if the water can follow the isobaths around the corner, and another if it cannot.

With the exception of Dixon Entrance, the overall circulation pattern is not overly sensitive to minor changes in the bathymetry. The fjords and inlets are aesthetically pleasing but not crucial to the model circulation.

F.3.3 Spatially Varying Wind

As reported in this thesis, the simulations conducted with the Hecate Strait Model used spatially uniform winds. As was discussed in Chapter 2, the spatial variability of the winds in the Queen Charlotte Islands region is not well defined. The discussion here is limited to results obtained with the Hecate Strait Model.

I conducted experiments with steady along-shore winds that were uniform in the along-shore direction and varied smoothly in the cross-strait direction. When compared to the uniform wind case, the velocity at any point varied qualitatively in the same sense as the change in the local wind stress. The transport through Hecate Strait was most sensitive to the value of the wind stress on the eastern side of the strait (where the volume transport is).

The storm systems that affect the Queen Charlotte Islands regions are generally large scale systems with a length scale of the order of 1000 km; this can be seen by watching the atmospheric pressure charts in the local newspapers. When a moving circular storm with a radius of 1000 km was used in the model, the results in Hecate Strait were very similar to the results obtained by assuming a spatially uniform wind with a value based on the proper value in the middle of Hecate Strait. The real storm systems are not circular, but the large scale means that in general the winds in Hecate Strait are a reasonable indicator of the winds in Queen Charlotte Sound and Dixon Entrance.

This does not mean that the spatial variability of the winds is not important. As was shown in Section F.2, a wind localized over Queen Charlotte Sound can force water through Hecate Strait. The experiments reported there are examples of extreme spatial variability in the wind stress field. The velocity at any point depends on the local pressure gradient as well as the wind stress. As was seen in Section F.2 and Chapter 6, the along-shore pressure gradient depends on the wind stress in Queen Charlotte Sound and Dixon Entrance.

Based on these results, I believe that the character of the results presented in this thesis does not depend on the assumption of spatially uniform winds. A more sophisticated model would address the issue of the spatial variability of the wind stress field.

Appendix G

Friction, Coriolis Parameter and Transport

G.1 Steady State Transport

The results of numerical experiments examining the relationship between the bottom friction, the Coriolis parameter and the steady state transport through Hecate Strait are listed in Table G.18. The data is plotted in Fig. 7.50 and Fig. 7.51. The localized wind is an along-shore wind localized over Hecate Strait, with a maximum wind stress of 0.1 Pa (see Appendix F). The uniform wind has a constant wind stress of 0.1 Pa over the whole model domain (except near the off-shore boundary – Chapter 6).

f/f_0	localized wind		uniform wind
	$k = 0.5 \times 10^{-3} \text{ s}^{-1}$	$k = 2.0 \times 10^{-3} \text{ s}^{-1}$	$k = 0.5 \times 10^{-3} \text{ s}^{-1}$
0	0.55	0.141	0.68
0.1	0.46	0.139	62
0.5	0.20	0.11	0.38
0.75	0.15	–	–
1.0	0.115	0.08	0.26
1.5	0.08	–	–
2.0	0.06	0.51	0.19
6.0	0.02	0.02	0.11

Table G.18: Steady-state transport (Sv) through Hecate Strait as a function of Coriolis parameter. The wind stress $\tau = 0.1 \text{ Pa}$, $f_0 = 1.1 \times 10^{-4} \text{ s}^{-1}$, and $\mu = 3 \times 10^{-3} \text{ s}^{-1}$.

For the localized wind experiments, the parameter W/L was estimated as follows. By analogy with rotation-limited-flux, a curve of the form

$$Q = \frac{B}{1 + Cf/f_0} \tag{G.84}$$

k 10^{-3} s^{-1}	B Sv	C	h^* m	λ 10^{-6} s^{-1}	W/L $C\lambda/f_0$
0.5	0.55 ± 0.02	3.4 ± 0.4	60	8.6	0.27 ± 0.03
			70	7.4	0.23 ± 0.02
			80	6.5	0.20 ± 0.02
2.0	0.147 ± 0.004	0.81 ± 0.1	60	30.	0.24 ± 0.02
			70	29	0.21 ± 0.02
			80	25	0.19 ± 0.02

Table G.19: Localized wind experiment. Estimating the parameter W/L from the steady-state transport. The wind stress $\tau = 0.1 \text{ Pa}$, $f_0 = 1.1 \times 10^{-4} \text{ s}^{-1}$, and $\mu = 3 \times 10^{-3} \text{ s}^{-1}$.

was fit to the data defining the steady-state transport as a function of Coriolis parameter. The functional form is discussed in Chapter 7. This was done for both values of k . The effective relaxation constant was computed from $\lambda = k/h + \mu$, where k and μ are known and the effective depth was estimated from the charts and the steady-state transport vector field (Fig. 6.44): $h^* = 70 \text{ m}$ was deemed reasonable. The results are listed in Table G.19.

k 10^{-3} s^{-1}	μ 10^{-6} s^{-1}	B Sv	C	λ 10^{-6} s^{-1}	W/L $C\lambda/f_0$
use data at $f = 0$					
0.5	0.3	0.63 ± 0.01	2.0 ± 0.1	7.0	0.13
do not use data at $f = 0$					
0.5	0.3	0.69 ± 0.01	2.5 ± 0.1	7.0	0.16
0.55	2.7	0.53 ± 0.01	2.3 ± 0.1	10.0	0.21
1.1	2.7	0.29 ± 0.01	1.2 ± 0.1	18.0	0.17
2.2	2.7	0.15 ± 0.01	0.55 ± 0.1	34.0	0.16

Table G.20: Uniform wind experiment. Estimating the parameter W/L from the steady-state transport. The wind stress $\tau = 0.1 \text{ Pa}$, $f_0 = 1.1 \times 10^{-4} \text{ s}^{-1}$, and $h^* = 70 \text{ m}$.

A slightly modified version of rotation-limited-flux was used for fitting to the uniform wind data. The form (G.84) was replaced with

$$Q = \frac{B}{1 + Cf/f_0} + \frac{B}{10} \quad (\text{G.85})$$

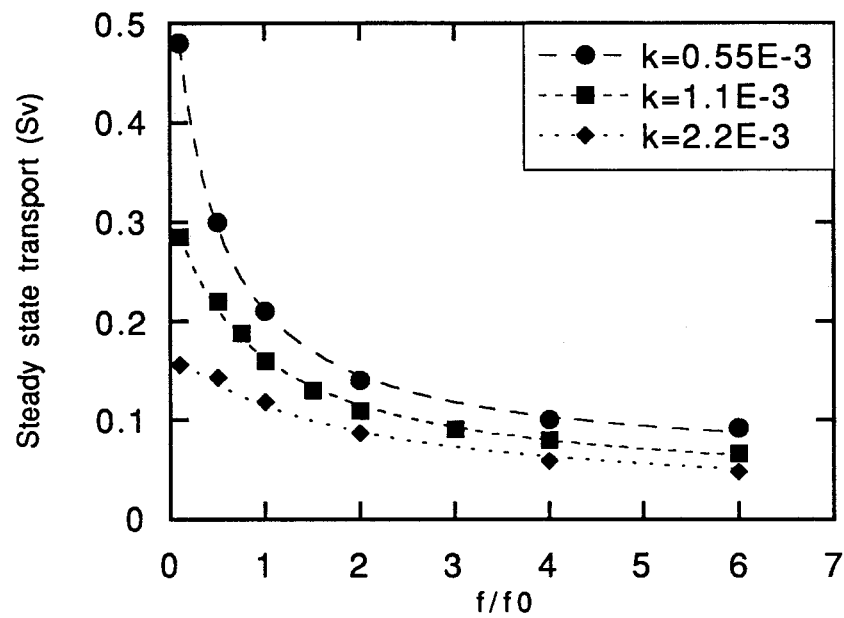


Figure G.98: Uniform wind experiment. Steady-state transport as a function of Coriolis parameter for three values of k and $\mu = 2.7 \times 10^{-6} \text{ s}^{-1}$. The wind stress $\tau = 0.1 \text{ Pa}$.

The modification arose because it was evident that (G.84) did not provide a good fit: the steady-state transports did not go to zero fast enough. To account for this a fit of the form

$$Q = \frac{B}{1 + Cf/f_0} + D \quad (\text{G.86})$$

was tried where B , C , and D are all fit parameters. In experiments with several different values of the wind stress, I noticed that D scaled with the wind stress and that $D = B/10$ was a good approximation.

The estimates of W/L in Table G.20 were computed using using $h^* = 70$ m. The three sets of experiments with $\mu = 2.7 \times 10^{-6} \text{ s}^{-1}$ (10 times the standard value) were computed using an older version of the model and the steady-state transport at $f = 0$ was never computed. For comparison, the values of B , C , and W/L were computed from the standard experiment without using the data point at $f = 0$. The results are very similar. Notice that the background component $B/10$ represents 1/4 to 1/3 of the total steady state transport when $f/f_0 = 1$.

The data from the standard version is listed in Table G.18 and plotted in Fig. 7.51. The three curves from the experiments with $\mu = 2.7 \times 10^{-6} \text{ s}^{-1}$ are plotted in Fig. G.98.

G.2 Adjustment Time

The parameters for the straight line fits through the adjustment time data shown Fig 7.53 are listed in Table G.21. The value of W/L is 2 to 3 times the value computed from the steady state transport. The value of the intercept changed much more than the slope, when the fit was recomputed without using the data at $f = 0$,

k 10^{-3} s^{-1}	μ 10^{-6} s^{-1}	intercept d^{-1}	slope d^{-1}	W/L slope/ f_0
use data at $f = 0$				
0.5	0.3	0.42	5.7	0.60
2.0	0.3	2.3	4.4	0.46
do not use data at $f = 0$				
0.5	0.3	0.25	5.9	0.62
2.0	0.3	2.0	4.5	0.46

Table G.21: Localized wind experiment. Estimating the parameter W/L from the spin-up time constant data. The wind stress $\tau = 0.1 \text{ Pa}$, $f_0 = 1.1 \times 10^{-4} \text{ s}^{-1}$, and $\mu = 3 \times 10^{-3} \text{ s}^{-1}$.

G.3 Discussion

Hecate Strait does not have a flat bottom and this raises concerns about the validity of the rotation-limited-flux model. In Chapter 8 I showed that topographic steering causes the flow in Hecate Strait to follow the local depth contours. In northern Hecate Strait, the velocity pattern is established during the first 12 hours. After that the flow is generally parallel to the local depth contours and only the magnitude of the velocity vectors changes. Once the pattern is established, the depth variations are not an impediment to the flow.

Tang (1990) showed that the presence of along-strait depth gradients required the introduction of the concept of the effective length of the strait. In general the effective length is less than the physical length.

I have tried to avoid the issue of the correct value for the length of the strait. I used the Hecate Strait Model to compute a reasonable value for the important parameter W/L .

In this thesis, I make the following claims:

- Rotation-limited-flux provides a useful qualitative description of the observed spatial pattern of subsurface pressure fluctuations in Hecate Strait.

- In the Hecate Strait Model, rotation-limited-flux provides a useful guide to understanding the dependence of the steady-state transport on the Coriolis parameter and the bottom friction.
- The Hecate Strait Model results are consistent with the ratio $W/L \approx 0.2$. The analysis of the steady-state results in this appendix gives values in the range $0.1 \leq W/L \leq 0.3$.

When the model is pushed beyond these areas, it starts to break down. In particular, rotation-limited-flux does not provide a useful tool for analyzing the adjustment time data in the spin-up experiments conducted with the Hecate Strait Model.

I believe that the limitations of rotation-limited-flux arise from the fact that Hecate Strait does not have a flat bottom and that the vorticity dynamics play an important role during the first 12 hours, when the flow pattern in northern Hecate Strait is being established.